Technische Universität München
TUM School of Computation, Information and Technology

Trajectory-based Stress Tensor Visualization and its Application in Structural Design and Optimization

Junpeng Wang

Vollständiger Abdruck der von der TUM School of Computation, Information and Technology der Technischen Universität München zur Erlangung des akademischen Grades eines

Doktors der Naturwissenschaften (Dr. rer. nat.)

genehmigten Dissertation.

Vorsitz:	Prof. Dr. Martin Schulz
Prüfer der Dissertation:	1. Prof. Dr. Rüdiger Westermann
	2. Prof. Dr. Gerik Scheuermann,
	3. Prof. Charlie C.L. Wang, Ph.D.

Die Dissertation wurde am 18.11.2022 bei der Technischen Universität München eingereicht und durch die TUM School of Computation, Information and Technology am 07.05.2023 angenommen.

To my family and friends

Abstract

The design of lightweight structures is a fundamental task in structural engineering, which involves stress analysis and structural optimization. Stress tensor visualization provides advanced opportunities for understanding the stress field, however, its role in structural optimization is less clear and less explored. This thesis is dedicated to trajectory-based stress tensor visualization and its application in structural design and optimization. In specific, we contribute to three major aspects: 1) new methods for trajectory-based stress tensor visualization; 2) analysis and solution of the convergence issue of the popular porous infill optimization using stress tensor visualization techniques; 3) novel methods for structural design and topology optimization by means of principal stress lines (PSLs).

Firstly, we consider the two special issues existing in trajectory-based stress tensor visualization, its limitation in conveying the local stress state of the 2D stress field, and the lack of a dedicated method and the corresponding standard tool in visualizing the major, medium, and minor PSLs of the 3D stress field simultaneously. For the former, we present a globally conforming lattice structure composed of a set of beams. The beams are partitioned into conforming lattices, whose edges follow the PSLs and shapes convey the local stress anisotropy. The conformity at the beam intersections is ensured by solving a specifically-designed constrained optimization problem. For the latter, we develop the visual analysis tool called the 3D trajectory-based Stress Visualizer (3D-TSV), which is publicly available under the BSD license. In the design of 3D-TSV, in order to reduce visual clutter and occlusion in the resulting visualization, we propose a novel seeding algorithm for generating a domain-filling and evenly spaced set of PSLs by explicitly promoting the intersections among different types of PSLs. Furthermore, we also enable the extraction of a level-of-detail representation with the adjustable sparseness of PSLs along a certain stress direction.

Secondly, built upon the methods above and thus the obtained insights into the stress tensor, we study the convergence issue of the recently established and widely spread porous infill optimization from the perspective of stress topology analysis. The authors already show that the porous infill optimization results in 2D have good agreement with the corresponding stress tensor fields that are simulated on the solid design domain. We notice that this method cannot converge well in some

design settings. Further, we find a correlation between the convergence issue and the topology of this stress tensor field by means of the stress tensor visualization techniques. Specifically, low convergence regions are observed surrounding the so-called trisector degenerate points. Based on this observation, we propose an automatic initialization process that prescribes the topological skeleton of the stress field into the density field as solid simulation elements. These elements guide the material deposition around the degenerate points, but can also be remodeled or removed during the optimization. We demonstrate significantly improved convergence rates in a number of use cases with complex stress topology.

Lastly, we investigate the use of the domain-filling and evenly spaced PSLs in structural topology optimization, covering the mainstream density-based topology optimization and homogenization-based topology optimization. Specifically, we propose to use the PSLs to initialize the starting guess of the density-based topology optimization. Compared to the commonly used homogeneous starting guess, the convergence rate of density-based topology optimization under the local volume constraint can be significantly improved using the proposed method. Consequently, the result of the density-based topology optimization under the global volume constraint gives rise to more design details and shows better robustness concerning local damage. We also present a highly efficient method to directly generate the lightweight structure with PSLs. By employing a strain energy-based metric to adapt the thicknesses of PSL trajectories, the resulting structure shows comparable mechanical performance with the one by density-based topology optimization using the local volume constraint. We then shed light on using streamlines, which are also essentially PSLs in the context of this thesis, to de-homogenize the homogenization-based topology optimization results. Compared to the majority of prior de-homogenization approaches that represent the final structure as a binary field, our approach obtains an explicit representation in the format of a quad-dominant mesh, whose edges are assigned specific widths. This feature is beneficial for downstream operations such as user editing and fabrication process planning.

Zusammenfassung

Die Bemessung von Leichtbaustrukturen ist eine grundlegende Aufgabe der Bauchtechnik, die Spannungsanalyse und Strukturoptimierung beinhaltet. Die Spannungstensorvisualisierung bietet erweiterte Möglichkeiten zum Verständnis von Spannungsfeldern. Ihre Rolle bei der strukturellen Optimierung ist jedoch weniger klar und erforscht. Diese Dissertation widmet sich der trajektorienbasierten Spannungstensorvisualisierung und ihrer Anwendung in der Baukonstruktion und -optimierung. Insbesondere tragen wir zu drei Hauptaspekten bei: 1) neue Methoden zur trajektorienbasierten Visualisierung von Spannungstensoren; 2) Analyse und Lösung des Konvergenzproblems der populären Optimierung poröser Füllungen unter Verwendung von Spannungstensor-visualisierungstechniken; 3) neue Methoden für Strukturdesign und Topologieoptimierung mittels Hauptspannungslinien (PSLs).

Erstens betrachten wir die beiden speziellen Probleme, die bei der trajektorienbasierten Spannungstensorvisualisierung bestehen, ihre Limitationen bei der Vermittlung des lokalen Spannungszustands der 2D-Spannungsfelder und das Fehlen einer dedizierten Methode und korrespondierender Hilfsprogramme zur gleichzeitigen Visualisierung der PSLs der drei Hauptspannungsrichtungen des 3D-Spannungsfeldes. Für Ersteres stellen wir eine global konforme Gitterstruktur vor, die aus einer Menge von Balken besteht. Die Balken werden in konforme Gitter unterteilt, deren Kanten den PSLs folgen und deren Formen die lokale Spannungsanisotropie vermitteln. Die Konformität an den Balkenkreuzungen wird durch Lösen eines speziell entworfenen eingeschränkten Optimierungsproblems sichergestellt. Für letzteres entwickeln wir das visuelle Analysetool namens 3D Trajectory-based Stress Visualizer (3D-TSV), das unter der BSD-Lizenz öffentlich verfügbar ist. Um visuelle Unordnung und Verdeckungen in der resultierenden Visualisierung zu reduzieren, schlagen wir beim Design von 3D-TSV einen neuartigen Seeding-Algorithmus zum Generieren einer bereichsfüllenden und gleichmäßig verteilten Menge an PSLs vor, indem explizit Schnittpunkte zwischen verschiedenen Arten von PSLs begünstigt werden. Überdies ermöglichen wir auch die Extraktion einer Level-of-Detail Darstellung mit einstellbarer Besetzungsdichte von PSLs entlang einer bestimmten Spannungsrichtung.

Zweitens untersuchen wir, aufbauend auf den oben genannten Methoden und den daraus

gewonnenen Erkenntnissen über den Spannungstensor, die Konvergenzfrage der kürzlich neuerdings etablierten und weit verbreiteten Optimierung poröser Füllungen aus der Perspektive der Spannungstopologieanalyse. Die Autoren zeigen bereits, dass die Optimierungsergebnisse für poröse Füllungen in 2D eine gute Übereinstimmung mit den entsprechenden Spannungstensorfeldern haben, die auf der Solid-Design-Domäne simuliert werden. Wir stellen fest, dass diese Methode in einigen Designeinstellungen nicht gut konvergieren kann. Darüber hinaus finden wir eine Korrelation zwischen dem Konvergenzproblem und der Topologie dieses Spannungstensorfeldes mit Hilfe der Spannungstensorvisualisierungstechniken. Insbesondere werden Bereiche niedriger Konvergenz in der Umgebung sogenannter degenerierter Trisektorpunkte beobachtet. Basierend auf dieser Beobachtung schlagen wir einen automatischen Initialisierungsprozess vor, der das topologische Skelett des Spannungsfeldes als solide Simulationselemente in das Dichtefeld einschreibt. Diese Elemente führen den Materialauftrag um die degenerierten Punkte herum, können aber bei der Optimierung auch umgeformt oder entfernt werden. Wir zeigen deutlich verbesserte Konvergenzraten in einer Reihe von Anwendungsfällen mit komplexer Spannungstopologie.

Schließlich untersuchen wir die Verwendung der bereichsfüllenden und in regelmäßigen Abständen platzierten PSLs in der strukturellen Topologieoptimierung, wobei wir die vorherrschende dichtebasierte Topologieoptimierung und die homogenisierungsbasierte Topologieoptimierung abdecken. Insbesondere schlagen wir vor, die PSLs zu verwenden, um die Anfangsschätzung der dichtebasierten Topologieoptimierung zu initialisieren. Gegenüber der allgemein verwendeten homogenen Startschätzung kann mit dem vorgeschlagenen Verfahren die Konvergenzrate der dichtebasierten Topologieoptimierung unter der lokalen Volumenbeschränkung deutlich verbessert werden. In der Folge führt das Ergebnis der dichtebasierten Topologieoptimierung unter der globalen Volumenbeschränkung zu mehr Designdetails und zeigt eine bessere Robustheit gegenüber lokalen Beschädigungen. Wir präsentieren außerdem eine hocheffiziente Methode, um die Leichtbaustruktur direkt mit PSLs zu erzeugen. Durch die Verwendung einer auf Dehnungsenergie basierenden Metrik zur Anpassung der Dicken von PSL-Trajektorien zeigt die resultierende Struktur vergleichbare mechanische Eigenschaften wie eine durch dichtebasierte Topologieoptimierung unter Verwendung der lokalen Volumenbeschränkung erzeugte Struktur. Anschließend beleuchten wir die Verwendung von Stromlinien, die im Kontext dieser Arbeit ebenfalls im Wesentlichen PSLs sind, um die Ergebnisse der homogenisierungsbasierten Topologieoptimierung zu dehomogenisieren. Im Vergleich zu den meisten früheren Dehomogenisierungsansätzen, die die endgültige Struktur als binäres Feld darstellen, erhält unser Ansatz eine explizite Darstellung im Format eines viereckdominanten Netzes, dessen Kanten bestimmte Breiten zugewiesen werden. Diese Funktion ist für nachgelagerte Vorgänge wie Benutzerbearbeitung und Fertigungsprozessplanung von Vorteil.

Acknowledgments

First and foremost, I want to give my sincere appreciation to Prof. Dr. Rüdiger Westermann for the supervision and support, he is one of the best Ph.D. supervisors one could wish for. What impresses me most is his style of supervising. Once we set a new project, he is always available for discussion and giving suggestions but without any hard restrictions, and is open to whatever I want to try during the project. The magic part is that he seems always has the ability to pull the project back on the right track on time in the end, no matter how far I go in the less related direction. In this way, all of my projects have proceeded smoothly, and my knowledge has been broadened significantly. I also admire his scientific attitude, every time on the eve of paper submission, he always has the full passion to polish the paper manuscript tirelessly, from details like image layout and linguistic expression. Another thing I've been enjoying so much during my 4-years stay here is his funny remarks on every topic, and our chats are always joyful. From these experiences, I get to know not only how to do professional research, but also how to be a good researcher.

Next, I want to give my special thanks to Prof. Dr. Dr. Jun Wu at TU Delft. As the mentor of my degree program, he has given me a lot of advice in arranging the career of my Ph.D. Furthermore, he, being the co-author, has also deeply participated in all of my research projects involved in this thesis. The wide extension of my research to structural topology optimization heavily relies on his guidance. Every time having a discussion with him, he can always grasp the critical point of the project quickly and give me constructive suggestions. I'd also like to sincerely thank my other co-authors Christoph Neuhauser and Dr. Xifeng Gao. Without their generous help and collaboration, the publications included in this thesis would be impossible.

I'm thankful to Susanne Weitz and Sebastian Wohner for their organizational and technical supports. Susanne has helped me with my contracts, business trip applications, and reimbursement, etc. Our system administrator Sebastian has helped me remove all of the barriers to hardware and website configuration. My colleagues Dr. Rachel Mengyu Chu, Sebastian Weiss, Dr. Alexander Kumpf, Christian Reinbold, Seyedbehdad Ghaffari, You Xie, Dr. Ji Hou, Dr. Michael Kern, Ludwig Leonard, Kevin

Höhlein, Fatemeh Farokhmanesh, Josef Stumpfegger and Dr. Mathias Kanzler have made my work and life experience here unforgettable. I'd also like to thank Jianyu Wang, Shichao Wei, Hao Chen, He Luo, Dr. Huan Zhao, Yingjian Liu, Dr. Shuangshuang Meng, Prof. Jinyou Xiao and Prof. Junjie Rong, we had very fruitful discussions during my Ph.D. career.

Last but not least, I'm grateful for the enormous support from my girlfriend Zhijuan, my parents, and my sister. The encouragement and stability they have been giving to me have been helping me pursue the desired goal without worries.

This work was supported by the German Research Foundation (DFG) under grant number WE 2754/10-1 titled *Stress Visualization via Force-Induced Material Growth*.

Contents

1 Introduction

Stress analysis is one of the fundamental approaches in structural engineering and widely exists in mechanical, civil, and biomechanical structural design, etc. The general purpose of performing stress analysis is to test the strength of the structural design under some specific boundary conditions, thus, evaluating the rationality of the design, and further, guiding the improvement and optimization of it. With the help of some properly designed stress visualization techniques, the obtained stress features can even be directly used in the design and optimization of lightweight structures, e.g., one can place material along the stress trajectories to obtain the lightweight structure [KSZ*14, TM15, KLC16]. Compared to conventional methods like mainstream topology optimization [PP19, WSG21], one can obtain multiple unique advantages in lightweight structure design and optimization by leveraging stress tensor features, for instance, significantly lower computational burden, and more degrees of freedom on shape control of the design. However, such a realm has not yet been explored systematically for various methodological and practical reasons.

This thesis first presents novel methods to tackle the two concrete issues in stress tensor visualization, encoding local stress states into the grids generated by the intersected major and minor principal stress lines (PSLs) inherently, and a dedicated seeding approach for evenly spaced PSLs. Then by means of the obtained visualization techniques and insights into the stress tensor field, we shift to structural design and optimization, therein, we specifically investigate the convergence behavior of the density-based topology optimization and the de-homogenization process of homogenization-based topology optimization. Apart from the concrete contributions to methodology, this thesis is also devoted to conceptually boosting the interaction of developments between stress tensor visualization and structural design and optimization.

The stress state at each point in a solid object under load is fully described by the three normal stress components and three shear stress components, which , in general, are arranged into a symmetric second-order tensor, i.e., stress tensor. Accordingly, the stress field across the domain can be represented

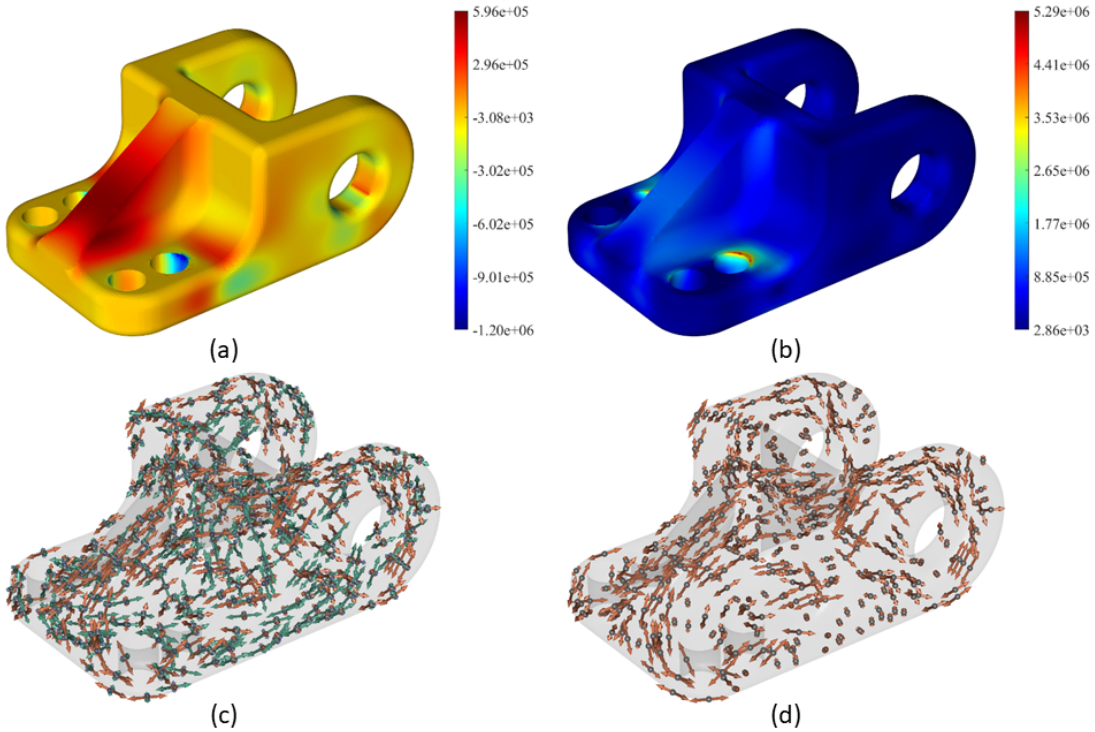

Figure 1.1: The demonstration of stress visualization in practical engineering application. (a) The distribution of a single shear stress component. (b) Von Mises stress. (c) The stress tensor is shown by arrowheads at a set of sampling points. (d) A single principal stress component. The used mesh is courtesy of [GSP19].

by a symmetric second-order tensor field.

Stress visualization can provide intuitive visual clues for investigating the stress distribution. Yet, it's still a challenging task to visualize the entire stress tensor field due to the potential visual clutter and occlusion, especially in 3D. Thus, in practical engineering applications, one usually treats the stress tensor field as a set of scalar fields, then visualizes them independently, e.g., the six Cartesian stress components, amplitudes of principal stresses, and the von Mises stress derived from the maximum distortion criterion. This can be achieved by color mapping (Figure 1.1a, b).

Taking the stress tensor field as a set of the scalar fields and visualizing them separately can already provide the basic information about the stress field, e.g., the spatial distribution of the maximum stress, thus, helping the engineer spot the potential weakness of the structural design. However, some tensor features are missing from such stress visualization. For instance, the correlation among different stress tensor attributes, the stress tensor orientations, and the topology of the stress tensor field. This inevitably restricts the understanding of the stress field. A rather straightforward way to present the stress tensors is to show a set of arrowheads at the picked sampling points in the domain, where the orientations and lengths of the arrowheads indicate the principal stress directions

and the corresponding principal stress amplitudes. The principal stress directions are defined as the directions where the shear stress components vanish, and the corresponding normal stresses are termed principal stress amplitudes. As can be seen from Figure 1.1c, however, such visualization incurs severe visual clutter and occlusion, meanwhile, violates the continuity of the stress field. In order to improve the visual quality, one can also investigate each single principal stress direction independently (see Figure 1.1d), but still the perceptual issues cannot be avoided essentially. To this end, one needs to resort to some dedicated stress tensor visualization techniques.

One can obtain a deeper insight into the stress field via the stress tensor features, thus, evaluating the structural strength more comprehensively. More importantly, several works in recent years have shown that stress tensor features themselves can play a significant role in the design and optimization of lightweight structures.

The optimality of structure is measured by the compliance minimization in this thesis, i.e., with the same material consumption and under the same boundary condition, the optimal design shall give rise to minimal strain energy. Compared to the mainstream techniques like topology optimization, for now, the related methods of using stress tensor features for structural optimization have only appeared sporadically. There are multiple reasons for this, e.g., lack of well-established stress tensor visualization tools, and insufficient interaction of the research between stress tensor visualization and structural optimization. Despite this, such methods have already shown the unique power of using stress tensor features in structural design and optimization. For instance, it can provide a more computationally economical way to perform structural optimization and produce novel and functional patterns of the material layouts. Refer to [KAH14, TM15, KLC16, DFLW17, WWG21].

Having the mentioned above in mind, this thesis is built upon the study of these two topics below:

- ***How to visualize the stress tensor field?***
- ***How does stress visualization benefit structural design and optimization?***

In general, the existing stress tensor visualization techniques can be categorized into topology-, glyph- and trajectory-based methods [KASH13, HBK*21].

Topology-based approaches for stress tensor visualization abstract from the depiction of stress directions and focus on revealing specific topological characteristics of the tensor field, for instance, the *degeneracy* and *separatrices* [DH94, HLL97], which can reveal some essential features of the stress tensor field, see Figure 1.2a. However, the robust extraction of these topological characteristics and the interpretation of their physical significance are still under exploration, especially for the 3D stress field simulated on the arbitrary hexahedral or even hybrid meshes [ZP04, RKZZ18].

In the glyph-based method, the stress tensor field is depicted by a set of well-designed geometric primitives placed at the selected positions, here, the geometric primitive is termed the tensor glyph,

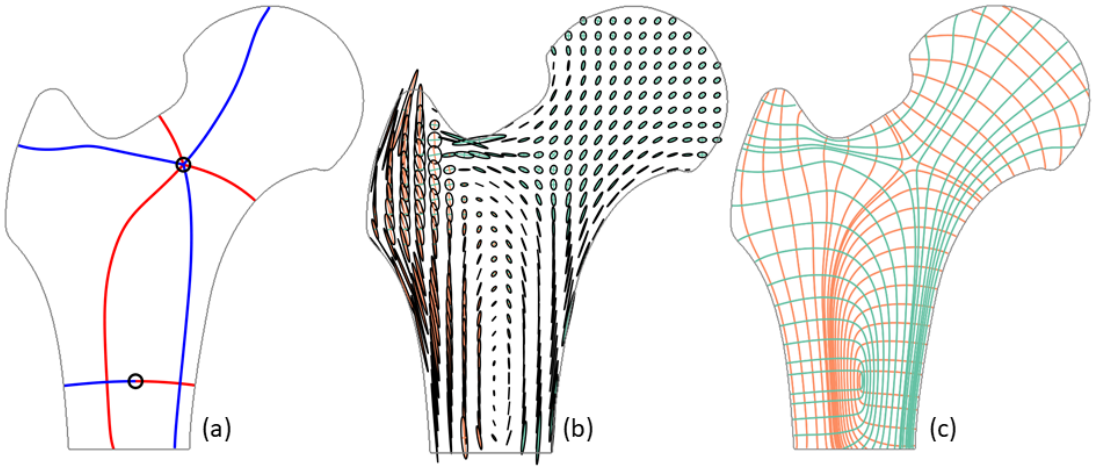

Figure 1.2: Demonstration of different stress tensor visualization techniques. (a) The topology-based approach shows the degenerate points (black circle) and separatrices (red and blue trajectories). (b) The glyph-based approach shows the tensor glyphs at the selected positions, the axes of each ellipse point to the directions of major and minor principal stresses, and the signs of principal stresses are distinguished by different colors (orange for positive, turquoise for negative). (c) Trajectory-based approach shows the major (orange) and minor (turquoise) PSLs.

see Figure 1.2b. It's efficient to convey the local stress state via the tensor glyph. Yet, it violates the continuity of stress field visually, and causes severe visual occlusion when used in 3D. To evade such situation, a series of works on the glyph placement strategy have been proposed [KAH14].

Trajectory-based methods choose the PSLs as visual abstractions of the stress field, which are generated by performing numerical integral along the principal stress directions (Figure 1.2c). PSLs can approximately but intuitively indicate the transfer path of load within the solid and show the mutual relationships between the different principal stress directions [DH93, DGBW09]. However, due to the mutual orthogonality among different types of PSLs, the trajectory-based visualization is accompanied by the visual clutter when showing different types of PSLs simultaneously. One of the critical challenges of trajectory-based stress tensor visualization is how to generate a set of PSLs, which can convey the directions of the entire stress tensor field completely while incurring less visual clutter. This obstacle prevents the wide adoption of such visualization, and drags the development of a standard tool for such an analysis, though it's promising to obtain an informative visualization of the stress directions in a 3D solid.

The correlation between the optimal structure and the stress tensor field was firstly expounded by Michell in the seminal work on structural optimization [Mic04], i.e., the sub-structs of the optimal structure should only bear either the pure tension or compression stress. In other words, the sub-structs follow the principal stress directions such that the shear stresses vanish, also known as Michell's theorem. Michell's theorem lays the foundation of lightweight structure design and optimization, yet,

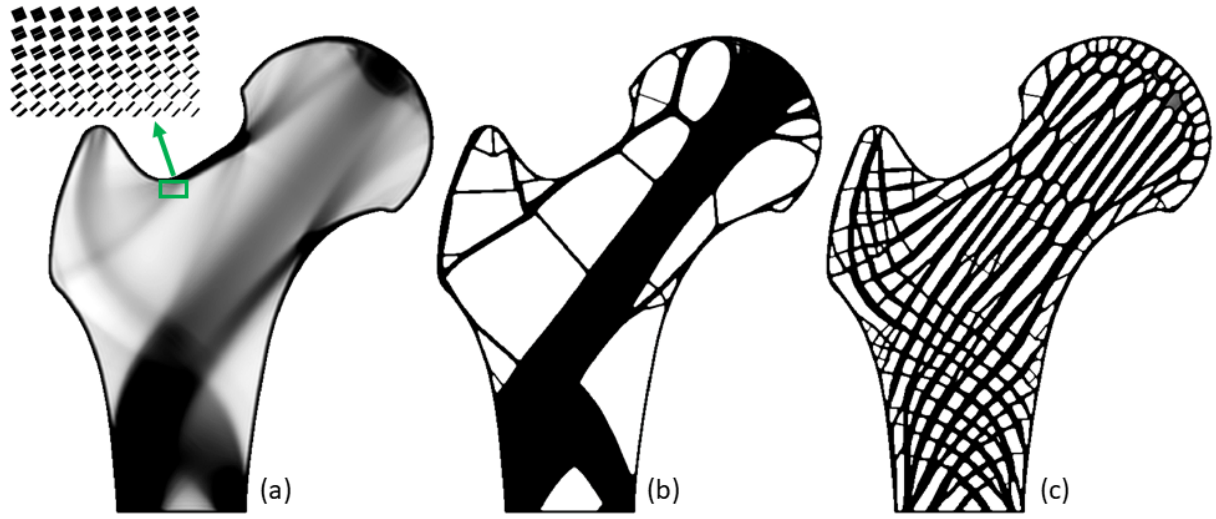

Figure 1.3: Demonstration of different topology optimization techniques. (a) Homogenization-based topology optimization ($c = 6.892, v = 0.500$). (b) Density-based topology optimization under global volume constraint ($c = 7.427, v = 0.500$). (c) Density-based topology optimization under local volume constraint ($c = 8.891, v = 0.539$). Here c is the compliance value of the structural design, and v is the volume fraction of the material consumption.

it's very difficult to obtain its exact analytic solution. One usually uses some numerical methods to get the near-optimal solution of Michell's theorem. This is often formulated as an optimization problem, e.g., topology optimization, in which the material distribution is optimized. The homogenization-based topology optimization and density-based topology optimization are two major branches in structural topology optimization for compliance minimization.

In the seminal work of homogenization-based topology optimization by Bendsøe and Kikuchi [BK88], they employed a material model, i.e., the square unit cell with a rectangular hole, to characterize the material with infinitely fast variation in solid and void regions. The material properties of such cells can be constructed using homogenization [AA14]. The cell orientations and hole sizes are adjusted to minimize the compliance of the structure during the course of optimization, see Figure 1.3a. It's worth pointing out that the optimal cell orientation is aligned with the corresponding principal stress direction subject to the single loading case [Ped89]. The homogenization-based approach results in a mathematical specification of theoretically optimal structure. Yet how to translate the specification of spatially varying cells into a globally consistent geometry has remained a challenge. The lack of a consistent geometry means that the optimal structure is not manufacturable. Recent years have seen a revival of homogenization-based topology optimization since Pantz and Trabelsi pioneered the way for the projection-based post-process [PT08]. This post-process is now generally referred to as *de-homogenization*, focusing on interpreting the multi-scale result of homogenization-based topology optimization into a single-scale description. It's appealing to combine the homogenization-

based topology optimization and de-homogenization since it enables to obtain the high-resolution design from the solution simulated on the coarse scale in a highly efficient way, as demonstrated in [GS18, GSA*20].

Density-based topology optimization can be an alternative solution concerning the manufacturing challenge of the homogenization-based one. It optimizes the distribution of a homogeneous isotropic material, e.g. using a material model known as *Solid Isotropic Material with Penalization* (SIMP) [Ben89, ZR91, Mle92]. Density-based topology optimization commonly starts from a homogeneous starting guess, then iteratively adjusts the relative density value of each simulation element to optimize for structural performance under the available material budget, i.e., the global volume constraint (Figure 1.3b). It produces the binary material layout (1 for the fully deposited region and 0 for the void region) as the final design, which significantly benefits the downstream fabrication process. Being a full-scale method, the resolution of the density-based topology optimization result depends on the simulation resolution. As known that the theoretically optimal structures are multi-scale, and in principle, the density-based topology optimization can approach such design as long as a sufficiently fine simulation mesh and well-designed continuation scheme are utilized. This, however, is computationally expensive. Wu *et al.* subtly mitigated this limitation by replacing the global volume constraint with a local one [WAWS18]. This constraint explicitly controls the deposition ratio around each simulation element, thereby, a domain-filling structural design is obtained by density-based topology optimization simulated on a relatively low resolution. The resulting structure under such a constraint spans multiple length scales, see Figure 1.3c. As a side-effect, the convergence behavior of density-based topology optimization is negatively affected to some extent because of such a constraint. Comparing the compliance values of the different structural designs shown in Figure 1.3, we see that the homogenization-based topology optimization gives rise to minimal compliance, and the density-based topology optimization under local volume constraint with the largest compliance.

Altogether, we first study the stress tensor visualization in this thesis, including 1) how to combine the advantages of both the trajectory- and glyph-based methods in a single visualization, and 2) how to effectively visualize the three mutually orthogonal principal stress directions in 3D solids. Built upon the proposed stress tensor visualization techniques and thus the insights into the stress tensor field, we comprehensively investigate the application of the stress tensor in topology optimization.

We consider constructing the de-homogenization strategy for the homogenization-based topology optimization by using streamlines of the direction field extracted from the cell orientations, here the streamlines are essentially also PSLs since the cell orientation is given by principal stress direction. Specifically, we convert the optimized cells into a consistent and editable parametrization space that is depicted by a lattice structure composed of quadrilateral and triangular cells whose edges follow the principal stress directions. With the proposed method, the singularity issue, which needs additional efforts in existing de-homogenization approaches, can be solved using the stress tensor topology

analysis inherently.

For the density-based topology optimization, we aim to promote the material deposition to converge to a structure composed of sub-structures spanning multiple length scales in place of a mono-scale one, meanwhile, avoiding the use of the extremely fine mesh resolution. To this end, we consider employing the domain-filling and evenly spaced PSLs as starting guess to guide the material distribution, given that topology optimization in practice is a non-convex problem. As a secondary goal, the convergence rate should also be improved by the proposed starting guess, given that such a starting guess is closer to the optimal design than the homogeneous starting guess.

In addition, inspired by the good agreement between the optimized porous infill achieved by the density-based topology optimization and the corresponding principal stress directions [WAWS18], we also consider generating the near-optimal structure directly from the PSL layout instead of an iterative optimization process. We aim to reduce the computational complexity of structural optimization significantly, meanwhile, releasing more degrees of freedom to the user for shape control of the final design.

1.1 Contributions

In close collaboration with other researchers, several contributions are made in this thesis to handle the research questions mentioned above. We present the globally conforming lattice structure for stress visualization, which simultaneously conveys divergence/convergence and stress anisotropy by intersected PSLs. We also develop the 3D-TSV to visualize the three mutually orthogonal principal stress directions simultaneously. For structural design and optimization, we solve the convergence issue of porous infill optimization by means of stress topology analysis. With using the domain-filling and evenly spaced PSLs to initialize the starting guess of density-based topology optimization, the results spanning multiple length scales are obtained from the topology optimization under global volume constraint. And the convergence process of topology optimization under local volume constraint is accelerated significantly, accompanied by improved regularity of the resulting design. Such initialization strategy also inspires another work of designing near-optimal lightweight structures directly using PSLs in a highly efficient way. Motivated by the use of PSLs in structural design and optimization, we propose an essentially PSLs-guided de-homogenization for homogenization-based topology optimization. Besides the improved computational efficiency, more importantly, the proposed method represents the final design with an explicit geometrical description, the quad-dominant mesh, which is beneficial to user editing and fabrication.

Besides the concrete contributions to methodology, all these works also make a step to get the research of stress tensor visualization and structural design and optimization better interact mutually. In other words, taking some specific requirements for structural design and optimization into the

construction of stress tensor visualization may lead to novel visualization methods, in return, properly designed stress tensor visualization techniques can also empower structural design and optimization. The detailed contributions of this thesis are divided into five aspects corresponding to the five associated publications below:

- Considering the limitation of trajectory-based stress tensor visualization in conveying local stress state and the deficiency of glyph-based method in presenting the continuity of stress field, we propose the *globally conforming lattice* for stress tensor visualization in 2D (Paper A [WWW20]). We introduce the use of beams instead of single lines to create a stress-following grid structure in multiple dimensions, and to encode the ratio of principal stresses into the geometry of the beam elements. Thus, only line segments coinciding with stress lines are shown, along all principal directions. Conformity of beams at intersections is achieved via the solution of a constrained optimization problem. The optimization computes for all intersection points the size and aspect ratio of corresponding beam elements, so that the ratio of principal stresses is maintained and the edges of connected elements meet when continued along the respective PSL. To circumvent the sudden divergence of PSLs near the singularity of the stress field, the stress topology analysis is also utilized to guide the placement of beams. To a certain extent, the proposed method combines the advantages of both the trajectory- and glyph-based methods by solving a specifically-designed constrained optimization problem
- We present the 3D Trajectory-based Stress Visualizer (3D-TSV) in Paper B [WNW*22], a dedicated system and methodology for the visual analysis of the PSLs in 3D stress fields. 3D-TSV builds upon existing techniques for line seeding in vector fields [JL97, MTHG03], but extends them towards the specific use for stress tensor visualization by considering the three principal stress directions in the seeding process simultaneously. 3D-TSV produces a set of domain-filling and evenly spaced PSLs, meanwhile, different types of PSLs are promoted to intersect with each other for improved regularity of the visualization. This is achieved by enforcing the new PSL to "grow out" from the existing PSLs that belong to other principal stress directions during the sequential seeding process. In addition, the seeding process is parameterized using different distance thresholds for each type of PSL, which allows controlling separately the sparseness of the PSLs of each type. We use this possibility to enable a level-of-detail (LoD) visualization that combines a dense seeding of a selected PSL type with a seeding at a user-selected sparseness level of the respective other PSLs. 3D-TSV is made publicly available under a BSD license.
- We study the convergence issue of the popular porous infill optimization [WAWS18] and solve it by introducing a stress topology-guided initialization strategy (Paper C [WWW22b]). Porous infill optimization has become a popular branch in density-based topology optimization, which produces a structural layout that has good agreement with the principal stress directions of the

corresponding stress field. In some design settings, however, the iterative optimization process converges only slowly, or not at all even after hundreds or thousands of iterations. Specifically, we find that the low convergence region appears around the so-called *trisector degenerate point* of the corresponding stress field. According to our analysis, this is due to the high isotropy of the stress tensor close to a tri-sector degenerate point, consequently, a locally consistent binary material layout cannot be efficiently decided by the optimizer. Based on this discovery, and considering the topology optimization is a non-convex problem, i.e., depending on the initialization a different local optimum can be reached, we propose an automatic initialization strategy to guide the material deposition around the trisector degenerate point. This initialization strategy is based on the computation of the *topological skeleton* of trisector degenerate point and achieved by giving the simulation elements visited by the topological skeleton a higher density value than others in the starting guess. We also observe that the optimization keeps the initialized elements more or less unchanged, this further demonstrates the good agreement between the 2D optimized porous infill and the principal stress directions.

- Built upon the methods in Paper C and Paper C, we in Paper D [WWW22c] present a novel method of using PSLs for density-based topology optimization. In particular, we use domain-filling and evenly spaced PSLs to initialize the starting guess of porous infill optimization [WAWS18], which not only significantly improves the convergence rate but also leads to a more regular design that follows the PSLs on the whole. We also extend this initialization strategy to the classic density-based topology optimization, i.e., under the global volume constraint, which usually produces a predominantly mono-scale structure. We find that some PSL trajectories used for initialization are also maintained in such optimization settings, thereby, the final design exhibits more sub-structures that span different length scales. We demonstrate that such design is more robust with respect to the local damage compared to the original one. Further, we present a PSLs-guided material layout approach for quick structural design and optimization. A strain energy-based importance metric is proposed to adjust the thickness of different PSL trajectories for improving mechanical performance. Through our test, this result shows a similar appearance and comparable mechanical performance with porous infill optimization but obtained in a highly computationally economical way.
- Inspired by Paper D using PSLs for structural design, we present a novel de-homogenization approach for the homogenization-based topology optimization result to achieve the efficient design of high-resolution load-bearing structures (Paper E [WWW22a]). The proposed approach is built upon the parametrization of using streamlines, here the streamlines are essentially PSLs in the context of this thesis. This approach avoids the projection step to optimize for a consistent fine-grid scalar field (e.g., in [GS18]), and thus is computationally efficient. We first parameterize the design domain using a set of domain-filling and evenly spaced streamlines that

are aligned with the edges of optimized cells. The streamlines are then converted into a graph, from which we construct a quad-dominant mesh whose edges follow the optimized direction fields. In contrast to the majority of prior de-homogenization approaches that represent the final structure as a binary field, our approach generates an explicit representation in the form of a quad-dominant mesh, each edge of which is assigned a unique width according to the average direction and volume fraction of the optimized cells covered by an element. This compact representation is beneficial for downstream operations such as user editing and fabrication process planning.

1.2 Outline

The reminder of this thesis is organized as follows: In Chapter 2, we review the related works in detail regarding the research scopes of this thesis. The fundamental theorem and methods involved are introduced in Chapter 3 to make this thesis self-contained. From Chapter 4 to Chapter 8, we list the abstracts and the individual author contributions of each published paper that are part of the thesis, sequentially. Chapter 9 concludes this thesis, and the associated publications with this thesis are appended at the end of the document.

1.3 List of Publications

The methods described in this thesis have been originally proposed and published in the following peer-reviewed journal and conference proceedings. To facilitate readers to navigate it, we also use an additional diagram (Figure 1.4) to show the relation of each publication to the main scope of this thesis and the correlation among different publications:

Paper A: **Junpeng Wang**, Jun Wu, and Rüdiger Westermann.
"A Globally Conforming Lattice Structure for 2D Stress Tensor Visualization".
In: *Computer Graphics Forum*, Volume 39, Number 3, pp. 417-427, June 2020.
doi: 10.1111/cgf.13991

Paper B: **Junpeng Wang**, Christoph Neuhauser, Jun Wu, Xifeng Gao, and Rüdiger Westermann.
"3D-TSV: The 3D Trajectory-based Stress Visualizer".
In: *Advances in Engineering Software*, Volume 170, August 2022.
doi: 10.1016/j.advengsoft.2022.103144

Paper C: **Junpeng Wang**, Jun Wu, and Rüdiger Westermann.
"Stress Topology Analysis for Porous Infill Optimization".
In: *Structural and Multidisciplinary Optimization*, Volume 65, Number 3, pp. 1-13, February

2022.
doi: 10.1007/s00158-022-03186-0

Paper D: **Junpeng Wang**, Jun Wu, and Rüdiger Westermann.
"Stress trajectory guided structural design and topology optimization".
In: *ASME IDETC-CIE: 42nd Computers and Information in Engineering Conference (CIE)*, November 2022.
doi: 10.1115/DETC2022-89030

Paper E: **Junpeng Wang**, Rüdiger Westermann, and Jun Wu.
"Streamline guided De-Homogenization for High-Resolution Structural Design".
In: *ASME Journal of Mechanical Design*, December 2022.
doi: 10.1115/1.4056148

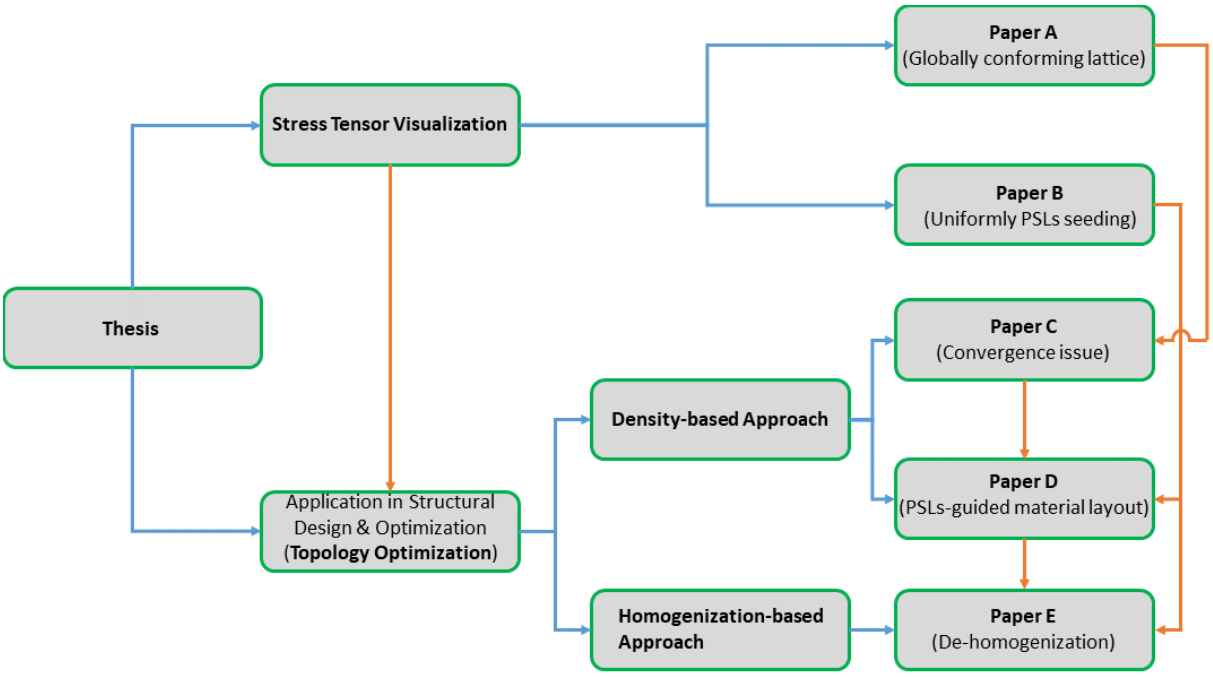

Figure 1.4: Navigation map of the thesis. The orange arrowheads indicate the dependence between the different modules.

2

Related Work

In this chapter, we systematically review the prior work that lies in the scope of this thesis, covering stress tensor visualization, structural topology optimization, and stress in structural design and optimization. Specifically, stress tensor visualization is expounded from the perspectives of trajectory-, glyph- and topology-based methods in Section 2.1. Then coming to the structural topology optimization in Section 2.2, at which the density-based approach and homogenization-based approach are visited, the latter is accompanied by a so-called de-homogenization process to obtain the manufacturable design. In Section 2.3, we recall the concrete work about using stress tensor features in structural design and optimization, herein, it also serves as a bridge between the stress tensor visualization and structural topology optimization.

2.1 Stress Tensor Visualization

The stress tensor is a representative symmetric second-order tensor, thus, its visualization also applies to the established classification of second-order tensor visualization. In the review work [KASH13], the tensor visualization techniques are categorized into tensor field segmentation, local tensor visualization methods, and continuous tensor visualization methods. The tensor field segmentation is devoted to dividing the entire data into regions that exhibit similar features, thereby, facilitating the analysis and interpretation of the data. Such methods are typically about obtaining the *degeneracy* and *separatrices* of the tensor data by means of the topology analysis. The local tensor visualization methods focus on the design and placement of tensor glyphs. The continuous tensor visualization methods are further subdivided into the scalar visualization methods, the vector visualization methods, and the texture-based methods. The latest review work [HBK*21] shares a similar view with [KASH13] in terms of the classification of the tensor field visualization, except splitting the continuous tensor visualization

methods into the geometry-based methods and texture-based methods, meanwhile, omitting the scalar visualization methods.

After comprehensively considering these two classification criteria and the latest advances on this topic, this thesis methodologically classifies the stress tensor visualization into the trajectory-, glyph- and topology-based methods.

2.1.1 Trajectory-based Methods

Trajectory-based stress tensor visualization focuses on conveying the continuity and directionality of the stress field, this can be achieved either by the principal stress lines (PSLs) or the stress texture depicting the principal stress directions.

The concept of tensor lines can be dated back to the original work [Dic89], where they defined that the tensor lines follow the eigenvector directions of the given tensor field, and each eigenvector field corresponds to one family of tensor lines. Here the tensor lines can be taken as the generalization of streamlines of second-order tensor fields, and the PSLs are subject to the concept of tensor lines. Building upon PSLs, Delmarcelle and Hesselink [DH92, DH93] introduced the concept of *hyperstreamlines*. A hyperstreamline shows a cylinder-like geometric structure, which is formed by extruding ellipses along a selected PSL. The directions and lengths of the major- and minor-axis of the ellipses correspond to the directions and amplitudes of the other two principal stresses. Even though hyperstreamlines were introduced for the visualization of 3D stress fields, they can be adapted straightforwardly to 2D scenarios. A direct extension of the hyperstreamlines is the so-called *hyperstreamsurface*, which is formed by seeding a set of hyperstreamlines on a given region, then connecting the integration points of these hyperstreamlines by polygons [JSF*02, VBVP04]. In order to tackle the limitation of hyperstreamlines in revealing the ratio among the three principal stresses, Kretzschmar *et al.* introduced a variant of hyperstreamline, called *tensor spines* [KGSS20], where the PSL is depicted with a circular tube and two perpendicular surfaces through the central axis of this tube. The radius of the tube and widths of the two surfaces represent the absolute values of the three principal stresses, respectively. In this way, an intuitive comparison of the ratio of the three principal stresses is provided. This technique was later extended to visualize the stress on the surface when optimizing the interface connection between different components [KRG*22]. *Stress-nets* [WB05] are achieved by rendering together major and minor PSLs, at the same time trying to place them evenly to reduce clustering, which has been used to investigate the crack propagation and new features of the data are obtained, but its utility is restricted in 2D. Dick *et al.* [DGBW09] presented a real-time application to aid implant planning in orthopedics by means of the PSLs, where the major and minor PSLs are traced from the loaded regions and colored with the selected scalar stress components. This application can give high-quality rendering results and instant response to user interaction because of the use of advanced techniques in computer graphics.

The placement of PSLs has a strong influence on the quality of the visualization, i.e., revealing the data effectively without losing critical information, meanwhile, incurring fewer perceptual problems like visual clutter and occlusion [SBGC20]. Dick *et al.* [DGBW09] only considered the major and minor PSLs traced from the seed points that are randomly distributed in the loaded regions, which clearly shows the stress trajectories from the loaded area to the fixed area. However, such a method leaves large sub-domains uncovered and not showing the mutual variations of the stress directions. A seemingly viable way is to consider the tensor field as a set of independent vector fields, then borrow the well-established idea of creating domain-filling and evenly spaced streamlines in vector fields. Turk and Banks [TB96] and Jobard and Lefer [JL97] were one of the first to introduce seeding strategies for generating evenly spaced streamlines in 2D vector field. Numerous extensions and improvements of these concepts have been proposed since then. In particular, Mattausch *et al.* [MTHG03] constructed a level-of-detail streamline visualization from the evenly spaced seeding. Vilanova *et al.* [VBVP04] proposed an extension of the approach by Jobard and Lefer to diffusion tensor fields, which detects the distance between the new streamline and the existing ones during the tracing process. They demonstrated the generation of evenly spaced streamlines, however, the approach suffers from 'unfinished' streamlines that are caused by an artificial stopping criterion and only considers a single eigenvector field at a time.

For 3D flow visualization, dedicated approaches have been developed to reduce the visual clutter and occlusion of densely distributed streamlines in 3D fields [YKP05, YWSC11, KFW16]. Though these methods can ensure an evenly spaced PSL distribution in a single principal stress field, they do not necessarily reduce the visual clutter and occlusion when showing the different types of PSLs simultaneously because of the mutual orthogonality among different principal stress directions. The visual clutter can be reduced by visualizing the single stress directions side-by-side, yet juxtaposition makes it difficult to effectively relate the three mutual orthogonal stress directions to each other. As such, a dedicated evenly spaced seeding approach for tensor fields is needed. In Paper B [WNW*22], we presented a dedicated seeding approach to visualize the three types of mutually orthogonal PSLs simultaneously. This method is adapted from the classic evenly spaced streamline seeding for vector field but improves the visual quality of the resulting visualization via explicitly promoting the intersections among different types of PSLs during the course of seeding.

Besides PSLs, the texture-related method also plays an important role in trajectory-based stress tensor visualization, which doesn't give the stress trajectories explicitly but can clearly convey an overview of the stress direction information. The texture-related methods are mainly based on the classic Line Integral Convolution (LIC) that is originally used for vector field [CL93]. Zheng and Pang [ZP03] presented the *HyperLIC* method, which generates a texture encoding the anisotropic properties of a 2D or 3D tensor field. However, this method may lead to misinterpretations on the stress state since it doesn't distinguish the signs of the principal stress values. The fabric-like texture [HFH*04, HFH*06]

overcame the limitation of the *HyperLIC* in distinguishing the signs of principal stress values. Instead of visualizing the original stress field directly, they visualized a proxy tensor field, which shares the same topology with the original stress field but is positive-definite. Finally, the regions with negative principal stress values (under compression) are encoded in a dense texture, and regions with positive principal stress values (under tension) are encoded in a sparse texture. Besides conveying the direction, the resulting visualization even exhibits a grid-like structure, thereby, improving the visual quality. The fabric-like texture visualization has been extended to visualize the tensor fields on arbitrary surfaces [EHHS12], and even a further extension to guide the lightweight structure design [KSZ*14].

2.1.2 Glyph-based Methods

Glyph-based methods depict the tensor field by a set of well-designed geometric primitives, i.e., the so-called tensor glyphs. Each single tensor at the selected position can be visualized into a tensor glyph, thereby, the primary advantage of this approach lies in revealing the local state of the tensor field. In general, the glyph-based methods involve the glyph design and placement [KAH14].

The *Mohr's circle* and *Lamé's stress ellipsoid* are the two most fundamental stress tensor glyphs. The former is widely used in studying the local stress state at single position being selected [CRBC04, CRB*05, KMH11], while the latter usually appears as a group of glyphs to convey a global+local view of the stress field in works about structural engineering [WBWD12, WAWS18, AJL*19, WWW22b]. In the design of Mohr's circle, all the potential combinations of the normal stresses and shear stresses at the selected position are encoded into a triad of circles. The position and radius of the circles are determined by the three principal stresses, and the abscissa and ordinate of each point on the circle represent the magnitudes of the normal stress and shear stress components, respectively. The three axes of Lamé's stress ellipsoid orient to the major, medium, and minor principal stress directions, and are scaled by the corresponding principal stress values. Lamé's stress ellipsoid can clearly indicate the local stress directions and the proportion of different principal stress values, however, it cannot distinguish the sign of the principal stress without additional color coding. This is considered critical in stress analysis since the sign tells whether the material at the selected position is under tension or compression. For 2D situation, the ellipsoid degenerates to an ellipse. Besides these two fundamental stress tensor glyphs, there are also some other stress tensor glyphs developed out of different analysis requirements. In order to emphasizing the major principal stress, Haber [Hab90] adapted Lamé's stress ellipsoid into a combination of a disk and shaft whose dimensions are scaled by the corresponding principal stress values, where the disk is expanded by the medium and minor principal stresses, the shaft points to the major principal stress direction. *Reynolds glyph* [MSM95] was designed to highlight the normal stress, and as a counterpart, the *HWY glyph* presented in [HYW03] focuses more on shear stress. Besides designing the dedicated stress tensor glyphs, it's also viable to use the general tensor glyphs to visualize the stress field, for instance, the widely-spread *Superquadric tensor glyphs* based on

superquadric surfaces. The superquadric tensor glyph was originally designed for glyph-based diffusion tensor visualization [Kin04], and later adapted to visualize positive definite tensors [KWS*08], general symmetric tensors [SK10], as well as asymmetric tensors [SK16, GRT17]. Zobel *et al.* adapted the superquadrics for visualizing fiber orientation tensors and presented a new type of glyph showing the admissible fiber directions, which provided the engineers the additional visual clues to improve their design [ZSS15]. The design of the glyphs for showing the gradients of stress tensor was also preliminarily explored in [ZSS17].

Specific placement strategies can be used to reduce the number of glyphs and occlusions, thereby, improving the visual quality of the glyph-based methods [War02]. Kindlmann *et al.* [KW06] arranged the glyphs into a dense pattern by using a particle system with anisotropic potential energy profiles, meanwhile, the full tensor information exhibited by each tensor glyph is still distinguishable. This method was further improved by Hlawitschka *et al.* [HSH07], where they introduced a parameterless acceleration structure that has low computational complexity and allows interactive tensor visualization using glyph placement. Based on the anisotropic Voronoi cells, Feng *et al.* [FHHJ08] presented an automatic packing algorithm to generate the uniformly distributed elliptical glyphs whose distribution fulfills the blue noise properties. By deriving a local metric from the tensor field, Kratz *et al.* [KKH11] proposed a particle-based method to generate the unstructured distributions of elliptical glyphs, which dismissed the restrictions of methods in [HSH07, FHHJ08] in controlling the overlap of samples. Patel and Laidlaw [PL20] proposed to guide the placement of glyphs by principal trajectories in the underlying field, and thus to provide a better understanding of the global relationships in this field. We in Paper A [WWW20] propose a globally conforming lattice structure for stress tensor visualization, which is computed via a constrained optimization problem. It, on the one hand, belongs to the category of trajectory-based methods since the lattice edges are formed by PSL, however, on the other hand, the stress anisotropy is encoded into the lattice shape, thus, it also exhibits the characteristics of the glyph-based methods. While this method is effective in 2D, it was shown that a direct extension to 3D is not possible since the 3D PSLs do not intersect necessarily.

2.1.3 Topology-based Methods

Topology-based approaches for stress tensor visualization abstract from the depiction of stress directions and focus on revealing specific topological characteristics of the tensor field. Delmarcelle and Hesselink originally studied the topology of 2D symmetric second-order tensor fields in their seminal work [DH94], and introduced the fundamental concepts of *degenerate points* and *topological skeleton*. At a degenerate point, the two eigenvalues of the 2D tensor are equal to each other, and there are two types of stable degenerate points, i.e., *Trisector* and *Wedge*, which are determined by the characteristic patterns of the tensor lines in the vicinity of the degenerate point. The trajectories of the topological skeleton start from the degenerate point and partition the tensor field into several sub-domains, within each of

which the tensor directions behave similarly, thus, the topological skeleton is also called as *separatrices*. This theory was later extended to 3D symmetric second-order tensor fields by Hesselink *et al.* [HLL97]. Since the newly-added third dimension, the degeneracy is classified into double degeneracy and triple degeneracy according to the number of the repeating eigenvalues appearing. Further, they depicted the structure of tensor lines in the vicinity of the degenerate point corresponding to different degeneracy, which forms the separating surfaces of the 3D domain. These two papers pioneered this area, however, less progress was seen for the next about 10 years since then, until Zheng and Pang discussed the robust extraction of the degeneracy in their work [ZP04, ZPP05b]. Zheng and Pang showed that the degenerate features in the 3D symmetric second-order tensor field form stable topological lines rather than points, named *degenerate curves*. In addition, they also pointed out that triple degeneracy is extremely rare and not stable in real data, and they further demonstrated the theoretical basis of computing the separating surfaces in their follow-up work [ZPP05a]. Afterward, a period of relative calm was once again maintained in this field, during which Tricoche *et al.* [TKW08] showed that the degenerate lines in tensor fields are crease (ridge and valley) lines of a particular tensor invariant called *mode*. They leveraged the previous work on the extraction of crease manifolds in image processing and computer vision, and presented a versatile framework for topology analysis. To a certain extent, this method overcame the shortcomings of the existing methods in dealing with the practical noisy data. Towards a similar goal, a different approach based on the Lagrangian coherent structures (LCS) was also proposed by Tricoche *et al.* in their later work [THBG12].

With the introduction of new topological features and analysis methods, a revival of this field has been appearing since 2015. Zhang *et al.* [ZTZ15] proved that the number of degenerate curves in a 3D linear tensor field is in the range of one to four under the assumption of structurally stable conditions. They also summarized the open challenges in 3D symmetric tensor fields from the perspectives of the development of fundamental concepts, robust extraction of topological features, and the corresponding physical interpretation [ZZ15]. Further, Zhang *et al.* [ZRSZ17] gave an estimate of the maximum number of transition points on degenerate curves, at which the tensor behavior switches from linear to planar. The notion of the feature surfaces of the symmetric tensor field represented by the degenerate curves was enriched with the introduction of *neutral surfaces* and *traceless surfaces* by Palacios *et al.* [PYW*15]. Later Roy *et al.* [RKZZ18] discussed the robust and fast extraction of these feature surfaces. Zobel and Scheuermann proposed the notion of *extremal points* to analyze the complete invariant part of the tensor [ZS18]. Raith *et al.* presented a general approach for the generation of separating surfaces in the invariant space [RBN*18]. The concept of core line used in vector field was also extended to the 3D second-order tensor fields by Oster *et al.* [ORT18]. Qu *et al.* [QRZZ20] further generalized the concepts of *degenerate curves* and *neutral surfaces* to a unified framework called *mode surfaces*. Taking the 2D stress field as an example, Zhang *et al.* [ZGZ17] explored the physical significance of degenerate points. Jankowai *et al.* [JWH19] analyzed the robustness of tensor topology

and presented a simplification strategy for tensor topology based on the robustness measurement to the degenerate points.

2.2 Structural Topology Optimization

Achieving the highest stiffness while using the least amount of material is a fundamental task in mechanical design. This is often formulated as an optimization problem, e.g., topology optimization, in which the material layout is optimized to obtain minimal compliance that is measured by total strain energy [BS04, SM13]. Here, the strain energy is usually computed by performing the finite element analysis (FEA) on the discretized design domain corresponding to the specific material layout. Depending on different assumptions of the material model, most of the existing topology optimization approaches can be roughly categorized into the homogenization-based approaches [BK88] and the ones optimizing the distribution of solid isotropic materials. The latter covers topology optimization methods based on density [Ben89, ZR91, Mle92], level-sets [WWG03, AJT04], evolutionary procedures [XS93], and explicit geometric descriptions [NHTB04, GZZ14], etc.

In homogenization-based topology optimization, the material is assumed to have an infinitely fast variation in solid and void regions. At the microscopic scale, these micro-structures are assumed to be uniform and can be represented by periodic unit cells, e.g., the cell based on the well-known rank-n laminates [Ave87], and square cell with a rectangular hole [BK88]. The equivalent material properties of such cells can usually be evaluated with homogenization [AA14, BS04, Gro18]. In general, homogenization-based approaches take each cell's deposition specifications and orientation as design variables to achieve anisotropy and generate theoretically optimal structures. Homogenization-based topology optimization results are multi-scale, and thus, cannot be manufactured directly. How to robustly obtain the single-scale interpretation of the homogenization-based topology optimization results has remained a challenge, until the appearance of the so-called de-homogenization strategy [PT08].

To circumvent the limitation of homogenization-based topology optimization, a simpler material assumption called Solid Isotropic Material with Penalization (SIMP) was introduced, also known as the power-law approach, from which the density-based topology optimization was proposed in [Ben89, ZR91, Mle92]. Here, the material within each simulation element is assumed to be isotropic and homogeneous, and the relative density value of each element is taken as the design variable. The relative density value continuously varies between 0 and 1, where 0 refers to void and 1 for solid. Young's modulus is defined as the relative material density raised to some power then times Young's modulus of solid material. SIMP received several criticisms for not being explainable physically from the beginning until Bendsøe and Sigmund confirmed its physical rationality [BS99]. Afterward, density-based topology optimization grows into one of the pillar solutions for lightweight structure design rapidly, and is widely adopted from lab works to engineering applications [SM13, ZZX16, WSG21].

In this thesis, we narrow down the discussion on topology optimization within the scopes of density- and homogenization-based approaches towards compliance-minimization optimization.

2.2.1 Density-based Approaches

Built upon the pioneering works on density-based topology optimization developed since around 1990 [Ben89, ZR91, Mle92, DS95, BS99], Sigmund published the landmark paper "A 99 line topology optimization code written in Matlab" in 2001, which lays the foundational paradigm for density-based topology optimization and significantly improves its accessibility for beginners [Sig01]. As an improved successor, the "88 lines of topology optimization code" contributes similarly [ACS*11].

In practical topology optimization, the design domain is frequently seen being discretized into the first-order quadrilateral (2D) or hexahedral (3D) meshes, which are built from the Cartesian grid obtained by voxelizing the design domain. Compared to the boundary-aligned unstructured mesh, the Cartesian mesh not only simplifies the modeling process but also significantly facilitates the construction of the efficient linear system solver for high-resolution FEA simulations. A side impact of using such mesh is incurring the so-called checkerboard pattern in the resulting material layout because of the numerical instability [DS95], however, this can be overcome by a well-defined mesh-independent density filtering [Bou01, WLS11]. The idea of mesh-independent density filtering is also utilized to counteract the unpredictability of the optimized results with the increase of the simulation resolution. I.e., instead of generating a better description of the design with using the high-resolution model, it may converge to a totally different design with many tiny features being introduced, which is not preferred in topology optimization, especially for the downstream manufacturing stage. Both the checkerboard pattern and design unpredictability can be attributed to the mesh dependence issue [GPB04, WLS11]. The core idea of building the mesh-independent density filter is to introduce an auxiliary design variable as the physical density value in optimization, which is defined to be a weighted average of the neighboring design variables. Different methods but for the similar goal are also reported in [Sig07, LS11]. Given that the density filtering leads to the gray region and inevitably drags the convergence process, the Heaviside projection operator is usually adopted to promote the binary design [XCC10, WLS11].

Topology optimization is computationally intensive since it needs to iteratively update the design. At each iteration, it needs to perform the FEA simulation to evaluate the objective function, then the design variables are updated based on sensitivity analysis for the next iteration. The method of moving asymptotes (MMA) presented by Svanberg [Sva87] and the optimality criteria reported in [Ben95] are commonly used as updating schemes. Aage and Lazarov also published the parallel framework for topology optimization using MMA [AL13]. The performance bottleneck of topology optimization is majorly up to the FEA simulation, which consumes about 85% of the total processing time [WDW15]. Benefiting from using the Cartesian mesh in topology optimization, i.e., the nice accessibility for a

matrix-free computing stencil, the geometric multigrid solvers have been demonstrated to be the appropriate solution for FEA simulation in high-resolution topology optimization. Refer to [BHM00] for details of multigrid methods. Amir *et al.* explored the specific characteristics of a multigrid preconditioned conjugate gradients solver and presented a computational approach for efficient topology optimization [AAL14], later Aage *et al.* published the fully parallel open-source framework, PETSc, for topology optimization [AAL15]. Dick and Westermann [DGW11] presented an elasticity simulation system, where the elastic object is discretized into the Cartesian mesh, the static equilibrium FEA equation is solved by a geometric multigrid solver accelerated by CUDA parallel programming API provided on NVIDIA GPU. Built upon this, Wu and Westermann [WDW15] developed a highly efficient simulation system for high-resolution topology optimization, which can handle the model with 14 million elements on a desktop PC equipped with a single CPU, 8GB of RAM, and 6GB of GPU VRAM within 20 minutes. Apart from the advanced solving techniques, using the self-adaptive mesh for topology optimization is also a viable way to achieve a tradeoff between computational efficiency and simulation fidelity [LC18, SdTT18]. Another efficient idea can also be found in optimizing the sparse and thin structures using the narrow-band approach, where the real simulation only happens around the high-density regions, thus, avoiding the wasted computational effort on large void regions. Liu *et al.* presented such a method, which is able to accommodate computational domains with over one billion simulation elements on a single shared-memory multiprocessor platform [LHZ*18]. In recent years, data-driven approaches have also started playing roles in solving topology optimization [ZZZ*20, WTTL20, NLJK21].

Since the theoretically optimal structures are multi-scale, the density-based approach in principle shall be able to approach such a material layout. I.e., the final design is composed of sub-structures with different length scales toward optimality, meanwhile, fulfilling the manufacturing condition. This, however, is only possible by using sufficiently fine meshes for discretizing the material distribution, and requires careful continuation techniques [AALS17, LHZ*18, BSPA20]. Therefore, commonly seen topology optimization results are predominantly mono-scale. In order to explore the optimal structure patterns, it has become a popular branch to study shape control over topology optimization, especially since Wu *et al.* proposed the porous infill optimization achieved by a local volume constraint [WAWS18]. As a comparison, the constraint of the classic density-based topology optimization mentioned above can be named global volume constraint since it's only up to the permitted material budget.

Inspired by [Gue09] where they introduced a projection filter to impose the maximum length control, Wu *et al.* [WAWS18] introduced the local volume constraint, which is also formed into a projection process yet in an approximate manner, thereby, facilitating a fast numerical solution. The local volume constraint prevents the forming of large solid regions and, consequently, creates porous structures distributed more evenly across the design domain. This approach has been extended, in conjunction with a coating approach proposed by [CAS15], to design concurrently structures and porous sub-

structures therein, referred to as shell-infill composites [WCS17]. It has also been applied to design porous shell structures [TSA21]. Other notable extensions include the design of porous structures with gradation in the porosity and pore size [SPG19, DS20], use of multiple materials [LGLT20, ZZ21], and fiber-reinforced structures [LGL*21]. Besides by density-based approaches, porous infill structures have been designed using an evolutionary design approach [QJJ*20] and machine learning [CYR19]. The convergence behavior of the porous infill optimization was investigated in our work Paper C [WWW22b] from the perspective of stress topology analysis. In Paper D [WWW22c], we presented an evenly spaced PSLs-guided strategy for the starting guess of the density-based topology optimization. On the one hand, the proposed approach promotes the generation of more detailed sub-structures in the results of density-based topology optimization under global volume constraint, thus, improving the robustness of the optimized result concerning the local damage. On the other hand, it also speeds up the convergence of density-based topology optimization under local volume constraint, meanwhile, the regularity of the optimized result is improved as well.

2.2.2 Homogenization-based Approaches

The homogenization-based topology optimization was originally proposed in [BK88] and can produce a mathematical specification of theoretically optimal structures, which is multi-scale. Hassani and Hinton systematically reviewed the homogenization and topology optimization from the theory, analytic and numerical solution, and solving scheme in their series of works [HH98c, HH98a, HH98b]. Afterward, however, the development of homogenization-based topology optimization has been rather silent, especially in the first 10 years of the 21st century, while at the same time the density-based topology optimization was booming prosperously. The major obstacle to preventing the homogenization-based topology optimization a further spread is the lack of effective methods in interpreting its multi-scale result into a single-scale geometry for the downstream fabrication.

The milestone work by Pantz and Trabelsi [PT08] reversed this trend, where they proposed one of the first solutions to post-process the homogenization-based topology optimization result by means of the projection operation, thereby, obtaining a manufacturable design. This method also keeps the optimal mechanic performance to a certain extent. Since then, a revival of the homogenization-based topology optimization has been seen, especially with a focus on the post-process of translating the results of homogenization-based topology optimization into a manufacturable geometry, this post-process is now often referred to as *de-homogenization*.

Given that the cells used in homogenization-based topology optimization can usually be described by a Fourier series [RP12, RPDK15], the key advantage of such a combination of homogenization-based topology optimization and de-homogenization is the low computational complexity. I.e., such a combination enables the possibility of mapping the solution obtained on the coarse scale to a fine

scale with minor loss in performance, thereby, improving the efficiency of performing high-resolution topology optimization significantly. This feature has been confirmed in [GS18, GSA*20].

In sense of implementation, the homogenization-based topology optimization shares the same objective and constraint functions as the classic density-based topology optimization. Moreover, the mesh-independent filter for getting rid of the numerical instability [WLS11] and the scheme for updating the design variables [Sva87, Ben95] introduced for density-based topology optimization can still work for the homogenization-based topology optimization. One just needs to treat the multiple design variables of each element separately. The critical difference is the description of the simulation cells based on different assumptions of material properties. It has been shown that the optimal solution for minimum compliance problems is in the space of layered materials, i.e., the so-called rank-n laminates. The rank-2 laminates are optimal for plane problems subject to a single load case, and rank-3 laminates are optimal for plane problems subject to multiple load cases [Ave87, Gro18]. The rank-2 laminates can also be replaced with the unit cell with a rectangular hole for simplicity [BK88], which is widely used in a number of subsequent works on homogenization-based topology optimization [PT08, AGDP19, GS18]. Whether the simulation cell is based on the assumption of rank-n or the unit cell with a rectangular hole, its material properties can always be obtained via analytical or numerical homogenization [AA14, Gro18]. During the course of optimization, the design variables describing the deposition situation of each cell, e.g., the size of the rectangular hole of the unit cell, are usually updated via MMA ([Sva87]) or the optimality criteria ([Ben95]). The cell orientation can be computed by the gradient descent methods [SGSB20], it's worth emphasizing that the optimal cell orientation can also be given by the local principal stress directions when the structure is subject to a single load [Ped89].

The de-homogenization proposed in [PT08] was revisited and improved by Groen and Sigmund [GS18] and Allaire et al. [AGDP19]. These approaches have since been extended to 3D [GSA*20, GDAP20], and to deal with singularities in the optimized orientation fields [SGSB20]. A key component in these approaches is computing a fine-grid scalar field whose gradients are aligned with optimized orientations from homogenization-based topology optimization. Wu et al. reformulated this post-process as quad/hex-dominant meshing, i.e., constructing quad/hex-dominant meshes whose edges are aligned with the optimized orientations [WWG21]. Stutz *et al.* [SOG*22] reported a method to generate high-resolution multi-laminar structures from frame fields by tracing the *stream surface*. They further formulated the finding of such a set of well-spaced stream surfaces as an optimization problem. Convolutional neural networks have also been found useful for de-homogenization [EABS22]. Alternative de-homogenization approaches include [LKY*21, ZLD*19]. Apart from the single loading case considered in existing de-homogenization works, recently, Jensen *et al.* [JSG22] also made the move to de-homogenize the optimal 2D topologies subject to multiple loading cases using the rank-3 laminate for homogenization-based topology optimization. In Paper E [WWW22a], we presented

a novel de-homogenization strategy, which is based on a set of domain-filling and evenly spaced streamlines generated from the cell orientations. Here the streamlines are essentially PSLs, and the seeding approach proposed in Paper B [WNW*22] can be used to generate the evenly spaced streamlines. In contrast to the majority of prior de-homogenization approaches that represent the final structure as a binary field, our approach generates an explicit representation in the form of a quad-dominant mesh constructed from the streamlines. This compact representation is beneficial for downstream operations such as user editing and fabrication process planning.

2.3 Stress in Structural Design and Optimization

For the optimal solution to compliance-minimization problems under a single loading case, Mechell's theory indicates that the optimal design forms a truss structure and the truss members follow the principal stress directions [Mic04]. The basic theory of homogenization-based topology optimization also shows that the optimal design can be described by a set of spatially varying orthotropic cells [BK88], whose orientations can be given by the local principal stress directions [Ped89]. In recent works, Wu *et al.* showed that there is a good agreement between the material layout produced by density-based topology optimization under the local volume constraint and the principal stress directions of the stress field that is simulated on the fully solid design domain with the same boundary conditions [WAWS18]. Stutz *et al.* obtained the optimal design by interpreting the 3D multi-scale homogenization-based topology optimization results with the stream surface that is traced from the corresponding stress field [SOG*22].

All of these above point to the potential that stress can play more roles in structural design and optimization, e.g., guiding the material layout using principal stress directions, instead of just being a measure of structural strength. The significant advantage of doing so is the possibility of converting the computationally intensive and operationally cumbersome mechanical optimization problem into a relatively efficient and straightforward geometry modeling problem. Though the mechanical performance of the obtained structural design might not be rigorously optimal, it releases more design freedoms to users on the shape control over the final design, which is desired in some application scenarios, e.g., architectural structure design.

Kratz *et al.* [KAH14] presented a method of using the texture of stress trajectories for structural design, and introduced a concrete case study by considering the design of a reinforcement structure. Tam and Mueller [TM15] investigated the stress line generation for structurally performative architectural design. A novel PSLs-based growth strategy for topology optimization of the point-loaded situation was reported in [KLC16]. Daynes *et al.* [DFLW17] presented an approach to generate optimized functionally graded lattice core structure based on a set of isostatic lines, which are constructed from the local principal stresses. Arora *et al.* used a parametrization-based approach to generate

the volumetric Michell Trusses, whose orientations align with a frame field constructed from the stress field [AJL*19]. By combining topology optimization and frame-aligned parameterization, Wu *et al.* [WWG21] presented an appealing method to design lattice structures that confirm both the principal stress directions and the boundary of the optimized shape. In Paper D [WWW22c], we proposed a highly efficient method of generating the near-optimal 2D structure directly from the domain-filling and evenly spaced PSLs. The proposed method overcomes the limitations of the method of [KLC16] in dealing with the distributed loading conditions, in addition, it leads to a design that shows comparable mechanical performance with the result of porous infill optimization in [WAWS18].

3

Fundamentals

In this chapter, we introduce the fundamental concepts and methods that form the theoretical and technical basis of this thesis, from which the inspirations and the primary results of the associated publications of this thesis are also expounded in the sectional summaries. We start with reviewing the general description of stress, therein, the basic concept of this thesis, i.e., stress tensor, is introduced in Section 3.1. Then followed by the introduction to the PSLs in Section 3.2, covering PSL tracing, seeding to visualizing. Next, the method for stress topology analysis is explained in Section 3.3. Finally, we shed light on the density-based topology optimization in Section 3.4 and the homogenization-based topology optimization in Section 3.5, respectively.

3.1 General Description of Stress

Stress is a measurement of the internal force induced when a solid object is under load. Considering a cross-section s inside the solid, and the internal force acted on s is $\boldsymbol{f}$, which is continuously distributed across s. Taking a differential area $\triangle s$ from s, and assuming the internal force acting on it is $\triangle \boldsymbol{f}$. Thereby, the average stress on $\triangle s$ can be given by $\frac{\triangle f}{\triangle s}$. If we let $\triangle s$ shrinks infinitely and approaches point P, $\frac{\triangle \boldsymbol{F}}{\triangle A}$ will reach a limit

$$\lim_{\triangle s \to 0} \frac{\triangle \boldsymbol{f}}{\triangle s} = \boldsymbol{p} \tag{3.1}$$

Here, the limit vector $\boldsymbol{p}$ is the stress at P, and the direction of $\boldsymbol{p}$ is the same as the limit direction of $\triangle \boldsymbol{f}$. The stress $\boldsymbol{p}$ at any cross-section can be decomposed into components p_x, p_y and p_z along the coordinate axes, or components along the normal (σ) and tangent (τ) of the cross-section, respectively.

To study the stress state at any position P in the solid, one usually sets a differentiable tetrahedron $PABC$, where ABC is a plane near P, the edges PA, PB and PC are parallel to the three coordinate

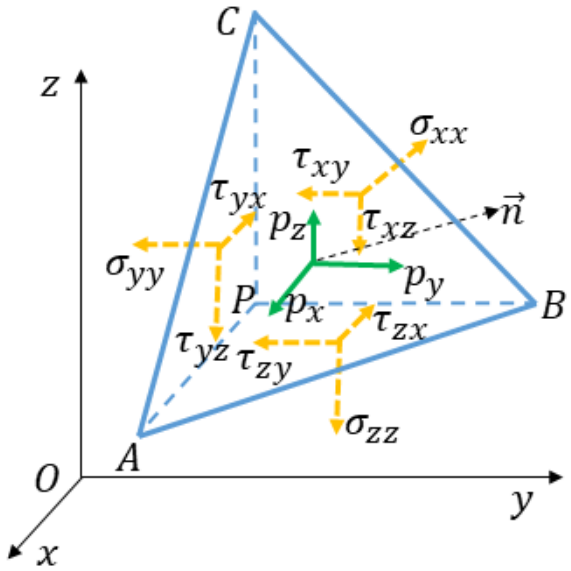

Figure 3.1: Description of stress state at position P. The normal stress is denoted by σ and shear stress by τ, whose first subscript indicates which axis its acting plane is perpendicular to, the second subscript gives the acting direction.

axes, respectively, see Figure 3.1. The stress on the plane ABC corresponds to the stress at P when tetrahedron $PABC$ approaches to the point P.

Let the external normal of plane ABC be $\vec{n}$, and its directional cosines are given by

$$\cos(\vec{n},x)=l,\quad \cos(\vec{n},y)=m,\quad \cos(\vec{n},z)=n. \tag{3.2}$$

Assuming that the volume of tetrahedron $PABC$ is $\triangle V$, the area of plane ABC is $\triangle S$, accordingly, the areas of plane PBC, PAC and PAB are $l\triangle S$, $m\triangle S$ and $n\triangle S$, respectively. According to the static equilibrium condition of the tetrahedral under force, i.e., $\sum F_x=0$, $\sum F_y=0$ and $\sum F_z=0$, where F_x, F_y and F_z are the the resultant forces of this tetrahedron along the three coordinate axes. Taking F_x as example, we can obtain the static equilibrium equation below

$$p_x\triangle S-\sigma_{xx}l\triangle S-\tau_{yx}m\triangle S-\tau_{zx}n\triangle S+f_x\triangle V=0 \tag{3.3}$$

where, f_x is the component of the volume force of this tetrahedron along the coordinate axes. let Equation 3.3 be divided by $\triangle S$, and rearrange the items

$$p_x-f_x\frac{\triangle V}{\triangle S}=l\sigma_{xx}+m\tau_{yx}+n\tau_{zx} \tag{3.4}$$

Given that $\triangle V$ is a higher order trace than $\triangle S$, i.e., the item $\frac{\triangle V}{\triangle S}\to 0$ when tetrahedron $PABC$

approaches to the point P, thereby, Equation 3.4 can be re-arranged into

$$p_x = l\sigma_{xx} + m\tau_{yx} + n\tau_{zx} \tag{3.5}$$

Analogously, $\sum F_y = 0$ and $\sum F_z = 0$ lead to

$$p_y = m\sigma_{yy} + l\tau_{zy} + l\tau_{xy} \tag{3.6}$$

and

$$p_z = n\sigma_{zz} + n\tau_{xz} + m\tau_{yz} \tag{3.7}$$

Assuming the normal stress on plane ABC is σ, then it can be depicted by

$$\sigma = lp_x + mp_y + np_z \tag{3.8}$$

Substituting Equation 3.5, Equation 3.6 and Equation 3.7 into Equation 3.8, we can get

$$\sigma = l^2\sigma_{xx} + m^2\sigma_{yy} + n^2\sigma_{zz} + mn\tau_{yz} + mn\tau_{zy} + nl\tau_{zx} + nl\tau_{xz} + lm\tau_{xy} + mn\tau_{yx} \tag{3.9}$$

According to the torque equilibrium condition, we know that the shear stresses acting on the two orthogonal planes and perpendicular to the intersection lines of these two planes are equal to each other, i.e., $\tau_{yz} = \tau_{zy}$, $\tau_{xz} = \tau_{zx}$ and $\tau_{xy} = \tau_{yx}$, thus, Equation 3.9 can be simplified to

$$\sigma = l^2\sigma_{xx} + m^2\sigma_{yy} + n^2\sigma_{zz} + 2mn\tau_{yz} + 2nl\tau_{zx} + 2lm\tau_{xy} \tag{3.10}$$

If we let the shear stress on plane ABC be τ, and since

$$p^2 = p_x^2 + p_y^2 + p_z^2 = \sigma^2 + \tau^2 \tag{3.11}$$

the shear stress τ can be described by

$$\tau^2 = p_x^2 + p_y^2 + p_z^2 - \sigma^2 \tag{3.12}$$

Through Equation 3.10 and Equation 3.12, we can see that the stress state at any position P in the domain can be fully described by the six stress components: σ_{xx}, σ_{yy}, σ_{zz}, τ_{xy}, τ_{yz} and τ_{xz}.

The derivation process above shows that the stress at a specific point in a solid domain due to internal stresses depends not just on the specific location in the domain but also on the orientation of

the considered plane. Thus, in order to facilitate measuring the stress on it in various directions, these six stress components are usually arranged into a tensor, i.e., stress tensor

$$\boldsymbol{T} = \begin{bmatrix} \sigma_{xx} & \tau_{xy} & \tau_{xz} \\ \tau_{xy} & \sigma_{yy} & \tau_{yz} \\ \tau_{xz} & \tau_{yz} & \sigma_{zz} \end{bmatrix} \tag{3.13}$$

The stress tensor is a real symmetric second-order tensor. According to Cauchy's stress theorem [Irg08], stress state at any point P in a solid associated with an orientated plane can be found through the coordinate transformation of the stress tensor at P.

Principal Stress. A critical concept in stress analysis is the so-called principal stress, which is defined as the normal stress component on the plane where the shear stress component vanishes, here the normal of the corresponding plane is called the principal stress direction. Combining with the attribution of normal and shear stress components in the stress tensor (Equation 3.13), we can clearly see that there are three real principal stresses at any position P in a 3D solid domain, which correspond to the three eigenvalues of the stress tensor. Accordingly, the three eigenvectors of the stress tensor are the corresponding principal stress directions, i.e.,

$$\boldsymbol{T} = \begin{bmatrix} \sigma_{xx} & \tau_{xy} & \tau_{xz} \\ \tau_{xy} & \sigma_{yy} & \tau_{yz} \\ \tau_{xz} & \tau_{yz} & \sigma_{zz} \end{bmatrix} = \begin{bmatrix} \boldsymbol{v_1} & \boldsymbol{v_2} & \boldsymbol{v_3} \end{bmatrix} \begin{bmatrix} \sigma_1 & & \\ & \sigma_2 & \\ & & \sigma_3 \end{bmatrix} \begin{bmatrix} \boldsymbol{v_1} & \boldsymbol{v_2} & \boldsymbol{v_3} \end{bmatrix}^{\mathrm{T}} \tag{3.14}$$

Here, the eigenvalues σ_1, σ_2 and σ_3 are the principal stresses. In descending order, calling σ_1 the major principal stress, σ_2 the medium principal stress, and σ_3 the minor principal stress, correspondingly, eigenvectors $\boldsymbol{v_1}$, $\boldsymbol{v_2}$ and $\boldsymbol{v_3}$ the major, medium and minor principal stress directions, respectively. Since $\boldsymbol{T}$ is a real symmetric matrix, different eigenvectors are orthogonal to each other when there are no repeating eigenvalues. Note that the principal stress direction is bidirectional since it's the eigenvector, i.e., $\boldsymbol{v_i}$ and $-\boldsymbol{v_i}$ $(i = 1, 2, 3)$ are equivalent in describing the principal stress directions.

The principal stress also indicates the maximum and minimum values of the normal stress and shear stress at the position being considered. The maximum and minimum normal stresses are given by the major principal stress σ_1 and the minor one σ_3. The maximum and minor shear stresses correspond to $\pm\frac{1}{2}(\sigma_1 - \sigma_3)$, acting on the planes that pass through the medium principal stress direction and equally divide the included angle between the major and minor principal stress directions.

Stress Simulation. The finite element analysis (FEA) is frequently used in practical stress analysis, which, in general, gives σ_{xx}, σ_{yy}, σ_{zz}, τ_{xy}, τ_{yz} and τ_{xz} at the element vertices. To investigate the

stress state inside the element, one can perform element interpolation according to the shape function used in FEA.

3.2 Principal Stress Lines

The trajectory-based stress tensor visualization is achieved by principal stress lines (PSLs), involving how to trace PSL, how to seed PSL set for better visual quality, and what kind of visual abstract is used to convey the tensor information the PSL carries.

3.2.1 Tracing

The PSLs are traced by numerically integrating massless particles in each single principal stress field, i.e., every single PSL only follows the major, medium, or minor principal stress directions. Here we term the PSLs traced from the major, medium, and minor principal stress fields as the major, medium, and minor PSLs, respectively. Different integration schemes can be used for PSL tracing, including the 1st-order Euler method, and the 2nd- and 4th-order Runge-Kutta methods, etc. In each integration step, the involved stress tensor $\boldsymbol{T}$ is interpolated, then the principal stresses are computed from the interpolated tensor.

Figure 3.2 shows a schematic diagram of tracing the PSL while the 1st-order Euler method is employed. Here for sake of illustration, only the major PSL is considered and the constant integration step size δ is used. Note that the bi-directional feature of the principal stress direction, i.e., every time coming to a new integration point P_i, one needs to decide whether the direction vector $\boldsymbol{v}(P_i)$ or $-\boldsymbol{v}(P_i)$ is the right direction to compute the next integration point P_{i+1}. This issue can be solved by comparing the direction deviations of $\boldsymbol{v}(P_i)$ and $-\boldsymbol{v}(P_i)$ to the previous direction $\boldsymbol{v}(P_{i-1})$ and selecting the one incurring least deviation to $\boldsymbol{v}(P_{i-1})$.

In general, PSL integration is stopped when the next integration point is outside of the solid domain. However, some PSLs would not approach the domain boundary since the potential singularity of the stress field, e.g., forming a closed orbit. In order to avoid such situation, one needs to set a threshold for the permitted maximum integration steps. An extreme case of tracing PSL is due to the so-called *degenerate point* where two or more eigenvalues are equal, thereby, the PSL direction cannot be decided in the vicinity of these points. The principal stress values at a degenerate point fulfill either $\sigma_1 = \sigma_2 > \sigma_3$ or $\sigma_1 > \sigma_2 = \sigma_3$. Therefore, when tracing along a principal stress direction, one also needs to test whether the eigenvalue σ_i corresponding to this direction is too close to another eigenvalue σ_j, e.g., using $deg = \frac{1}{2}\left|\frac{\sigma_i - \sigma_j}{\sigma_i + \sigma_j}\right| < 10^{-6}$ as a metric. If this is the case and the direction deviation between the PSL tangents at the current and next integration point is large, the integration

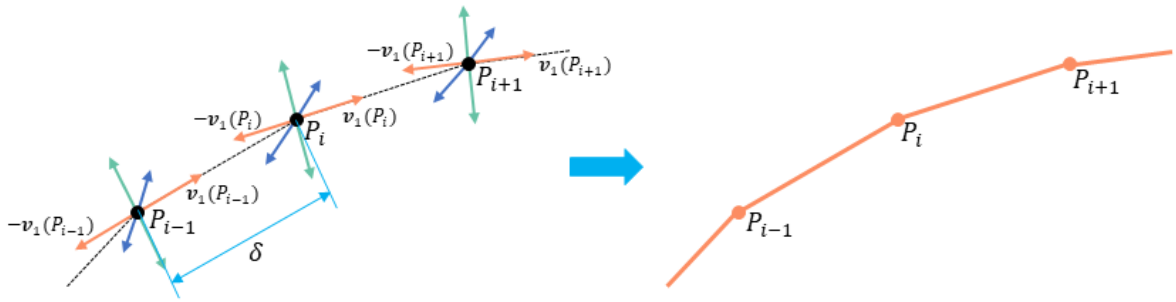

Figure 3.2: The schematic diagram for tracing PSL using the 1st-order Euler method is shown on the left, $\boldsymbol{v_1}$ showing in orange arrowhead is the major principal stress direction, the traced major PSL segment is shown on the right. The blue and turquoise arrowheads indicate the medium and minor principal stress directions, respectively, the corresponding marks $\boldsymbol{v_2}$ and $\boldsymbol{v_3}$ are omitted for clarity.

process should be stopped. The triple degenerate points with $\sigma_1 = \sigma_2 = \sigma_3$ are not considered here, since they rarely exist under structurally stable conditions [ZP04].

To obtain the principal stress directions during tracing PSL, the stress tensor at the integration point needs to be determined, which is usually achieved by performing element interpolation if the stress tensor field is defined at the grid vertices. To this end, one needs to identify the element where the integration point is located. For the Cartesian mesh, the element in which the integration point is located can be easily identified by the coordinate of the integration point. However, for the arbitrary mesh, e.g., the unstructured hexahedral mesh (hex-mesh), the element mentioned can only be robustly and efficiently identified from its adjacent and known elements. Toward this end, one usually needs to establish a mesh tree including the element and vertex adjacency information. Below, the unstructured hex-mesh is chosen as the example to depict the general idea of generating PSL, given its popularity in FEA stress analysis and representative in constructing the tracing algorithm.

A widely accepted criterion in tracing PSL is that no element is skipped between two adjacent integration points. This can be easily achieved for Cartesian mesh via an appropriately selected integration step size δ, e.g., letting δ at least be half of the element diameter. However, it becomes challenging to fulfill such criteria rigorously in unstructured hex-mesh. A theoretically ideal way of handling this challenge is to let the integration points be located on the element faces. I.e., the next integration point P_{i+1} is always on the face of the element e_{i+1} that shares the same element face with the element e_i containing the current integration point P_i. This can be achieved by calculating the intersection point of the principal stress direction vector and the corresponding element face. The special cases, like the integration point exactly at the element vertex or edge, are considered independently, in general. Apparently, one needs to precisely obtain the normals of the element faces to perform such a scheme. Especially when the integration point P_i is close to the element face, edge or vertex, otherwise, the next element e_{i+1} may get positioned incorrectly, thereby, the PSL is led in the

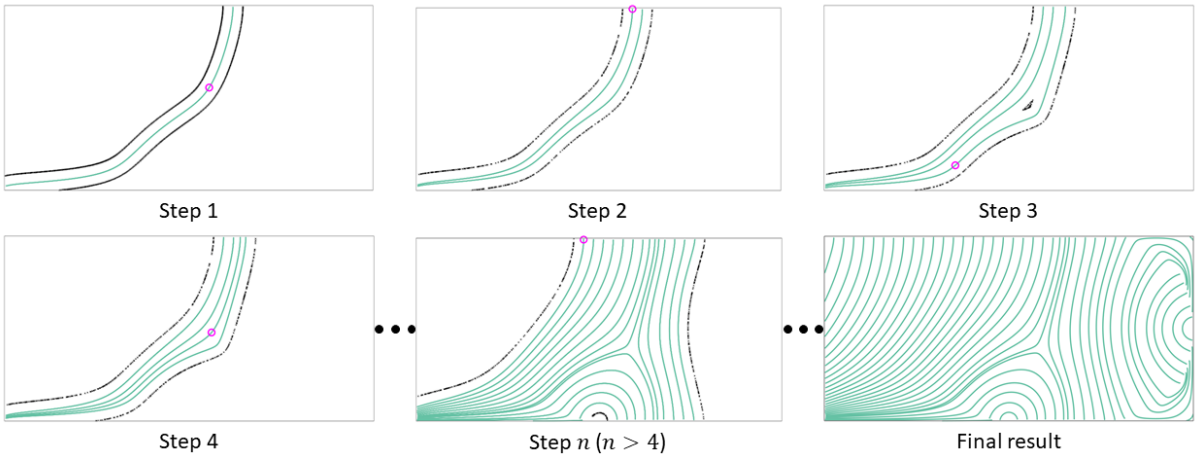

Figure 3.3: Evenly spaced streamline seeding in a vector field. The turquoise trajectories are the generated streamlines from the given vector field, magenta circles indicate the positions of seeds, black dots are the potential positions of the seeds.

wrong direction. The premise of obtaining the precise face normals of the hexahedral element is that the four vertices of each element's face are on a single plane. In practical use, however, this condition is not always true. Some hexahedral elements with low quality usually show that the four vertices of each element face are on two slightly different planes, in this case, the computed face normal can only be an approximation, thereby, introducing numerical instability to the subsequent tracing process. Consequently, this approach is always with a robustness problem.

3.2.2 Seeding

The trajectory-based stress tensor visualization involves a set of PSLs. How to appropriately place these PSLs in the domain, thus, conveying the information being needed meanwhile incurring fewer perceptual issues, is usually interpreted as PSL seeding. The positions being used for tracing PSLs are termed seed points.

Though there are various seeding strategies for specific stress visualization purposes, e.g., distributing seed points in the loaded or fixed area of the solid object to show the PSLs in the considered regions. From the perspective of generality and providing a global view, however, it's always the fundamental task to have the PSL set be domain-filling and evenly spaced in the trajectory-based stress tensor visualization.

The dedicated visualization tools that are able to show all principal stress directions simultaneously are rare. One usually considers different types of principal stress fields as separate vector fields, then resorts to the well-established evenly spaced streamline seeding approaches for vector visualization to show PSLs in each principal stress direction field. The development of evenly spaced streamline

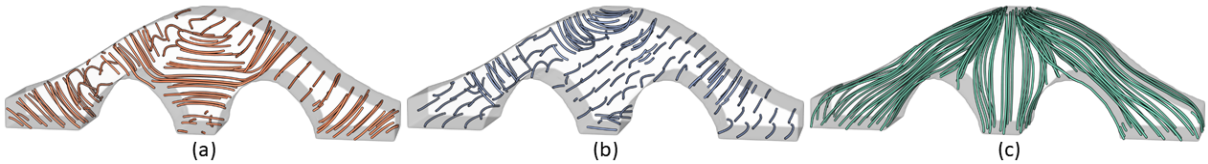

Figure 3.4: Domain-filling and evenly spaced PSL seeding in each single principal stress field. (a) Major PSLs. (b) Medium PSLs. (c) Minor PSLs.

seeding can date back to the seminal work by Jobard *et al.* [JL97], and later the extension focusing on a level-of-detail streamline distribution by Mattausch *et al.* [MTHG03], the related variants of this method have been systematically reviewed in the survey paper [SBGC20]. The core idea of such methods is to control the density of streamlines locally. I.e., in principle, the new streamline doesn't appear in the vicinity of the existing ones, here the vicinity is measured by a user-defined distance parameter ε.

The evenly spaced streamline seeding can be technically formulated into an iterative process, as demonstrated by the schematic diagram in Figure 3.3. Here for the sake of clarity, we describe the seeding strategy in the context of 2D vector fields: Starting from Step 1, the first streamline (the turquoise trajectory) is generated, and the associated potential seed points surrounding the first streamline are computed and shown in black dots, which are the points having a constant distance (i.e., the given minimum distance threshold ε) to this streamline. In Step 2, a new seed point is selected from the potential seed points associated with the first streamline, and the second streamline is traced from it. Accordingly, the new associated potential seed points of this streamline are computed, note here that the potential seed points, which are associated with the first streamline but are within the vicinity of the second streamline, are excluded from the potential seed points for the next streamline generation. Continue to Step 3, a new seed point is selected from the potential seed points to trace the third streamline. Here for the selection of seed point, the potential seed points that are associated with the earlier traced streamline have a higher priority of being selected than the potential seed points that are associated with the later traced streamline. Repeating the process in Step 3 until no potential seed points are left, then the final result is obtained.

Extending the evenly spaced seeding above to 3D and performing it in the major, medium and minor principal stress fields independently (Figure 3.4). It can be seen that the PSLs are placed in a rather uniform way and the visual clutter is well controlled in the separate principal stress fields. However, the juxtaposition makes it difficult to effectively relate the three mutual orthogonal stress directions to each other. A straightforward way to counteract such an issue is to show the major, medium and minor PSLs in a single image simultaneously, i.e., combining all the major, medium, and minor PSLs together, see Figure 3.5a. In this case, however, the visual clutter and occlusions are increased drastically due to the mutual orthogonality of different types of PSLs.

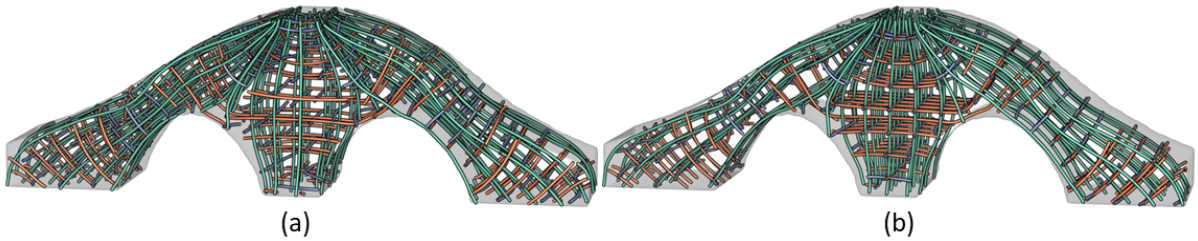

Figure 3.5: The domain-filling and evenly spaced PSL distribution. (a) Combining the domain-filling and evenly spaced major, medium, and minor PSLs shown in Figure 3.4 in one single image. (b) By our proposed method in [WNW*22].

3.2.3 Visual Abstract

The PSL not only visually indicates the principal stress direction it follows, but also includes the other two principal stress directions at the integration points, as well as the corresponding principal stress amplitudes. How to exhibit these features in the visual abstract of PSL is also important in trajectory-based stress tensor visualization.

One of the most frequently used visual abstracts for PSL is the so-called *hyperstreamline* [DH93], which expands every single PSL into a cross-section varying cylinder-like geometry, and color codes the corresponding principal stresses along this PSL. The cross-sections of the hyperstreamline are a set of ellipses whose semi-major and semi-minor axes convey the other two principal stresses along the PSL being considered. Specifically, the semi-major and semi-minor axes point to the other two principal stress directions, and their lengths reveal the corresponding principal stress amplitudes, respectively (Figure 3.6a). In this way, the information of the major, medium, and minor principal stresses can be integrated into a single geometry, see Figure 3.6b.

Sectional discussion and summary. Though the hyperstreamline is widely accepted, there are still several limitations of it. Firstly, the silhouettes and ridges of a hyperstreamline do not necessarily coincide with principal stress directions, possibly misleading the user in the interpretation of the underlying stress field, e.g., the convergence and divergence of the field. Secondly, the spatial extent of hyperstreamlines prohibits placing them close to each other, making it difficult to reveal the potential correlation among different types of PSLs. Last but not least, it's still difficult to distinguish the other two principal stress directions along each hyperstreamline, especially when they have close stress magnitudes, as shown in Figure 3.6b. Towards this end, we in Paper A [WWW20] presented the globally conforming lattice structure. The lattice edges follow the PSLs and convey the divergent/convergent behavior of principal stress directions, and the stress anisotropy is encoded into the lattice shapes. This approach is global in that it allows following the paths along which stresses are transmitted through the domain. The construction of a 2D conforming lattice is formulated as an optimization problem,

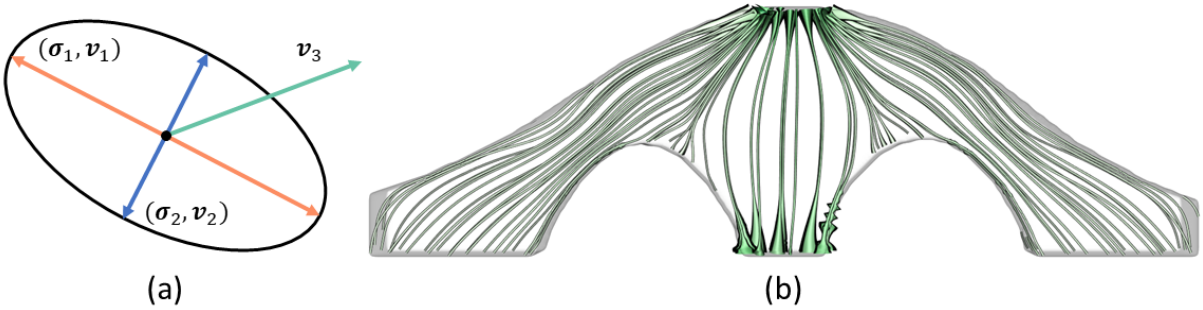

Figure 3.6: (a) Cross section design of *hyperstreamline* expanded from the minor PSL. (b) Illustration of a set of *hyperstreamline*.

which adjusts the lattice elements so that they conform to the local stress state. We have shown a modification to visualize 3D stress fields, by progressively building a beam structure comprised of hexahedral elements using a sequential growth process.

As shown in Figure 3.5a, we can see that such a visualization option of showing the three types of PSLs simultaneously suffers from severe visual clutter and occlusions, despite that the major, medium, and minor PSL sets are already seeded in a rather evenly spaced way, respectively. Due to their mutual orthogonality, the visualizations appear irregular and unstructured, and perceptual coherence breaks up even for sparse sets of trajectories. In order to improve the visual quality of such visualization, we present the 3D Trajectory-based Stress Visualizer (3D-TSV) in Paper B [WNW*22]. 3D-TSV is a system and methodology for the visual analysis of the PSLs in 3D stress fields. 3D-TSV builds upon existing techniques for line seeding in vector fields [JL97, MTHG03], and it extends them towards the specific use case by considering simultaneously the three principal stress directions in the seeding process. 3D-TSV is designed to achieve improved regularity of the extracted PSLs, i.e., it aims for a grid-like structure where PSLs roughly intersect and uniformly cover the domain. To achieve this, in the sequential seeding process every new seed point is located on an existing PSL belonging to a different principal stress direction. For comparison, we show in Figure 3.5b the result produced by 3D-TSV, it can be clearly seen that the visual quality is improved.

3.3 Stress Topology Analysis in 2D

We study the convergence issue of the 2D porous infill optimization proposed in [WAWS18] from the perspective of stress behavior. To this end, we shed light on the topology analysis of the 2D stress field.

In the 2D stress field, the stress components along the third direction (depicted by z-direction by convention) become zeros, i.e., $\sigma_{zz} = 0$, $\tau_{xz} = 0$, and $\tau_{yz} = 0$, thereby, the 2D stress tensor is written into

$$\boldsymbol{T_{2D}} = \begin{bmatrix} \sigma_{xx} & \tau_{xy} \\ \tau_{xy} & \sigma_{yy} \end{bmatrix} \tag{3.15}$$

Apparently, there are two principal stresses in the 2D situation, we still use σ_1 and σ_2 to represent the principal stresses. Letting $\sigma_1 \geq \sigma_2$, then σ_1 is the major principal stress, σ_2 the minor principal stress. Note there is a difference about the meaning of σ_2 in 2D (minor) and 3D (medium).

Topology analysis of 2D symmetric second-order tensor fields (e.g., stress tensor fields) has been introduced in the seminal work of [DH94]. The topology of a 2D stress tensor field is composed of its *degenerate points* and the corresponding *topological skeleton*. At a degenerate point, the stress tensor has repeating eigenvalues, i.e., $\sigma_1 = \sigma_2$, meaning that the major and minor stress directions cannot be decided. The topological skeleton is given by principal stress lines—so-called *separatrices*—that start from degenerate points.

In the following, the computation of the locations of degenerate points and the topological skeleton are discussed. According to the definition, a degenerate point can be located by solving the following system of equations:

$$\begin{aligned} &\sigma_{xx}(x^*, y^*) - \sigma_{yy}(x^*, y^*) = 0, \\ &\tau_{xy}(x^*, y^*) = 0, \end{aligned} \tag{3.16}$$

Here (x^*, y^*) denotes the coordinates of the point to be solved for. The general situation in 2D topology optimization is considered in the context of this thesis, i.e., the finite element analysis is performed using axis-aligned quadrilateral finite elements with bilinear shape functions. Thus, each element has four nodes that coincide with the element's vertices, and the values at the nodes are bilinearly interpolated within the element. Then, Equation 3.16 becomes a non-linear system of equations, which can be solved by the Newton-Raphson method.

Since degenerate points usually appear only in a few elements, an efficient way is required to test whether a cell can contain such a point and needs to be further analyzed, or can be excluded right away. Therefore, each element is first classified according to the following conditions:

$$\begin{aligned} &\sigma_{xx}(x_i, y_i) - \sigma_{yy}(x_i, y_i) > 0, \quad i = 1:4 \quad \text{or} \\ &\sigma_{xx}(x_i, y_i) - \sigma_{yy}(x_i, y_i) < 0, \quad i = 1:4 \quad \text{or} \\ &\tau_{xy}(x_i, y_i) > 0, \quad i = 1:4 \quad \text{or} \\ &\tau_{xy}(x_i, y_i) < 0, \quad i = 1:4 \end{aligned} \tag{3.17}$$

where $(x_i, y_i),\ i = 1:4$ refers to the four nodal coordinates of a finite element. It can be easily shown that an element cannot contain a degenerate point if any of the conditions in Equation 3.17 is true. If none of the conditions holds, the element needs to be further analyzed to confirm the existence of a degenerate point in its interior. Figure 3.7a shows a possible distribution of the eigenvalues

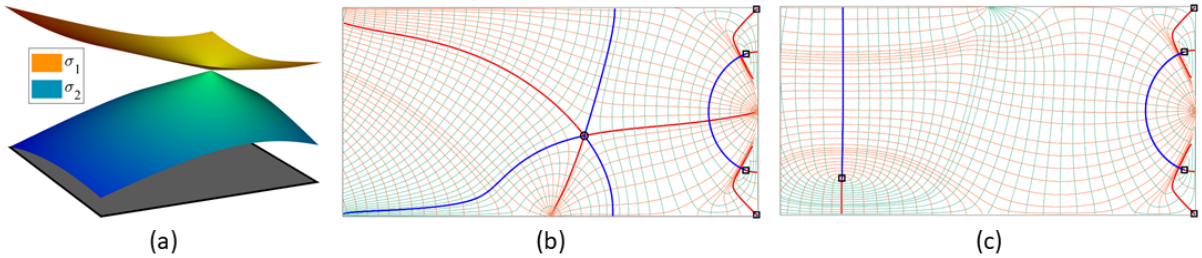

Figure 3.7: (a) The eigenvalues corresponding to the major (σ_1) and minor (σ_2) principal stresses are shown as height fields over the domain of a simulation element (grey square), at a degenerate point, both eigenvalues have the same value. (b) and (c) show two demonstration stress fields, where the thick red and blue trajectories indicate the topological skeleton following major and minor principal stress directions, and the black circle and squares locate the trisector and wedge degenerate points, respectively. The major and minor PSLs shown in thin orange and turquoise trajectories are provided as a reference for understanding the degenerate points and topological skeleton.

corresponding to the major and minor principal stress directions in a quadrilateral simulation element containing a degenerate point.

An isolated degenerate point can be classified by the winding number of one of the eigenvector fields on a loop surrounding the degenerate point. Delmarcelle and Hesselink [DH94] proposed an invariant to perform this classification stably. They further demonstrated that there are two types of degenerate points existing: *trisector* and *wedge*, which are indicated by characteristic patterns of the PSLs in their vicinity, and are determined from the so-called tensor gradients. To identify the type of a degenerate point, first, the partial derivatives of the tensor are introduced as

$$\begin{aligned} a &= \frac{1}{2}\frac{\partial(\sigma_{xx}-\sigma_{yy})}{\partial x} & b &= \frac{1}{2}\frac{\partial(\sigma_{xx}-\sigma_{yy})}{\partial y} \\ c &= \frac{\partial \tau_{xy}}{\partial x} & d &= \frac{\partial \tau_{xy}}{\partial y} \end{aligned} \tag{3.18}$$

These derivatives are then used to compute the invariant under rotation

$$\delta = ad - bc. \tag{3.19}$$

The sign of δ determines the type of the degenerate point. I.e., a trisector degenerate point is indicated by $\delta < 0$, and a wedge degenerate point is indicated by $\delta > 0$. At a trisector degenerate point, there are three major and three minor separatrices starting from this point. In contrast, two separatrices start from a wedge, one coincides with the major PSL and the other one with the minor PSL. These separatrices are termed the topological skeleton of a stress tensor field, i.e., the topological skeleton is composed of the PSLs starting from the degenerate points. Compared to the PSLs not belonging to the topological skeleton, the tangent of the topological skeleton at the degenerate point is not unique, since there is an infinite set of principal stress directions at such points. To solve this problem, Delmarcelle

and Hesselink [DH94] proposed that the tangents to the topological skeleton at the degenerate points are the real root(s) of the cubic equation

$$dx^3 + (c+2b)x^2 + (2a-d)x - c = 0. \tag{3.20}$$

At the trisector degenerate point, Equation 3.20 has three different real roots, from which three major and three minor PSLs can be traced as the topological skeleton, see Figure 3.7b. At the wedge degenerate point, only one real root exists, thus, the topological skeleton is composed of only one major PSL and one minor PSL, see Figure 3.7b,c.

The discussion about topology analysis for 3D stress field is omitted since it's out of the scope of this thesis. For the interested readers, we refer to the seminal work [HLL97], where the fundamental concepts of the topology of symmetric second-order tensor fields in 3D are introduced. And the work by Zheng and Pang [ZP04] on how to robustly extract the topological features of the 3D stress tensor field. In the latest work [QRZZ20], a more generalized concept over the classic degenerate curves, called *mode surface*, for topology analysis of the 3D symmetric second-order tensor fields is introduced.

Sectional discussion and summary. The stress topology analysis does not serve as a methodological contribution to this thesis, yet we in our work Paper C [WWW22b], make use of it to analyze and solve the convergence issue of porous infill optimization. The porous infill optimization was originally proposed by Wu *et al.* [WAWS18], and has become a popular branch in density-based topology optimization. We'll re-visit the fundamental theory of the density-based topology optimization in Section 3.4, afterward, we'll give the corresponding discussions about using stress topology analysis to solve the convergence issue of porous infill optimization.

3.4 Density-based Topology Optimization

Density-based topology optimization plays a critical role in structural design and optimization, ranging from scientific research to industrial applications. The mechanism of density-based topology optimization is to optimize the distribution of solid isotropic materials towards specific objectives and constraints. In density-based topology optimization, the material properties in each simulation element are assumed constant and the design variables are the relative densities of each element, also known as the volume fraction. Here the simulation elements are usually obtained from voxelizing the design domain, each voxel laying in the domain corresponds to a first-order quadrilateral (2D) or hexahedral (3D) finite element, i.e., the deformation field within the element is approximated by bi-linear (2D) or tri-linear (3D) shape function [Sig01, WDW15].

The density-based topology optimization usually starts from a homogeneous density field (i.e., starting guess, see Figure 3.8a) and proceeds by iteratively adjusting the density value of each simulation element till a binary material layout is obtained. In the end of optimization, each simulation element shall only be solid or empty in the final result, thereby in principle, the optimized result can be built directly. In the context of this thesis, the objective is the stiffness-optimal structure, i.e., achieving the minimum compliance under the specific constraint. Two representative constraints are considered separately, the well-known *Global Volume Constraint*, which is also, by default, treated as the classic topology optimization in a number of articles and applications, and the recently established *Local Volume Constraint* by Wu et al [WAWS18], also known as porous infill optimization.

3.4.1 Optimization Equation

In general, the optimization problem for structural compliance minimization is formulated into

$$\min_{\boldsymbol{\phi}} \quad c(\boldsymbol{\phi}) = \frac{1}{2}\boldsymbol{U}^T\boldsymbol{K}\boldsymbol{U}, \tag{3.21}$$

$$\text{s.t.} \quad \boldsymbol{K}(\boldsymbol{\phi})\boldsymbol{U} = \boldsymbol{F}, \tag{3.22}$$

$$g(\boldsymbol{\phi}) \leq 0, \tag{3.23}$$

$$\phi_e \in [0.0,\ 1.0],\ \forall e. \tag{3.24}$$

Here, $\boldsymbol{\phi}$ is the relative density value of each simulation element, serving as the design variable. The objective function is the compliance measured by the strain energy c. $\boldsymbol{K}$ is the global stiffness matrix in FEA, assembled from the element stiffness matrices $\boldsymbol{K}^e = \int_{\Omega_e} \boldsymbol{B}^T\boldsymbol{D}^e\boldsymbol{B}\,\mathrm{d}V$, $\boldsymbol{B}$ is the element strain matrix, $\boldsymbol{D}$ is the linear material law described by Young's modulus E and Poisson's ratio μ of each element. $\boldsymbol{U}$ is the displacement vector, obtained by solving the static elasticity equation (Eq. 3.22), where $\boldsymbol{F}$ is the loading vector of the given external force. $g(\boldsymbol{\phi})$ is the constraint function whose expression depends on the specific design specification, e.g., the global volume constraint, the local volume constraint.

Solving. The control equation of the optimization (Equation 3.21-Equation 3.24) can be iteratively solved via several different approaches, and at each iteration step, three major stages are involved in general:

- **FEA**. Solve the static elasticity equation (Equation 3.22) to evaluate the objective function c. For high-resolution models, the scheme of solving the linear system based on the *Geometric Multigrid Solver* has been proven highly efficient [AAL15, WDW15, LHZ*18].

- **Sensitivity analysis**. Compute the derivatives of the objective function and constraint function with respect to the design variable $\boldsymbol{\phi}$, i.e., $\frac{\partial c}{\partial \phi}$ and $\frac{\partial g}{\partial \phi}$.
- **Design update**. Based on the sensitivity analysis result, update the design variables by means of the numerical optimizer, e.g., the Optimality Criteria (OC) methods [Sig01], Sequential Linear Programing (SLP), the Method of Moving Asymptotes (MMA) [Sva87, AL13].

Filtering. It leads to the mesh-dependent solution if directly taking the design variable $\boldsymbol{\phi}$ as the physical density in topology optimization. I.e., the tiny sub-structures or void regions that are comparable with the element size might be introduced when refining the mesh for obtaining a better description of the final design [WLS11]. On the one hand, the optimization process might converge to a completely different topology with respect to different mesh resolutions, on the other hand, these artificially-added tiny structural details might violate the restriction of the permitted minimum thickness in the downstream manufacturing stage [WDW15], both of which are undesirable in topology optimization. Furthermore, the design might also suffer from the well-known checkerboard pattern, i.e., the alternately appearing empty and solid elements in the final material layout, when the first-order quadrilateral or hexahedral finite elements are used for simulation [DS95]. To get rid of such limitations, a popular way is to introduce a density filter that converts the density value of each element to the weighted average of its neighboring values, where the neighborhood is defined by a circle (2D) or sphere (3D) with a specific radius, see Equation 3.25

$$\tilde{\phi}_e = \frac{\sum_{i \in M_e} w_{i,e} \phi_i}{\sum_{i \in M_e} w_{i,e}}, \quad M_e = \{i | \parallel x_i - x_e \parallel_2 \leq r_e\}, \ \forall e \tag{3.25}$$

Here $\tilde{\phi}_e$ is the auxiliary design variable of ϕ_e. x_e and x_i are the center coordinates of the simulation elements corresponding to design variables ϕ_e and ϕ_i, M_e is the number of elements that lay in the range centered at x_e with radius r_e. $w_{i,e}$ is the weighting factor and can be defined by different radial functions. Here, the method in [WLS11, WAWS18] is employed, which lets $w_{i,e}$ vary linearly with respect to the distances of x_i to x_e

$$w_{i,e} = r_e - |x_i - x_e| \tag{3.26}$$

Projection. The density-based topology optimization is supposed to obtain a binary density layout, i.e., the volume fraction of each simulation element should converge to either 1 (solid) or 0 (empty) in the final design. However, by using the density filtering in Equation 3.26, the gray transition regions with intermediate density values between 0 and 1 are encouraged inherently, thereby, dragging the convergence speed of the optimization process inevitably. In order to promote the binary density layout, various projection techniques that project the auxiliary design variable $\tilde{\phi}_e$ into 0/1 space have been

proposed [GPB04, Sig07, WLS11]. For instance, the popular Heaviside projection, which promotes a 0-1 solution by thresholding the auxiliary design variable $\tilde{\phi}_e$ at the value of $\frac{1}{2}$, and is usually arranged into a compact expression using the $tanh$ function

$$\rho_e(\tilde{\phi}_e) = \frac{\tanh(\frac{\beta}{2}) + \tanh(\beta(\tilde{\phi}_e - \frac{1}{2}))}{2\tanh(\frac{\beta}{2})}. \tag{3.27}$$

Here, ρ_e is the proxy density value of the original design variable ϕ_e, bridged by the auxiliary design variable $\tilde{\phi}_e$, and will be taken as the actual density value in FEA simulation. The smoothed Heaviside function has a parameter, β, to control its sharpness. For improving convergence behavior, a continuation scheme is applied to gradually increase its sharpness, e.g., starting with a smaller value (e.g., $\beta = 1$) and double its value every 40 iterations until it reaches the permitted maximum value. In [WAWS18, WWW22b], this maximum value is set to 128.

Material Interpolation. The modified Solid Isotropic Material with Penalization (SIMP) material model is usually used to model the material properties of the isotropic material

$$E_e(\rho_e) = E_{min} + \rho_e^{\gamma}(E_0 - E_{min}), \tag{3.28}$$

where E_0 is the Young's Modulus of a fully solid element ($\rho_e = 1$). E_{min} is a minimum Young's modulus (e.g., $E_{min} = 1.0e^{-6}E_0$), introduced to avoid the singularity of the global stiffness matrix. γ is the penalization factor, which is typically set to 3 [BS99]. $E_e(\rho_e)$ is the interpolated Young's Modulus of the element with density ρ_e. It's worth mentioning that the final design becomes more detailed and exhibits lower compliance when letting γ start from a smaller value and gradually increase to 3 during the course of optimization.

Practical Issues. In the practical use of density-based topology optimization, one may encounter the situation where the geometry of some parts of the design domain needs to be kept during optimization, e.g., the specifically-reserved holes in the domain, and the silhouette of the domain. It's unavailable to exclude these parts from the design domain since they're also bearing loads. To this end, the so-called *Passive Elements* are introduced, which are set fully solid during the optimization, i.e., contributing to the global stiffness but not involving sensitivity analysis.

In order to facilitate the quantification of the convergence behavior of the optimization result, one also introduces the concept of *Sharpness* measured by

$$s = \frac{4}{n}\sum_e \rho_e(1-\rho_e) \tag{3.29}$$

Here, n is the number of simulation elements, a small value of s indicates a sharper binary design of the optimized density field.

In addition, due to the introduction of the auxiliary design variable $\tilde{\phi}_e$ and the proxy density value ρ_e, the chain rule needs to be used in computing $\frac{\partial c}{\partial \phi}$ and $\frac{\partial g}{\partial \phi}$ for sensitivity analysis.

3.4.2 Global Volume Constraint

In the classic topology optimization for compliance minimization, the total amount of permitted material consumption is taken as the constraint (α_{global}), i.e., the global volume constraint

$$\frac{1}{n}\sum_e \rho_e \leq \alpha_{\text{global}}. \tag{3.30}$$

Thereby, the corresponding constraint in Equation 3.23 is given by

$$g(\boldsymbol{\phi}) = \frac{\sum_e \rho_e}{n\alpha_{\text{global}}} - 1 \leq 0 \tag{3.31}$$

Substitute Equation 3.31 into Equation 3.23, then the control equation of the density-based topology optimization under global volume constraint is established. Taking the problem description in Figure 3.8h as an example, and solving the optimization problem, the corresponding optimized density layout can be found in Figure 3.8b.

3.4.3 Local Volume Constraint

The topology optimization under local volume constraint, also known as porous infill optimization, produces the bone-mimic infill pattern, and has become a popular branch in topology optimization [WAWS18]. Unlike the global volume constraint that only considers the total material consumption, the local volume constraint introduces an upper bound of the material consumption for each simulation element and its vicinity locally. Thereby, a compliance-minimized design composed of sub-structures spanning different length scales is generated.

The local volume fraction ($\bar{\rho}_e$) is measured on a circular (2D) or sphere (3D) region which is centered at the centroid of the element (x_e) with radius R_e

$$\bar{\rho}_e = \frac{\sum_{i\in N_e}\rho_i}{\sum_{i\in N_e} 1}, \quad N_e = \{i|\parallel x_i - x_e \parallel_2 \leq R_e\},\ \forall e, \tag{3.32}$$

where $\rho_i \in [0,1]$ is the proxy density value of the simulation element e_i (see Equation 3.27). x_i is the coordinate of centroid of element e_i. N_e denotes the number of elements laying in the region centered

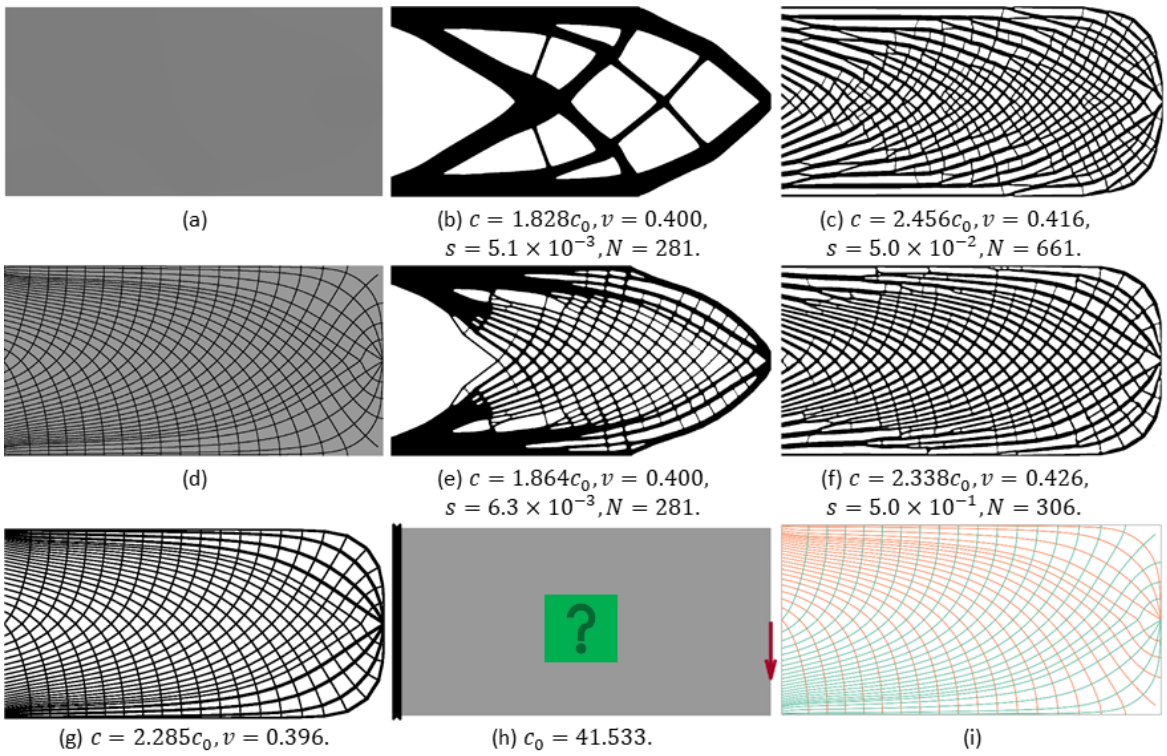

Figure 3.8: Result demonstration of the density-based topology optimization. (a) The commonly-used homogeneous starting guess for density-based topology optimization, the corresponding topologically optimized density layouts under global volume constraint and local volume constraint are given in (b) and (c), respectively. (d) The proposed PSLs-guided starting guess [WWW22c]. (e) and (f) show the corresponding results under the global and volume constraints, separately. (g) The directly generated structural design from the PSLs using the proposed method in [WWW22c]. (h) The problem description used for topology optimization here, the design domain is discretized by 1280×640 simulation elements. (i) The PSLs corresponding to the PSLs-guided starting guess in (d) and PSLs-guided structural design in (g). Here, c_0 is the compliance of the fully solid domain when applying for the same boundary condition, c is the optimized compliance value, v is the volume fraction of the design, s is the sharpness value, N is the number of iterations needed to approach the corresponding sharpness value.

at x_e with radius R_e, note here that R_e is set by users according to the specific design preference but should be larger than the radius of the density filter (r_e).

The local volume constraint is achieved by imposing an upper bound (α_e, $0 < \alpha_e < 1$) on the local volume fraction of each element in the design domain, i.e.,

$$\bar{\rho}_e \leq \alpha_e. \tag{3.33}$$

Apparently, the local volume constraint involves two parameters, α_e and R_e. α_e effectively determines the porosity, R_e indirectly controls the spacing between sub-structures. R_e and α_e are prescribed as constant values in the original approach. However, they can also be set spatially-varying scalar fields, thus, to achieve the gradations of the pore size and porosity of the optimized porous structures [SPG19, DS20, ZZ21].

Assigning a local volume constraint to each element leads to a large number of constraints that need to be considered by the optimizer. A seemingly alternative way is to replace them with $\max_{\forall e}(\bar{\rho}_e)$, yet, this constraint is not differentiable. In order to overcome this problem, $\max_{\forall e}(\bar{\rho}_e)$ are aggregated by the $p-$mean function first, then divided by α_e from both sides

$$\left(\frac{1}{n}\sum_e\left(\frac{\bar{\rho}_e}{\alpha_e}\right)^p\right)^{\frac{1}{p}} \leq 1, \tag{3.34}$$

$p = 16$ is found to give a good approximation [WAWS18]. Finally, the local volume constraint in Equation 3.23 can be given by

$$g(\boldsymbol{\phi}) = \left(\frac{1}{n}\sum_e\left(\frac{\bar{\rho}_e}{\alpha_e}\right)^p\right)^{\frac{1}{p}} - 1 \leq 0 \tag{3.35}$$

Substitute Equation 3.35 into Equation 3.23 to complete the control equation of the density-based topology optimization under local volume constraint. Figure 3.8c shows the corresponding optimized density layout of the problem description in Figure 3.8g.

Sectional discussion and summary. Density-based topology optimization under the local volume constraint has been widely accepted, however in our practice, we noticed that this method incurs the convergence issue in some optimization scenarios. I.e., the sharp binary design cannot be achieved in certain regions even after thousands of iterations, see Figure 3.9a-c. Given that it has been revealed in the original work [WAWS18] that the optimized topology has good agreement with the stress field that is simulated on the solid design domain, we resort to investigating this problem from the perspective of stress behavior. In particular, we found that the trisector degenerate points of the corresponding stress field are located in these low-convergence regions, see Figure 3.9d-f. We analyze the reason why

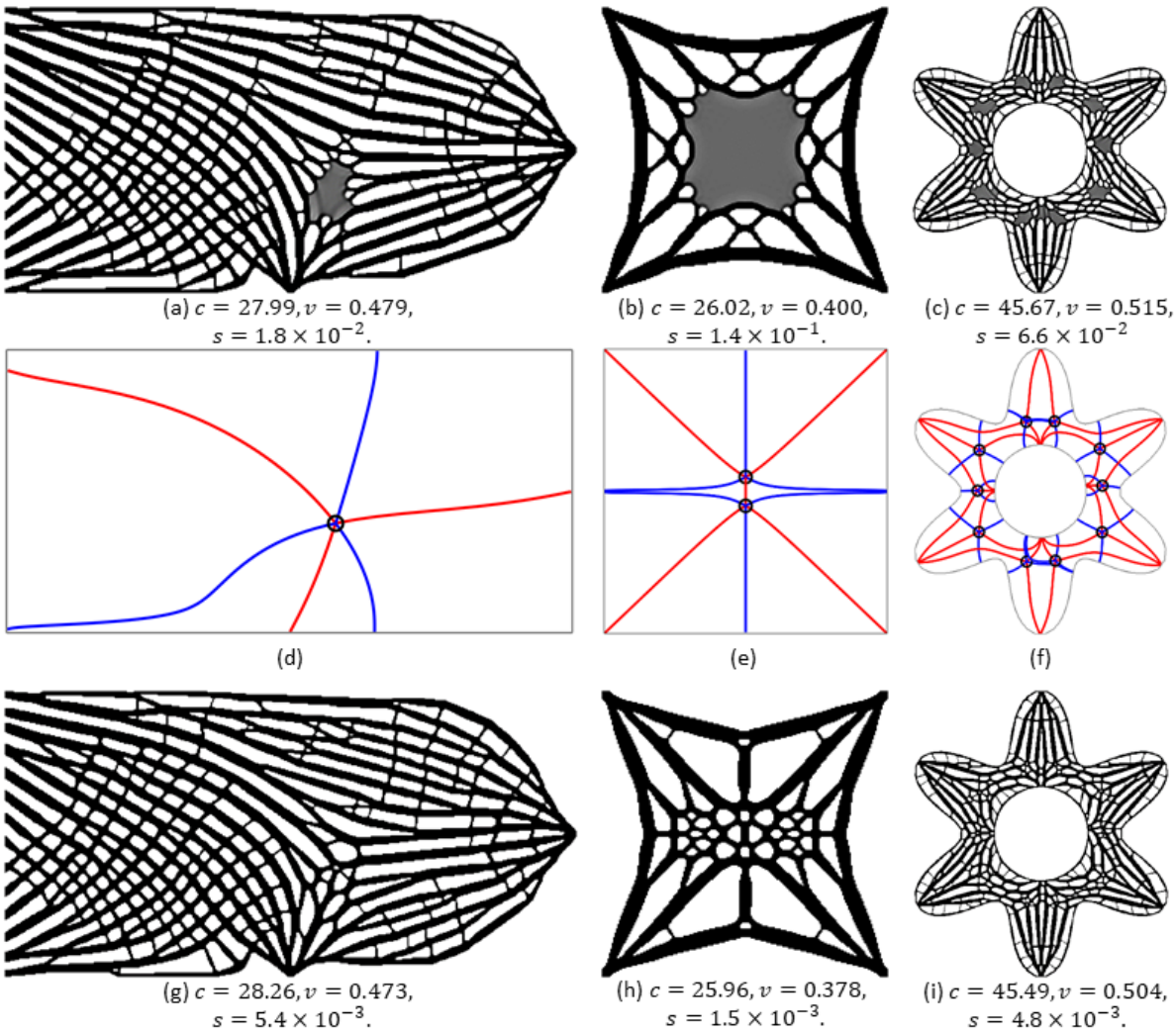

Figure 3.9: Demonstration of the convergence issue existing in the density-based topology optimization under local volume constraint. (a)-(c) Optimized density layouts using homogeneous starting guesses. (d)-(f) The trisector degenerate points (black circles) and associated topological skeleton corresponding to the stress fields of (a)-(c), the red and blue trajectories distinguish the topological skeleton following the major or minor PSLs, respectively. (g)-(i) Optimized density layouts corresponding to (a)-(c) but using the proposed starting guess in Paper C [WWW22b]. All of the results in (a)-(c) and (g)-(i) experience 800 iterations. Here, c is the optimized compliance value, v is the volume fraction of the design, and s is the sharpness value.

it cannot converge well is that the stress state there is of high isotropy, consequently, the optimizer cannot effectively decide the direction of material growth. Built upon this observation, and given the fact that density-based topology optimization is a non-convex problem, i.e., the final result is dependent on the starting guess, we propose to replace the commonly-used homogeneous starting guess of optimization with a new one, which is supposed to disturb this high isotropy there. Specifically, we assign a higher density value to the regions passed by the topological skeleton at the beginning of optimization, but note the optimizer can still decide whether to remove or keep these prescribed regions during the course of optimization. This can be arranged into an automatic initialization strategy and integrated into the original porous infill optimization. In this way, the convergence issue is solved efficiently (Figure 3.9g-i). To better observe the convergence behavior, we also show in Figure 3.10 the comparison of the optimization history of these three examples involved in Figure 3.9. We refer to our work Paper C [WWW22b] for details about the methodology.

Apart from the known characteristics of being non-convex of density-based topology optimization and the good agreement between the optimized topology and the corresponding stress field, the results in Paper C [WWW22b] further show that part of the prescribed starting guess is kept after optimization. More importantly, the optimized mechanical performance is not violated. All these features bring us to make a more aggressive step in initializing the starting guess for porous infill optimization, i.e., using the domain-filling and evenly spaced PSLs instead of only the topological skeleton for starting guess, see Figure 3.8d. Towards this end, we propose a PSLs-guided initialization strategy for the density-based topology optimization in our work Paper D [WWW22c]. The proposed method not only significantly accelerates the convergence of the density-based topology optimization under local volume constraint, but also promotes a more regular design since most of the mutually orthogonal trajectories are kept in the final design (Figure 3.8f). One can compare Figure 3.8f to Figure 3.8c. Inspired by this, we also propose a PSL-guided material layout strategy for structural design in [WWW22c]. With the thickness of PSLs being adjusted according to a strain energy-based importance metric, the compliance of the resulting design is en par with those generated by porous infill optimization, see Figure 3.8g. This method is highly efficient since it avoids the iterative optimization process. The involved PSLs in Figure 3.8g can be created by 3D-TSV presented in Paper B [WNW*22].

As seen from Figure 3.8b the result of density-based topology optimization under global volume constraint is predominantly mono-scale. However, it is known that stiffness optimal structures comprise spatially varying geometric patterns that span multiple length scales. To approach such an optimal design, one usually needs to perform the topology optimization on the sufficiently fine mesh, and carefully design the continuation techniques [AALS17, LHZ*18, BSPA20]. Given that part of the material used as PSLs-guided starting guess is kept during the density-based topology optimization under local volume constraint, it motivates a possible solution to promote the optimization under global volume constraint to converge to a more detailed design efficiently. I.e., we extend the proposed

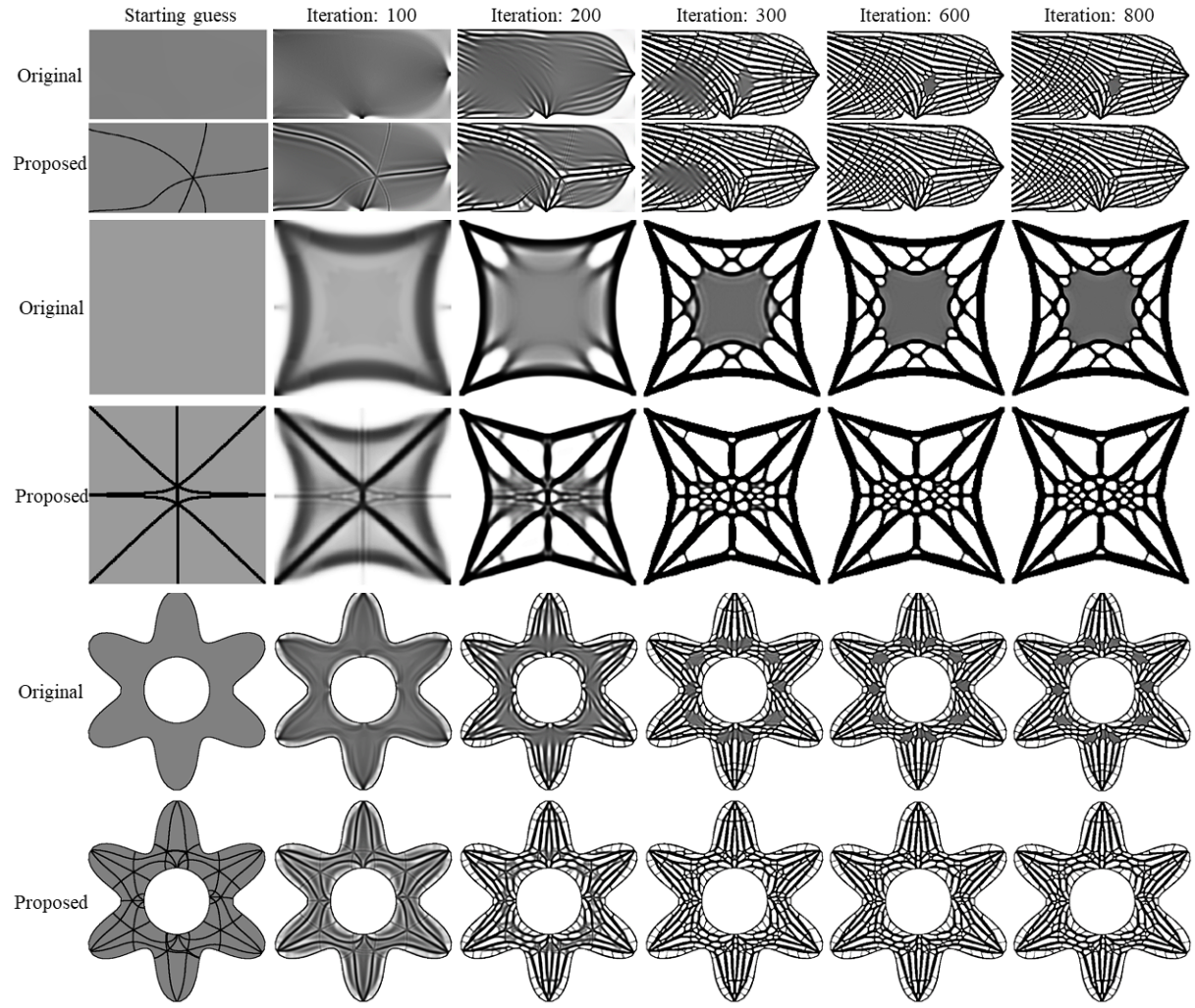

Figure 3.10: The intermediate density layouts that correspond to the three examples in Figure 3.9. 1st row: Figure 3.9a. 2nd: Figure 3.9g. 3rd row: Figure 3.9a. 4th row: Figure 3.9g. 5th row: Figure 3.9c. 6th row: Figure 3.9i.

PSLs-guided initialization strategy to the density-based topology optimization under global volume constraint. In this way, we find the resulting design exhibits sub-structures that span multiple length scales without losing the mechanical performance, see Figure 3.8e and compare it to Figure 3.8b. We demonstrate in [WWW22c] that such a design is more robust than the predominantly mono-scale design concerning the local damage.

3.5 Homogenization-based Topology Optimization

Though the various advantages, the density-based topology optimization only generates near-optimal results since it cannot ensure a global optimality. In addition, as a full-scale method [WSG21], it needs a high simulation resolution to obtain a better description of the final design, which incurs a heavy computational burden. As an alternative, the homogenization-based topology optimization can generate a mathematical specification of theoretically optimal structures. More importantly, by combining with the well-designed post-process strategy, it enables the possibility of deriving a near-optimal high-resolution design from the optimization result that is obtained from the coarse simulation resolution, thus, significantly saving processing time [GS18, GSA*20].

For structures under a single load, the theoretically optimal structural layout can be approximated by optimizing the distribution of square cells with a rectangular hole [BK88]. As illustrated in Fig. 3.11, the design domain is discretized into finite elements, each of which represents a repetition of an adapted configuration of the unit cell. The square cell has a unit side length, within it, there is a rectangular hole. The configuration of the unit cell is thus described by the hole sizes α_x and α_y and rotation angle θ, which expand the the design space of homogenization-based topology optimization over the density-based topology optimization where only one design variable $\boldsymbol{\phi}$ is involved. The material properties of the unit cell with a rectangular hole are constructed using homogenization. For the detailed theory about homogenization, one is referred to [GK90, HH98c, AA14].

The paradigm of the compliance-minimization optimization equations for the density-based topology optimization shown in Equation 3.21-Equation 3.24 also applies for the homogenization-based topology optimization. Accordingly, the numerical optimizers and density filters introduced for density-based topology optimization in Subsection 3.4.1 can also be reused here, but note the *Projection* stage is not needed since the homogenization-based topology optimization is not supposed to produce a binary design. In principle, the total material consumption is the only constraint in homogenization-based topology optimization, thus, the control equation of the homogenization-based topology optimization can be formulated into

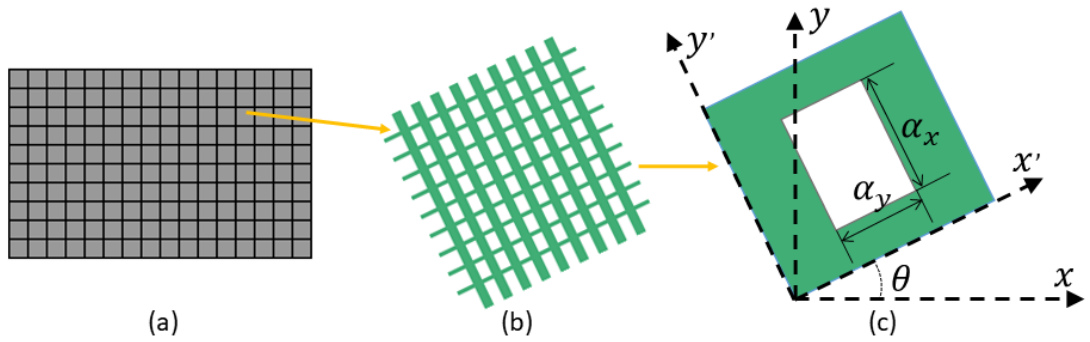

Figure 3.11: (a) The design domain is discretized into bilinear square grids. (b) Each square element is assumed to be filled by the orthotropic material. (c) The size and orientation of the approximately equivalent orthotropic cell, i.e., the square element with rectangular hole, are taken as design variables in homogenization-based topology optimization.

$$\begin{aligned} \min_{\boldsymbol{\phi}} \quad & c\left(\boldsymbol{\alpha}_x, \boldsymbol{\alpha}_y, \boldsymbol{\theta}\right) = \frac{1}{2}\boldsymbol{U}^T\boldsymbol{K}\boldsymbol{U}, \\ \text{s.t.} \quad & \boldsymbol{K}(\boldsymbol{\alpha}_x, \boldsymbol{\alpha}_y, \boldsymbol{\theta})\boldsymbol{U} = \boldsymbol{F}, \\ & g\left(\boldsymbol{\alpha}_x, \boldsymbol{\alpha}_y\right) = \frac{\sum_e (1-\alpha_x\alpha_y)}{n\alpha_{\text{global}}} - 1 \leq 0, \\ & \alpha_x \in [0.0,\ 1.0], \alpha_y \in [0.0,\ 1.0],\ \forall e. \end{aligned} \tag{3.36}$$

Seeing from Equation 3.36, the difference between the density-based topology optimization and homogenization-based one is the assumption of material properties, consequently, the elasticity tensors are different. In specific, the density-based topology optimization employs the isotropic material model, in which the simulation cell is described by the sole design variable ϕ. While the homogenization-based approach employs the orthotropic material model achieved by the unit cell with a rectangular hole, where the hole size parameters α_x and α_y describe the different capacities for load-carrying in the orthogonal directions of the simulation cell, and θ depicts the orientation of the simulation cells.

The mechanical property of the unit cell with a rectangular hole is orthotropic. The volume fraction or deposition ratio (ρ_e) of each cell is measured by $1-\alpha_x\alpha_y$. The elasticity tensor of the orthotropic cell is computed by

$$C(\alpha_x, \alpha_y, \theta) = R^T(\theta)C^H(\alpha_x, \alpha_y)R(\theta), \tag{3.37}$$

where $R(\theta)$ is the well-known rotation matrix. $C^H(\alpha_x, \alpha_y)$ represents the effective elasticity tensor for an axis-aligned unit cell with α_x, α_y, and can be evaluated by numerical homogenization proposed in [AA14].

At each iteration step of the optimization, the numerical optimizers used in the density-based topology optimization can also be utilized to update the design variables α_x and α_y here. The rotation

angle (θ) of each orthotropic cell is determined according to the corresponding principal stress direction, as presented in [Ped89, Ped90] that the optimal orientation of an orthotropic composite coincides with the principal stress directions if the structure is under a single load. An alternative solution for updating θ is by the gradient descent methods, which can work for both the single- and multi-loads situations but are less efficient than using principal stress directions in the single-load cases [AGDP19, SGSB20]. The educational code provided in [WSG21] can be used for the introduced homogenization-based topology optimization above.

It's worth emphasizing that the unit cell with a rectangular hole, i.e., the orthotropic cell, does not appear physically in discretizing the design domain. Instead, the Cartesian grid is still used to obtain the finite elements, and the cell orthotropy is only achieved by the design variables α_x, α_y, and θ. Besides the square cell with a rectangular hole, the rank-2 laminates material model can also be used to approximate such optimized design [Ave87, Gro18]. For the multiple loading cases, the orthotropic cells are inferior to describe the optimal anisotropic microstructure models, at which one needs to resort to the rank-3 laminates [JSG22].

Still take the problem description in Figure 3.8a as an example to perform the homogenization-based topology optimization, but a lower simulation resolution (80×40) is used, Figure 3.12 shows the optimized distribution of the orthotropic cells. It can be seen that this result gives the optimal stiffness with compliance value $c = 1.760c_0$, which is lower than the compliance of the results by the density-based topology optimization in Figure 3.8, despite the potential discretizing error between different mesh resolutions 80×40 and 1280×640. However, the result shown in Figure 3.12 cannot be directly used for manufacturing since the specification of these spatially-varying orthotropic cells is not a globally consistent geometry.

To tackle the manufacturing limit, the focus of homogenization-based approaches has shifted to the post-process of translating the results of homogenization-based topology optimization into a manufacturable geometry. This post-process is now often referred to as *de-homogenization*, which is supposed to efficiently generate high-resolution structural designs from the result of homogenization-based topology optimization performed on a coarse grid.

De-homogenization. The theoretical foundation of performing de-homogenization on the coarse homogenization-based topology optimization result to obtain the high-resolution design is that the periodic cells used in homogenization-based topology optimization can usually be described by a Fourier series [RP12, RPDK15], thereby, the new features can be interpreted from the coarse simulation results.

From the distribution of the optimized orthotropic cells, one can derive an equivalent density field and a direction field, which are described by $1-\alpha_x\alpha_y$ and θ of each cell, respectively, see Figure 3.13. The principle of de-homogenization is to re-distribute the density field so that 1) a fine-grid binary

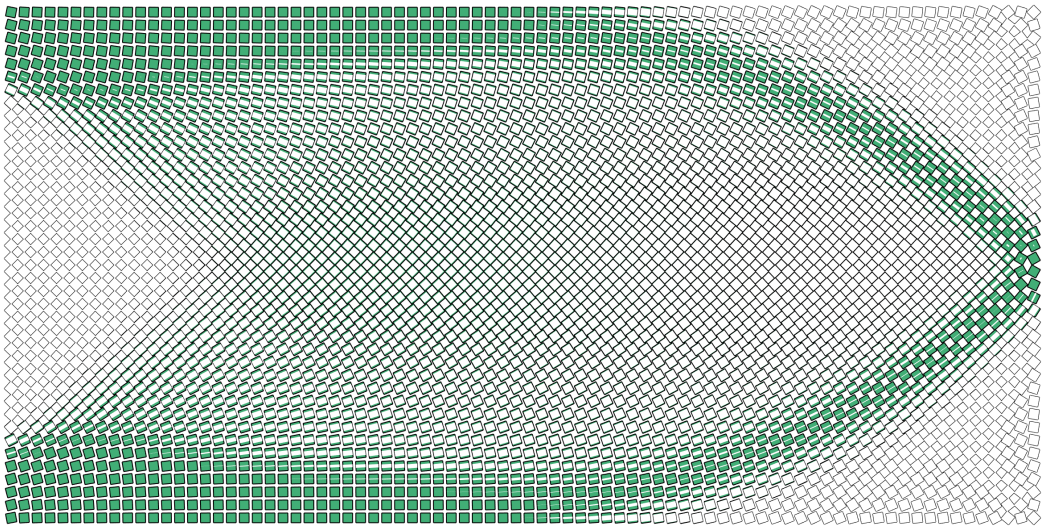

Figure 3.12: The optimized orthotropic cells by the homogenization-based topology optimization ($c = 1.760c_0, v = 0.400$).

density layout is generated, 2) a continuous transition among the local structures are obtained, and 3) the orientations of orthotropic cells are reflected in the binary density layout. In this way, one can expect to obtain a manufacturable result that shares the same volume fraction with the density field, meanwhile, inherits the mechanical performance of the optimal structure in a relaxed but controlled manner.

The key component in the existing de-homogenization strategies is to compute a fine-grid scalar field whose gradients are aligned with the direction field, which is achieved mainly by means of the so-called Projection. To do so, the design space is parametrized by using the two orthogonal periodic layers, e.g., the cosine waves, to represent the orthotropic cells. The Heaviside projection introduced in Equation 3.27 are usually used to promote the sharp binary design. Combining with some shape control schemes, the high-resolution manufacturable structure can be obtained [WSG21]. It's worth emphasizing that the singularity of the direction field (Figure 3.13b) usually needs to be treated carefully to avoid the nonintegrability [SGSB20].

Sectional discussion and summary. In terms of computational efficiency, the existing de-homogenization methods are already appealing in generating the high-resolution optimal structure compared to the density-based topology optimization. However, such methods still involve several cumbersome processes to obtain the final design, e.g., determining the scalar field (Projection), handling singularity of the direction field, controlling the design shape, and removing the un-related structural members. In our work Paper E [WWW22a], we consider de-homogenization from a rather intuitive perspective. In specific, the design space is parametrized with a quad-dominant mesh whose

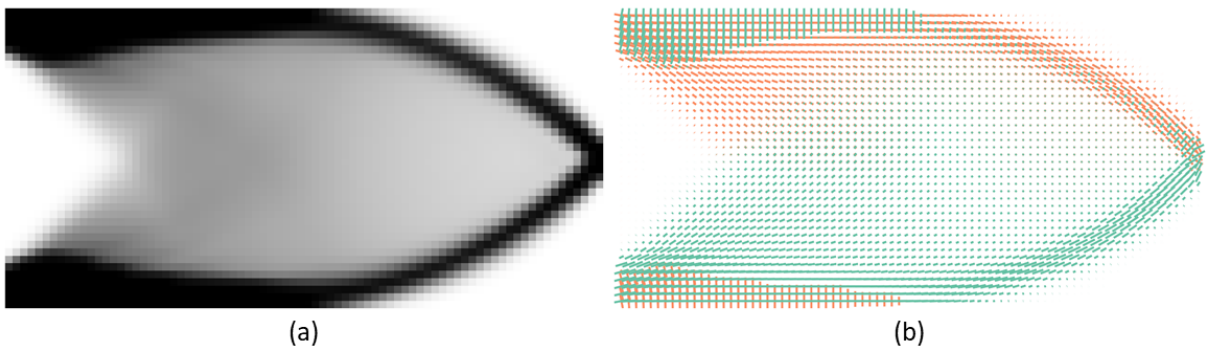

Figure 3.13: (a) Density distribution characterized by $1-\alpha_x\alpha_y$ of the optimized orthotropic cells. (b) Direction field extracted from the orientation of the optimized orthotropic cells.

edges are the piecewise linear streamlines traced from the direction field, the thicknesses of the mesh edges are adjusted inward according to the density and anisotropy of the optimized orthotropic cells, see Figure 3.14a-c. One can also take the elements of the quad-dominant mesh as a set of macroscopic near-orthotropic cells in an intuitive manner. Since the direction field is given by the principal stress direction in the current context, i.e., the streamlines are PSLs essentially. Thereby, the evenly spaced PSL seeding proposed in [WNW*22] can be directly used, and the singularity of the direction field can be tackled by means of the topology analysis to the corresponding stress field. This method avoids the projection step and thus is computationally efficient. In addition, since the final design of our method is described by an explicit representation in the form of a quad-dominant mesh with each edge being assigned a unique width, it would be beneficial for downstream operations such as user editing and fabrication process planning, see Figure 3.14d for the high-resolution result by our method.

Comparing the structural designs from de-homogenizing the homogenization-based topology optimization result (Figure 3.14d) and density-based topology optimization under global volume constraint (Figure 3.8b, e), we see that they have very close compliance values under the same material consumption. Though both of the structural designs have the same resolution (1280×640) in the end, the homogenization-based approach only needs to perform optimization on a significantly coarse resolution (e.g., 80×40 here) and then interpret the result on a higher resolution mesh via de-homogenization. In contrast, the density-based one needs to perform the optimization on the full-scale resolution (1280×640), thus, consuming much more processing time.

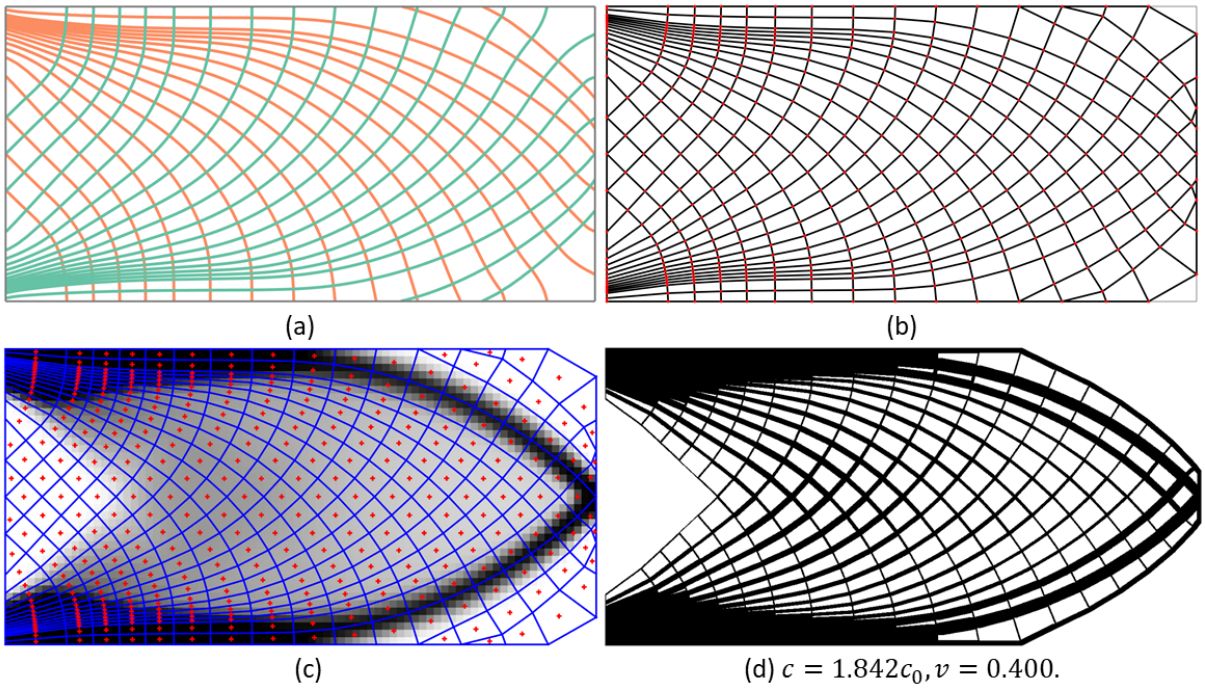

Figure 3.14: Method overview of the proposed de-homogenization strategy in our work Paper E [WWW22a]. (a) The streamlines generated from the direction field shown in Figure 3.13a. The constructed quad-dominant mesh (c) whose edges follow the piecewise linear streamlines (b) converted from the domain-filling and evenly spaced streamlines (a) that are generated from the direction field shown in Figure 3.13a. (d) The de-homogenized structural design (1280×640), c is the optimized compliance value, v is the volume fraction of the design.

4

Paper A: A Globally Conforming Lattice Structure for 2D Stress Tensor Visualization[1]

Abstract of paper We present a visualization technique for 2D stress tensor fields based on the construction of a globally conforming lattice. Conformity ensures that the lattice edges follow the principal stress directions and the aspect ratio of lattice elements represents the stress anisotropy. Since such a lattice structure cannot be space-filling in general, it is constructed from multiple intersecting lattice beams. Conformity at beam intersections is ensured via a constrained optimization problem, by computing the aspect ratio of elements at intersections so that their edges meet when continued along the principal stress lines. In combination with a coloring scheme that encodes relative stress magnitudes, a global visualization is achieved. By introducing additional constraints on the positional variation of the beam intersections, coherent visualizations are achieved when external loads or material parameters are changed. In a number of experiments using non-trivial scenarios, we demonstrate the capability of the proposed visualization technique to show the global and local structure of a given stress field.

Author Contribution The first author was responsible for the implementation of the whole method, including the construction of the constrained optimization equations. Prof. Dr. Dr. Jun Wu gave the physical interpretation of the obtained visualization and suggested the solving scheme of the constrained optimization problem. Prof. Dr. Rüdiger Westermann proposed the original idea for the project, i.e., achieving such a visualization by optimization. The paper was finished under close collaboration among the co-authors.

5

Paper B: 3D-TSV: The 3D Trajectory-based Stress Visualizer[1]

Abstract of paper In this paper, we present novel algorithms for visualizing the three mutually orthogonal principal stress directions in 3D solids under load and we discuss the efficient integration of these algorithms into the 3D Trajectory-based Stress Visualizer (3D-TSV), a visual analysis tool for the exploration of the principal stress directions of 3D stress field. In the design of 3D-TSV, several perceptual problems have been solved. We present a novel algorithm for generating a space-filling and evenly spaced set of stress lines. The algorithm obtains a more regular appearance by considering the locations of lines, and enables the extraction of a level-of-detail representation with adjustable sparseness of the trajectories along a certain stress direction. A new combined visualization of two principal directions via oriented ribbons enables to convey ambiguities in the orientation of the principal stress directions. Additional depth cues have been added to improve the perception of the spatial relationships between trajectories. 3D-TSV provides a modular and generic implementation of key algorithms required for a trajectory-based visual analysis of principal stress directions, including the automatic seeding of space-filling stress lines, their extraction using numerical schemes, their mapping to an effective renderable representation, and rendering options to convey structures with special mechanical properties. 3D-TSV is accessible to end users via a C++- and OpenGL-based rendering frontend that is seamlessly connected to a MatLab-based extraction backend. The code (BSD license) of 3D-TSV as well as scripts to make ANSYS and ABAQUS simulation results accessible to the 3D-TSV backend are publicly available.

Author Contribution The first author is responsible for the design of the seeding algorithm for evenly-spaced and domain-filling PSL distribution and developed the backend of the tool 3D-TSV. Christoph Neuhauser deeply participated in the discussion of the PSL rendering and developed the

frontend of the tool of 3D-TSV. Prof. Dr. Dr. Jun Wu and Dr. Xifeng Gao gave the practical and conceptual inspiration and guidance for this project, respectively. Discussions with Prof. Dr. Rüdiger Westermann led to the final paper.

6

Paper C: Stress Topology Analysis for Porous Infill Optimization[1]

Abstract of paper The optimization of porous infill structures via local volume constraints has become a popular approach in topology optimization. In some design settings, however, the iterative optimization process converges only slowly, or not at all even after several hundreds or thousands of iterations. This leads to regions in which a distinct binary design is difficult to achieve. Interpreting intermediate density values by applying a threshold results in large solid or void regions, leading to sub-optimal structures. We find that this convergence issue relates to the topology of the stress tensor field that is simulated when applying the same external forces on the solid design domain. In particular, low convergence is observed in regions around so-called trisector degenerate points. Based on this observation, we propose an automatic initialization process that prescribes the topological skeleton of the stress field into the material field as solid simulation elements. These elements guide the material deposition around the degenerate points, but can also be remodelled or removed during the optimization. We demonstrate significantly improved convergence rates in a number of use cases with complex stress topologies. The improved convergence is demonstrated for infill optimization under homogeneous as well as spatially varying local volume constraints.

Author Contribution The first author found the correlation between the convergence issue of the porous-infill optimization and the stress topology and was responsible for the implementation of the whole method. Prof. Dr. Dr. Jun Wu suggested the use of a topological skeleton as the initialization. Prof. Dr. Rüdiger Westermann gave the analysis on the relation between the convergence issue and the stress topology. The final paper was made under close collaboration among the co-authors.

7

Paper D: Stress trajectory guided structural design and topology optimization[1]

Abstract of paper Density-based topology optimization using global and local volume constraints is a key technique to automatically design lightweight structures. It is known that stiffness optimal structures comprise spatially varying geometric patterns that span multiple length scales. However, both variants of topology optimization have challenges to efficiently converge to such a structural layout. In this paper, we investigate material layouts that are generated from stress trajectories, i.e., to compile a globally consistent structure by tracing the stress trajectories from finite element simulation of the solid design domain under external loads. This is particularly appealing from a computational perspective, since it avoids iterative optimization that involves finite element analysis on fine meshes. By regularizing the thickness of each trajectory using derived strain energy measures along them, stiff structural layouts can be generated in a highly efficient way. We then shed light on the use of the resulting structures as initial density fields in density-based topology optimization, i.e., to generate an initial density field that is then further optimized via topology optimization. We demonstrate that by using a stress trajectory guided density initialization in lieu of a uniform density field, convergence issues in density-based topology optimization can be significantly relaxed at comparable stiffness of the resulting structural layouts.

Author Contribution The first author was responsible for the whole method. Discussions with Prof. Dr. Dr. Jun Wu and Prof. Dr. Rüdiger Westermann led to the final paper.

8

Paper E: Streamline guided De-Homogenization for High-Resolution Structural Design[1]

Abstract of paper We present a novel de-homogenization approach to generate a high-resolution and manufacturable structure from the continuous density layout produced by homogenization-based topology optimization. The proposed approach builds upon a streamline-based parametrization of the design domain, using a set of space-filling and evenly-spaced streamlines in the two mutually orthogonal direction fields that are obtained by globally optimizing the orientation of orthotropic cells via a homogenization-based approach. Streamlines in this field are converted into a graph structure, which is then used to construct a lattice structure composed of quadrilateral and triangular cells whose edges follow the direction fields. The manufacturable design, i.e., the binary density layout, is achieved by extruding material from the edges of each lattice element inward, according to the volume fraction of the continuous density field in each element. In this way, the volume fraction of each de-homogenized lattice element remains equal to the corresponding homogeneous elements. In addition, we propose a metric to evaluate the anisotropy of lattice elements, and use it to allocate more material along the lattice edges bearing larger stresses. In a number of examples we demonstrate high mechanical performance and regular appearance of the resulting binary designs, as well as high computational efficiency of the proposed construction process.

Author Contribution The first author was responsible for the design and implementation of the whole method. Prof. Dr. Dr. Jun Wu brought the preliminary idea for this project. Discussions with Prof. Dr. Rüdiger Westermann led to the final paper.

9 Final Discussion

9.1 Conclusion

This thesis presents a series of methods to answer the two questions proposed in Introduction: *How to visualize the stress tensor field? And how does stress visualization benefit structural design and optimization?*

Via the globally conforming lattice structure proposed in Paper A, we have demonstrated that the grids generated by the inherently intersected major and minor PSLs in 2D stress fields can be leveraged to encode the local stress anisotropy. This enables the construction of a hybrid visualization that integrates the advantages of trajectory- and glyph-based stress visualization into a globally consistent structure, such as stress direction, continuity, divergence/convergence, and anisotropic properties. Herein, the conformity is achieved by a constrained optimization problem. We have also shown a modification to visualize 3D stress fields, by progressively building a beam structure comprised of hexahedral elements using a sequential growth process. The 3D-TSV is presented in Paper B, which is, to the best of our knowledge, the first dedicated tool to visualize the major, medium, and minor PSLs simultaneously. 3D-TSV builds upon a novel seeding strategy, which can generate a domain-filling and evenly spaced set of PSLs. This seeding approach is derived from the classic evenly-spaced streamline seeding methods for vector field visualization, and tailored for stress tensor visualization. Specifically, during the course of seeding, all three types of PSLs are considered simultaneously, and different types of PSLs are encouraged to intersect. We have demonstrated that, in this way, the visual quality of the resulting PSL distribution can be improved. We've also formed a consistent multi-resolution hierarchy of PSLs by incorporating different merging thresholds for each PSL type into the seeding process. 3D-TSV works for both 2D and 3D situations and is made publicly available under the BSD 2-Clause License.

We have investigated the convergence behavior of density-based topology optimization by means of

the stress tensor visualization techniques. In specific, we in Paper C have concluded that the existence of trisector degenerate points in the stress field simulated on the design domain is the major cause of low convergence when the local volume constraint is employed in topology optimization. To this end, we have proposed a stress topology-based starting guess that quickly guides the optimization towards a stable binary design. This starting guess generates an initial solid material layout along the topological skeleton of the stress field, which is comprised of principal stress lines starting at the trisector degenerate points. Built upon the insights of Paper C, we've made a more aggressive step in initializing the starting guess for density-based topology optimization, i.e., using the domain-filling and evenly spaced PSLs instead of only the topological skeleton (Paper D). In particular, we've found that the convergence rate of topology optimization under local volume constraint can be further improved without violating the optimal mechanical performance, meanwhile, the resulting structure exhibits a more regular appearance. The topology optimization under global volume constraint converges to a structure that spans multiple length scales, in lieu of a predominantly mono-structure. Thereby, the robustness of the final design with respect to the local damage is improved. We've also proposed a method to create the near-optimal lightweight structure by directly using the domain-filling and evenly spaced PSLs. This method is highly efficient since it avoids the iterative optimization process, and the resulting structure shows comparable mechanical performance with the one by topology optimization under local volume constraint.

In the end, we in Paper E have proposed a novel streamline-based de-homogenization strategy for the homogenization-based topology optimization results, which enables the quick design of the high-resolution lightweight structure. Here, the streamlines are essentially PSLs in the scope of this thesis. The compliance of the de-homogenized high-resolution structures is very close to that of the optimal design from homogenization-based optimization, and it is consistently superior to the compliance achieved via density-based topology optimization. The resulting structures exhibit a globally regular appearance, uniformly covering the domain with quad-dominant mesh elements. More importantly, the final design is described by an explicit representation in the form of a quad-dominant mesh, which can benefit downstream operations such as user editing and fabrication process planning.

Apart from the concrete contributions to the methodology and techniques, our work combined also leads to a conceptual conclusion. I.e., with properly-designed stress visualization methods, the significance of the stress field in structural design and optimization is not only a metric for evaluating the rationality of structural design but also can bring new solutions for structural design and optimization. In return, the novel stress tensor visualization methods could be spawned by considering some concrete requirements for structural design and optimization when constructing the stress tensor visualization algorithms. Altogether, it's promising to promote the interaction of research between stress tensor visualization and structural design and optimization.

9.2 Future Work

Both in Paper D ([WWW22c]) and Paper E ([WWW22a]), the core idea of our work is essentially to parametrize the design space of structural topology optimization by leveraging the structured visualization of the stress tensor field. Thereby, in terms of methodology and results, we obtain several appealing features over the conventional topology optimization, for instance, the high computational efficiency, regular appearance of structural design, and the explicit geometrical representation of the design. The limitation is that we only shed light on 2D situations in these works. Thus, in future work, our primary goal is to extend these proposed methods to 3D. The preliminary outlook of this extension would be 1) guiding the density-based topology optimization under the local volume constraint converge to a truss-like design instead of a wall-like one. 2) promoting the density-based topology optimization under the global volume constraint to generate a relatively multi-scale structure instead of a mono-scale one, but without using the extremely high simulation resolution. 3) enabling the quick design of the high-resolution infill structure using PSLs. In principle, such an extension is straightforward. Yet, as we know that the 3D lines do not intersect necessarily though we've tried to let more PSLs intersect via 3D-TSV ([WNW*22]). Such a feature would bring a negative impact on the structural design from the view of optimal stiffness. Thus, we need to study the PSL intersection issue first during the extension. Towards a similar goal, the existing approaches typically resort to the frame-aligned parametrization and the hex-mesh generation built upon it [AJL*19, WWG21]. To get rid of the effect of the degeneracy, such approaches first convert the original stress field into a smooth frame field for subsequent parametrization. A different method is achieved by using the so-called *stream surfaces* that strictly align with the input frame field, where they circumvent the singularity issue based on their observation that the structures they seek are not affected by the singularities [SOG*22]. Unlike the methods in [AJL*19] and [WWG21] producing the truss-like designs, [SOG*22] gives rise to the wall-like design. Built upon the existing methods, our ambitious goal is still to construct the parametrization from PSLs. In specific, we plan to explore the feasibility of introducing a controllable relaxing scheme to make the PSL set well intersected, meanwhile, conveying the singularity of the stress field distinctly. If necessary, we also plan to investigate the use of interactive editing for the design. The ultimate result shall be a new structured grid-like visualization of the 3D stress tensor field but can also serve as a parametrization to the design domain for structural design and optimization.

In Paper C ([WWW22b]), we study the convergence issue of the porous infill optimization ([WAWS18]) from a novel perspective. We make use of the stress topology analysis to predict the potential low-convergence regions and solve this convergence issue effectively by employing a stress topological skeleton-guided initialization strategy. However, the discussion in this work is restricted only to 2D, we aim for extending it to 3D in future work. To this end, we need a visualizer to help spot the low-convergence regions in the density field during the course of topology optimization, which,

in principle, can be arranged into a direct volume rendering problem. In addition, we also need a robust solution to obtain the topological features like degeneracy and topological skeleton of the stress field in 3D. Through this way, we can study the potential correlation between the convergence issue and the stress topology. The major challenge of such idea would be the robust identification of degeneracy due to the well-known issue of numerical instability. Given that it's not necessary to compute the precise positions of degeneracy if we just want to compare the spatial distributions of the low-convergence regions and the degeneracy, we plan to circumvent this challenge via a relaxed scheme. Specifically, we'll define a degeneracy metric over each element, which is supposed to quantify the scale of degeneracy within each element that may contain the degeneracy, then we can convert the rigorous stress topology analysis problem into a rendering problem. In this way, we can expect to obtain an intuitive impression of the possible correlation between the low-convergence regions and the stress topology. If this correlation holds, we'll consider using PSLs around the degeneracy to initialize the starting guess of the porous infill optimization in 3D.

This thesis only covers the single loading condition in structural topology optimization, while the topology optimization subjected to multiple loading cases is also an important concern in some application scenarios. It won't bring too much difference to the density-based topology optimization when the multiple loading cases are considered, one usually just needs to sum up the compliance values corresponding to different loading conditions with the assigned weighting factors of each. When coming to homogenization-based topology optimization, however, things get complex. It has been proposed in [Ave87] and further confirmed in [JSG22] that rank-3 laminates are optimal for such situations. In contrast, the orthotropic material models used for the single loading case, like rank-2 laminates and the square unit cell with a rectangular hole, cannot characterize the anisotropy here. Consequently, one needs three direction vectors to describe the orientation of each cell. Technically, the existing projection-based de-homogenization methods (e.g., [GS18]) for the single loading case can also be adapted to handle such an issue, see [JSG22]. However, the resulting design is exhibited in a less structured way since the rather random intersections among the sub-structures that follow the three different direction fields. We aim for seeking a compact geometric description of such a design. Specifically, we plan to generate a conforming triangular mesh to parameterize the design domain. For each triangular element, the three edges follow the three optimized direction vectors, respectively. Compared to the existing method, the planned one incurs fewer vertices and is supposed to provide better regularity and manufacturability. Further, we'll also explore the feasibility of extending such an idea to 3D, where the triangular mesh would be replaced with the tetrahedral mesh. The key component of this work package is the meshing algorithm, i.e., how to generate a conforming triangular mesh from a direction field where three different vector fields exist.

Bibliography

[AA14] ANDREASSEN E., ANDREASEN C. S.: How to determine composite material properties using numerical homogenization. *Computational Materials Science 83* (2014), 488–495. doi:10.1016/j.commatsci.2013.09.006.

[AAL14] AMIR O., AAGE N., LAZAROV B. S.: On multigrid-cg for efficient topology optimization. *Structural and Multidisciplinary Optimization 49*, 5 (2014), 815–829. doi:10.1007/s00158-013-1015-5.

[AAL15] AAGE N., ANDREASSEN E., LAZAROV B. S.: Topology optimization using petsc: An easy-to-use, fully parallel, open source topology optimization framework. *Structural and Multidisciplinary Optimization 51*, 3 (2015), 565–572. doi:10.1007/s00158-014-1157-0.

[AALS17] AAGE N., ANDREASSEN E., LAZAROV B. S., SIGMUND O.: Giga-voxel computational morphogenesis for structural design. *Nature 550*, 7674 (2017), 84–86. doi:10.1038/nature23911.

[ACS*11] ANDREASSEN E., CLAUSEN A., SCHEVENELS M., LAZAROV B. S., SIGMUND O.: Efficient topology optimization in matlab using 88 lines of code. *Structural and Multidisciplinary Optimization 43*, 1 (2011), 1–16. doi:10.1007/s00158-010-0594-7.

[AGDP19] ALLAIRE G., GEOFFROY-DONDERS P., PANTZ O.: Topology optimization of modulated and oriented periodic microstructures by the homogenization method. *Computers & Mathematics with Applications 78*, 7 (2019), 2197–2229. doi:10.1016/j.camwa.2018.08.007.

[AJL*19] ARORA R., JACOBSON A., LANGLOIS T. R., HUANG Y., MUELLER C., MATUSIK W., SHAMIR A., SINGH K., LEVIN D. I.: Volumetric michell trusses for parametric design & fabrication. In *Proceedings of the ACM Symposium on Computational Fabrication* (2019), ACM, pp. 1–13. doi:10.1145/3328939.3328999.

[AJT04] ALLAIRE G., JOUVE F., TOADER A.-M.: Structural optimization using sensitivity analysis and a level-set method. *Journal of Computational Physics 194*, 1 (2004), 363–393. doi:10.1016/j.jcp.2003.09.032.

[AL13] AAGE N., LAZAROV B. S.: Parallel framework for topology optimization using the method of moving asymptotes. *Structural and multidisciplinary optimization 47*, 4 (2013), 493–505. doi:10.1007/s00158-012-0869-2.

[Ave87] AVELLANEDA M.: Optimal bounds and microgeometries for elastic two-phase composites. *SIAM Journal on Applied Mathematics 47*, 6 (1987), 1216–1228. doi:10.1137/0147082.

[Ben89] BENDSØE M. P.: Optimal shape design as a material distribution problem. *Structural Optimization 1*, 4 (1989), 193–202. doi:10.1007/BF01650949.

[Ben95] BENDSØE M. P.: *Optimization of structural topology, shape, and material*, vol. 414. Springer, 1995. doi:10.1007/978-3-662-03115-5.

[BHM00] BRIGGS W. L., HENSON V. E., MCCORMICK S. F.: *A multigrid tutorial*. SIAM, 2000.

[BK88] BENDSØE M. P., KIKUCHI N.: Generating optimal topologies in structural design using a homogenization method. *Computer Methods in Applied Mechanics and Engineering 71*, 2 (1988), 197–224. doi:10.1016/0045-7825(88)90086-2.

[Bou01] BOURDIN B.: Filters in topology optimization. *International journal for numerical methods in engineering 50*, 9 (2001), 2143–2158. doi:10.1002/nme.116.

[BS99] BENDSØE M. P., SIGMUND O.: Material interpolation schemes in topology optimization. *Archive of applied mechanics 69*, 9 (1999), 635–654. doi:10.1007/s004190050248.

[BS04] BENDSØE M., SIGMUND O.: *Topology Optimization: Theory, Methods, and Applications*. Springer Berlin Heidelberg, 2004.

[BSPA20] BAANDRUP M., SIGMUND O., POLK H., AAGE N.: Closing the gap towards super-long suspension bridges using computational morphogenesis. *Nature communications 11*, 1 (2020), 1–7. doi:10.1038/s41467-020-16599-6.

[CAS15] CLAUSEN A., AAGE N., SIGMUND O.: Topology optimization of coated structures and material interface problems. *Computer Methods in Applied Mechanics and Engineering 290* (2015), 524–541. doi:10.1016/j.cma.2015.02.011.

[CL93] CABRAL B., LEEDOM L. C.: Imaging vector fields using line integral convolution. In *Proceedings of the 20th annual conference on Computer graphics and interactive techniques* (1993), pp. 263–270. doi:10.1145/166117.166151.

[CRB*05] CROSSNO P., ROGERS D. H., BRANNON R. M., COBLENTZ D., FREDRICH J. T.: Visualization of geologic stress perturbations using mohr diagrams. *IEEE Transactions on Visualization and Computer Graphics 11*, 5 (2005), 508–518. doi:10.1109/TVCG.2005.86.

[CRBC04] CROSSNO P., ROGERS D. H., BRANNON R. M., COBLENTZ D.: Visualization of salt-induced stress perturbations. In *IEEE Visualization 2004* (2004), IEEE, pp. 369–376. doi:10.1109/VISUAL.2004.115.

[CYR19] CANG R., YAO H., REN Y.: One-shot generation of near-optimal topology through theory-driven machine learning. *Computer-Aided Design 109* (2019), 12–21. doi:10.1016/j.cad.2018.12.008.

[DFLW17] DAYNES S., FEIH S., LU W. F., WEI J.: Optimisation of functionally graded lattice structures using isostatic lines. *Materials & Design 127* (2017), 215–223. doi:10.1016/j.matdes.2017.04.082.

[DGBW09] DICK C., GEORGII J., BURGKART R., WESTERMANN R.: Stress tensor field visualization for implant planning in orthopedics. *IEEE Transactions on Visualization and Computer Graphics 15*, 6 (2009), 1399–1406. doi:10.1109/TVCG.2009.184.

[DGW11] DICK C., GEORGII J., WESTERMANN R.: A real-time multigrid finite hexahedra method for elasticity simulation using cuda. *Simulation Modelling Practice and Theory 19*, 2 (2011), 801–816.

[DH92] DELMARCELLE T., HESSELINK L.: Visualization of second order tensor fields and matrix data. In *Proceedings Visualization'92* (1992), IEEE, pp. 316–317. doi:10.1109/VISUAL.1992.235193.

[DH93] DELMARCELLE T., HESSELINK L.: Visualizing second-order tensor fields with hyperstreamlines. *IEEE Computer Graphics and Applications 13*, 4 (1993), 25–33. doi:10.1109/38.219447.

[DH94] DELMARCELLE T., HESSELINK L.: The topology of symmetric, second-order tensor fields. In *Proceedings Visualization'94* (1994), IEEE, pp. 140–147. doi:10.1109/VISUAL.1994.346326.

[Dic89] DICKINSON R. R.: A unified approach to the design of visualization software for the analysis of field problems. In *Three-dimensional visualization and display technologies* (1989), vol. 1083, SPIE, pp. 173–180. doi:10.1117/12.952885.

[DS95] DIAZ A., SIGMUND O.: Checkerboard patterns in layout optimization. *Structural optimization 10*, 1 (1995), 40–45. doi:10.1007/BF01743693.

[DS20] DAS S., SUTRADHAR A.: Multi-physics topology optimization of functionally graded controllable porous structures: Application to heat dissipating problems. *Materials & Design 193* (2020), 108775. doi:10.1016/j.matdes.2020.108775.

[EABS22] ELINGAARD M. O., AAGE N., BÆRENTZEN J. A., SIGMUND O.: De-homogenization using convolutional neural networks. *Computer Methods in Applied Mechanics and Engineering 388* (2022), 114197. doi:10.1016/j.cma.2021.114197.

[EHHS12] EICHELBAUM S., HLAWITSCHKA M., HAMANN B., SCHEUERMANN G.: Fabric-like visualization of tensor field data on arbitrary surfaces in image space. In *New Developments in the Visualization and Processing of Tensor Fields*. Springer, 2012, pp. 71–92. doi:10.1007/978-3-642-27343-8_4.

[FHHJ08] FENG L., HOTZ I., HAMANN B., JOY K.: Anisotropic noise samples. *IEEE Transactions on Visualization and Computer Graphics 14*, 2 (2008), 342–354. doi:10.1109/TVCG.2007.70434.

[GDAP20] GEOFFROY-DONDERS P., ALLAIRE G., PANTZ O.: 3-d topology optimization of modulated and oriented periodic microstructures by the homogenization method. *Journal of Computational Physics 401* (jan 2020), 108994. doi:10.1016/j.jcp.2019.108994.

[GK90] GUEDES J. M., KIKUCHI N.: Preprocessing and postprocessing for materials based on the homogenization method with adaptive finite element methods. *Computer Methods in Applied Mechanics and Engineering 83*, 2 (1990), 143–198. doi:10.1016/0045-7825(90)90148-F.

[GPB04] GUEST J. K., PRÉVOST J. H., BELYTSCHKO T.: Achieving minimum length scale in topology optimization using nodal design variables and projection functions. *International journal for numerical methods in engineering 61*, 2 (2004), 238–254. doi:10.1002/nme.1064.

[Gro18] GROEN J. P.: *Multi-scale design methods for topology optimization*. DTU Mechanical Engineering, 2018.

[GRT17] GERRITS T., RÖSSL C., THEISEL H.: Glyphs for space-time jacobians of time-dependent vector fields. *Journal of WSCG 25*, 1 (2017), 31–38.

[GS18] GROEN J. P., SIGMUND O.: Homogenization-based topology optimization for high-resolution manufacturable microstructures. *International Journal for Numerical Methods in Engineering 113*, 8 (2018), 1148–1163. doi:10.1002/nme.5575.

[GSA*20] GROEN J. P., STUTZ F. C., AAGE N., BÆRENTZEN J. A., SIGMUND O.: De-homogenization of optimal multi-scale 3d topologies. *Computer Methods in Applied Mechanics and Engineering 364* (jun 2020), 112979. doi:10.1016/j.cma.2020.112979.

[GSP19] GAO X., SHEN H., PANOZZO D.: Feature preserving octree-based hexahedral meshing. In *Computer graphics forum* (2019), vol. 38, Wiley Online Library, pp. 135–149. doi:10.1111/cgf.13795.

[Gue09] GUEST J. K.: Imposing maximum length scale in topology optimization. *Structural and Multidisciplinary Optimization 37*, 5 (2009), 463–473. doi:10.1007/s00158-008-0250-7.

[GZZ14] GUO X., ZHANG W., ZHONG W.: Doing topology optimization explicitly and geometrically—a new moving morphable components based framework. *Journal of Applied Mechanics 81*, 8 (2014). doi:10.1115/1.4027609.

[Hab90] HABER R. B.: Visualization techniques for engineering mechanics. *Computing Systems in Engineering 1* (1990), 37–50. doi:10.1016/0956-0521(90)90046-N.

[HBK*21] HERGL C., BLECHA C., KRETZSCHMAR V., RAITH F., GÜNTHER F., STOMMEL M., JANKOWAI J., HOTZ I., NAGEL T., SCHEUERMANN G.: Visualization of tensor fields in mechanics. In *Computer Graphics Forum* (2021), Wiley Online Library. doi:10.1111/cgf.14209.

[HFH*04] HOTZ I., FENG L., HAGEN H., HAMANN B., JOY K., JEREMIC B.: Physically based methods for tensor field visualization. In *IEEE Visualization 2004* (2004), IEEE, pp. 123–130. doi:10.1109/VISUAL.2004.80.

[HFH*06] HOTZ I., FENG L., HAGEN H., HAMANN B., JOY K.: Tensor field visualization using a metric interpretation. In *Visualization and processing of tensor fields*. Springer, 2006, pp. 269–281. doi:10.1007/3-540-31272-2_16.

[HH98a] HASSANI B., HINTON E.: A review of homogenization and topology opimization ii—analytical and numerical solution of homogenization equations. *Computers & Structures 69*, 6 (1998), 719–738. URL: https://www.sciencedirect.com/science/article/pii/S0045794998001321, doi:https://doi.org/10.1016/S0045-7949(98)00132-1.

[HH98b] HASSANI B., HINTON E.: A review of homogenization and topology optimization iii—topology optimization using optimality criteria. *Computers & Structures 69*, 6 (1998), 739–756. URL: https://www.sciencedirect.com/science/article/pii/S0045794998001333, doi:https://doi.org/10.1016/S0045-7949(98)00133-3.

[HH98c] HASSANI B., HINTON E.: A review of homogenization and topology optimization i—homogenization theory for media with periodic structure. *Computers & Structures 69*, 6 (1998), 707–717. URL: https://www.sciencedirect.com/science/article/pii/S004579499800131X, doi:https://doi.org/10.1016/S0045-7949(98)00131-X.

[HLL97] HESSELINK L., LEVY Y., LAVIN Y.: The topology of symmetric, second-order 3d tensor fields. *IEEE Transactions on Visualization and Computer Graphics 3*, 1 (1997), 1–11. doi:10.1109/2945.582332.

[HSH07] HLAWITSCHKA M., SCHEUERMANN G., HAMANN B.: Interactive glyph placement for tensor fields. In *International Symposium on Visual Computing* (2007), Springer, pp. 331–340. doi:10.1007/978-3-540-76858-6_33.

[HYW03] HASHASH Y. M., YAO J. I.-C., WOTRING D. C.: Glyph and hyperstreamline representation of stress and strain tensors and material constitutive response. *International journal for numerical and analytical methods in geomechanics 27*, 7 (2003), 603–626. doi:10.1002/nag.288.

[Irg08] IRGENS F.: *Continuum mechanics*. Springer Science & Business Media, 2008.

[JL97] JOBARD B., LEFER W.: Creating evenly-spaced streamlines of arbitrary density. In *Visualization in Scientific Computing 1997*. Springer, 1997, pp. 43–55. doi:10.1007/978-3-7091-6876-9_5.

[JSF*02] JEREMIĆ B., SCHEUERMANN G., FREY J., YANG Z., HAMANN B., JOY K. I., HAGEN H.: Tensor visualizations in computational geomechanics. *International Journal for Numerical and Analytical Methods in Geomechanics 26*, 10 (2002), 925–944. doi:10.1002/nag.223.

[JSG22] JENSEN P. D. L., SIGMUND O., GROEN J. P.: De-homogenization of optimal 2d topologies for multiple loading cases. *Computer Methods in Applied Mechanics and Engineering 399* (2022), 115426. doi:10.1016/j.cma.2022.115426.

[JWH19] JANKOWAI J., WANG B., HOTZ I.: Robust extraction and simplification of 2d symmetric tensor field topology. In *Computer Graphics Forum* (2019), vol. 38, Wiley Online Library, pp. 337–349. doi:10.1111/cgf.13693.

[KAH14] KRATZ A., AUER C., HOTZ I.: Tensor invariants and glyph design. In *Visualization and Processing of Tensors and Higher Order Descriptors for Multi-Valued Data*. Springer, 2014, pp. 17–34. doi:10.1007/978-3-642-54301-2_2.

[KASH13] KRATZ A., AUER C., STOMMEL M., HOTZ I.: Visualization and analysis of second-order tensors: Moving beyond the symmetric positive-definite case. In *Computer Graphics Forum* (2013), vol. 32, Wiley Online Library, pp. 49–74. doi:10.1111/j.1467-8659.2012.03231.x.

[KFW16] KANZLER M., FERSTL F., WESTERMANN R.: Line density control in screen-space via balanced line hierarchies. *Computers & Graphics 61* (2016), 29–39. doi:10.1016/j.cag.2016.08.001.

[KGSS20] KRETZSCHMAR V., GÜNTHER F., STOMMEL M., SCHEUERMANN G.: Tensor spines-a hyperstreamlines variant suitable for indefinite symmetric second-order tensors. In *2020 IEEE Pacific Visualization Symposium (PacificVis)* (2020), IEEE, pp. 106–110. doi:10.1109/PacificVis48177.2020.1008.

[Kin04] KINDLMANN G.: Superquadric tensor glyphs. In *Proceedings of the Sixth Joint Eurographics-IEEE TCVG conference on Visualization* (2004), pp. 147–154. doi:10.5555/2384225.2384248.

[KKH11] KRATZ A., KETTLITZ N., HOTZ I.: Particle-based anisotropic sampling for two-dimensional tensor field visualization. In *VMV* (2011), pp. 145–152.

[KLC16] KWOK T.-H., LI Y., CHEN Y.: A structural topology design method based on principal stress line. *Computer-Aided Design 80* (2016), 19–31. doi:10.1016/j.cad.2016.07.005.

[KMH11] KRATZ A., MEYER B., HOTZ I.: A visual approach to analysis of stress tensor fields. In *Dagstuhl Follow-Ups* (2011), vol. 2, Schloss Dagstuhl-Leibniz-Zentrum für Informatik. doi:10.4230/DFU.Vol2.SciViz.2011.188.

[KRG*22] KRETZSCHMAR V., ROCHA A., GÜNTHER F., STOMMEL M., SCHEUERMANN G.: Stress visualization for interface optimization of a hybrid component using surface tensor spines. *IEEE Computer Graphics and Applications 42*, 2 (2022), 45–55. doi:10.1109/MCG.2022.3149875.

[KSZ*14] KRATZ A., SCHOENEICH M., ZOBEL V., BURGETH B., SCHEUERMANN G., HOTZ I., STOMMEL M.: Tensor visualization driven mechanical component design. In *2014 IEEE Pacific Visualization Symposium* (2014), IEEE, pp. 145–152. doi:10.1109/PacificVis.2014.51.

[KW06] KINDLMANN G., WESTIN C.-F.: Diffusion tensor visualization with glyph packing. *IEEE transactions on visualization and computer graphics 12*, 5 (2006), 1329–1336. doi:10.1109/TVCG.2006.134.

[KWS*08] KINDLMANN G., WHALEN S., SUAREZ R., GOLBY A., WESTIN C.: Quantification of white matter fiber orientation at tumor margins with diffusion tensor invariant gradients. In *Proc. Intl. Soc. Mag. Reson. Med* (2008), vol. 16, p. 429.

[LC18] LAMBE A. B., CZEKANSKI A.: Topology optimization using a continuous density field and adaptive mesh refinement. *International Journal for Numerical Methods in Engineering 113*, 3 (2018), 357–373. doi:10.1002/nme.5617.

[LGL*21] LI H., GAO L., LI H., LI X., TONG H.: Full-scale topology optimization for fiber-reinforced structures with continuous fiber paths. *Computer Methods in Applied Mechanics and Engineering 377* (2021), 113668. doi:10.1016/j.cma.2021.113668.

[LGLT20] LI H., GAO L., LI H., TONG H.: Spatial-varying multi-phase infill design using density-based topology optimization. *Computer Methods in Applied Mechanics and Engineering 372* (2020), 113354. doi:10.1016/j.cma.2020.113354.

[LHZ*18] LIU H., HU Y., ZHU B., MATUSIK W., SIFAKIS E.: Narrow-band topology optimization on a sparsely populated grid. *ACM Transactions on Graphics (TOG) 37*, 6 (2018), 1–14. doi:10.1145/3272127.3275012.

[LKY*21] LEE J., KWON C., YOO J., MIN S., NOMURA T., DEDE E. M.: Design of spatially-varying orthotropic infill structures using multiscale topology optimization and explicit de-homogenization. *Additive Manufacturing 40* (2021), 101920. doi:10.1016/j.addma.2021.101920.

[LS11] LAZAROV B. S., SIGMUND O.: Filters in topology optimization based on helmholtz-type differential equations. *International Journal for Numerical Methods in Engineering 86*, 6 (2011), 765–781. doi:10.1002/nme.3072.

[Mic04] MICHELL A. G. M.: Lviii. the limits of economy of material in frame-structures. *The London, Edinburgh, and Dublin Philosophical Magazine and Journal of Science 8*, 47 (1904), 589–597.

[Mle92] MLEJNEK H.: Some aspects of the genesis of structures. *Structural optimization 5*, 1-2 (1992), 64–69. doi:10.1007/BF01744697.

[MSM95] MOORE J. G., SCHORN S. A., MOORE J.: Methods of classical mechanics applied to turbulence stresses in a tip leakage vortex. In *Turbo Expo: Power for Land, Sea, and Air* (1995), vol. 78828, American Society of Mechanical Engineers, p. V005T16A006. doi:10.1115/95-GT-220.

[MTHG03] MATTAUSCH O., THEUSSL T., HAUSER H., GRÖLLER E.: Strategies for interactive exploration of 3d flow using evenly-spaced illuminated streamlines. In *Proceedings of the 19th spring conference on Computer graphics* (2003), Association for Computing Machinery, pp. 213–222. doi:10.1145/984952.984987.

[NHTB04] NORATO J., HABER R., TORTORELLI D., BENDSØE M. P.: A geometry projection method for shape optimization. *International Journal for Numerical Methods in Engineering 60*, 14 (2004), 2289–2312. doi:10.1002/nme.1044.

[NLJK21] NIE Z., LIN T., JIANG H., KARA L. B.: Topologygan: Topology optimization using generative adversarial networks based on physical fields over the initial domain. *Journal of Mechanical Design 143*, 3 (2021). doi:10.1115/1.4049533.

[ORT18] OSTER T., RÖSSL C., THEISEL H.: Core lines in 3d second-order tensor fields. *Computer Graphics Forum 37*, 3 (2018), 327–337. doi:10.1111/cgf.13423.

[Ped89] PEDERSEN P.: On optimal orientation of orthotropic materials. *Structural optimization 1*, 2 (1989), 101–106. doi:10.1007/BF01637666.

[Ped90] PEDERSEN P.: Bounds on elastic energy in solids of orthotropic materials. *Structural optimization 2*, 1 (1990), 55–63. doi:10.1007/BF01743521.

[PL20] PATEL M., LAIDLAW D. H.: Visualization of 3d stress tensor fields using superquadric glyphs on displacement streamlines. *IEEE Transactions on Visualization and Computer Graphics 27*, 7 (2020), 3264–3276. doi:10.1109/TVCG.2020.2968911.

[PP19] PLOCHER J., PANESAR A.: Review on design and structural optimisation in additive manufacturing: Towards next-generation lightweight structures. *Materials & Design 183* (2019), 108164. doi:10.1016/j.matdes.2019.108164.

[PT08] PANTZ O., TRABELSI K.: A post-treatment of the homogenization method for shape optimization. *SIAM Journal on Control and Optimization 47*, 3 (2008), 1380–1398. doi:10.1137/070688900.

[PYW*15] PALACIOS J., YEH H., WANG W., ZHANG Y., LARAMEE R. S., SHARMA R., SCHULTZ T., ZHANG E.: Feature surfaces in symmetric tensor fields based on eigenvalue manifold. *IEEE transactions on visualization and computer graphics 22*, 3 (2015), 1248–1260. doi:10.1109/TVCG.2015.2484343.

[QJJ*20] QIU W., JIN P., JIN S., WANG C., XIA L., ZHU J., SHI T.: An evolutionary design approach to shell-infill structures. *Additive Manufacturing 34* (2020), 101382. doi:10.1016/j.addma.2020.101382.

[QRZZ20] QU B., ROY L., ZHANG Y., ZHANG E.: Mode surfaces of symmetric tensor fields: Topological analysis and seamless extraction. *IEEE Transactions on Visualization and Computer Graphics 27*, 2 (2020), 583–592. doi:10.1109/TVCG.2020.3030431.

[RBN*18] RAITH F., BLECHA C., NAGEL T., PARISIO F., KOLDITZ O., GÜNTHER F., STOMMEL M., SCHEUERMANN G.: Tensor field visualization using fiber surfaces of invariant space. *IEEE transactions on visualization and computer graphics 25*, 1 (2018), 1122–1131. doi:10.1109/TVCG.2018.2864846.

[RKZZ18] ROY L., KUMAR P., ZHANG Y., ZHANG E.: Robust and fast extraction of 3d symmetric tensor field topology. *IEEE transactions on visualization and computer graphics 25*, 1 (2018), 1102–1111. doi:10.1109/TVCG.2018.2864768.

[RP12] RUMPF R. C., PAZOS J.: Synthesis of spatially variant lattices. *Optics express 20*, 14 (2012), 15263–15274. doi:10.1364/OE.20.015263.

[RPDK15] RUMPF R. C., PAZOS J. J., DIGAUM J. L., KUEBLER S. M.: Spatially variant periodic structures in electromagnetics. *Philosophical Transactions of the Royal Society A: Mathematical, Physical and Engineering Sciences 373*, 2049 (2015), 20140359. doi:10.1098/rsta.2014.0359.

[SBGC20] SANE S., BUJACK R., GARTH C., CHILDS H.: A survey of seed placement and streamline selection techniques. In *Computer Graphics Forum* (2020), vol. 39, Wiley Online Library, pp. 785–809. doi:10.1111/cgf.14036.

[SdTT18] SALAZAR DE TROYA M. A., TORTORELLI D. A.: Adaptive mesh refinement in stress-constrained topology optimization. *Structural and Multidisciplinary Optimization 58*, 6 (2018), 2369–2386. doi:10.1007/s00158-018-2084-2.

[SGSB20] STUTZ F. C., GROEN J. P., SIGMUND O., BÆRENTZEN J. A.: Singularity aware de-homogenization for high-resolution topology optimized structures. *Structural and Multidisciplinary Optimization* (aug 2020). doi:10.1007/s00158-020-02681-6.

[Sig01] SIGMUND O.: A 99 line topology optimization code written in Matlab. *Structural and multidisciplinary optimization 21*, 2 (2001), 120–127. doi:10.1007/s001580050176.

[Sig07] SIGMUND O.: Morphology-based black and white filters for topology optimization. *Structural and Multidisciplinary Optimization 33*, 4 (2007), 401–424. doi:10.1007/s00158-006-0087-x.

[SK10] SCHULTZ T., KINDLMANN G. L.: Superquadric glyphs for symmetric second-order tensors. *IEEE transactions on visualization and computer graphics 16*, 6 (2010), 1595–1604. doi:10.1109/TVCG.2010.199.

[SK16] SELTZER N., KINDLMANN G.: Glyphs for asymmetric second-order 2d tensors. *Computer Graphics Forum 35*, 3 (2016), 141–150. doi:10.1111/cgf.12890.

[SM13] SIGMUND O., MAUTE K.: Topology optimization approaches. *Struct. Multidiscip. Optim. 48*, 6 (2013), 1031–1055. doi:10.1007/s00158-013-0978-6.

[SOG*22] STUTZ F. C., OLSEN T. F., GROEN J. P., AAGE N., SIGMUND O., SOLOMON J., BÆRENTZEN J. A.: Synthesis of frame field-aligned multi-laminar structures. *ACM Transactions on Graphics* (2022). doi:https://doi.org/10.1145/3516522.

[SPG19] SCHMIDT M.-P., PEDERSEN C. B., GOUT C.: On structural topology optimization using graded porosity control. *Structural and Multidisciplinary Optimization 60*, 4 (2019), 1437–1453. doi:10.1007/s00158-019-02275-x.

[Sva87] SVANBERG K.: The method of moving asymptotes—a new method for structural optimization. *International journal for numerical methods in engineering 24*, 2 (1987), 359–373. doi:10.1002/nme.1620240207.

[TB96] TURK G., BANKS D.: Image-guided streamline placement. In *Proceedings of the 23rd annual conference on Computer graphics and interactive techniques* (1996), Association for Computing Machinery, pp. 453–460. doi:10.1145/237170.237285.

[THBG12] TRICOCHE X., HLAWITSCHKA M., BARAKAT S., GARTH C.: Beyond topology: a lagrangian metaphor to visualize the structure of 3d tensor fields. In *New Developments in the Visualization and Processing of Tensor Fields*. Springer, 2012, pp. 93–109. doi:10.1007/978-3-642-27343-8_5.

[TKW08] TRICOCHE X., KINDLMANN G., WESTIN C.-F.: Invariant crease lines for topological and structural analysis of tensor fields. *IEEE Transactions on Visualization and Computer Graphics 14*, 6 (2008), 1627–1634. doi:10.1109/TVCG.2008.148.

[TM15] TAM K.-M. M., MUELLER C. T.: Stress line generation for structurally performative architectural design. In *35th Annual Conference of the Association for Computer Aided Design in Architecture* (Cincinnati, Ohio, USA, 2015), ACADIA. doi:1721.1/125063.

[TSA21] TRÄFF E. A., SIGMUND O., AAGE N.: Topology optimization of ultra high resolution shell structures. *Thin-Walled Structures 160* (2021), 107349. doi:10.1016/j.tws.2020.107349.

[VBVP04] VILANOVA A., BERENSCHOT G., VAN PUL C.: Dti visualization with streamsurfaces and evenly-spaced volume seeding. In *Proceedings of the Sixth Joint Eurographics-IEEE TCVG conference on Visualization* (2004), pp. 173–182. doi:10.5555/2384225.2384252.

[War02] WARD M. O.: A taxonomy of glyph placement strategies for multidimensional data visualization. *Information Visualization 1*, 3-4 (2002), 194–210. doi:10.1057/PALGRAVE.IVS.9500025.

[WAWS18] WU J., AAGE N., WESTERMANN R., SIGMUND O.: Infill optimization for additive manufacturing – approaching bone-like porous structures. *IEEE Transactions on Visualization and Computer Graphics 24*, 2 (2018), 1127–1140. doi:10.1109/TVCG.2017.2655523.

[WB05] WILSON A., BRANNON R.: Exploring 2d tensor fields using stress nets. In *VIS 05. IEEE Visualization, 2005.* (2005), IEEE, pp. 11–18. doi:10.1109/VISUAL.2005.1532771.

[WBWD12] WU J., BÜRGER K., WESTERMANN R., DICK C.: Interactive residual stress modeling for soft tissue simulation. *VCBM 12* (2012), 81–89.

[WCS17] WU J., CLAUSEN A., SIGMUND O.: Minimum compliance topology optimization of shell–infill composites for additive manufacturing. *Computer Methods in Applied Mechanics and Engineering 326* (2017), 358–375. doi:10.1016/j.cma.2017.08.018.

[WDW15] WU J., DICK C., WESTERMANN R.: A system for high-resolution topology optimization. *IEEE transactions on visualization and computer graphics 22*, 3 (2015), 1195–1208. doi:10.1109/TVCG.2015.2502588.

[WLS11] WANG F., LAZAROV B. S., SIGMUND O.: On projection methods, convergence and robust formulations in topology optimization. *Structural and Multidisciplinary Optimization 43*, 6 (2011), 767–784. doi:10.1007/s00158-010-0602-y.

[WNW*22] WANG J., NEUHAUSER C., WU J., GAO X., WESTERMANN R.: 3d-tsv: The 3d trajectory-based stress visualizer. *Advances in Engineering Software 170* (2022), 103144. doi:10.1016/j.advengsoft.2022.103144.

[WSG21] WU J., SIGMUND O., GROEN J. P.: Topology optimization of multi-scale structures: a review. *Structural and Multidisciplinary Optimization* (2021), 1–26. doi:10.1007/s00158-021-02881-8.

[WTTL20] WANG C., TAN X., TOR S., LIM C.: Machine learning in additive manufacturing: State-of-the-art and perspectives. *Additive Manufacturing 36* (2020), 101538. doi:10.1016/j.addma.2020.101538.

[WWG03] WANG M. Y., WANG X., GUO D.: A level set method for structural topology optimization. *Computer Methods in Applied Mechanics and Engineering 192*, 1 (2003), 227–246. doi:10.1016/S0045-7825(02)00559-5.

[WWG21] WU J., WANG W., GAO X.: Design and optimization of conforming lattice structures. *IEEE Transactions on Visualization and Computer Graphics 27*, 1 (2021), 43–56. doi:10.1109/TVCG.2019.2938946.

[WWW20] WANG J., WU J., WESTERMANN R.: A globally conforming lattice structure for 2d stress tensor visualization. *Computer Graphics Forum 39*, 3 (2020), 417–427. doi:10.1111/cgf.13991.

[WWW22a] WANG J., WU J., WESTERMANN R.: Streamline guided de-homogenization for high-resolution structural design. *arXiv preprint* (2022). doi:10.48550/arXiv.2207.09172.

[WWW22b] WANG J., WU J., WESTERMANN R.: Stress topology analysis for porous infill optimization. *Structural and Multidisciplinary Optimization 65*, 3 (2022), 1–13. doi:10.1007/s00158-022-03186-0.

[WWW22c] WANG J., WU J., WESTERMANN R.: Stress trajectory guided structural design and topology optimization. In *International Design Engineering Technical Conferences and Computers and Information in Engineering Conference* (2022), vol. 1, American Society of Mechanical Engineers, p. 1.

[XCC10] XU S., CAI Y., CHENG G.: Volume preserving nonlinear density filter based on heaviside functions. *Structural and Multidisciplinary Optimization 41*, 4 (2010), 495–505. doi:10.1007/s00158-009-0452-7.

[XS93] XIE Y., STEVEN G.: A simple evolutionary procedure for structural optimization. *Computers & Structures 49*, 5 (1993), 885 – 896. doi:10.1016/0045-7949(93)90035-C.

[YKP05] YE X., KAO D., PANG A.: Strategy for seeding 3d streamlines. In *VIS 05. IEEE Visualization, 2005.* (2005), IEEE, pp. 471–478. doi:10.1109/VISUAL.2005.1532831.

[YWSC11] YU H., WANG C., SHENE C.-K., CHEN J. H.: Hierarchical streamline bundles. *IEEE Transactions on Visualization and Computer Graphics 18*, 8 (2011), 1353–1367. doi:10.1109/TVCG.2011.155.

[ZGZ17] ZHANG Y., GAO X., ZHANG E.: Applying 2d tensor field topology to solid mechanics simulations. In *Modeling, Analysis, and Visualization of Anisotropy*. Springer, 2017, pp. 29–41. doi:10.1007/978-3-319-61358-1_2.

[ZLD*19] ZHU Y., LI S., DU Z., LIU C., GUO X., ZHANG W.: A novel asymptotic-analysis-based homogenisation approach towards fast design of infill graded microstructures. *Journal of the Mechanics and Physics of Solids 124* (2019), 612 – 633. doi:10.1016/j.jmps.2018.11.008.

[ZP03] ZHENG X., PANG A.: Hyperlic. In *IEEE Visualization, 2003. VIS 2003.* (2003), IEEE, pp. 249–256. doi:10.1109/VISUAL.2003.1250379.

[ZP04] ZHENG X., PANG A.: Topological lines in 3d tensor fields. In *IEEE Visualization 2004* (2004), IEEE, pp. 313–320. doi:10.1109/VISUAL.2004.105.

[ZPP05a] ZHENG X., PARLETT B., PANG A.: Topological structures of 3d tensor fields. In *VIS 05. IEEE Visualization, 2005.* (2005), IEEE, pp. 551–558. doi:10.1109/VISUAL.2005.1532841.

[ZPP05b] ZHENG X., PARLETT B. N., PANG A.: Topological lines in 3d tensor fields and discriminant hessian factorization. *IEEE Transactions on Visualization and Computer Graphics 11*, 4 (2005), 395–407. doi:10.1109/TVCG.2005.67.

[ZR91] ZHOU M., ROZVANY G.: The COC algorithm, part ii: Topological, geometrical and generalized shape optimization. *Computer Methods in Applied Mechanics and Engineering 89*, 1 (1991), 309–336. doi:10.1016/0045-7825(91)90046-9.

[ZRSZ17] ZHANG Y., ROY L., SHARMA R., ZHANG E.: Maximum number of transition points in 3d linear symmetric tensor fields. In *Topological Methods in Data Analysis and Visualization* (2017), Springer, pp. 237–250. doi:10.1007/978-3-030-43036-8_15.

[ZS18] ZOBEL V., SCHEUERMANN G.: Extremal curves and surfaces in symmetric tensor fields. *The Visual Computer 34*, 10 (2018), 1427–1442. doi:10.1007/s00371-017-1450-1.

[ZSS15] ZOBEL V., STOMMEL M., SCHEUERMANN G.: Feature-based tensor field visualization for fiber reinforced polymers. In *2015 IEEE Scientific Visualization Conference (SciVis)* (2015), IEEE, pp. 49–56. doi:10.1109/SciVis.2015.7429491.

[ZSS17] ZOBEL V., STOMMEL M., SCHEUERMANN G.: Visualizing gradients of stress tensor fields. In *Modeling, Analysis, and Visualization of Anisotropy*. Springer, 2017, pp. 65–81. doi:10.1007/978-3-319-61358-1_4.

[ZTZ15] ZHANG Y., TZENG Y.-J., ZHANG E.: Maximum number of degenerate curves in 3d linear tensor fields. In *Topological Methods in Data Analysis and Visualization* (2015), Springer, pp. 221–234. doi:10.1007/978-3-319-44684-4_13.

[ZZ15] ZHANG E., ZHANG Y.: 3d symmetric tensor fields: What we know and where to go next. In *Topological and Statistical Methods for Complex Data*. Springer, 2015, pp. 111–124. doi:10.1007/978-3-662-44900-4_7.

[ZZ21] ZHAO Z., ZHANG X. S.: Design of graded porous bone-like structures via a multi-material topology optimization approach. *Structural and Multidisciplinary Optimization 64*, 8 (2021), 677—698. doi:10.1007/s00158-021-02870-x.

[ZZX16] ZHU J.-H., ZHANG W.-H., XIA L.: Topology optimization in aircraft and aerospace structures design. *Archives of Computational Methods in Engineering 23*, 4 (2016), 595–622. doi:10.1007/s11831-015-9151-2.

[ZZZ*20] ZHOU Y., ZHAN H., ZHANG W., ZHU J., BAI J., WANG Q., GU Y.: A new data-driven topology optimization framework for structural optimization. *Computers & Structures 239* (2020), 106310. doi:10.1016/j.compstruc.2020.106310.

Eurographics Conference on Visualization (EuroVis) 2020
M. Gleicher, T. Landesberger von Antburg, and I. Viola
(Guest Editors)

Volume 39 (2020), Number 3

A Globally Conforming Lattice Structure for 2D Stress Tensor Visualization

Junpeng Wang[1], Jun Wu[2] & Rüdiger Westermann[1]

[1] Chair for Computer Graphics and Visualization, Technical University of Munich, Germany
[2] Department of Design Engineering, Delft University of Technology, The Netherlands

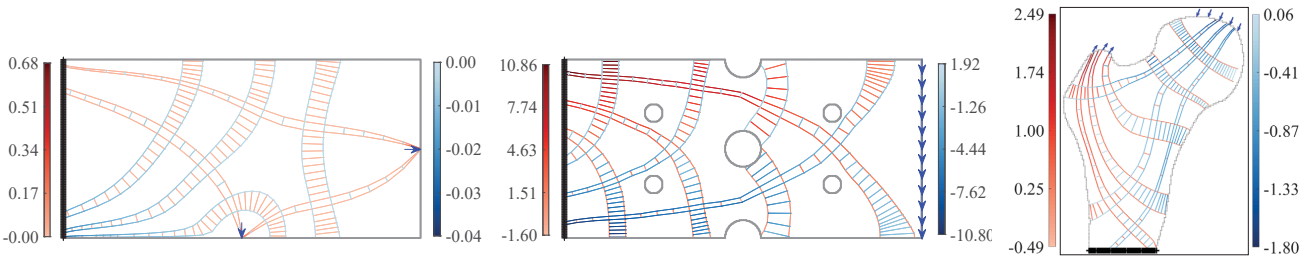

Figure 1: *Visualization of stress tensor fields in 2D solid objects under load using the conforming lattice. From left to right: Plate, perforated plate, slice through a femur. Arrows indicate the applied loads and bold black lines the fixation regions. Stress direction, convergence and divergence is shown by principal stress lines along the major (red) and minor (blue) principal directions. Stress ratio is shown by the elements' shape. Tension and compression is encoded into shades of red and blue.*

Abstract

We present a visualization technique for 2D stress tensor fields based on the construction of a globally conforming lattice. Conformity ensures that the lattice edges follow the principal stress directions and the aspect ratio of lattice elements represents the stress anisotropy. Since such a lattice structure cannot be space-filling in general, it is constructed from multiple intersecting lattice beams. Conformity at beam intersections is ensured via a constrained optimization problem, by computing the aspect ratio of elements at intersections so that their edges meet when continued along the principal stress lines. In combination with a coloring scheme that encodes relative stress magnitudes, a global visualization is achieved. By introducing additional constraints on the positional variation of the beam intersections, coherent visualizations are achieved when external loads or material parameters are changed. In a number of experiments using non-trivial scenarios, we demonstrate the capability of the proposed visualization technique to show the global and local structure of a given stress field.

1. Introduction

Techniques for visualizing the stress distribution in solid objects under load are important in a number of applications ranging from lightweight structure design over implant planning to the design of support structures. Such visualizations improve our understanding of the material response to external load conditions, and give rise to improved object designs regarding their mechanical properties.

At each point in a stress field, the state of stress is fully described by the stress vectors for three mutually orthogonal orientations of a differential area element at that point. From these orientations, the so-called principal stresses can be computed, i.e., the normal stresses into the directions where the shear stress components vanish. These normal stresses, which include the maximum and minimum normal stress components acting at a point, are fundamental to the visualization of stress tensor fields. Their visualization, however, is challenging due to several reasons:

- It requires to find visual abstractions of the stress tensor, to convey the principal stress directions and magnitudes in a meaningful way. This includes distinguishing between the different types of normal stresses, i.e., tension and compression, as well as the ratio of the principal stresses. This information should be visualized simultaneously, to reveal the mutual variations of the principal stresses across the solid body.
- The visualization should provide a global view of the stress field,

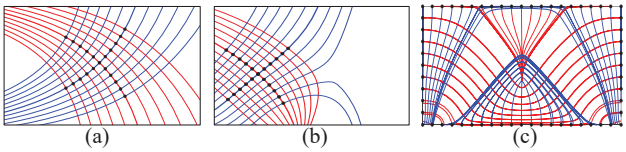

Figure 2: *(a, b) Minor Principal Stress Lines (PSLs) (blue) are seeded at equally spaced seed points (•) along the initial PSL (bold orange). Additional major PSLs (orange) are then seeded along one of the minor PSLs (bold blue). (a) The resulting grid cells do not represent the local stress ratio. (b) The domain is incompletely covered. (c) PSLs concentrate despite uniform seeding density along the domain boundaries.*

to convey a general impression of the major mechanical properties of the body under load, as well as their spatial dependencies under varying load conditions and when shape or topology variations are applied.

- It is desired to show continuous stress trajectories, i.e., the principal stress lines (PSLs), that reveal along which paths external loads are transmitted. This supports finding paths along which loads are predominantly transmitted from one boundary to another, to analyse how load transmission is affected by variations in the structure of the simulated material and external load conditions, and to indicate where the reduction of distances between the PSLs come along with a simultaneous increase of stresses.

In engineering, the most common visualization of 2D tensor fields is by means of so-called trajectory images, which show selected PSLs in the domain [Tim83, Fro48]. Such visualizations are generated by selecting an initial seed point to start the PSLs and placing new seed points automatically along the initial trajectory, or by seeding uniformly along the object's boundary. Even though this kind of visualization can provide a global view on the stress distribution, it has weaknesses if PSLs are not selected carefully. As shown in Fig. 2, the resulting grid structure usually does not convey the local stress state, since the size and aspect ratio of the generated grid cells is dictated by the initial seeding strategy. Furthermore, such visualizations can result in strongly varying trajectory density, which can mislead the interpretation of stress concentration.

1.1. Contribution

We propose a visualization technique for 2D stress fields using PSLs, which considers the aforementioned requirements and overcomes some of the limitations of classical trajectory images. We introduce the *globally conforming lattice*, a grid structure that aligns with the principal stress directions. Yet it is not domain-filling but comprised of quadrilateral (2D) elements aligned along the principal stress directions, so called beams. Beams are selected interactively, and the geometry of the beam elements is constructed so that they convey the anisotropy of the principal stresses. In 2D, where beams intersect and share an element at the intersection, this element has to conform the geometry of both beams. By ensuring conformity at all beam intersections, a globally conforming structure is generated. Our method builds upon the following specific contributions:

- We introduce the use of beams instead of single lines to create a stress-following grid structure in multiple dimensions, and to encode the ratio of principal stresses into the geometry of the beam elements. Thus, only line segments coinciding with stress lines are shown, along all principal directions.
- Conformity of beams at intersections is achieved via the solution of a constrained optimization problem. The optimization computes for all intersection points the size and aspect ratio of corresponding beam elements, so that the ratio of principal stresses is maintained and the edges of connected elements meet when continued along the respective PSL.
- We provide different color mappings for points along the trajectories to distinguish between tension and compression or the relative stress magnitudes along the principal stress directions.

For different solids and load conditions, we demonstrate the capability of our method to provide a globally conforming visualization of a 2D stress distribution. We further demonstrate the use of this method for visualizing 3D tensor fields. In 3D, PSLs do not intersect, in general, so that forming a beam structure with cycles as in 2D becomes unfeasible. Thus, we let the user interactively select seed positions and progressively grow new beams composed of hexahedral elements along the PSLs. The growth process considers the design decisions underlying the construction of a conforming lattice in 2D, and, thus, adheres to the identified requirements.

2. Related work

Besides the use of trajectory images, 2D stress tensor fields can be visualized in a number of different ways, each coming with its own strength and weakness. Let us refer here to the work by Kratz et al. [KASH13], which provides a thorough discussion of the properties of many different stress visualization techniques.

For an overview of the stress state in a solid object, one often resorts to the visualization of scalar stress measures like the von Mises stress [DGBW09, KMH11] or the material's index of refraction when loaded [BES15]. Such measures are derived from the components of the stress tensor, and they can be visualized using standard techniques like direct volume rendering or iso-contouring. Yet since these techniques simplify the complex stress state to a single scalar number, they cannot accurately convey the shape of load transmission pathways. In particular, the mutual dependencies between major and minor stresses—which are important for a structural stress analysis of a solid under load—are lost.

Another alternative to visualize stress tensor fields is by means of tensor glyphs, i.e., geometric primitives encoding tensor invariants by visual attributes like shape and color. Tensor glyphs originate from early work on glyph-based diffusion tensor visualization [Kin04], and a number of variants have been designed for the visualization of positive definite tensors [KWS*08], general symmetric tensors [SK10], as well as non-symmetric tensors [ZP05, SK16, GRT17]. Placement strategies for dense glyph visualizations help to reduce visual clutter [KW06, HSH07], and special glyph designs have been proposed to support the comparative visualization of diffusion tensors [ZYLL08].

While tensor glyphs can effectively convey the local stress state, due to their discrete nature they make it difficult to accurately infer

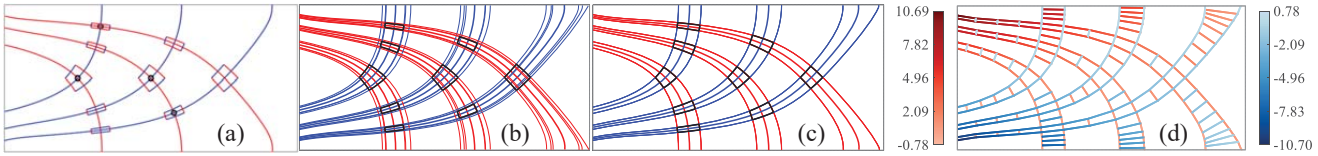

Figure 3: *Method overview: (a) Selected nodes (black circles) and computed intersections, skeleton trajectories, seed elements oriented along PSLs. (b) Edges of connected nodes do not lay on the same PSL, (c) but do so due to anisotropic scaling during optimization. (d) Conforming lattice, where beams of elements connect the seed elements. Coloring indicates stress magnitude, tension and compression.*

the global shape and the divergent or convergent behavior of load transmission pathways. In contrast, the technique we propose aims at encoding the local stress state by the cells of a conforming grid, and achieving a continuous impression—also revealing the global relationships between induced loads and material response—by growing these cells along PSLs.

To generate the conforming grid, we build upon the computation of continuous stress trajectories by using Lagrangian particle tracing in the principal stress direction fields. In the work by Delmarcelle and Hesselink [DH93], stress trajectories are used to generate so-called hyperstreamlines. A hyperstreamline shows a cylinder-like geometric structure, which is formed by extruding ellipses along a selected major PSL. The major- and minor-axis of the ellipses correspond to the direction and length of the eigenvectors and -values of the medium and minor stresses. Even though hyperstreamlines were introduced for the visualization of 3D stress fields, they can be adapted straightforwardly to 2D scenarios.

Silhouettes and ridges of a hyperstreamline, however, do not coincide with stress lines, possibly misleading the user in the interpretation of the underlying stress field. The spatial extent of hyperstreamlines prohibits placing them close to each other, making it difficult to reveal contracting behaviour of the PSLs. In 3D, it is also difficult to extract the orientation of a hyperstreamline when the medium and minor stresses have similar magnitude. By using a grid structure that is solely composed of (segments) of PSLs, we overcome these limitations.

Visualizations building solely upon PSLs have also been proposed in previous works. Stress-nets [WB05] are obtained by rendering together major and minor PSLs, at the same time trying to place them evenly to reduce clustering. Dick et al. [DGBW09] select random seed points in the 3D domain and trace PSLs along all principal directions, simultaneously encoding tension and compression by color. Both approaches, due to the random selection of PSLs, face the same problems as classical trajectory images and cannot adhere to our specified requirements in general. For surface remeshing, Alliez et al. [ACSD*03] build an initial control mesh that follows the principal curvature directions, derived from the curvature tensor. When applied to stress tensor fields, this approach produces visualizations similar to trajectory images, and cannot effectively control the shape and local density of elements. Hotz et al. [HFH*06] smear out dye along along the PSLs using line integral convolution, to generate a density field that resembles a grid-like structure, This approach provides a global overview of the stress distribution, yet it cannot accurately reveal the local stress state and does not produce continuous load transmission pathways.

Besides visualizing the directional information in a stress field, a number of works have studied the topology of symmetric 2D and 3D tensor fields [DH94, HLL97]. They characterize the topology of a tensor field by degenerate structures where two or more eigenvalues are equal. The robust extraction of the topological skeleton using numerical schemes has been addressed by Zheng and Pang [ZP04] and Roy et al. [RKZZ18]. Topological approaches are different to our approach, since they focus on the extraction of specific points or surfaces where the eigenvector fields behave in a specific way. Let us refer to the works by Zobel and Scheuermann [ZS18] and Raith et al. [RBN*19] for thorough overviews of this field.

3. Mechanical foundations and method overview

In the following, we first describe the mechanical foundations underlying the computation of stress trajectories, and then briefly summarize how our proposed technique makes use of these trajectories. Since the fundamental relationships required for the computation of stress trajectories in 2D solids can be derived as special cases of the 3D case, we focus on the latter case in the following.

3.1. Trajectories in mechanics

In a material under load, the point-wise stress vector σ is defined as $\sigma = dF/dA$, where dF is the force which the material on one side of an infinitely small area element dA exerts on the material on the other side. At each point, the state of stress is fully described by the stress vectors for three mutually orthogonal orientations of the area element. In particular, the second-order stress tensor S, represented by a 3×3 matrix, contains the stress vectors for the three orientations corresponding to the axes of a Cartesian coordinate system:

$$S = \begin{bmatrix} \sigma_x & \tau_{yx} & \tau_{zx} \\ \tau_{yx} & \sigma_y & \tau_{zy} \\ \tau_{zx} & \tau_{zy} & \sigma_z \end{bmatrix} \quad (1)$$

Here, the mixed index components correspond to the shear stresses, and they are equal on mutually orthogonal planes.

For an arbitrary orientation of the area element specified by its normal vector n, the stress vector is determined by Sn. This vector can be decomposed into a normal stress and a shear stress component, acting orthogonally and tangentially on the area element, respectively. For each stress tensor, there are three mutually orthogonal orientations of the area element where the shear stress components vanish. For these orientations, the normal stresses are called the principal stresses of the stress tensor.

The solution of the eigenvalue problem for S results in the three eigenvalues, which represent—sorted in descending order—the principal stresses σ_1, σ_2, and σ_3. If the eigenvalues are different, the corresponding eigenvectors are linearly independent and even mutually orthogonal due to the symmetry of S. The eigenvectors have unique direction, yet their orientation cannot be decided in general.

For an arbitrary start point, the PSLs are computed by a numerical integration scheme over the selected eigenvector field. We use a Runge-Kutta RK2(3) scheme with fixed integration step size δ. Since there is no consistent orientation of the eigenvectors, rather than interpolating eigenvectors, we interpolate the stress state in 2D in the form σ_x, σ_y and τ_{xy}. From the interpolated quantities, the principal stress components are derived.

3.2. Method overview

Our method starts with a discrete grid structure on which stress tensors are given. It needs to be equipped with an interpolation scheme, so that continuous stress trajectories can be computed. In addition, we provide the user information about the location of degenerate points where multiple eigenvalues are equal and the PSLs can cross. This guides the user towards regions where the generated grid structure has high deformation.

Selection: The user interactively picks points in the domain. If a selected location is close to an existing trajectory, the point is snapped to that trajectory. For each point, the PSL passing through that point (if not available from a previous selection) and the intersection points between the new and existing trajectories are computed instantly (Fig. 3a). We subsequently call the computed trajectories the *skeleton trajectories*, and the intersection points the *nodes*.

Lattice initialization: For each new set of PSLs and nodes along them, the globally conforming lattice is computed in turn. Firstly, each node is used as center point for a quadrilateral element, the so-called *lattice seed element*. The ratio of the edge lengths of seed elements is according to the ratio of the principal stresses (Fig. 3a), its edges are along PSLs. A global scale factor controls the size of elements. The elements' edges, per construction, lay on stress trajectories, and we consider them in the upcoming stages to construct a conforming lattice.

Constrained optimization: Given the lattice seed elements, with their nodes being connected via the skeleton trajectories, we aim at connecting the edges of connected elements via stress trajectories. Edges along the major or minor stress direction, respectively, should be connected via a major or minor stress trajectory. However, the edges of connected elements lay on different stress trajectories in general (as shown in Fig. 3b). Thus, we pose an optimization problem with the objective to scale the seed elements individually so that corresponding edges of connected elements lay (approximately) on the same PSL (Fig. 3c). We call the scaled seed elements conforming.

Beam construction: From the conforming seed elements we construct so-called *beams*, which connect the elements along the skeleton trajectories. Beams are sequences of lattice elements, starting and ending in a seed element, and having center points on the connecting skeleton trajectory. The beam elements vary linearly in size and edge ratio along the connecting trajectories (Fig. 3d). The lengths of the beam elements along this trajectory are relaxed to obtain a smooth transition between the seed elements. Notably, due to this construction the shapes of the beam elements cannot indicate any non-linear behavior of the stress ratio along a beam.

In the conforming lattice, the beams follow the principal stress directions only approximately. In extreme cases, the optimization might even suggest element shapes that do not accurately represent the local stress state. By an additional coloring, such cases can be emphasized, hinting towards regions where the lattice needs to be refined. In the following, we describe the major components of the construction process for generating a conforming lattice. We focus on generating such a lattice for a given 2D stress field, and provide details for the handling of 3D stress fields later on.

4. Element construction

Our approach aims at encoding the stress anisotropy into the shape of lattice elements, i.e., the ratio of the edge lengths along the major (l_1) and minor (l_2) principal directions should be equal to σ_1/σ_2. Because of the intrinsic divergence/convergence of PSLs, however, it's not feasible, in general, to strictly ensure this ratio for all lattice elements. Thus, we explicitly enforce this constraint only at the lattice seed elements.

4.1. Lattice seed elements

The lengths of the edges of seed elements are determined as

$$\begin{aligned} l_1 &= l_{max} \cdot \sqrt[p]{|\sigma_1| / \max(|\sigma_1|, |\sigma_2|)} \\ l_2 &= l_{max} \cdot \sqrt[p]{|\sigma_2| / \max(|\sigma_1|, |\sigma_2|)}, \end{aligned} \tag{2}$$

where we prescribe the permitted maximum length l_{max}, as well as a penalty term p that reduces the effect of local extreme values on the construction process. We set $p = 2$ in our examples. Lengths below a prescribed length l_{min} are clamped to this value.

To create the lattice seed element with the computed edge lengths for a given node, we create two points on each the major and the minor PSL going through that node (Fig. 4a). From the intersection of the minor and major PSL, respectively, going through these points, the element corners are determined.

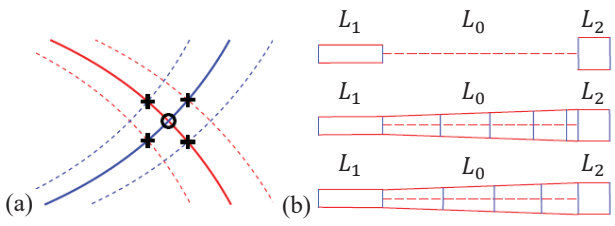

Figure 4: *(a) Lattice seed element construction. (b) From top to bottom, the two seed elements, the non-fitting beam elements, and the fitting elements improved by Eqn. 3.*

4.2. Beam elements

Beams connecting the seed elements along the trajectory skeleton are created by inserting new lattice elements along the skeleton via a relaxation process. Therefore, let us assume that the seed elements have been scaled properly (via the optimization described in Sec. 5, so that the edges of connected elements lay on the same PSL. The construction process considers the length of the PSL from one node to the other one, as well as the lengths of the edges of the lattice seed elements corresponding to these nodes (Fig. 4b).

According to Fig. 4b, let us assume that L_1 and L_2, respectively, refer to the length of the longer and shorter element, and the construction proceeds from L_1 to L_2. L_0 is the distance between the two nodes along the skeleton trajectory. Then, the number of new elements is the number of times an element with average length $l = 0.5 \cdot (L_1 + L_2)$ can be placed between the two nodes, i.e., $N_l = round(l_0/l)$. If $N_l - 1 > 0$, the size l_i of the $i-th$, $i = 1 : N_l$ element is given by

$$l_i = \beta_1 + \beta_2 \cdot (N_l - i), \tag{3}$$

where $\beta_1 = (L_0 - (L_1 - L_2))/N_l$ and $\beta_2 = (L_1 - L_2)/\sum_{k=1}^{N_l-1} k$.

Since it is not always possible to fill exactly the distance between two nodes with new elements, the remaining portion is distributed equally to all elements along the connection. The length of the element edges along the respective other principal stress direction is linearly interpolated between the corresponding values at the nodes.

5. The conforming lattice structure

The seed elements have to be scaled properly so that the edges of connected elements lay on the same PSL. We propose a constrained optimization process and compute the optimized seed elements via a gradient-based optimizer, so that the matching is achieved as good as possible.

5.1. The constrained optimization problem

The optimization problem can be described as

$$\begin{aligned} &\min_x \quad f(x), \\ &\text{s.t.} \quad g(x) \leqslant 0, \quad \textit{and} \quad l_{\min} < x < \lambda l_{\max} \end{aligned} \tag{4}$$

Here, x is the design variable, $f(x)$ is the objective function that measures the un-matching situation, and $g(x)$ is the constraint function that keeps the changes of seed elements within a permitted range. λ is a magnification factor to expand the design domain of the design variables. It is set to 1.5 in our experiments.

Design variables As mentioned in Sec. 4.1, the seed elements are constructed by placing 4 new points around each node, and using the major and minor PSLs through these points to determine the element corners. We take the distances of the new points to the node as the design variables (Fig. 5).

The 4 design variables at each node are the local design variables, and the 4 PSLs traced from each of these nodes are the local

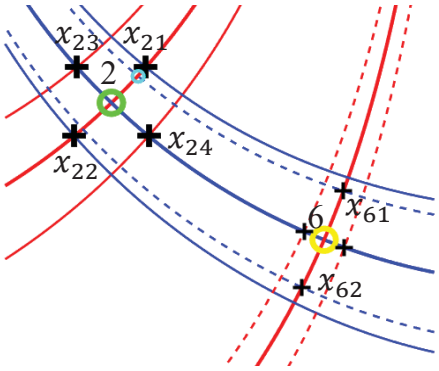

Figure 5: *Schematic illustrating of the optimization process for nodes 2 (green) and 6 (yellow). Thin solid and dashed lines are the support trajectories, crosses refer to the design variables. The first concomitant design variable of x_{21} is x_{61}.*

support trajectories. Let us also introduce the concomitant design variables and support trajectories. By this, we mean the local design variables and PSLs from the nodes that are connected to the current node (Fig. 5).

Constraints The optimization constraints are used to ensure that the seed elements still encode the stress ratio in their shape. According to Fig. 5, the ratio of the i-th seed element is given by

$$r_i = \frac{x_{i1} + x_{i2}}{x_{i3} + x_{i4}}, \tag{5}$$

Furthermore, Eqn. 6 is used to make the change of the seed elements not exceed a predefined range

$$(\frac{r_i - r_i^*}{r_i^*})^2 \leqslant \xi^2. \tag{6}$$

Here, r_i^* refers to the initial shape of the element, and ξ is the permitted change of the element's shape. From this, we obtain the constraint function $g_i(x)$ as

$$g_i(x) = (\frac{1}{r_i^*}\frac{x_{i1} + x_{i2}}{x_{i3} + x_{i4}} - 1)^2 - \xi^2 \leqslant 0, \quad i = 1 : m, \tag{7}$$

where m is the number of nodes. The value of ξ has a significant effect on the convergence of the optimization process and the generated results. A small ξ ensures a limited change to the shape of seed lattice elements. However, it necessitates more iterations in the optimization process and may even lead to non-convergent results.

5.2. Objective function

The objective function is designed to measure how far the current lattice structure is from conformity. To characterize the conformity, we measure the deviation between the local support trajectory and the corresponding concomitant support trajectories. Considering x_{ij}, the j-th design variable of the i-th node, and assuming it has K_{ij} concomitant support trajectories, then the conformity $f_{ij}(x)$ for x_{ij} is defined as

$$f_{ij}(x) = \sum_{k=1}^{K_{ij}} (x_{ij} - \hat{x}_{ijk})^2, \tag{8}$$

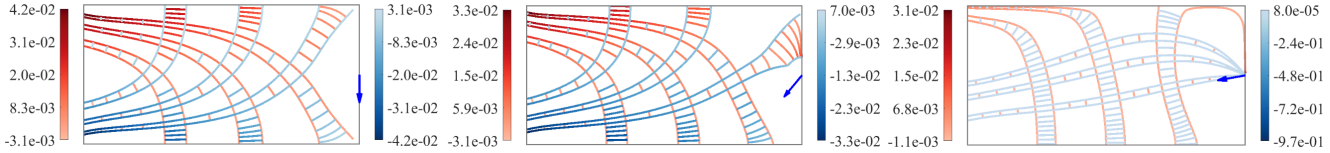

Figure 6: *Coherence of conforming lattices that are generated automatically from the leftmost lattice when different load conditions (indicated by blue arrows) are applied to the 2D cantilever (Fig. 7a).*

where $\hat{x}_{ijk}$ is the distance between the i-th node and the intersection of the k-th concomitant support trajectory with the PSL through x_{ij}. The global conformity $f(x)$, considering m nodes with all 4 design variables, is then given by

$$f(x) = \sum_{i=1}^{m} \sum_{j=1}^{4} \sum_{k=1}^{K_{ij}} (x_{ij} - \hat{x}_{ijk})^2 \tag{9}$$

By substituting Eqns. 7 and 9 into Eqn. 4, we obtain the optimization problem.

Solving the optimization problem requires to trace PSLs and compute their intersections in each iteration step. Therefore, we relax $\hat{x}_{ijk}$ to efficiently find an approximation without computing PSLs. This relaxation builds upon our observation that the design variables are mutually dependent via the concomitant design variables. Thus, the objective function becomes an explicit function with respect to the design variables, if the approximation $h_{ijk}(x)$ of $\hat{x}_{ijk}$ is explicit with respect to x.

To construct $h_{ijk}(x)$, we use polynomial interpolation of samples that are obtained by moving the concomitant design variable in a limited range and computing the induced corrections. Then, the coefficients of the polynomial are computed by solving

$$\begin{bmatrix} X_1^{N-1} & X_1^{N-2} & \cdots & X_1^0 \\ X_2^{N-1} & X_2^{N-2} & \cdots & X_2^0 \\ \vdots & \vdots & \ddots & \vdots \\ X_N^{N-1} & X_N^{N-2} & \cdots & X_N^0 \end{bmatrix} \begin{bmatrix} p_1 \\ p_2 \\ \vdots \\ p_N \end{bmatrix} = \begin{bmatrix} Y_1 \\ Y_2 \\ \vdots \\ Y_N \end{bmatrix} \tag{10}$$

Here, p_s, $s = 1:N$ are the coefficients of the polynomial, N is the number of samples, and X_i and Y_i, $i = 1:N$ are the sampled concomitant design variables and their corresponding corrections. The variables $\hat{x}_{ijk}$ can now be approximated via

$$\hat{x}_{ijk} \approx h_{ijk}(x) = \sum_{s=1}^{N} p_s \cdot x^{N-s}. \tag{11}$$

N is set to 3 in our experiments. By substituting Eqn. 11 into Eqn. 9, the explicit expression of the objective function with respect to the design variable is available, and the final optimization equation becomes

$$\begin{aligned} &\min_x \ f(x) = \sum_{i=1}^{m} \sum_{j=1}^{4} \sum_{k=1}^{K_{ij}} (x_{ij} - h_{ijk}(x))^2, \\ &\text{s.t. } g_i(x) = \left(\tfrac{1}{r_i^*} \tfrac{x_{i1}+x_{i2}}{x_{i3}+x_{i4}} - 1\right)^2 - \xi^2 \leqslant 0, \ i = 1:m, \\ &\quad l_{\min} < x < \lambda l_{\max} \end{aligned} \tag{12}$$

This function, since its derivatives can be computed analytically, gives rise to efficient gradient-based optimizers, like the method of moving asymptotes (MMA) [Sva87] that is used in our work.

5.3. Coherent visualization of stress changes

In many practical applications, domain experts are interested in analysing the variations in the internal stress state due to changes in the external load conditions or when a different material is simulated. To enable an effective comparison of different stress states, their visualizations should not change significantly when only marginal changes have occurred.

With our method this is difficult to achieve, because the user specifies only few initial seed nodes, while the other nodes are computed automatically from the intersections of the traced PSLs. When the seed nodes are fixed and used for generating the conforming lattice for a new stress state, due to changes in the PSLs the other nodes might be at vastly different locations than they occurred in the previous lattice. On the other hand, if the initial nodes were only slightly moved in the new field, the resulting lattice structure might be very similar to the initial one.

To preserve positional coherence of all nodes—and thus structural coherence of the lattice structures—for varying stress states, we introduce a globally optimal placement scheme that attempts to minimize the summed positional changes over all nodes when generating a conforming lattice for a new stress distribution. Therefore, we establish the following equation for the placement optimization:

$$\begin{aligned} &\min \longrightarrow \quad \sum_{i=1}^{m} |p_i - \hat{p}_i|^2, \\ &\text{s.t.} \quad p_j \in \Gamma_j, \ j = 1:\hat{m} \end{aligned} \tag{13}$$

Here, $\hat{p}_i$ and p_i, $i = 1:m$, respectively, are the node positions in the previous and current lattice. p_j, $j = 1:\hat{m}$ are the seed nodes, which are the design variables in the optimization. Γ_j, $j = 1:\hat{m}$ are the corresponding design domains, which restrict the movements

of the seed nodes. Thus, the locations of nodes that are created automatically are regularized by these nodes. Since it is not possible, in general, to derive a differentiable formulation of the automatically computed locations of new points with respect to the seed points, a gradient-based optimizer cannot be used. Instead, we resort to the derivative-free optimizer CMA-ES proposed in [Han16], which only requires iterative evaluations of the free node positions for varying seed positions. I.e., in every iteration the seed nodes are slightly moved so that the positional changes of all nodes are optimized.

As an example, consider the 2D cantilever in Fig. 7a, to which a concentrated force is applied at the point P_3. The initial load direction is downward, and it is then changed continually in 9 steps of 20 degrees clockwise, so that eventually the load direction turns to 180 degrees and the structure is under an upward force. We input three seed nodes p_1, p_2 and p_3, with initial positions (125,125), (250,125) and (375,125), respectively. The corresponding design domains Γ_i, $i = 1:3$ of p_i are indicated by circles around each p_i.

When comparing the lattice structures from different simulation steps in Fig. 6, it can be seen that number of nodes and skeleton trajectories do not change, the lattice slightly rotates clockwise, and the region where the structure is under compression becomes increasingly larger from left to right (see the shape change of the lattice elements). In particular, even though significant changes in the stress field occur, the conforming lattices do not change their topology and geometric changes are tried to be minimized. This gives rise to an effective comparison of all fields.

6. Results and analysis

We use the solid structures in Fig. 7 to validate our method. Stress fields are computed by finite hexahedral element analysis, with the Young's modulus and Poisson ratio of all solids set to 1 and 0.3, respectively. The second solid in Fig. 7 is obtained from the first one by inserting holes.

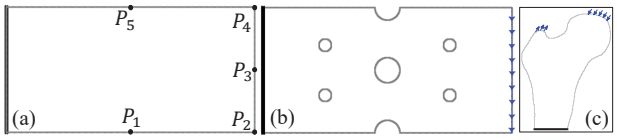

Figure 7: *The 2D solid objects used in our experiments. Blue arrows indicate the load conditions. (a) Cantilever with fixed left edge, discretized into* 250×500 *finite elements. Points* $P_1, \ldots, P_5$ *indicate the positions were different loads are applied. (b) Perforated plate, adapted from the cantilever. (c) Slice through a 3D CT-scan of a femur, fixed at the bottom and discretized into* 182×140 *finite elements.*

All experiments are carried out using the *MATLAB R2019a - academic use* release, on a workstation running Windows 10 and equipped with 8 cores (Intel Xeon W-2123, @3.60Ghz) and 64GB RAM. The processing times range from roughly 5 seconds for the 2D examples up to almost 25 seconds for the 3D examples discussed below. Since the number of constraint functions in Eqn. 12 equals the number of nodes that are used to construct the skeleton trajectories (i.e., Sec. 5), processing times strongly depend on this number. For large numbers, also the probability to get stuck in local optima increases.

To validate the capability of our method to represent complicated stress scenarios, we simulate the stress distribution in the 2D cantilever (Fig. 7a) using three different load conditions: The 1st test case is obtained by applying a rightward concentrated force and a downward force on P_3 and P_1, respectively. The 2nd case is generated by applying two rightward concentrated forces on P_3 and P_5 separately. The 3rd case is obtained by applying a downward distributed force on the edge P_2P_4. The 1st and 2nd test cases are used to demonstrate the construction of a conforming lattice when a trisector and a wedge degenerate point, respectively, exist. Via the 3rd case we shed light on a scenario where a large number of nodes is initially specified. In all test cases, we set $l_{min} = 2.5\delta$ and $l_{max} = 4l_{min}$. In Eqn. 12, $\xi = 0.3$ is used to restrict the change of the seed lattice shape during the optimization, here setting it 0.3 is a consideration from both the convergence and effectiveness after observing a series numerical examples.

For all three test cases, the support trajectories before and after optimization are shown in Fig. 8, In a pre-process, degenerate points are computed and shown together with the corresponding topological skeleton. The topological skeleton divides the domain into sub-domains where the corresponding PSLs have similar behavior [DH94]. In particular, this information is used to avoid placing seed nodes too close to critical points or topological skeletons, so that the computed beam structures overlap multiple topological regions.

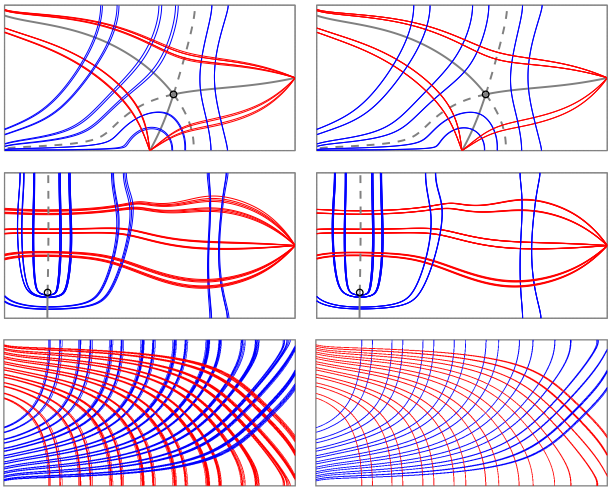

Figure 8: *Top to bottom: Support trajectories for the 2D cantilever under different loads before (left) and after (right) optimization, including degenerate points (small circles), and the topological skeleton with PSLs along the major (grey solid lines) and minor (dashed lines) principal directions.*

Notably, the optimization fails if the support trajectories fall within different topological regions (Fig. 9). In this case, either the

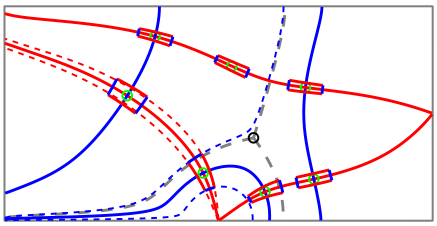

Figure 9: *Failure case. Support trajectories (blue dashed lines) enclosing a degenerate point (circle). Topological skeleton in grey.*

size of the lattice seed elements needs to be scaled down or the selected node needs to be relocated.

The conforming lattices for the three test cases are shown in Fig. 10 and Fig. 1(left). The values of σ_1 and σ_2 along the major and minor principal directions are encoded in shades of red and blue. Visualization of stress anisotropy are shown in the Appendix.

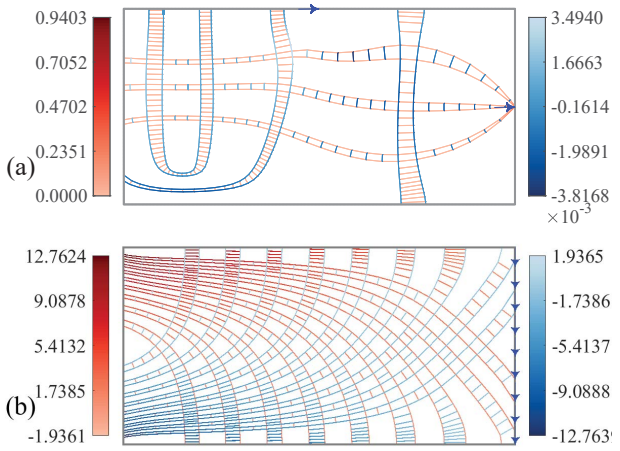

Figure 10: *Visualization of stresses in the cantilever under different loads using conforming lattices. Blue arrows indicate the loads corresponding to our 2nd (top) and 3rd (bottom) test case.*

The perforated plate (Fig. 7b) is used as an additional test case to validate our method. The stress field is simulated by applying a distributed force acting downward on the right boundary of the plate. The optimized support trajectories are shown in the top of Fig. 11, with color coding according to major and minor stress direction (left) and according to the von Mises stress (right) to show the potential stress concentration. In the bottom of Fig. 11, the same visualizations are shown for the 2D femur slice. The loads mimic compression due to body weight (downward acting loads) and tension due to muscle forces (upward acting loads). In Fig. 1(middle) and Fig. 1(right), major and minor principal stresses along the PSLs in both datasets are encoded into shades of red and blue.

Convergence A conforming lattice is constructed by a constrained optimization. The convergence behavior of both the objective function and the constraint function for all five test cases are collectively shown in Fig. 12a and b. Here, the normalized objective

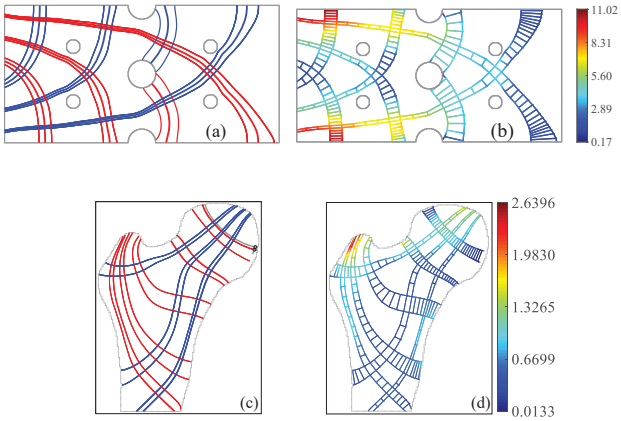

Figure 11: *Perforated plate (top) and 2D femur slice (bottom). Optimized support trajectories (left), and conforming lattice with von Mises stress encoded along principal directions (right). In the femur stress field, PSLs cannot reach the boundary in the right upper region, because of the two degenerate points (black circles).*

function $f^*(x) = f(x)/max(f(x))$ is used. The convergence plots indicate that the optimization always converges after less than 50 iterations. We further analyse the accuracy by which the edges of beam elements follow the PSLs. Therefore, we measure the average directional deviation between the element edges at the element corner points and the exact direction of the PSLs. This deviation is always below 4 degrees, yet we also observed outliers of more than 20 degrees in highly diverging situations. Fig. 12c, b shows the seed elements before and after optimization, superimposed for comparison, for the 2nd and 3rd test case, respectively. A numerical analysis verifies that all changes in aspect ratio are within the prescribed tolerance, $\xi = 0.3$, which confirms convergence of the optimization process.

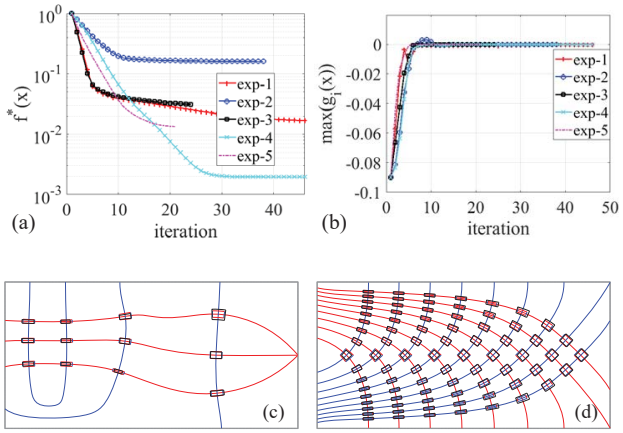

Figure 12: *Top: Convergence analysis for all 2D experiments. (a) Normalized objective function. (b) Constraint function. Bottom: Comparisons of seed elements before and after optimization, for the 2nd (c) and 3rd (d) test case. Elements with colored edges depict the initial seed elements, black edges indicate optimized elements.*

7. 3D lattice structure

In principle, the conforming lattice in a 3D stress tensor field can be computed in much the same way as in 2D. However, since the PSLs in a 3D tensor field do not intersect in general, our proposed optimization process is not applicable. Thus, in 3D we waive this process and only make use of the proposed beam construction process. Conformity is ensured by progressively growing beams along the PSLs, thereby adjusting the cells' extents to convey the local stress state.

7.1. Beam growth

The seed element in 3D is constructed so that its edges are aligned with the three principal stress directions and the edge lengths are according to the ratio of the principal stresses. Since the edges do not necessarily coincide with PSLs, we place points at the edge midpoints, compute the PSLs corresponding to the edge direction, and relax the cell corner points towards these PSLs. This process is repeated iteratively until the changes are below a given tolerance.

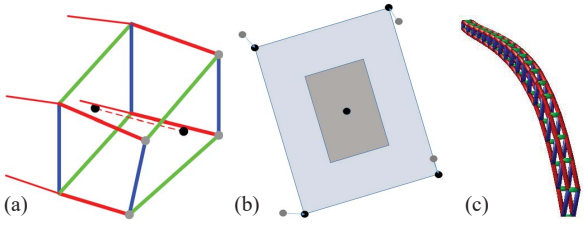

Figure 13: *Illustration of the element construction process. (a) Tracing along PSLs, (b) Fitting of element face. (c) The final beam structure in 3D.*

For every face of the seed element and starting from the face's corner points, we trace out 4 new points along the PSLs "orthogonal" to that face. The step size along the PSLs is the same as the length of the seed element along that direction (Fig. 13a). When connecting the new points (grey dots in Fig. 13b) to form a face of the new element, however, the edges of that face do not coincide with PSLs in general. Thus, we also trace out a 5th point along the skeleton trajectory of the current beam, using the same step size as before (black dot in Fig. 13a). We then center a planar quadrilateral at that point, with its edges aligned along the respective other PSLs at this point, and the edge lengths according to the stress ratio along these PSLs (dark grey quadrilateral in Fig. 13b). The newly generated points are projected onto the plane of the quadrilateral (grey dots in Fig. 13b). Since we know which corner point of the quadrilateral corresponds to which new point, we now scale the quadrilateral isotropically so that the sum of the distances between it's corner points and their corresponding new points is minimized (light grey quadrilateral in Fig. 13b). The new points are then snapped to their corresponding corner points to form the final face. Fig. 13c shows an entire beam that is generated as described.

It is clear that the edges of the beam elements do not follow the PSLs exactly, since they are aligned solely with the PSLs at the selected center point. Apart from cases where trajectories are highly diverging, however, the elements align fairly well with the PSLs in all of our experiments. In particular, the average directional deviation between the element edges at the element corner points and the exact direction of the PSLs was always below 5 degrees. An extraordinary case occurs when two trajectories have been snapped to each other. Then, the elements at the start and end points are generated along different beams, and they do not consider the stress variation along the connection. We handle this case by interpolating the beam elements linearly along the connection, in the same principal way as described for the 2D setting.

7.2. Visual mapping

To visualize the generated 3D beam structure, all element edges are rendered as tubes for improved visibility. In addition, the stress magnitudes along the major, medium, and minor PSLs are mapped to red, green, and blue, respectively, with the magnitudes from lowest to highest encoded by increasing saturation. To reduce visual clutter, beam elements are rendered as opaque cubes, and the strength of anisotropy of the stress magnitudes is encoded into greyscales of the element faces. Here, the following coloring scheme is used to compute the intensity γ_{3D}:

$$\gamma_{3D} = \ln\left(\frac{\max(|\sigma_1|,|\sigma_3|)}{\min(|\sigma_1|,|\sigma_3|)}\right) \tag{14}$$

7.3. Test cases

In our experiments we consider two solid objects (Fig. 14), a 3D cantilever and a human femur. In the first two experiments using the 3D cantilever, we apply a distributed force to face $P_1P_2P_3P_4$, which is then exchanged by a distributed force exerting on edge P_1P_2 to introduce a torque.

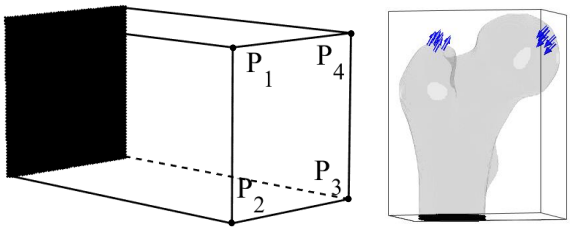

Figure 14: *The 3D solid objects used in our experiments. Blue arrows indicate the load conditions, regions where the objects are fixed are shown in black. Left: 3D cantilever with fixed left face, discretized into* $50 \times 100 \times 50$ *finite elements. Different loads are applied at points* $P_1,\ldots,P_4$*. Right: Femur fixed at the bottom, discretized into* $140 \times 92 \times 182$ *finite elements.*

In Fig. 15a, b, beam structures in the cantilever stress fields are shown when only one single beam is traced along the PSLs at the initial seed point. Most importantly, the 3D beam structures can simultaneously visualize the principal stress directions, the divergence and convergence of PSLs, as well as the anisotropy of the stress magnitudes. Notably, the torque that is introduced by the load in the second experiment is clearly conveyed by the torsion of the beams along the major and minor stress directions. Visually,

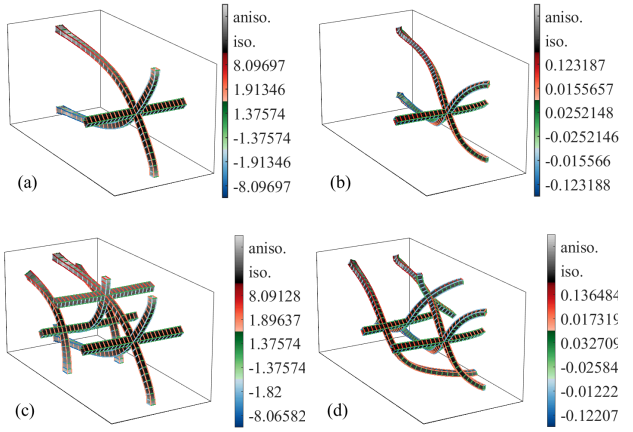

Figure 15: *Beam structures showing the stresses in the 3D cantilever under different load conditions. Shades of grey characterize the strength of anisotropy of the beam elements. Top: One single seed element is selected. Bottom: Beam structures are extended by growing beams from additional elements.*

the single beams look similar to hyperstreamlines, yet there are essential differences between them. The most important are that the beams encode (relative) local and global information concerning all three major stress directions, and can be stitched together in a conforming way to better represent the 3D stress distribution. The latter is demonstrated in Fig. 15c, d, where additional beam elements are selected and new branches are grown along them.

We perform one last experiment using the 3D femur (Fig. 14right), where multiple seeds are input sequentially in order to obtain a complete image of the stress distribution. As seen in Fig. 16, faces colored in light greyscale also appear in some middle parts of the beams, i.e., high anisotropy does not only occur in regions close to where the loads are applied, but also in the interior. Region of high compression due to body weight and high tension due to muscle forces can be conveyed effectively in the upper right and left part of the femur, respectively. In addition, the twisting of beams indicate that the stress field is under severe torsion. It is worth noting that these effects are difficult to convey via alternative techniques like hyperstreamlines or by drawing single PSLs along any of the major stress directions.

8. Conclusion and outlook

We have introduced a novel method to visualize 2D stress tensor fields via a conforming lattice that follows the PSLs, conveys their divergent/convergent behaviour, and encodes stress type and relative stress magnitude. The method is global in that it allows following the paths along which stresses are transmitted through the domain. The construction of a 2D conforming lattice is formulated as an optimization problem, which adjusts the lattice elements so that they conform to the local stress state. We have shown a modification to visualize 3D stress fields, by progressively building a beam structure comprised of hexahedral elements using a sequential growth process.

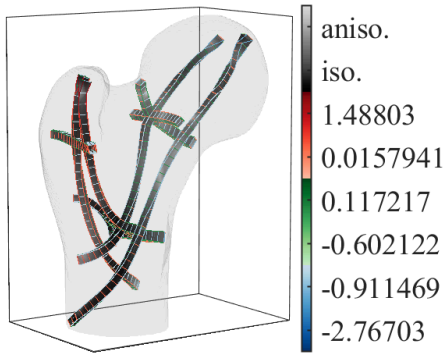

Figure 16: *Visualization of stresses in the 3D femur using beams that are grown progressively from user selected seed elements.*

In the future, we aim to extend the method to generate a space-filling stress-following grid in 2D and 3D. In 2D, we will further investigate construction processes that consider sharing of support trajectories between beams, in combination with seeding strategies that can automatically distribute beams so that they densely cover the domain. In 3D, since a globally conforming structure does not exist in general, we will investigate relaxation schemes to compute a pseudo-conforming yet dense grid structure. Therefore, it will be interesting to look into hex-meshing approaches for arbitrary geometries, and to adapt them to the specific needs. Since occlusions become paramount already in the case of rather sparse 3D spatial grid structures, we will further investigate dedicated visualization techniques for such structures, e.g., by considering focus+context techniques including feature-based element highlighting.

9. Acknowledgements

This work was partially funded by the German Research Foundation (DFG) under grant number WE 2754/10-1 "Stress Visualization via Force-Induced Material Growth".

10. Appendix

We provide additional visualizations of the anisotropy of minor and major stresses in the 2D cantilever under different loads (Fig. 10). Fig. 17 shows the anisotropy measured by $\gamma_{2D} = \ln(\frac{|\sigma_1|}{|\sigma_2|})$. By comparing the anisotropy with the aspect ratio of beam elements in Fig. 10, good agreement of the aspect ratio of elements and the anisotropy can be observed.

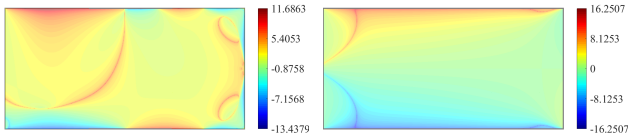

Figure 17: *Anisotropy of local stresses in the cantilever under different loads (2nd (left) and 3rd (right) test case).*

References

[ACSD*03] ALLIEZ P., COHEN-STEINER D., DEVILLERS O., LÉVY B., DESBRUN M.: Anisotropic polygonal remeshing. *ACM Trans. Graph. 22*, 3 (July 2003), 485–493. 3

[BES15] BUSSLER M., ERTL T., SADLO F.: Photoelasticity raycasting. In *Computer Graphics Forum* (2015), vol. 34, Wiley Online Library, pp. 141–150. 2

[DGBW09] DICK C., GEORGII J., BURGKART R., WESTERMANN R.: Stress tensor field visualization for implant planning in orthopedics. *IEEE Transactions on Visualization and Computer Graphics 15*, 6 (2009), 1399–1406. 2, 3

[DH93] DELMARCELLE T., HESSELINK L.: Visualizing second-order tensor fields with hyperstreamlines. *IEEE Computer Graphics and Applications 13*, 4 (1993), 25–33. 3

[DH94] DELMARCELLE T., HESSELINK L.: The topology of symmetric, second-order tensor fields. In *Proceedings of the conference on Visualization'94* (1994), IEEE Computer Society Press, pp. 140–147. 3, 7

[Fro48] FROCHT M. M.: *Photoelasticity*, vol. 2. J. Wiley, 1948. 2

[GRT17] GERRITS T., RÖSSL C., THEISEL H.: Glyphs for space-time jacobians of time-dependent vector fields. 2

[Han16] HANSEN N.: The cma evolution strategy: A tutorial. *arXiv preprint arXiv:1604.00772* (2016). 7

[HFH*06] HOTZ I., FENG L., HAGEN H., HAMANN B., JOY K.: Tensor field visualization using a metric interpretation. In *Visualization and processing of tensor fields*. Springer, 2006, pp. 269–281. 3

[HLL97] HESSELINK L., LEVY Y., LAVIN Y.: The topology of symmetric, second-order 3d tensor fields. *IEEE Transactions on Visualization and Computer Graphics 3*, 1 (1997), 1–11. 3

[HSH07] HLAWITSCHKA M., SCHEUERMANN G., HAMANN B.: Interactive glyph placement for tensor fields. In *International Symposium on Visual Computing* (2007), Springer, pp. 331–340. 2

[KASH13] KRATZ A., AUER C., STOMMEL M., HOTZ I.: Visualization and analysis of second-order tensors: Moving beyond the symmetric positive-definite case. In *Computer Graphics Forum* (2013), vol. 32, Wiley Online Library, pp. 49–74. 2

[Kin04] KINDLMANN G.: Superquadric tensor glyphs. In *Proceedings of the Sixth Joint Eurographics-IEEE TCVG conference on Visualization* (2004), Eurographics Association, pp. 147–154. 2

[KMH11] KRATZ A., MEYER B., HOTZ I.: A visual approach to analysis of stress tensor fields. In *Dagstuhl Follow-Ups* (2011), vol. 2, Schloss Dagstuhl-Leibniz-Zentrum für Informatik. 2

[KW06] KINDLMANN G., WESTIN C.-F.: Diffusion tensor visualization with glyph packing. *IEEE Transactions on Visualization and Computer Graphics 12*, 5 (2006), 1329–1336. 2

[KWS*08] KINDLMANN G., WHALEN S., SUAREZ R., GOLBY A., WESTIN C.: Quantification of white matter fiber orientation at tumor margins with diffusion tensor invariant gradients. In *Proc. Intl. Soc. Mag. Reson. Med* (2008), vol. 16, p. 429. 2

[RBN*19] RAITH F., BLECHA C., NAGEL T., PARISIO F., KOLDITZ O., GÜNTHER F., STOMMEL M., SCHEUERMANN G.: Tensor field visualization using fiber surfaces of invariant space. *IEEE Transactions on Visualization and Computer Graphics 25*, 1 (Jan 2019), 1122–1131. 3

[RKZZ18] ROY L., KUMAR P., ZHANG Y., ZHANG E.: Robust and fast extraction of 3d symmetric tensor field topology. *IEEE transactions on visualization and computer graphics 25*, 1 (2018), 1102–1111. 3

[SK10] SCHULTZ T., KINDLMANN G. L.: Superquadric glyphs for symmetric second-order tensors. *IEEE transactions on visualization and computer graphics 16*, 6 (2010), 1595–1604. 2

[SK16] SELTZER N., KINDLMANN G.: Glyphs for asymmetric second-order 2d tensors. In *Computer Graphics Forum* (2016), vol. 35, Wiley Online Library, pp. 141–150. 2

[Sva87] SVANBERG K.: The method of moving asymptotes—a new method for structural optimization. *International journal for numerical methods in engineering 24*, 2 (1987), 359–373. 6

[Tim83] TIMOSHENKO S. S.: *History of Strength of Materials*. Dover, 1983. 2

[WB05] WILSON A., BRANNON R.: Exploring 2d tensor fields using stress nets. In *VIS 05. IEEE Visualization, 2005.* (Oct 2005), pp. 11–18. 3

[ZP04] ZHENG X., PANG A.: Topological lines in 3d tensor fields. In *Proceedings of the conference on Visualization'04* (2004), IEEE Computer Society, pp. 313–320. 3

[ZP05] ZHENG X., PANG A.: 2d asymmetric tensor analysis. In *VIS 05. IEEE Visualization, 2005.* (2005), IEEE, pp. 3–10. 2

[ZS18] ZOBEL V., SCHEUERMANN G.: Extremal curves and surfaces in symmetric tensor fields. *The Visual Computer 34*, 10 (Oct 2018), 1427–1442. 3

[ZYLL08] ZHANG E., YEH H., LIN Z., LARAMEE R. S.: Asymmetric tensor analysis for flow visualization. *IEEE Transactions on Visualization and Computer Graphics 15*, 1 (2008), 106–122. 2

Advances in Engineering Software 170 (2022) 103144

Contents lists available at ScienceDirect

Advances in Engineering Software

journal homepage: www.elsevier.com/locate/advengsoft

3D-TSV: The 3D trajectory-based stress visualizer

Junpeng Wang [a], Christoph Neuhauser [a], Jun Wu [*,b], Xifeng Gao [c], Rüdiger Westermann [a]

[a] Technical University of Munich, Boltzmannstr. 3, Garching, 85748, Germany
[b] Delft University of Technology, Landbergstraat 15, Delft, 2628 CE, The Netherlands
[c] Lightspeed & Quantum Game Studios, Tencent America, Seattle, USA

ARTICLE INFO

Keywords:
3D stress visualization
Principal stress lines
Level of detail techniques

ABSTRACT

In this paper, we present novel algorithms for visualizing the three mutually orthogonal principal stress directions in 3D solids under load and we discuss the efficient integration of these algorithms into the 3D Trajectory-based Stress Visualizer (3D-TSV), a visual analysis tool for the exploration of the principal stress directions of 3D stress field. In the design of 3D-TSV, several perceptual problems have been solved. We present a novel algorithm for generating a space-filling and evenly spaced set of stress lines. The algorithm obtains a more regular appearance by considering the locations of lines, and enables the extraction of a level-of-detail representation with adjustable sparseness of the trajectories along a certain stress direction. A new combined visualization of two principal directions via oriented ribbons enables to convey ambiguities in the orientation of the principal stress directions. Additional depth cues have been added to improve the perception of the spatial relationships between trajectories. 3D-TSV provides a modular and generic implementation of key algorithms required for a trajectory-based visual analysis of principal stress directions, including the automatic seeding of space-filling stress lines, their extraction using numerical schemes, their mapping to an effective renderable representation, and rendering options to convey structures with special mechanical properties. 3D-TSV is accessible to end users via a C++- and OpenGL-based rendering frontend that is seamlessly connected to a MatLab-based extraction backend. The code (BSD license) of 3D-TSV as well as scripts to make ANSYS and ABAQUS simulation results accessible to the 3D-TSV backend are publicly available.

1. Introduction

Techniques for visualizing the three mutually orthogonal principal stress directions in 3D solids under load are important in a number of use cases in computational mechanics. In civil engineering such visualizations are used to develop and assess strategies for steel reinforcement of concrete support structures [38]. In mechanical engineering, where often massive components like engines and pumps are considered, one is interested in how forces "find" their way through these components. The development of lightweight load bearing structures is investigated in e.g., aerospace engineering, here stress directions provide the first indicators where structures can be hollowed [5,22,23]. In bio-mechanics, such techniques are used to show tension and compression pathways simultaneously, and compare different structural designs regarding their mechanical properties [8]. For an overview of stress tensor visualization, we refer to the recent review article by Hergl et al. [12].

An informative visualization of the stress directions in a 3D solid can be achieved via principal stress lines (PSLs), i.e., integral curves in 3D space along the principal stress directions. PSLs are effective in communicating the pathways along which external loads are transmitted, and they show the mutual relationships between the different principal stress directions [8,43]. In computational engineering, PSLs are used in particular to show where and how loads are internally redirected and deflected. Such visualizations are necessary for a first qualitative analysis, before a quantitative analysis of certain regions using derived scalar stress measures is commonly performed.

However, in computational mechanics stress trajectory visualizations are used in a rather inconsistent way, and, to the best of our knowledge, no standard tool for such an analysis exists. In many research groups in computational mechanics, own software packages for showing one particular principal stress direction starting at randomly selected locations are used. Often, CFD tools for flow visualization are used to show streamlines in a single principal stress direction field. Visualization tools that are able to show all principal stress directions

* Corresponding author.
E-mail addresses: junpeng.wang@tum.de (J. Wang), christoph.neuhauser@tum.de (C. Neuhauser), j.wu-1@tudelft.nl (J. Wu), xifgao@tencent.com (X. Gao), westermann@tum.de (R. Westermann).

https://doi.org/10.1016/j.advengsoft.2022.103144
Received 17 March 2022; Accepted 4 May 2022
Available online 13 May 2022

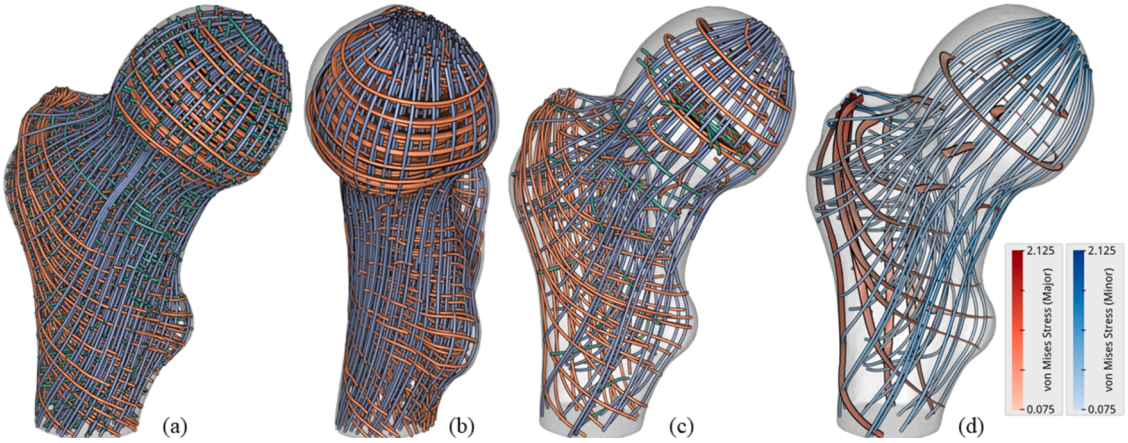

Fig. 1. (a) The 3D Trajectory-based Stress Visualizer generates a space-filling and evenly spaced set of principal stress lines (PSLs) in a 3D domain. (b) It supports a regular appearance by considering already selected lines when locating new seed points. (c,d) To reduce clutter, the density of PSLs can be adapted in a hierarchical manner. (d) Ambiguities in the assignment of stress types to directions are visualized by merging two principal stress directions into ribbons. Different scalar stress measures (d) can be mapped to color.

simultaneously are rare, and also available post-processing tools do not offer this functionality.

One reason preventing a wider adoption of such tools is visual clutter and occlusions that are produced when showing the different types of PSLs simultaneously. Due to their mutual orthogonality, the visualizations appear irregular and unstructured, and perceptual coherence breaks up even for sparse sets of trajectories. While this effect can be reduced by starting trajectories from narrow regions and following only a single type of PSLs, this leaves large sub-domains uncovered and does not show the mutual variations of the stress directions. In general, clutter can be reduced by visualizing the single stress directions side-by-side, yet juxtaposition makes it difficult to effectively relate the three mutual orthogonal stress directions to each other.

2. Contribution

This paper presents the 3D Trajectory-based Stress Visualizer (3D-TSV), a system and methodology for the visual analysis of the PSLs in 3D stress fields. Fig. 1 gives an overview of the visualization options provided by 3D-TSV. With 3D-TSV, we release a system that supports a comprehensive integral line-based analysis of 3D stress fields. To achieve this, 3D-TSV builds upon existing techniques for line seeding in vector fields [16,27], and it extends them towards the specific use case by considering simultaneously the three principal stress directions in the seeding process. 3D-TSV is designed to achieve improved regularity of the extracted PSLs, i.e., it aims for a grid-like structure where PSLs roughly intersect, uniformly cover the domain, and reveal symmetries in the underlying fields. To achieve this, in the sequential seeding process every new seed point is located on an existing PSL belonging to a different principal stress direction. As proposed for streamlines in [16, 27], the seeding process is parameterized using different distance thresholds for each type of PSL, which allows controlling separately the sparseness of the PSLs of each type. We use this possibility to enable a level-of-detail (LoD) visualization that combines a dense seeding of a selected PSL type with a seeding at a user-selected sparseness level of the respective other PSLs.

To ease integration into existing systems and accessibility to end users, 3D-TSV is implemented as a client-server tool connecting a MatLab PSL extraction backend with an OpenGL rendering frontend. The backend extracts trajectories from a given stress field using parameters that are either specified via the GUI that is built into the renderer, or a configuration file. We have chosen a MatLab backend due to the popularity of MatLab in mechanical engineering, and, thus, to enable engineers to easily integrate new model representations and algorithms. Currently, 3D-TSV works with hexahedral simulation grids, including MatLab code for trilinear and inverse distance-based interpolation of stress tensors in such grids. If other types of basis functions are used, the corresponding MatLab functions simply need to be exchanged. Due to the cell adjacency structure that is built internally to efficiently find the next cell during trajectory integration in deformed hexahedral grids, other cell types can be supported with only minor additional effort.

The frontend renders whatever set of lines that is sent from the backend using advanced rendering options such as depth cues, outlines, as well as ambient occlusion effects to improve the perception of the spatial relationships between trajectories. Furthermore, the user can select to visualize one pair of stress directions via ribbons. Ribbons follow one of the selected directions and twist according to the other one, and they can effectively convey regions where the assignment of the eigenvector directions to the type of PSL (i.e., major, medium, or minor) changes.

To summarize, the contributions of this work are

- an advanced and publicly available tool for trajectory-based stress tensor visualization supporting stress fields on arbitrary hexahedral grids,
- the adaptation of evenly spaced line seeding to create a space-filling set of PSLs with improved regularity,
- an adaptive level-of-detail visualization using varying PSL density and visual mappings to lines and ribbons.

The application of 3D-TSV is demonstrated in a number of experiments using datasets with different shapes and stress states. The code of 3D-TSV is made publicly available under a BSD license, and published on https://github.com/Junpeng-Wang-TUM/3D-TSV. In video1[1], the seeding of trajectories by 3D-TSV is compared to the seeding of trajectories separately in each principal stress direction field via evenly spaced seeding [16]. 3D-TSV can be used as client-server system as described (see video2[2]), or as standalone tool solely in MatLab providing rudimentary visualization options (see video3[3]). Also the frontend can be used standalone, reading the PSL specific information from "psl.dat" files (see video4[4]). Thus, any other backend can be used to generate PSLs and let the frontend visualize them. We also provide a script written in

[1] https://youtu.be/lN9CxgvfgNY
[2] https://youtu.be/h7BzP7Jg_-o
[3] https://youtu.be/99Jn938ZoVk
[4] https://youtu.be/zafBOAt9Xvs

the ANSYS built-in language APDL, which automatically converts the result of an ANSYS finite element stress analysis into the format required by the 3D-TSV backend (see video5[5]). To support the output from ABAQUS, the mesh information needs to be read from the ABAQUS input file (".inp"), and the stress data can be acquired from the result file (".rpt"). We provide datasets, description and configuration files, as well as scripts for all use cases of 3D-TSV on the publicly available GitHub repository.

3. Related work

3.1. Stress Tensor Field Visualization

Stress tensor field visualization can be classified into trajectory-, glyph- and topology-based methods [12,21]. Trajectory-based methods choose the PSLs as visual abstractions of the stress field, focusing on the directional structure of the principal stresses. Delmarcelle and Hesselink [6] introduced the concept of hyperstreamlines, a visual mapping of the medium and minor principal stresses onto a tube surface with a single selected major PSL as centerline. Dick et al. [8] trace the major and minor PSLs from randomly distributed seed points in the loading area of the solid object, and different types of stress state like tension and compression are distinguished by color. In order to identify and visualize regions where stress trajectories are of rotational or hyperbolic behavior, Oster et al. [28] proposed the concept of tensor core lines in 3D secondorder tensor fields. Hotz et al. [15] smear out dye along the PSLs using line integral convolution. In this way, a density field is generated that resembles a grid-like structure. This approach provides a global overview of a 2D stress distribution, yet an extension to 3D is problematic due to the generation of a dense volumetric field.

It's worth noting that even though stresses are frequently simulated and analysed in engineering applications, the use of trajectory-based visualizations that consider the whole stress field as a tensor field instead of several scalar fields are not commonplace. In particular, such functionality seems neither provided by any of the well-established software packages for stress simulation, like ABAQUS and ANSYS, nor by dedicated environments for visualizing finite-element simulation results [3,24,44].

Glyph-based methods, on the other hand, depict the stress field by a set of well-designed geometric primitives – so-called tensor glyphs. Tensor glyphs were originally designed for glyph-based diffusion tensor visualization [19], and later adapted to visualize positive definite tensors [18], general symmetric tensors [34], as well as asymmetric tensors [11,35]. Glyph-based techniques are problematic when used to visualize 3D stress fields, due to their inherent occlusion effects. Specific placement strategies can be used to reduce the number of glyphs and occlusions thereof [14,20]. Tensor glyphs are effective in showing the local stress states, but they cannot effectively communicate the global structure of stress lines. Patel and Laidlaw [30] proposed to guide the placement of glyphs by principal trajectories in the underlying field, and thus to provide a better understanding of the global relationships in this field.

Topology-based approaches for stress tensor visualization abstract from the depiction of stress directions and focus on revealing specific topological characteristics of the tensor field. Delmarcelle and Hesselink [7,13] studied the topology of symmetric 2D and 3D tensor fields, and introduced the fundamental concepts of degenerate points and topological skeletons. Zheng and Pang [49], and later Roy et al. [33], discussed the robust extraction of these topological features. Zobel and Scheuermann proposed the notion of extremal points to analyze the complete invariant part of the tensor [50]. Raith et al. presented a general approach for the generation of separating surfaces in the invariant space [32]. Palacios et al. introduced the eigenvalue manifold and visualized the 3D eigenvectors as curve surfaces [29]. Qu et al. [31] further generalized the concepts of degenerate curves and neutral surfaces to a unified framework called mode surfaces.

3.2. Streamline Seeding

Seeding strategies to control the density and placement of trajectories in vector fields are widely used in flow visualization. Turk and Banks [39] and Jobard and Lefer [16] were the first to introduce seeding strategies for generating evenly spaced sets of streamlines in 2D vector field. Numerous extensions and improvements of these concepts have been proposed since then. In particular, Vilanova et al. [41] proposed an extension of the approach by Jobard and Lefer to diffusion tensor fields, which detects the distance between the new streamline and the existing ones during the tracing process. They demonstrate the generation of evenly distributed streamlines, however, the approach suffers from 'unfinished' streamlines that are caused by an artificial stopping criterion and only considers a single eigenvector field at a time. For 3D flow visualization, dedicated approaches and frameworks have been developed to reduce the visual clutter and occlusion of densely distributed streamlines in 3D fields [4,17,47,48]. However, these techniques do not fit our goal of visualizing PSLs and their mutual relationships, which requires considering three sets of orthogonal PSLs simultaneously.

3.3. Streamline Visualization

Illuminated streamlines are often used as a means of visualizing streamlines in a 3D environment. The streamlines are mapped to tubes and then shaded, e.g., using the Blinn-Phong shading model [2]. Early work on illuminated streamlines was done by Zöckler et al. [51] and Mattausch et al. [27]. Stoll et al. [37] extended this work by introducing stylized line primitives, rendered by a hybrid CPU-GPU renderer. Liu [26] presented the DOXIV, a prototype framework for high-performance visual analysis of large flow data. Volpe [42] first introduced the concept of streamribbons for flow field visualization.

3.4. Hexahedral Meshing

An alternative approach to PSL-based stress field visualization is to generate a frame field from the principal stress field first and employ field-aligned hexahedral meshing to produce orthogonal edges that follow PSLs. The edges of such hex-meshes can follow the directions of PSLs excellently in situations where degenerate points are not present and the stress lines show low degrees of convergence and divergence. However, when guided with frame fields corresponding to realistic load situations, yet still much more benign than those demonstrated in this work, it is an unsolved problem to reliably produce an all-hex mesh. Hexahedral-dominant meshing has been resorted as an intermediate solution. For instance, Wu et al. [46] propose a conforming stress-guided lattice structure by combining topology optimization with the field-guided polyhedral meshing algorithm from [9]. Arora et al. [1] generate similar structural designs via the guidance of the principal stress field, where they modify the stress field to get a smooth frame field. However, hexahedral-dominant meshes often contain either T-junctions or non-hexahedral elements with non-orthgonal edges, significantly deviating from the PSLs and are, thus, not applicable for stress field analysis either.

4. Stress tensor directions

At each point in a 3D solid under load, the stress state is fully described by the stress vectors for three mutually orthogonal orientations. The second-order stress tensor

[5] https://youtu.be/Yri_B7m3AWU

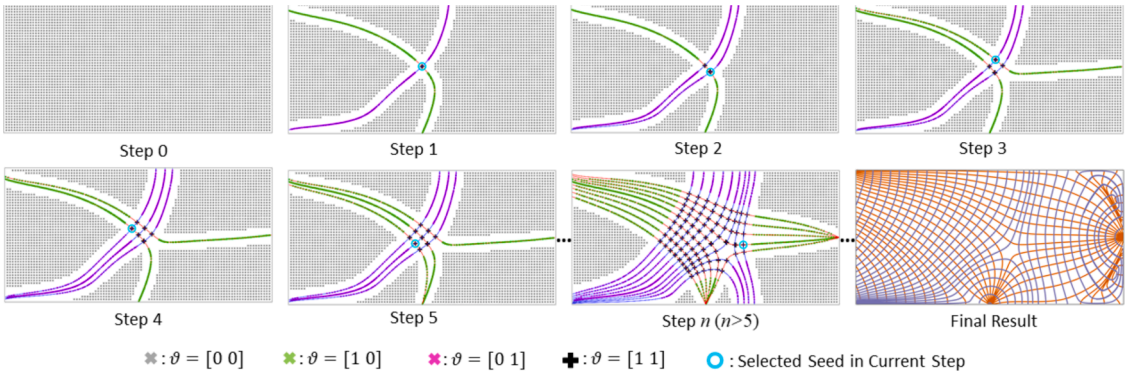

Fig. 2. Starting from a set of seeds with empty valence [0 0], the sampling process is performed until all the seed valences have been turned to [1 1]. The ocher and blue lines are the major and minor PSLs. (For interpretation of the references to colour in this figure legend, the reader is referred to the web version of this article.)

$$T = \begin{bmatrix} \sigma_{xx} & \tau_{xy} & \tau_{xz} \\ \tau_{xy} & \sigma_{yy} & \tau_{yz} \\ \tau_{xz} & \tau_{yz} & \sigma_{zz} \end{bmatrix} \tag{1}$$

contains these vectors for the axes of a Cartesian coordinate system. T is symmetric since the shear stresses given by the off-diagonal elements in T are equal on mutually orthogonal planes. The principal stress directions of the stress tensor indicate the three mutually orthogonal directions along which the shear stresses vanish. These directions are given by the eigenvectors of T, with magnitudes given by the corresponding eigenvalues. The signs of the principal stress magnitudes classify the stresses into tension (positive sign) or compression (negative sign). However, since there are three principal stresses acting at each point, the classification is with respect to a specific direction.

In descending order, the three eigenvalues of T represent the major σ_1, medium σ_2 and minor σ_3 principal stresses, with the corresponding eigenvectors indicating the principal stress directions at each point in the 3D solid. The trajectories along these directions are called the principal stress lines (PSLs). They are computed by numerically integrating massless particles in each single (normalized) eigenvector field.

In general, σ_1, σ_2 and σ_3 are mutually unequal, and the eigenvectors are linearly independent and even mutually orthogonal due to the symmetry of T. However, so-called degenerate points can exist where two or more eigenvalues are equal. In the vicinity of these points, which are classified by $\sigma_1 = \sigma_2 > \sigma_3$ or $\sigma_1 > \sigma_2 = \sigma_3$[6], the PSL direction cannot be decided. Therefore, when tracing along a principal stress direction, we test whether the eigenvalue σ_i corresponding to this direction is too close to another eigenvalue σ_j, i.e., $deg = \frac{1}{2}\left|\frac{\sigma_i - \sigma_j}{\sigma_i + \sigma_j}\right| < 10^{-6}$. If this is the case and the angle between the PSL tangents at the current and next integration point is too large, the integration is stopped. Furthermore, we provide the option to map *deg* to the color of a PSL via a color table (see Section 4.3), so that the proximity to a degenerate point is indicated. PSL integration is also stopped when the next integration point is located on a boundary face, the point is closer to a previous point on the same trajectory than a predefined distance threshold (i.e., to avoid running into closed orbits), or the number of integration steps reaches the pre-defined threshold.

The integration of PSLs requires to select seed points from which they start until they arrive at a degenerate point or the boundary. While uniform seeding in the entire domain is used as the default option, the user can select seeding from the boundary vertices as well as the vertices where loads are applied. Furthermore, different integration schemes can be used for PSL tracing, including the 1st-order Euler method, and the 2nd- and 4th-order Runge-Kutta methods, where the fixed integration step size δ is used for Cartesian meshes, and an adaptive δ for unstructured hexahedral meshes. In each integration step, the stress tensor T is interpolated, and the eigenvalues and eigenvectors are computed from the interpolated tensor. If none of the mentioned stopping criteria holds, the next step is performed in the direction with the least deviation from the previous direction.

[6] We do not consider triple degenerate points with $\sigma_1 = \sigma_2 = \sigma_3$, since they do not exist under structurally stable conditions [49].

5. PSL Seeding and level of detail

Finding a set of PSLs that effectively convey the principal stress directions in 3D stress fields requires to consider perceptual issues related to the visualization of large sets of trajectories. While in principle the PSLs of a single type, i.e., major, medium, or minor, can be visualized separately using techniques from flow visualization, in a stress field the different types of PSLs need to be shown simultaneously to understand their mutual interplay. However, an effective and efficient visual analysis is hindered by the mutual orthogonality of the different types, which is perceived as a disordered state even when a low number of PSLs is shown. Our proposed seeding strategy cannot completely avoid this problem, but it has some built-in regularity due to enforced PSL intersections.

5.1. Evenly spaced PSL seeding

The proposed seeding strategy builds upon the evenly spaced streamline seeding approach by Jobard and Lefer [16], and extends this approach in several ways to account for the application to PSLs. For the sake of clarity, we describe the strategy in the context of 2D stress fields, yet it will become clear that the extension to 3D is straightforward. However, when applied in 3D, the resulting PSL structures show a fundamental difference. Unlike in 2D, where due to the intersections between major and minor PSLs a fairly regular grid-like structure is generated, such intersections are rare or do not exist at all when seeding PSLs in 3D. This counteracts the impression of a consistent grid-like structure and results in a rather disordered appearance. We propose a seeding strategy that weakens this effect, but it needs to be considered that due to the nature of PSLs in 3D stress fields a globally consistent 3D grid-like structure is impossible to achieve in general.

Our method builds upon the selection of new seed points in the spirit of Jobard and Lefer, where the potential candidates are those points which are at least a prescribed distance away from any already extracted PSL. Of these candidates, the one with minimum distance is selected and a new trajectory is started at that point. In contrast, in our approach the distance is always wrt. the initial seed point, so that the PSLs grow around that point instead of being seeded at vastly different locations.

To adapt the seeding strategy to the situation of different types of PSLs, we first introduce the concept of *seed valence*. In 2D, the seed valence ϑ is a 2×1 binary array, which is associated to each seed point to indicate whether and of which type PSLs have been traced from this

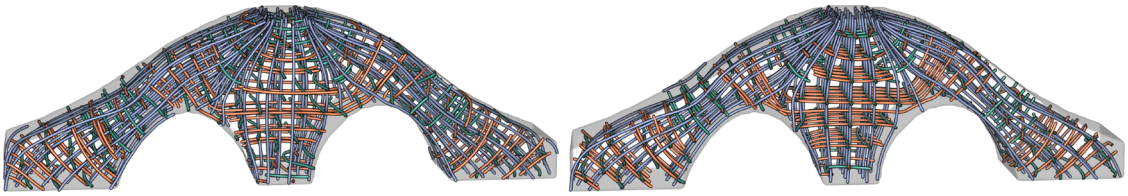

Fig. 3. PSLs in a bridge under load (see Figure 9 for the simulated load conditions). Major (ocher), medium (green) and minor (blue) PSLs generated by (left) separate seeding as proposed by [16] in each principal stress direction field, and (right) by our method. Note that since the stress field is not strictly symmetric, the PSL set shows some asymmetry. (For interpretation of the references to colour in this figure legend, the reader is referred to the web version of this article.)

point. ϑ can take on four different bit combinations, i.e., empty seed [0 0] (passed by no PSL), solid seed [1 1] (passed by both major and minor PSLs) and semi-empty seed [1 0] (only passed by major PSL) or [0 1] (only passed by minor PSL). The sampling process is repeated until all valences of all possible seed points become solid [1 1]. With this definition of seed valence, the sampling process is performed iteratively, by using the seed valence to characterize the state of each seed point at a specific iteration. To ensure that the generated PSLs are space-filling, the initial candidate seed points (with $\vartheta = [0\ 0]$) are located at the vertices of a space-filling Cartesian grid (step 0 in Fig. 2).

Seeding starts by selecting one of the candidate seed points and tracing the major and minor PSLs from it (Step 1 in Fig. 2), setting $\vartheta = [1\ 1]$ at this point. Per default, the system starts with the seed point closest to the center of the bounding box of the domain, to preserve an existing plane symmetry of the stress field in the PSLs (see Fig. 10 and Fig. 11). Then, all candidate seed points with ϑ not equal to [1 1] are re-classified with respect to the currently existing PSLs. To exclude candidates too close to an existing major or minor PSL, ϑ of these candidates is set to [1 0] or [0 1], respectively. If a point is classified as [1 0] or [0 1] and closer to a minor or major PSL, respectively, its valence is set to [1 1]. The distance between a point and a PSL is computed as the minimum distance between the point and any of the integration points on the PSL. Proximity is decided via a distance threshold ε, which also controls the density of the extracted PSLs.

To obtain a more regular PSL structure, each re-classified candidate point is re-located (i.e., merged) to the position of the closest integration point on the PSL causing its classification. This creates an "empty" band around the PSLs where no candidate seed point exists. The merging operation enforces that newly selected seed points lie on an existing PSL, so that the final PSL structure appears more regular and less cluttered (see Fig. 3 for a comparison to the seeding approach by Jobard and Lefer). By placing the initial seed point in a region deemed important, the user can specifically enforce regularity in this region.

If the last computed PSL was a major or a minor PSL, then the next seed point is selected from the set of candidates with $\vartheta = [1\ 0]$ or [0 1], respectively. Thus, we alternate the order of major and minor PSL extraction to obtain a uniform distribution of both types. Of all these, the one closest to the initial seed point is selected as the new seed point, and the respectively transverse PSL is computed. The entire procedure is then restarted until no more candidate is available (see steps 2–5 in Fig. 2).

We further consider the situation where some empty seed points may get too close (measured by ε) to the other type of existing PSLs after they are merged to the current PSL, e.g., the seed valence ϑ of some empty seed points become [1 0] after merging them to the newly traced major PSL. However, it can also happen that some of these merged seed points might be close to some of the existing minor PSLs, which would unavoidably cause inappropriate placement of minor PSLs in the final visualization. Given this, we identify those semi-empty seed points after merging, and compute the distances of them to the corresponding type of PSLs. If there are distances less than ε, the valences of these seed points are set to [1 1]. By simply making ϑ a binary array with three elements referring to the major, medium and minor PSL, the proposed seeding strategy can be lifted to 3D.

5.2. PSL LoD Structure

To change the density of the generated PSLs, the seeding process can simply be re-run with an appropriately set distance threshold ε. The larger this threshold is, the less PSLs are extracted. However, the different sets of PSLs that are generated for different thresholds are not nested, i.e., the PSLs at a coarser representation with lower PSL density are not a subset of the PSLs at a representation with higher density. Therefore, in an exploration session where the user interactively selects

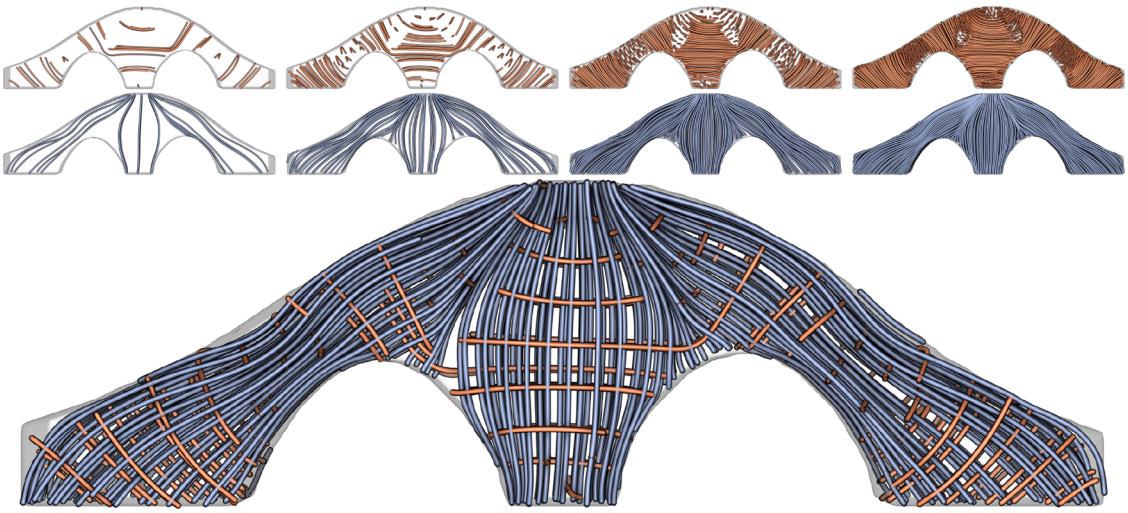

Fig. 4. PSL LoD hierarchy. Top: The major and minor PSLs at different LoDs, computed separately for each level. Bottom: Simultaneous extraction of the PSL structure using level $L2$ (context) for the major and $L3$ (focus) for the minor PSLs.

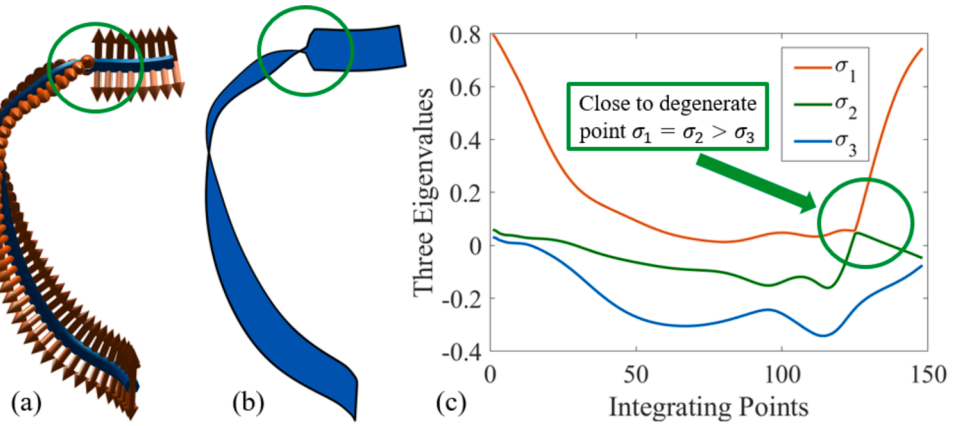

Fig. 5. When a PSL goes through a degenerate point (a), the ribbon-shaped geometry shows a sudden twist (b). (c) Behaviour of the eigenvalues along the ribbon's center PSL, from which the ribbon's direction and orientation is determined.

different PSL LoDs, there are abrupt changes when transitioning from one level to another. To avoid this, we propose to generate a nested PSL hierarchy.

The basic idea underlying the construction of a nested hierarchy is to let the PSLs at a level with higher PSL density 'grow out' sequentially from the PSLs at a lower density level. As a side effect, this enables saving computations by progressively computing a new level from the previous coarser level. For a given set of PSLs that have been generated with distance threshold ε_0, the refined set of PSLs according to a distance threshold $\varepsilon_1 < \varepsilon_0$ is computed as follows: Firstly, the candidate seed points are reset to their initial positions. Secondly, the candidate seed points are merged to the existing PSLs according to ε_1, to create "empty" bands around the existing PSLs. The valences are updated accordingly to [1 0], [0 1] or [1 1] depending on the types of PSL they are merged to. After this, some non-solid seeds are left, because ε_0 is larger than ε_1. With these seeds the seeding is subsequently performed, including the iteration of seed point selection, PSL computation, and re-classification as described in subsection 4.1.

To generate a full LoD PSL hierarchy, the user defines the minimum distance threshold ε and the number M of levels to construct. Then, the distance thresholds of each level are computed as $2^{(M-k)}\varepsilon,\ k = 1 : M$ from coarse to fine, and the hierarchy is constructed progressively from the coarsest resolution level (see 1st and 2nd rows in Fig. 4). To compute a PSL structure with different types of PSLs at different LoDs, the distance thresholds for each PSL type are first selected by the user, and then the multi-type LoD is computed by alternatively considering the different PSL types with their respective distances.

5.3. Ribbon-based stress visualization

Instead of rendering lines, the user can select a PSL type (i.e., major, medium, minor) and visualize ribbon-shaped geometry [40] that is centered at the PSLs of the selected type and twists according to the direction of another stress type (see Fig. 5 a,b). At each integration point along a PSL of the selected type, two lines with adjustable length are traced forward and backward along the other direction. The lines' endpoints at subsequent integration points are connected to form a ribbon. It is worth noting that the constructed ribbons don't coincide with streamsurfaces that are integrated from a PSL along one other stress direction. As shown by Raith et al. [32], such surface might not even exist, i.e., when integrating from two points on the same PSL over a certain length along another stress direction, the two endpoints are not lying on a PSL in general. The mapping of two principal stress directions to a ribbon geometry is conceptually similar to the well-known hyperstreamlines [6], i.e., a mapping of two principal stress directions to a tube centered at the PSL along the third direction.

We let the user select a visualization using ribbons to convey changes in the assignment of the eigenvector directions to the type of PSL in the vicinity of degenerate points. When a ribbon is formed as described, flips often occur in the vicinity of a degenerate point (see Fig. 5 (c)). This is because the two directions can exchange their classification as major, medium, and minor, since this depends only on their position in the sorted sequence of eigenvalues. Thus, ribbons provide an additional visual cue to indicate topological changes of the PSLs in the vicinity of degenerate points.

Fig. 6 compares the options to visualize principal stress directions via ribbons and lines, and combine them into a single visualization. As can be seen, twists in the ribbon geometry effectively hint to regions where degenerate points might exist. For lines, 3D-TSV can map the degeneracy measure introduced in Section 3 to color. An interesting observation is that high degeneracy and flips thereof frequently occur close to the object boundaries when Cartesian simulation meshes are used. These flips occur due to the well-known inaccuracies at curved boundaries that are represented by hexahedral simulation elements in a Cartesian grid.

6. System implementation

To implement the communication between the C++ visualization frontend and the MatLab extraction backend, the messaging library ZeroMQ is utilized, which can be used for communication over a wide variety of protocols, like TCP/IP. 3D-TSV relies on the request-reply pattern implemented in ZeroMQ, where the frontend issues a new request to the backend when the user changes simulation settings in the

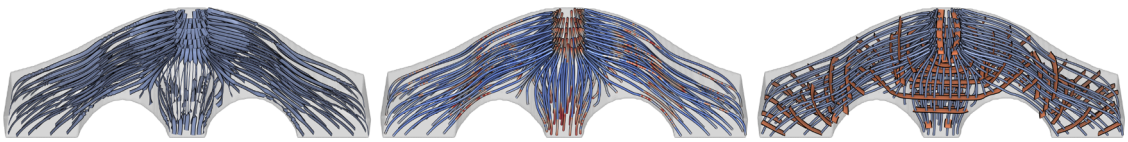

Fig. 6. Left: Ribbons are aligned along the minor PSLs and twist according to the medium principal stress direction. Middle: Minor PSLs with degeneracy measure mapped from blue (low) to red (high). Right: A visualization using lines for minor PSLs and ribbons for major PSLs. (For interpretation of the references to colour in this figure legend, the reader is referred to the web version of this article.)

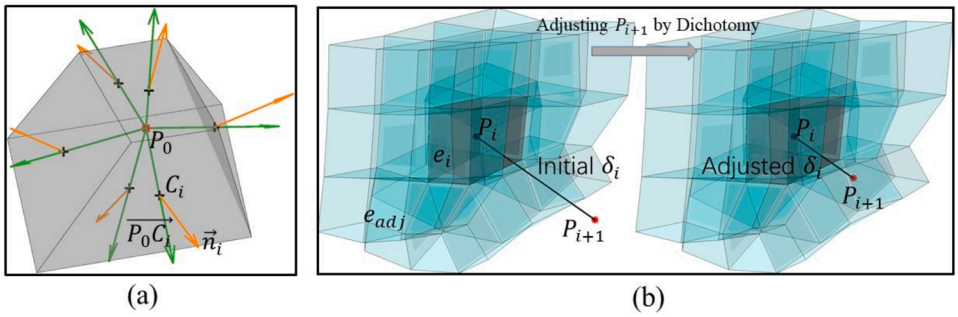

Fig. 7. (a) Quantities required to test whether a point P_0 (red $*$) is located in a hexahedral cell. Black " + " and orange arrows indicate centers C_i and out-facing normals $\vec{n}_i,\ i \in \{1, \cdots, 6\}$ of the six cell faces. Green arrows indicate the directional vectors $\overrightarrow{P_0C_i},\ i \in \{1, \cdots, 6\}$ that are used. (b) Point re-location is subsequently performed until the next integration point P_{i+1} is within the same cell e_i (grey cube) as the current point P_i, or is within one of the cells e_{adj} (cyan cubes) adjacent to e_i. (For interpretation of the references to colour in this figure legend, the reader is referred to the web version of this article.)

graphical user interface, and the backend sends back a reply as soon as the simulation is finished in order to notify the frontend of the availability of new data.

The reason why we turned to MatLab instead of C++ for the implementation of the backend is, on the one hand, that the sampling method is an inherently sequential algorithm. Thus, it cannot benefit significantly from multi-threaded PSL tracing or GPU parallelization. On the other hand, MatLab is widely spread in engineering, where most of our collaborators regarding stress visualization come from, and the engineers tend to use mainstream commercial software they are already familiar with to finish the design iteration quickly. In this case, they can run the MatLab backend independently without any complicated compilation and setup process. To this end, we also provide a slim MatLab visualization implementation, which can provide users a fast and easy way to explore the stress field, while discarding some more complex hardware-accelerated features from the C++ frontend, like depth cues or ambient occlusion effects. It is worth noting that also the rendering frontend can be used standalone, by reading trajectories from a file specifying the exchange format regarding PSL type and LoD representation.

6.1. Numerical PSL integration

3D-TSV is designed to support the visualization of PSLs in solids discretized by hexahedral grids, where the stress tensors are given at the grid vertices. When computing PSLs in Cartesian grids, component-wise trilinear interpolation of the tensors is used during numerical line integration. In deformed hexahedral cells, tensor interpolation is performed via inverse distance weighting [36].

To integrate PSLs in Cartesian grids, the system provides fixed-step integration schemes with user adjustable stepsize of at least half the cell diameter. In deformed hexahedral grids, a different approach is taken since the size of the simulation elements can vary, and with a constant stepsize the risk increases that multiple cells smaller than this size are missed in one single integration step. To reduce this risk, the integration stepsize is automatically adapted to the size (i.e., the length of the shortest edge) of the cell at the current integration point P_i. These values are pre-computed and stored per cell. In each integration step, the size s of the current cell is read and multiplied by a user selected scaling factor δ_s. δ_s can be made smaller than 1 to obtain more accurate PSLs. With the stepsize $s{\cdot}\delta_s$, the PSL is integrated from the current point P_i in cell e_i to the new point P_{i+1}. Then, the integration process is restarted with P_{i+1} and the cell e_{i+1} containing P_{i+1}.

To find e_{i+1}, it is first tested whether P_{i+1} is still contained in e_i. The following in-out criterion is used to test whether a point is located in a hexahedral cell: Given a hexahedral element with the centers and out-facing normal of its 6 faces C_i and $\vec{n}_i,\ i \in \{1, \cdots, 6\}$. Any point P_0 in the interior or on the boundary of the element satisfies $\max(\arccos(\overrightarrow{P_0C_i}, \vec{n}_i)) \leq \frac{\pi}{2},\ i \in \{1, \cdots, 6\}$, see Fig. 7 a. In practice, the criterion is slightly relaxed to $\max(\arccos(\overrightarrow{P_0C_i}, V_i)) \leq \frac{91\pi}{180},\ i \in \{1, \cdots, 6\}$, to account for non-planar cell faces, i.e., a slight variation of the normal vectors across the faces.

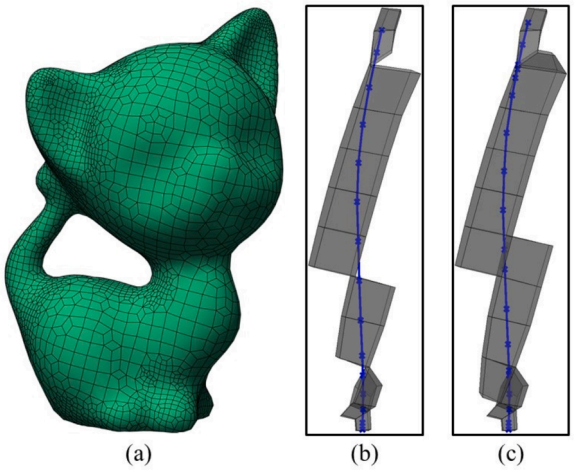

Fig. 8. (a) The deformed hexahedral simulation mesh. (b) A PSL (blue trajectory) in the simulated stress field. It is ensured that every next integration point is in the previous cell or in a cell adjacent to the previous cell. (c) Same as (b), but now every next integration point is in a face-adjacent cell. (For interpretation of the references to colour in this figure legend, the reader is referred to the web version of this article.)

If e_i does not contain P_{i+1}, the cell e_{i+1} needs to be determined. To this end, we further test whether P_{i+1} lies in any of the adjacent cells e_{adj} of e_i. For each cell, the set of adjacent cells as well as the adjacency type, i.e., face-, edge-, and vertex-adjacency, is pre-computed and stored. In case P_{i+1} is not within e_i or e_{adj}, we scale down the stepsize via a dichotomy strategy, i.e., $P_{i+1} = (P_{i+1} + P_i)/2$, until P_{i+1} is located in e_i or it's adjacent cells e_{adj}.

In the case where e_i and e_{i+1} are connected by a single edge or vertex, it may still happen that cells are skipped when going from P_i to P_{i+1}. In this situation, stepsize refinement is performed multiple times until the cell e_{i+1} shares a face with e_i or is below a user-selected threshold. The latter situation is encountered when the PSL goes through a cell vertex or edge, so that face-adjacency cannot be determined. In Fig. 8, for the given mesh two PSLs that have been extracted without and with additional stepsize refinement are compared. As can be seen, cells that would be skipped when using only face-to-face adjacency are now determined and considered in the integration.

6.2. Rendering

The line and ribbon primitives are rendered in a stylized fashion similar to the techniques by Zöckler et al. [51], Stoll et al. [37] and Mattausch et al. [27], using default colors, halos and depth cues as shown in the first three images in Fig. 1. Focus PSLs and contextual

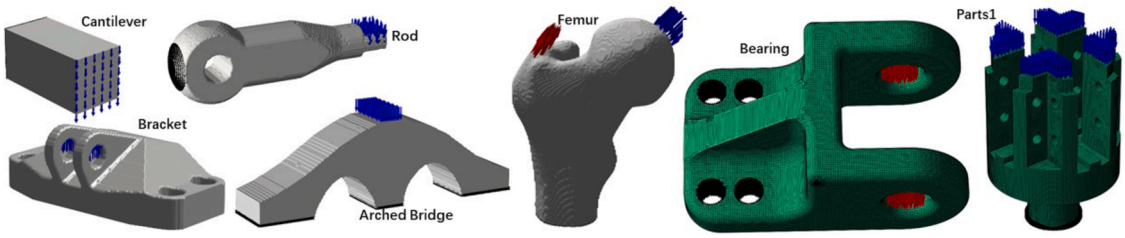

Fig. 9. The solid objects used in this work and the applied external loads. Red and blue arrows indicate the loading positions and directions, black regions indicate fixed boundaries. A finite-element-based elasticity analysis has been used to compute the stress field for each model under the predicted loads. The unstructured hexahedral meshes 'Parts' and 'Bearing' are courtesy of [25] and [10], respectively. All other meshes are Cartesian meshes. 'Arched Bridge' and 'Rod' are courtesy of [1] and [10], respectively. All simulated stress fields are made publicly available. (For interpretation of the references to colour in this figure legend, the reader is referred to the web version of this article.)

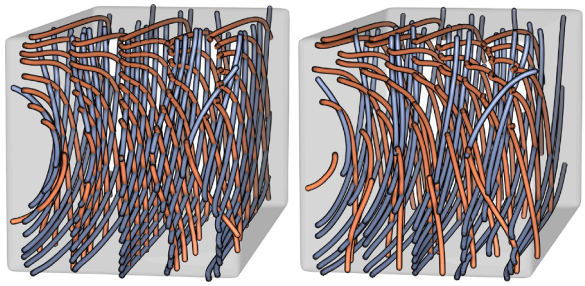

Fig. 10. PSLs in the 'Cantilever' stress field. PSLs by the proposed seeding strategy (left) and evenly spaced streamline seeding (right).

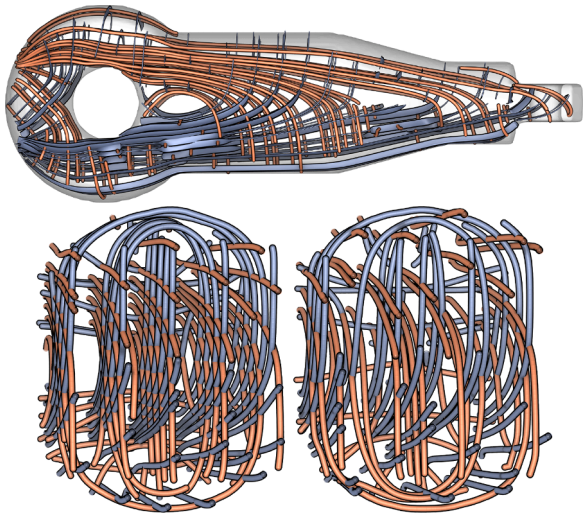

Fig. 11. Top: PSLs showing the principal stress directions in 'Rod'. Bottom: PSLs in 'Rod' from a different view. Left: PSLs computed by 3D-TSV. Right: PSLs computed via evenly spaced seeding as proposed by [16].

ribbons are rendered in ocher and blue, respectively. The base color is modulated using Blinn-Phong shading [2,51], which assumes a point light source at the world space position of the viewer (i.e., a head light).

The user can interactively change the color mapping—also separately for each PSL type—and can in particular switch to a mapping of some scalar quantity to color, as indicated in the last image in Fig. 1 using the scalar von Mises stress measure. The scalar values are issued via the backend as per-vertex attributes. The standard color scheme we use for the different principal stress directions (blue, green, ocher) is the '3-class Set2' transfer function from ColorBrewer[7]. It is colorblind safe and print friendly.

For enhanced depth perception, depth cues are added, i.e., with increasing distance to the camera, fragments are increasingly desaturated. A translucent simulation mesh outline hull can be rendered together with the stress field data in order to hint at the extents of the simulation domain.

6.3. 3D-TSV settings

3D-TSV provides a number of parameters that can be changed by the user to control the generation of PSLs. These parameters include the merging threshold ε and the number of levels M introduced in subsection 4.1 and subsection 4.2, respectively. Another set of parameters enables a user-guided interaction with the PSL distribution, including sliders for controlling the LoD resolution of major, medium and minor PSLs. In addition, the user can select the two PSL types that are used to generate ribbons. Via a drop-down menu, the user can select a scalar stress measures that are mapped to PSL color using a transfer function. The backend provides different stress components, such as the principal stress amplitudes, von Mises stress, and the six Cartesian stress components.

7. Results

In all of our experiments, PSL generation is performed on the CPU, i.e., a workstation running Ubuntu 20.04 with an AMD Ryzen 9 3900X @3.80GHz CPU and 32GB RAM. Rendering is done on an NVIDIA RTX 2070 SUPER GPU with 8GB of on-chip memory. The rendering times are always below 10 milliseconds. The data sets we use in our experiments are shown in Fig. 9. The stress fields are simulated by a finite element method (FEM), using the solid objects under the shown load conditions. Table 1 lists the numbers of simulation elements of each of the data sets, the seed points that are used to generate the PSLs, the number of generated PSLs, and the time required for PSL generation.

For the three models 'Bridge', 'Cantilever' and 'Rod', we demonstrate the improvements of the proposed seeding strategy over evenly spaced streamline seeding. 3D-TSV is used to visually analyze the stress fields in 'Femur' and 'Bracket'. These two data sets that are frequently seen in structural design and optimization [45]. Finally, we consider the two mechanical parts 'Bearing' and 'Parts1' to demonstrate the application of 3D-TSV to unstructured hexahedral simulation meshes.

Figs. 10 and 11 emphasize the improvements by the proposed seeding strategy regarding the regularity of the extracted set of PSLs. 3D-TSV generates a fairly uniform space-filling PSL structure, which, in particular, maintains the symmetry of the stress field in 'Cantilever'. Evenly spaced streamline seeding, on the other hand, generates a far less

[7] https://colorbrewer2.org/#type=qualitative&scheme=Set2&n=3

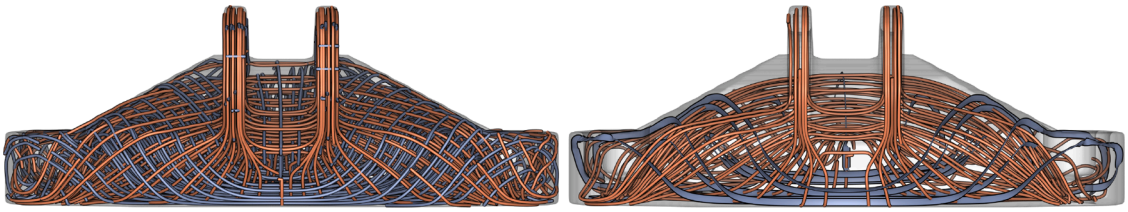

Fig. 12. Stress field in 'Bracket'. Left: PSLs at the finest level (according to Table 1). Right: major / minor PSLs at the third ($L3$) / first ($L1$) level of detail.

Table 1
Model and performance statistics. D_0 is the length of the shortest dimension of the bounding box of the stress field.

Data Set	#Cells	#Seeds	ε/D_0	M	#PSLs	Time (s)
Cantilever	250K	2K	1/5	1	85	0.4
Rod	536K	18K	1/5	1	174	2.1
Femur	696K	10K	1/18	3	823	9.0
Bracket	650K	9K	1/12	3	293	5.4
Bearing	189K	55K	1/18	3	1364	33.4
Parts1	253K	46K	1/20	3	1557	27.9

regular design which introduces severe visual clutter.

The visualization also highlights the importance of showing different PSL types simultaneously. In the analyzed tensor field, the signs of the eigenvalues along the major and minor PSLs are mostly positive and negative, respectively. This means that the major PSLs are mainly under tension and the minor PSLs mainly under compression. Thus, either of both effects could be shown by visualizing one PSL type, but not both.

Fig. 12 (left) shows the space-filling PSLs in the stress field in the interior of 'Bracket'. From the boundary condition in Fig. 9, we see that the structure is mainly under tension. Thus, we choose to show the major PSLs at the higher level of detail ($L2$) and the minor PSLs at lower level $L1$ (see Fig. 12 (right)). The minor PSLs are shown via ribbons, with the medium principal stress direction indicating the twist. This enables a fine granular analysis of the major principal stress directions, and simultaneously provide a coarse representation of the other principal directions. A similar setting has been selected to visualize the stress directions in 'Femur' (see Fig. 1).

3D-TSV works with Cartesian meshes and deformed hexahedral meshes, which are both frequently used in mechanical engineering applications. Here we use the stress fields due to external loads in the interior of 'Bearing' and 'Parts1', to demonstrate the capability of 3D-TSV. As shown in Fig. 9, especially in 'Bearing' the element sizes change considerably over the 3D domain. The distribution of PSLs of 'Bearing' is shown in Fig. 13 (left), and the right image shows the combination of major at the third level of detail ($L3$) and minor at $L1$, where the minor PSLs are shown via ribbons. The full distribution of PSLs of 'Parts1' can be seen in the Fig. 14 (left), on the right the minor PSLs at $L3$ and major PSLs at $L2$ are shown simultaneously, where the major PSLs are rendered via ribbons.

8. Conclusion and future work

In this paper, we have introduced 3D-TSV, a tool for visualizing the principal stress directions in 3D solids under load. 3D-TSV makes use of a novel seeding strategy, to generate a space-filling and evenly spaced set of PSLs. By considering all three types of PSLs simultaneously in the construction process, the regularity of the resulting PSL structure is improved. By incorporating different merging thresholds for each PSL type into the construction process, a consistent multi-resolution hierarchy is formed, which can be utilized to show different PSL types with different resolutions simultaneously. Efficient rendering options for lines and ribbons on the GPU enable interactive analysis of large sets of PSLs.

In the future, we intend to couple 3D-TSV with load simulation processes, so that dynamic changes of the stress field can be instantly monitored. Therefore, we will analyze whether the intrinsically iterative parts of the algorithm can be parallelized on modern multi-threading architectures. Furthermore, we are interested in using space-filling evenly spaced seeding to guide the material growth in topology optimization. Topology optimization seeks to distribute material in a way that makes the object resistant to external loads. To automatically generate support structures that follow the major stress directions and

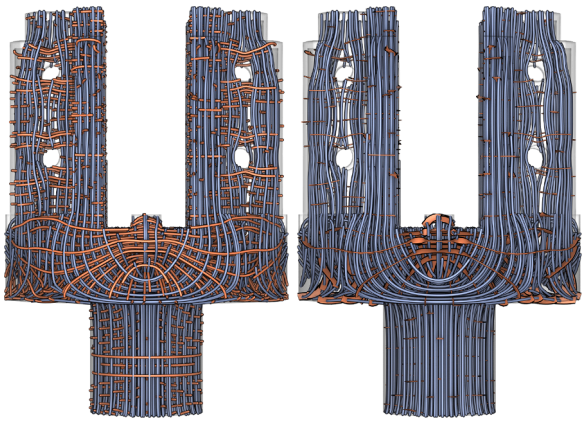

Fig. 14. Stress fields in 'Parts1'. Left: PSLs at the finest level. Right: major / minor PSLs at $L2$ / $L3$. Ribbons are along the major PSLs and twist according to medium principal stress direction.

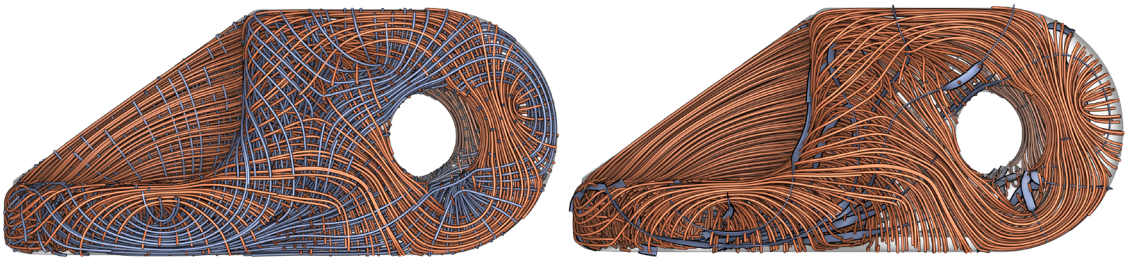

Fig. 13. Stress field in 'Bearing'. Left: PSLs at the finest level (according to Table 1). Right: major / minor PSLs at the third ($L3$) / first ($L1$) level of detail. Ribbons are along the minor PSLs and twist according to medium principal stress direction.

eventually can form a 3D grid-like structure, we aim at combining our seeding strategy with the automatic growth process underlying topology optimization.

CRediT authorship contribution statement

Junpeng Wang: Conceptualization, Methodology, Writing – review & editing, Software. **Christoph Neuhauser:** Methodology, Writing – review & editing, Software. **Jun Wu:** Conceptualization, Methodology. **Xifeng Gao:** Conceptualization, Methodology. **Rüdiger Westermann:** Conceptualization, Methodology, Writing – review & editing, Supervision, Funding acquisition.

Declaration of Competing Interest

The authors declare that they have no known competing financial interests or personal relationships that could have appeared to influence the work reported in this paper.

Acknowledgment

This work was supported in part by a grant from German Research Foundation (DFG) under grant number WE 2754/10-1. We acknowledge the help of Chunxiao Meng at Northwestern Polytechnical University and Yingjian Liu at The University of Texas at Dallas in adapting 3D-TSV to ANSYS and ABAQUS, respectively.

References

[1] Arora R, Jacobson A, Langlois TR, Huang Y, Mueller C, Matusik W, Shamir A, Singh K, Levin DIW. Volumetric michell trusses for parametric design & fabrication. Proceedings of the ACM symposium on computational fabrication. 2019. p. 1–13. https://doi.org/10.1145/3328939.3328999.

[2] Blinn JF. Models of light reflection for computer synthesized pictures. Proceedings of the 4th annual conference on computer graphics and interactive Techniques. New York, NY, USA: Association for Computing Machinery; 1977, ISBN 9781450373555. p. 192198. https://doi.org/10.1145/563858.563893.

[3] Bui HP, Tomar S, Courtecuisse H, Audette M, Cotin S, Bordas SPA. Controlling the error on target motion through real-time mesh adaptation: applications to deep brain stimulation. Int J Numer Method Biomed Eng 2018;34(5):e2958.

[4] Chen Y, Cohen J, Krolik J. Similarity-guided streamline placement with error evaluation. IEEE Trans Vis Comput Graph 2007;13(6):1448–55. https://doi.org/10.1109/TVCG.2007.70595.

[5] Daynes S, Feih S, Lu WF, Wei J. Optimisation of functionally graded lattice structures using isostatic lines. Materials & Design 2017;127:215–23. https://doi.org/10.1016/j.matdes.2017.04.082.

[6] Delmarcelle T, Hesselink L. Visualizing second-order tensor fields with hyperstreamlines. IEEE Comput Graph Appl 1993;13(4):25–33. https://doi.org/10.1109/38.219447.

[7] Delmarcelle T, Hesselink L. The topology of symmetric, second-order tensor fields. Proceedings visualization'94. IEEE; 1994. p. 140–7. https://doi.org/10.1109/VISUAL.1994.346326.

[8] Dick C, Georgii J, Burgkart R, Westermann R. Stress tensor field visualization for implant planning in orthopedics. IEEE Trans Vis Comput Graph 2009;15(6):1399–406. https://doi.org/10.1109/TVCG.2009.184.

[9] Gao X, Jakob W, Tarini M, Panozzo D. Robust hex-dominant mesh generation using field-guided polyhedral agglomeration. ACM Transactions on Graphics (TOG) 2017;36(4):1–13. https://doi.org/10.1145/3072959.3073676.

[10] Gao X, Shen H, Panozzo D. Feature preserving octree-based hexahedral meshing. Comput Graph Forum 2019;38(5):135–49. https://doi.org/10.1111/cgf.13795.

[11] Gerrits T, Rössl C, Theisel H. Glyphs for space-time jacobians of time-dependent vector fields. Journal of WSCG 2017.

[12] Hergl C, Blecha C, Kretzschmar V, Raith F, Günther F, Stommel M, Jankowai J, Hotz I, Nagel T, Scheuermann G. Visualization of tensor fields in mechanics. Computer Graphics Forum. Wiley Online Library; 2021. https://doi.org/10.1111/cgf.14209.

[13] Hesselink L, Levy Y, Lavin Y. The topology of symmetric, second-order 3d tensor fields. IEEE Trans Vis Comput Graph 1997;3(1):1–11. https://doi.org/10.1109/2945.582332.

[14] Hlawitschka M, Scheuermann G, Hamann B. Interactive glyph placement for tensor fields. International symposium on visual computing. Springer; 2007. p. 331–40. https://doi.org/10.1007/978-3-540-76858-6_33.

[15] Hotz I, Feng L, Hagen H, Hamann B, Joy K. Tensor field visualization using a metric interpretation. Visualization and processing of tensor fields. Springer; 2006. p. 269–81. https://doi.org/10.1007/3-540-31272-2_16.

[16] Jobard B, Lefer W. Creating evenly-spaced streamlines of arbitrary density. Visualization in scientific computing 1997. Springer; 1997. p. 43–55. https://doi.org/10.1007/978-3-7091-6876-9_5.

[17] Kanzler M, Ferstl F, Westermann R. Line density control in screen-space via balanced line hierarchies. Computers & Graphics 2016;61:29–39. https://doi.org/10.1016/j.cag.2016.08.001.

[18] Kindlmann G, Whalen S, Suarez RO, Golby AJ, Westin CF. Quantification of white matter fiber orientation at tumor margins with diffusion tensor invariant gradients. Proc. Intl. Soc. Mag. Reson. Med. vol. 16; 2008. p. 429.

[19] Kindlmann G. Superquadric tensor glyphs. Proceedings of the sixth joint Eurographics-IEEE TCVG conference on visualization. 2004. p. 147–54. https://doi.org/10.5555/2384225.2384248.

[20] Kindlmann G, Westin C-F. Diffusion tensor visualization with glyph packing. IEEE Trans Vis Comput Graph 2006;12(5):1329–36. https://doi.org/10.1109/TVCG.2006.134.

[21] Kratz A, Auer C, Stommel M, Hotz I. Visualization and analysis of second-order tensors: Moving beyond the symmetric positive-definite case. Computer Graphics Forum. vol. 32. Wiley Online Library; 2013. p. 49–74. https://doi.org/10.1111/j.1467-8659.2012.03231.x.

[22] Kratz A, Schoeneich M, Zobel V, Burgeth B, Scheuermann G, Hotz I, et al. Tensor visualization driven mechanical component design. 2014 IEEE Pacific Visualization Symposium. IEEE; 2014. p. 145–52. https://doi.org/10.1109/PacificVis.2014.51.

[23] Kwok T-H, Li Y, Chen Y. A structural topology design method based on principal stress line. Comput-Aided Des 2016;80:19–31. https://doi.org/10.1016/j.cad.2016.07.005.

[24] Lee E-J, El-Tawil S. FEMvrml: an interactive virtual environment for visualization of finite element simulation results. Adv Eng Software 2008;39(9):737–42. https://doi.org/10.1016/j.advengsoft.2007.10.006.

[25] Li Y, Liu Y, Xu W, Wang W, Guo B. All-hex meshing using singularity-restricted field. ACM Transactions on Graphics (TOG) 2012;31(6):1–11. https://doi.org/10.1145/2366145.2366196.

[26] Liu Z. A prototype framework for parallel visualization of large flow data. Adv Eng Software 2019;130:14–23. https://doi.org/10.1016/j.advengsoft.2019.02.004.

[27] Mattausch O, Theußl T, Hauser H, Gröller E. Strategies for interactive exploration of 3d flow using evenly-spaced illuminated streamlines. Proceedings of the 19th spring conference on computer graphics. 2003. p. 213–22. https://doi.org/10.1145/984952.984987.

[28] Oster T, Rössl C, Theisel H. Core lines in 3d second-order tensor fields. Comput Graphics Forum 2018;37(3):327–37. https://doi.org/10.1111/cgf.13423.

[29] Palacios J, Yeh H, Wang W, Zhang Y, Laramee RS, Sharma R, et al. Feature surfaces in symmetric tensor fields based on eigenvalue manifold. IEEE Trans Vis Comput Graph 2015;22(3):1248–60. https://doi.org/10.1109/TVCG.2015.2484343.

[30] Patel M, Laidlaw DH. Visualization of 3d stress tensor fields using superquadric glyphs on displacement streamlines. IEEE Trans Vis Comput Graph 2020. https://doi.org/10.1109/TVCG.2020.2968911.

[31] Qu B, Roy L, Zhang Y, Zhang E. Mode surfaces of symmetric tensor fields: topological analysis and seamless extraction. IEEE Trans Vis Comput Graph 2020;27(2):583–92. https://doi.org/10.1109/TVCG.2020.3030431.

[32] Raith F, Blecha C, Nagel T, Parisio F, Kolditz O, Günther F, et al. Tensor field visualization using fiber surfaces of invariant space. IEEE Trans Vis Comput Graph 2018;25(1):1122–31. https://doi.org/10.1109/TVCG.2018.2864846.

[33] Roy L, Kumar P, Zhang Y, Zhang E. Robust and fast extraction of 3d symmetric tensor field topology. IEEE Trans Vis Comput Graph 2018;25(1):1102–11. https://doi.org/10.1109/TVCG.2018.2864768.

[34] Schultz T, Kindlmann GL. Superquadric glyphs for symmetric second-order tensors. IEEE Trans Vis Comput Graph 2010;16(6):1595–604. https://doi.org/10.1109/TVCG.2010.199.

[35] Seltzer N, Kindlmann G. Glyphs for asymmetric second-order 2d tensors. Computer Graphics Forum. vol. 35. Wiley Online Library; 2016. p. 141–50. https://doi.org/10.1111/cgf.12890.

[36] Shepard D. A two-dimensional interpolation function for irregularly-spaced data. Proceedings of the 1968 23rd ACM national conference. 1968. p. 517–24. https://doi.org/10.1145/800186.810616.

[37] Stoll C, Gumhold S, Seidel H. Visualization with stylized line primitives. VIS 05. IEEE visualization, 2005.. 2005. p. 695–702. https://doi.org/10.1109/VISUAL.2005.1532859.

[38] Tam K-MM, Mueller CT. Stress line generation for structurally performative architectural design. 35th annual conference of the association for computer aided design in architecture. Cincinnati, Ohio, USA: ACADIA; 2015. doi:1721.1/125063.

[39] Turk G, Banks D. Image-guided streamline placement. Proceedings of the 23rd annual conference on computer graphics and interactive techniques. New York, NY, USA: Association for Computing Machinery; 1996, ISBN 0897917464. p. 453460. https://doi.org/10.1145/237170.237285.

[40] Ueng S-K, Sikorski C, Ma K-L. Efficient streamline, streamribbon, and streamtube constructions on unstructured grids. IEEE Trans Vis Comput Graph 1996;2(2):100110. https://doi.org/10.1109/2945.506222.

[41] Vilanova Bartroli A, Berenschot G, Van Pul C. DTI visualization with streamsurfaces and evenly-spaced volume seeding. Proceedings of the Joint Eurographics-IEEE TCVG symposium on visualization (VisSym04). vol. 19; 2004. p. 21.

[42] VOLPE G.. Streamlines and streamribbons in aerodynamics. 10.2514/6.1989-140.

[43] Wang J, Wu J, Westermann R. A globally conforming lattice structure for 2d stress tensor visualization. Computer graphics forum. vol. 39. Wiley Online Library; 2020. p. 417–27. https://doi.org/10.1111/cgf.13991.

[44] Weng W-C. Web-based post-processing visualization system for finite element analysis. Adv Eng Software 2011;42(6):398–407. https://doi.org/10.1016/j.advengsoft.2011.03.003.
[45] Wu J, Aage N, Westermann R, Sigmund O. Infill optimization for additive manufacturing – approaching bone-like porous structures. IEEE Trans Vis Comput Graph 2018;24(2):1127–40. https://doi.org/10.1109/TVCG.2017.2655523.
[46] Wu J, Wang W, Gao X. Design and optimization of conforming lattice structures. IEEE Trans Vis Comput Graph 2021;27(1):43–56. https://doi.org/10.1109/TVCG.2019.2938946.
[47] Ye X, Kao D, Pang A. Strategy for seeding 3d streamlines. VIS 05. IEEE visualization, 2005. IEEE; 2005. p. 471–8. https://doi.org/10.1109/VISUAL.2005.1532831.
[48] Yu H, Wang C, Shene C-K, Chen JH. Hierarchical streamline bundles. IEEE Trans Vis Comput Graph 2011;18(8):1353–67. https://doi.org/10.1109/TVCG.2011.155.
[49] Zheng X, Pang A. Topological lines in 3d tensor fields. IEEE visualization 2004. IEEE; 2004. p. 313–20. https://doi.org/10.1109/VISUAL.2004.105.
[50] Zobel V, Scheuermann G. Extremal curves and surfaces in symmetric tensor fields. Vis Comput 2018;34(10):1427–42. https://doi.org/10.1007/s00371-017-1450-1.
[51] Zöckler M, Stalling D, Hege H-C. Interactive visualization of 3d-vector fields using illuminated stream lines. Proceedings of the 7th conference on visualization '96. Washington, DC, USA: IEEE Computer Society Press; 1996, ISBN 0897918649107ff.. https://doi.org/10.1109/VISUAL.1996.567777.

Structural and Multidisciplinary Optimization (2022) 65:92
https://doi.org/10.1007/s00158-022-03186-0

RESEARCH PAPER

Stress topology analysis for porous infill optimization

Junpeng Wang[1] · **Jun Wu**[2] · **Rüdiger Westermann**[1]

Received: 21 August 2021 / Revised: 21 January 2022 / Accepted: 24 January 2022 / Published online: 16 February 2022

Abstract
The optimization of porous infill structures via local volume constraints has become a popular approach in topology optimization. In some design settings, however, the iterative optimization process converges only slowly, or not at all even after several hundreds or thousands of iterations. This leads to regions in which a distinct binary design is difficult to achieve. Interpreting intermediate density values by applying a threshold results in large solid or void regions, leading to sub-optimal structures. We find that this convergence issue relates to the topology of the stress tensor field that is simulated when applying the same external forces on the solid design domain. In particular, low convergence is observed in regions around so-called trisector degenerate points. Based on this observation, we propose an automatic initialization process that prescribes the topological skeleton of the stress field into the density field as solid simulation elements. These elements guide the material deposition around the degenerate points, but can also be remodelled or removed during the optimization. We demonstrate significantly improved convergence rates in a number of use cases with complex stress topologies. The improved convergence is demonstrated for infill optimization under homogeneous as well as spatially varying local volume constraints.

Keywords Topology optimization · Porous infill · Stress tensor

1 Introduction

Topology optimization aims at finding the optimal structural layout under relevant design specifications. Topology optimization of multi-scale structures, which dates back to the seminal paper by Bendsøe and Kikuchi (1988), has been a topic of great interest in recent years. The rapid development in this field is partially stimulated by the possibility to fabricate complex structures using additive manufacturing. For an overview of topology optimization approaches for designing multi-scale structures, we refer readers to a recent review article by Wu et al. (2021a).

It has been shown that density-based topology optimization for compliance minimization, under local volume constraints, creates porous infill structures similar to those found in bone (Wu et al. 2018). These bone-mimicking porous structures are lightweight, robust regarding material damages and loading variations, and stable with respect to buckling. The local volume constraints work similarly to maximum length scale control (Guest 2009). They prevent the forming of large solid regions and, consequently, create porous structures distributed more evenly over the design domain. This approach has been extended, in conjunction with a coating approach proposed by Clausen et al. (2015), to design concurrently structures and porous sub-structures therein, referred to as shell-infill composites (Wu et al. 2017). It has also been applied to design porous shell structures (Träff et al. 2021). Other notable extensions include the design of porous structures with gradation in the porosity and pore size (Schmidt et al. 2019; Das and Sutradhar 2020), use of multiple materials (Li et al. 2020; Zhao and Zhang 2021), and fiber-reinforced structures (Li et al. 2021). Besides by density-based approaches, porous infill structures have been designed using an evolutionary design approach (Qiu et al. 2020) and machine learning (Cang et al. 2019).

In this paper, we investigate the convergence behavior of density-based topology optimization with local volume constraints under a single load case. In density-based topology

Responsible Editor: Axel Schumacher

✉ Jun Wu
j.wu-1@tudelft.nl

[1] Computer Graphics and Visualzation, Technical University of Munich, Munich, Germany

[2] Department of Sustainable Design Engineering, Delft University of Technology, Delft, The Netherlands

optimization, an important convergence criterion is that the optimized density field converges to a binary or so-called black-white design, i.e., the pseudo density is close to 1 or 0. A few hundred iterations or even more are not uncommon to achieve black-white designs (Wu et al. 2017). To improve the convergence rate, a typical solution is to apply a continuation scheme where parameters are updated after a certain number of iterations. However, in some optimization scenarios under local volume constraints, we have observed that certain regions fail to converge to a binary design even after thousands of iterations (see Fig. 1). Interpreting these intermediate density values by applying a threshold results in large solid or void regions, leading to sub-optimal structures.

To analyze the regions where low convergence is observed, we investigate the stress distribution in these regions via trajectory-based visualization (Wang et al. 2020). In particular, we shed light on the relationship between the convergence behavior and the principal stress directions that occurs when simulating on the solid design domain. This approach is inspired by previous work on infill optimization, where uniformly seeded tensor glyphs have confirmed good agreement between the optimized porous infill and the principal stress directions in the solid under load (Wu et al. 2018). In this paper, we exploit advanced mechanisms to perform a topology-based analysis of the stress field, including the use of *degenerate points* and *topological skeletons*. At a degenerate point, the principal stress directions cannot be decided, yet a set of hyperbolic and parabolic sectors exist in its surrounding, in which similar patterns of neighboring trajectories are observed (Delmarcelle and Hesselink 1994). The topological skeleton consists of the boundaries between adjacent sectors—so-called separatrices—and indicates pathways along which the forces are steered towards the degenerate points. In topology optimization, degenerate points have been used to indicate locations where integrability conditions are violated and consistent domain parameterizations cannot be computed (Stutz et al. 2020).

When applying topology analysis to the stress tensor field, it reveals that low convergence occurs around a special type of degenerate points, known as trisectors. Notably, such degenerate points do not always appear, but if so, low convergence is often observed in their surrounding. Due to the isotropy of the stress tensor close to a trisector, the principal stress directions and, thus, a locally consistent binary material layout cannot be decided by the optimizer. In our work, we propose an automatic pre-process that supports the optimizer in finding such a layout, resulting in significantly improved convergence rates in settings where trisectors are paramount. In particular, we build upon the efficient

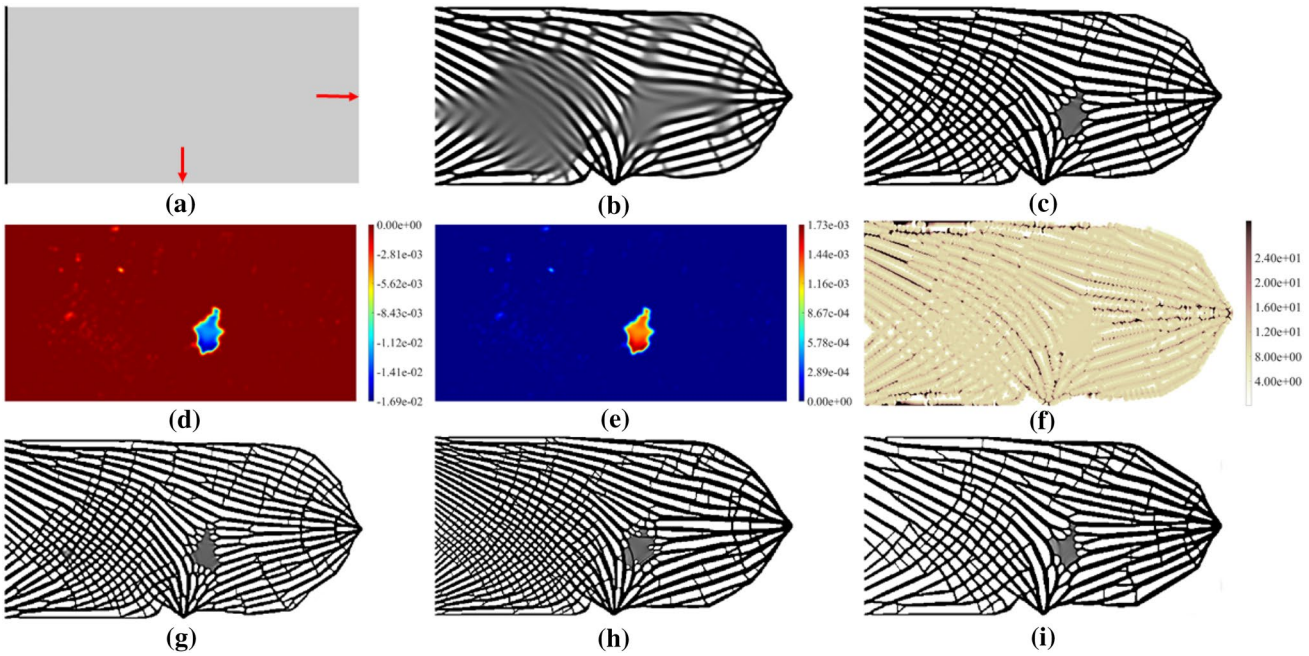

Fig. 1 **a** Illustration of the design domain (500x250 simulation elements) and boundary conditions. **b**, **c** The density distributions after 250 and 1000 iterations, respectively, from topology optimization under local volume constraints. Design parameters are $\alpha_e = 0.6$, $R_e = 18$ and $r_e = 4.5$. **d**, **e**, **f** The sensitivities at 1000 iterations, of the objective $\frac{\partial c}{\partial \rho}$, the constraint $\frac{\partial g}{\partial \rho}$, and $-\frac{\partial c}{\partial \rho} / \frac{\partial g}{\partial \rho}$. **g**, **h**, **i**. The optimized density fields under different parameter settings: **g** $R_e = 12$. **h** $r_e = 2.6$, R_e varies linearly from 8 to 24, from the left to right side of the design domain. **i** α_e varies linearly from 0.4 to 0.7, from the left to right side of the design domain. All other parameters are kept the same as in (**b**) and (**c**)

computation of degenerate point locations and separatrices, and prescribe an initial density field where elements along the separatrices are solid and all other elements take an intermediate value (i.e., the local volume upper bound). The solid elements along the separatrices can be changed over the course of the optimization to improve the structural performance, yet we observe that the optimization keeps them more or less unchanged and changes element densities in other parts accordingly. In the vicinity of trisectors, the initialization guides the optimizer towards a stable binary design and enables the optimization process to quickly converge towards a sound global layout. Interestingly, even though one might expect that the imposed initialization biases the optimizer towards a less stiff local optimum, the resulting binary designs show the same or even improved compliance compared to the designs generated by the original approach which exhibit unresolved intermediate density values in the presence of trisectors.

The remainder of this paper is organized as follows. In Sect. 2, we first review the problem formulation underlying porous infill optimization. Then, in Sect. 3 we analyse the convergence of porous infill optimization, elaborate on the relationships between optimization convergence and the existence of degenerate points in the stress field, and propose topology-guided density initialization to counteract low optimization convergence. The implementation details of performing the topology analysis to the stress tensor field are discussed in Sect. 4. We demonstrate the effectiveness of our approach in a variety of experiments in Sect. 5. Section 6 concludes the paper with a discussion of the proposed approach as well as future research directions.

2 Porous infill optimization

The low convergence in some design tasks is observed while using the infill optimization approach (Wu et al. 2018), on which and some of its extensions the effectiveness of our method will be demonstrated. For the sake of completeness, we briefly review the formulation of the density-based infill optimization with local volume constraints.

2.1 Local volume constraints

In a discretized design domain, the local volume ($\bar{\rho}_e$) of a circular region centered at the centroid of an element, x_e, is computed by

$$\bar{\rho}_e = \frac{\sum_{i \in N_e} \rho_i}{\sum_{i \in N_e} 1}, \quad N_e = \{i | \parallel x_i - x_e \parallel_2 \leq R_e\}, \ \forall e, \tag{1}$$

where $\rho_i \in [0, 1]$ is the pseudo density for the i-th element. R_e denotes the radius of the region on which the local volume is measured.

An upper bound (α_e, $0 < \alpha_e < 1$) is imposed on the local volume of each element in the design domain, i.e.,

$$\bar{\rho}_e \leq \alpha_e. \tag{2}$$

Thus, the local volume constraint involves two parameters, R_e and α_e. R_e indirectly controls the spacing between substructures, and α_e effectively controls the porosity (Wu et al. 2018). In the original approach, both input fields are prescribed to be homogeneous. Recent developments have demonstrated the use of heterogeneous fields to generate gradations of the porosity and pore size of the optimized porous structures (Schmidt et al. 2019; Das and Sutradhar 2020; Zhao and Zhang 2021).

Assigning a local volume constraint to each element results in a large number of constraints that need to be considered by the optimizer. Dividing both sides of Eq. 2 by α_e, these constraints are aggregated by the $p-$mean function,

$$\left(\frac{1}{n} \sum_e \left(\frac{\bar{\rho}_e}{\alpha_e} \right)^p \right)^{\frac{1}{p}} \leq 1, \tag{3}$$

where n is the number of elements. $p = 16$ is found to give a good approximation, and is used in this paper.

2.2 Optimization problem

With the local volume constraint defined, the optimization problem is given by

$$\min_{\boldsymbol{\phi}} \quad c = \frac{1}{2} \boldsymbol{U}^T \boldsymbol{K} \boldsymbol{U}, \tag{4}$$

$$\text{s.t.} \quad \boldsymbol{K}\boldsymbol{U} = \boldsymbol{F}, \tag{5}$$

$$g(\boldsymbol{\phi}) = \left(\frac{1}{n} \sum_e \left(\frac{\bar{\rho}_e}{\alpha_e} \right)^p \right)^{\frac{1}{p}} - 1 \leq 0, \tag{6}$$

$$\phi_e \in [0.0, \ 1.0], \ \forall e. \tag{7}$$

Here the objective is to minimize the compliance, measured by the strain energy c. $\boldsymbol{K}$ is the stiffness matrix in finite element analysis. $\boldsymbol{U}$ is the displacement vector, obtained by solving the static elasticity equation (Eq. 5), where $\boldsymbol{F}$ is the loading vector. $g(\boldsymbol{\phi})$ represents the aggregated local volume constraint.

The formulation takes ϕ_e as the design variable. The pseudo density field ($\boldsymbol{\rho}$) is computed from $\boldsymbol{\phi}$ by a density filter ($\boldsymbol{\phi} \rightarrow \tilde{\boldsymbol{\phi}}$), followed by a smoothed Heaviside projection

($\tilde{\boldsymbol{\phi}} \rightarrow \boldsymbol{\rho}$). The density filter, with a filter radius r_e smaller than R_e (Eq. 1), avoids checkerboard patterns resulting from numerical instabilities. The associated equations of this standard operator are omitted here but can be found in e.g., (Wang et al. 2011; Wu et al. 2018). The purpose of the projection $\tilde{\boldsymbol{\phi}} \rightarrow \boldsymbol{\rho}$ is to promote a 0-1 solution, by thresholding at the value of $\frac{1}{2}$,

$$\rho_e(\tilde{\phi}_e) = \frac{\tanh(\frac{\beta}{2}) + \tanh(\beta(\tilde{\phi}_e - \frac{1}{2}))}{2\ \tanh(\frac{\beta}{2})}. \tag{8}$$

The smoothed Heaviside function has a parameter, β, to control its sharpness. For improving convergence behaviour, a continuation scheme is applied to gradually increase its sharpness, i.e., we start with $\beta = 1$ and double its value every 40 iterations until it reaches 128.

To interpolate the Young's modulus for intermediate densities, we use the modified SIMP (Solid Isotropic Material with Penalization) model,

$$E_e(\rho_e) = E_{min} + \rho_e^{\gamma}(E_0 - E_{min}), \tag{9}$$

where E_0 is the Young's Modulus of a fully solid element. E_{min} is a minimum Young's modulus ($E_{min} = 1.0e^{-6}E_0$ in our test), introduced to avoid the singularity of the global stiffness matrix. γ is the penalization factor, which is typically set to 3. $E_e(\rho_e)$ is the interpolated Young's Modulus of the element with density ρ_e.

The commonly used global volume constraint is not included here, but can be added as an additional constraint. An example of incorporating both local and global volume constraints is shown in Fig. 9 in the results section. The average of local volume fractions, i.e., $\frac{\sum_e \alpha_e}{\sum_e 1}$, gives an estimation of the global volume fraction of the resulting optimized structure. To precisely control the global volume without resorting to an explicit global volume constraint, one may apply a continuation scheme, i.e., adjusting the local volume bound towards the end of optimization. Suppose the intended global volume fraction is α_{global}. The local volume bound can be scaled by $\alpha_e^{new} = \frac{\sum_e \alpha_{global}}{\sum_e \rho_e}\alpha_e$.

The optimization problem is solved using the method of moving asymptotes (MMA) (Svanberg 1987). In all experiments performed in this work, the move limit of design variables is set to 0.01 unless specified otherwise.

3 Convergence analysis and improvement

When applying topology optimization using local volume constraints, in some scenarios it is observed that the iterative optimization process converges very slowly. When inspecting such scenarios in more detail, for instance, by visualizing the density distribution of the intermediate designs, it turns out that in some regions even after several hundreds or thousands of iterations a distinct binary design cannot be achieved by the optimizer. One of such scenarios is shown in Fig. 1. The rectangular design domain is fixed on its left edge. A unit load is applied on the right, while another unit load on the bottom, both in the middle of the edges. In Fig. 1b, i.e., optimization after 250 iterations, two large grey regions can be observed. While the grey region on the left converges to a binary design after another 250 iterations, the grey region on the right does not result in a binary design even after a few thousands iterations. Applying a threshold to the intermediate densities to set them to either 0 or 1 results in large void or solid regions with sub-optimal mechanical properties or use of material.

To further analyze the cause of slow convergence, we examine the sensitivities at the 1000 iterations. In Fig. 1d, the plot of $\frac{\partial c}{\partial \rho}$, the region where low convergence is observed has a high absolute sensitivity, meaning that an increase in density shall be favored for reducing the objective. However, an increase of density in this region will greatly violate the aggregated local volume constraint, as can be seen in Fig. 1e, the plot of $\frac{\partial g}{\partial \rho}$. Shown in Fig. 1f is $-\frac{\partial c}{\partial \rho}/\frac{\partial g}{\partial \rho}$, a metric similarly used for deriving a fix-point type update scheme with the optimality criteria (Sigmund 2001). It can be seen that in the low convergence region the ratio is rather homogeneous and does not indicate a clear density update strategy.

3.1 Relationship between convergence and stress

Prior work in infill optimization has shown that the optimized porous structure is in many regions according to the principal stress directions that occur in the solid design domain under equal boundary conditions and external loads. At each point in a 2D solid under load, the stress state is fully described by the stress vectors for two mutually orthogonal orientations. The second-order stress tensor

$$S(x, y) = \begin{bmatrix} \sigma_{xx} & \tau_{xy} \\ \tau_{xy} & \sigma_{yy} \end{bmatrix}_{(x,y)} \tag{10}$$

contains these vectors for the axes of a Cartesian coordinate system. σ_{xx} and σ_{yy} are the normal stress components along the x and y directions, respectively, τ_{xy} is the shear stress component.

S is symmetric since the shear stresses given by the off-diagonal elements in S are equal on mutually orthogonal lines. The principal stress directions of the stress tensor indicate the two mutually orthogonal directions along which the shear stresses vanish. These directions are given by the eigenvectors of S, with magnitudes given by the corresponding eigenvalues σ_1 and σ_2 of S. For $\sigma_1 \geq \sigma_2$, σ_1 is called the major principal stress, and σ_2 the minor

principal stress. Accordingly, the corresponding eigenvectors v_1 and v_2 are called major and minor principal stress directions. The signs of the principal stress magnitudes classify the stresses into tension (positive sign) or compression (negative sign). However, since there are two principal stresses acting at each point, the classification is with respect to a specific direction.

Figure 2a shows a tensor glyph-based visualization of the stress field, corresponding to the scenario in Fig. 1. Here, the stress tensors are represented by oriented ellipses. The axes of the ellipses are oriented according to the eigenvectors of the stress tensor, and the lengths of their radii are determined by the eigenvalues. The colors of axes indicate the sign of the principal stresses, red for positive and green for negative values. Figure 1b, i.e., optimization after 250 iterations, has two large grey regions. Comparing it with Fig. 2a, it can be seen that the grey region on the left corresponds to $\sigma_1 \approx -\sigma_2$, and the one on the right corresponds to $\sigma_1 \approx \sigma_2$. While after a few hundred more iterations (see Fig. 1c) the grey region on the left converges to a binary design, the grey region on the right shrinks but remains visible. In these regions, the optimizer can favour material growths either along the major or the minor principal stress direction, and it seems that because no preferential direction is present the optimizer has problems to decide for any of them. In the regions where the optimizer doesn't converge, however, another specific property can be perceived in addition to isotropic stress. As indicated by principal stress lines (PSLs), which are computed by performing numerical integration along the major and minor principal stress directions (see Fig. 2b), these regions seem to cover locations where the PSLs indicate directional discontinuities in the tensor field. This observation gives rise to a stress topology-based analysis of the optimization convergence, which we provide in the following.

3.2 Stress topology-based analysis

Topology analysis of 2D symmetric second-order tensor fields (e.g., stress tensor fields) has been introduced in the seminal work of Delmarcelle and Hesselink (1994). The topology of a 2D stress tensor field is composed of its *degenerate points* and the corresponding *topological skeleton*. At a degenerate point, the stress tensor has repeating eigenvalues, i.e., $\sigma_1 = \sigma_2$, meaning that the major and minor stress directions cannot be decided. The topological skeleton is given by principal stress lines—so-called separatrices—that start from degenerate points.

An isolated degenerate point can be classified by the winding number of one of the eigenvector fields on a loop surrounding the degenerate point. Delmarcelle and Hesselink (Delmarcelle and Hesselink 1994) proposed an invariant to perform this classification in a stable way. In Sect. 4, we describe how the degenerate points are computed and classified for a stress tensor field given at the vertices of a Cartesian grid. A major/minor separatrix is a principal stress line starting at a degenerate point and following the major/minor eigenvector field. Let us also refer to Sect. 4 for a discussion of how to determine these directions. Figure 2c illustrates the major and minor separatrices in the stress field corresponding to the used test scenario in Fig. 1.

At a trisector there are three separatrices in the major (and three in the minor) principal direction field that divide the neighborhood into three sectors sharing this point. Around a wedge there can be either one sector or three sectors. In a sector, similar stress trajectories in the major and minor principal stress direction fields are observed. Figure 2c, as well as all other experiments we have performed, indicate that the regions where convergence cannot be achieved are always centered around a trisector, while wedges seem to have no influence on the convergence rate. Furthermore, regions where the convergence rate is low but the optimizer can eventually arrive at a stable binary design do not contain any degenerate point (Fig. 1b, left). These regions have

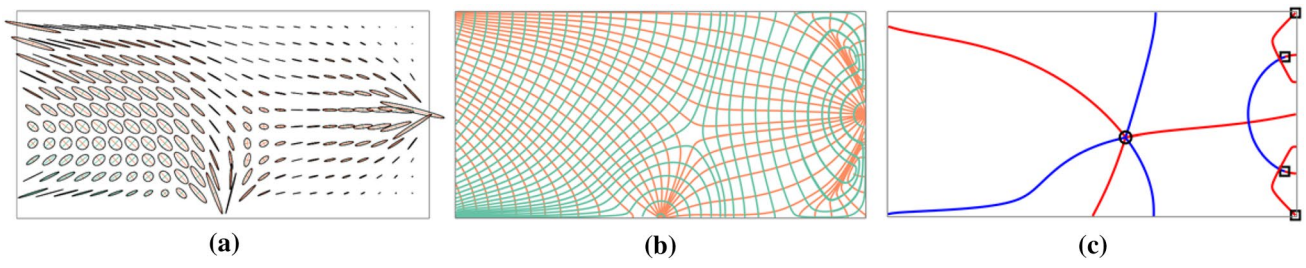

Fig. 2 Stress tensor field visualizations. The stress tensor field is according to the scenario shown in Fig. 1a, when simulating on the solid design domain. **a** Tensor glyphs are drawn at sampled vertices of the Cartesian simulation grid. Colors indicate the sign of the principal stresses, red for positive and green for negative values. **b** Trajectory-based visualization. Orange and turquoise trajectories represent the major and minor principal stress directions, respectively. **c** Topology-based visualization. The circle and quads indicate the trisector and wedge degenerate points, respectively, which are connected via the major (red) and minor (blue) topological skeletons

major and minor principal stresses that are close in their magnitudes but differ in signs, i.e., $\sigma_1 \approx -\sigma_2$, yet in these regions there are no topological changes in the stress field. In Fig. 3, we give two more examples which verify our observations, and clearly indicate the relationships between low convergence and existence of trisectors.

The topological skeletons can be perceived as limits of the principal stress lines close to the boundary between different stress regions. We hypothesize that the porous structures in regions where convergence is not achieved, if a stable binary design should be enforced, follow these skeletons, just as porous structures in other regions follow the principal stress directions. To validate this hypothesis, our idea is to guide the material deposition along the topological skeleton via a skeleton-based initialization of the density field. The initialization sets the optimizer to a state in which a stable binary design in the regions around trisectors is prescribed. The design can be changed during the course of the optimization, yet our experiments demonstrate that the optimizer maintains this design and builds additional support structures around it. These results empirically proof the validity of our hypothesis, and they indicate that the deviation from the prescribed skeleton is not favorable for the objective function.

3.3 Stress topology-guided initialization

Typically in density-based topology optimization, the density field is initialized with a constant value. For infill optimization, the constant is chosen as the local volume upper bound. In accordance to the observation that the material layout in porous infill optimization is guided by the principal stress directions, we propose to augment the initialization by setting the densities of elements close to the topological skeleton to a high value. This strategy is fully automatic, since the computation of neither the degenerate points nor the topological skeleton does involve any user intervention.

To generate the initial material layout, the elements which are near the topological skeleton are identified first. In the current implementation, all elements that are touched by any of the PSLs belonging to the skeleton are identified. Then, the initial volume fraction of these elements is set to solid at the beginning of the optimization process. In this way, the initial density field around a trisector degenerate point becomes inhomogeneous, giving rise to sensitivities favoring a unique topology layout. It is worth noting that these pre-embedded solid elements are not passive elements but still belong to the design space, i.e., the density at these elements can be adjusted by the optimizer if a stiffer design can be achieved. Figure 4 shows the initial density fields that are used in the test cases 'Cantilever', 'Bracket' and 'Bearing'.

The proposed initialization process can be integrated into porous infill optimization in a fully automated way. Once the design domain, material parameters, fixations and external load conditions are given, the following steps are performed:

(1) Finite element analysis to compute the stress field in the fully solid design domain.
(2) Topology analysis including the computation of all trisector degenerate points and the topological skeleton containing these points.
(3) Initialization of the density field according to the topological skeleton.

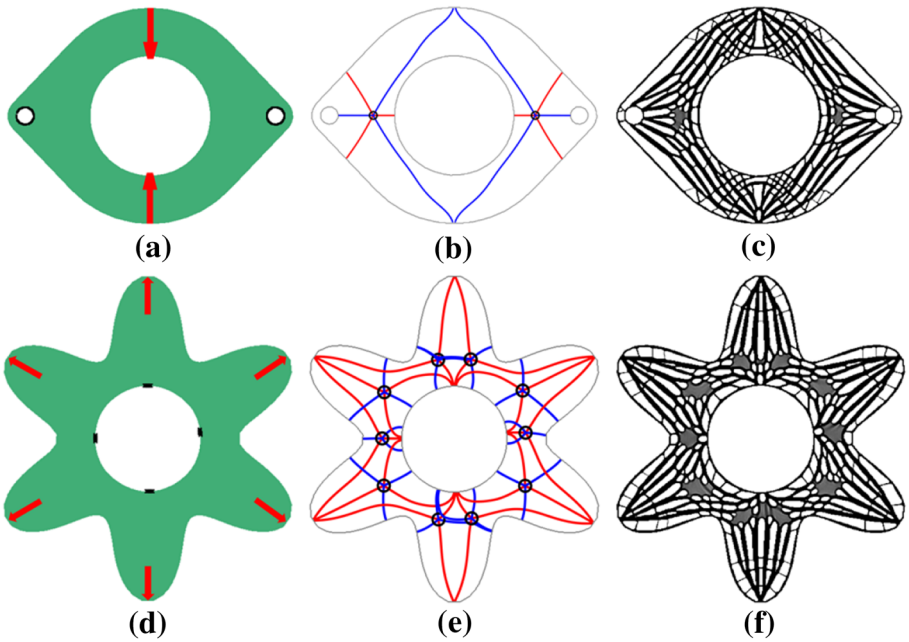

Fig. 3 Design domains and boundary conditions of models 'Bracket' (**a**) and 'Bearing' (**d**) using Cartesian simulation grids of resolutions 512×400 and 512×512, respectively. **b e** Trisector degenerate points and the corresponding topological skeletons. **c**, **f** Density distributions after 1000 optimization iterations with $\alpha_e = 0.6$, $R_e = 18$ and $r_e = 4.5$

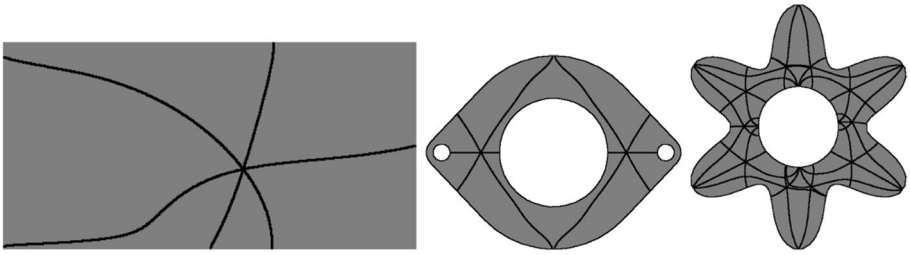

Fig. 4 The initialized density fields of the 'cantilever' in Fig. 1 and 'Bracket' and 'Bearing' in Fig. 3

(4) Topology optimization using local volume constraints for porous infill optimization.

4 Implementation details

In the following, we discuss the computation of the locations of degenerate points in a given Cartesian simulation grids, as well as the computation of the topological skeleton that is required to initialize the density field. Given the definition of degenerate points, a degenerate point can be located by solving the following system of equations:

$$\begin{aligned} &\sigma_{xx}(x^*, y^*) - \sigma_{yy}(x^*, y^*) = 0, \\ &\tau_{xy}(x^*, y^*) = 0, \end{aligned} \tag{11}$$

where (x^*, y^*) denotes the coordinates of the point to be solved for. Here we consider the general situation in topology optimization, i.e., the finite element analysis is performed using axis-aligned quadrilateral finite elements with bilinear shape functions. Thus, each element has four nodes that coincide with the element's vertices, and the values at the nodes are bilinearly interpolated within the element. Then, Eq. 11 becomes a non-linear system of equations, which can be solved by the Newton-Raphson method.

Since degenerate points usually appear only in a few elements, an efficient way is required to test whether a cell can contain such a point and needs to be further analysed, or can be excluded right away. Therefore, each element is first classified according to the following conditions:

$$\begin{aligned} &\sigma_{xx}(x_i, y_i) - \sigma_{yy}(x_i, y_i) > 0, \quad i = 1:4 \quad \text{or} \\ &\sigma_{xx}(x_i, y_i) - \sigma_{yy}(x_i, y_i) < 0, \quad i = 1:4 \quad \text{or} \\ &\tau_{xy}(x_i, y_i) > 0, \quad i = 1:4 \quad \text{or} \\ &\tau_{xy}(x_i, y_i) < 0, \quad i = 1:4 \end{aligned} \tag{12}$$

where (x_i, y_i), $i = 1:4$ refers to the four nodal coordinates of a finite element. It can be easily shown that an element cannot contain a degenerate point if any of the conditions in Eq. 12 is true. If none of the conditions is true, the element needs to be further analyzed to locate a degenerate point in its interior. Figure 5 shows a possible distribution of the eigenvalues corresponding to the major and minor principal stress directions in a quadrilateral simulation element containing a degenerate point.

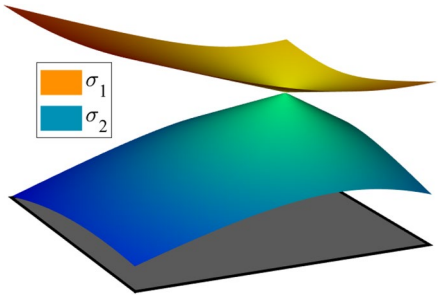

Fig. 5 The eigenvalues corresponding to the major (σ_1) and minor (σ_2) principal stress direction are shown as height fields over the domain of a simulation element (grey square). At a degenerate point, both eigenvalues have the same value

In a symmetric second tensor field, two types of stable degenerate points exist: trisectors and wedges. They are indicated by characteristic patterns of the PSLs in their vicinity, and are determined from the so-called tensor gradients (see Delmarcelle and Hesselink (1994) for a comprehensive derivation). First, the partial derivatives of the tensor are introduced as

$$\begin{aligned} a &= \frac{1}{2}\frac{\partial(\sigma_{xx}-\sigma_{yy})}{\partial x} \qquad b = \frac{1}{2}\frac{\partial(\sigma_{xx}-\sigma_{yy})}{\partial y} \\ c &= \frac{\partial \tau_{xy}}{\partial x} \qquad\qquad d = \frac{\partial \tau_{xy}}{\partial y} \end{aligned} \tag{13}$$

These derivatives are then used to compute the invariant under rotation

$$\delta = ad - bc. \tag{14}$$

The sign of δ determines the type of the degenerate point. I.e., a trisector degenerate point is indicated by $\delta < 0$, and a wedge degenerate point is indicated by $\delta > 0$. At a trisector degenerate point, there are three major and three minor separatrices starting from this point. In contrast, two separatrices start from a wedge, one coincides with the major PSL and the other one with the minor PSL (see Fig. 2c). These separatrices are termed the topological skeleton of a stress tensor field, i.e., the topological skeleton is composed of the PSLs starting from the degenerate points. Compared to the PSLs

not belonging to the topological skeleton, the tangent of the topological skeleton at the degenerate point is not unique, since there is an infinite set of principal stress directions at such points. To solve this problem, Delmarcelle and Hesselink (1994), propose that the tangents to the topological skeleton at the degenerate points are the real root(s) of the cubic equation

$$dx^3 + (c + 2b)x^2 + (2a - d)x - c = 0. \tag{15}$$

5 Results and discussions

In this section, we use several examples to demonstrate the effectiveness of the proposed initialization for density-based porous infill optimization. The initialization and optimization are both implemented in Matlab. The initialization involves a finite element analysis, followed by a stress topology analysis and computation of the topological skeleton. Running on a desktop PC with an Intel Xeon CPU at 3.60GHz, the initialization in our experiments took less than 2 seconds. All design domains are discretized by Cartesian finite element grids with unit size simulation elements. The Young's Modulus and Poisson's ratio are set to 1.0 and 0.3, respectively. Convergence improvement is quantified by the sharpness measurement

$$s = \frac{4}{n} \sum_e \rho_e (1 - \rho_e) \tag{16}$$

A small value of s indicates a sharper binary design of the optimized topology.

Figure 6 shows the binary designs that are generated using an initialization by topological skeleton. The same parameter settings as in Fig. 1 are used here. As can be seen, in all cases a binary design is achieved regardless of the area of the region around the degenerate point where convergence is not achieved by the original approach. Figure 7 compares the intermediate density distributions during the optimization using a uniform density initialization and the proposed topology-guided density initialization. Table 1 compares the mechanical properties of the designs generated by both approaches, as well as the used material and the sharpness (cf. Eq. 16) of the designs after 1000 optimization iterations. Notably, even after some thousands of iterations convergence cannot be reached via original porous infill optimization. As can be seen from the sharpness values, the proposed initialization strategy improves the convergence behavior of porous infill optimization considerably. In all test cases, a distinct binary design has been reached within the given number of iterations. The difference in compliance and material fraction is rather small.

Figure 8 shows the converged density distributions of the 'Bracket' and 'Bearing', obtained using the topology-guided initialization strategy. Low convergence regions from the original approach (cf. Fig. 3) are removed. The convergence is again confirmed by a reduction in the sharpness value. In the 'Bearing' result from the original approach (cf. Fig. 3f) the area of the low convergence regions is large. In this case, the sharpness value is reduced by an order of magnitude by

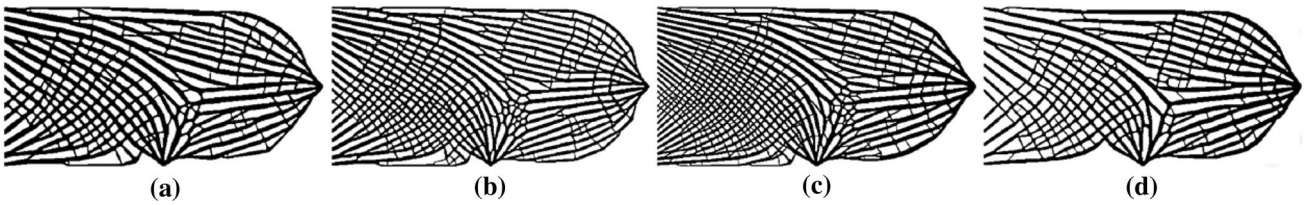

Fig. 6 Binary designs by porous infill optimization with stress topology-guided density initialization. The same parameter settings as in Fig. 1c, g, h and i, respectively, are used. A quantitative comparison is given in Table 1

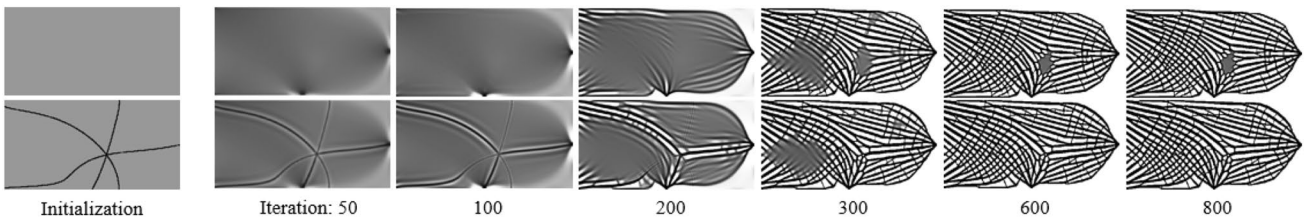

Fig. 7 Intermediate density distributions of the results in Fig. 1c (top, using a uniform density initialization) and Fig. 6a (bottom, using the proposed topology-guided density initialization)

Table 1 Quality and convergence comparison. Each pair of rows shows the compliance, the fraction of solid material, and the sharpness of the resulting designs when using porous infill optimization without (top) and with (bottom) stress topology-guided density initialization

Cases	Compliance	Solid fraction	Sharpness
Fig. 1c	27.99	0.479	1.8×10^{-2}
Fig. 6a	28.26	0.473	5.4×10^{-3}
Fig. 1g	27.37	0.501	1.1×10^{-2}
Fig. 6b	27.63	0.497	1.1×10^{-3}
Fig. 1h	35.49	0.377	1.0×10^{-2}
Fig. 6c	35.76	0.379	5.4×10^{-3}
Fig. 1i	27.98	0.482	1.2×10^{-2}
Fig. 6d	28.47	0.480	1.3×10^{-3}
Fig. 3c	19.15	0.490	1.7×10^{-2}
Fig. 8a	19.32	0.482	5.8×10^{-3}
Fig. 3f	45.67	0.515	6.6×10^{-2}
Fig. 8b	45.49	0.504	4.8×10^{-3}

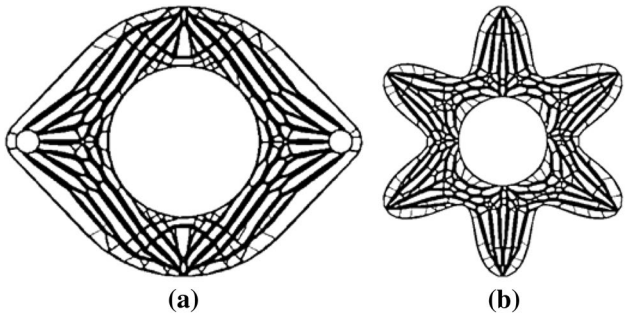

Fig. 8 The binary designs that are generated by stress topology-guided porous infill optimization for 'Bracket' (**a**) and 'Bearing' (**b**) from Fig. 3

the proposed initialization. It leads to a stiffer structure with less material consumption.

We further test the applicability of the proposed initialization on topology optimization with both local and global volume constraints. The global volume constraint is

$$\frac{1}{n}\sum_{e}\rho_e - \alpha_{global} \leq 0. \tag{17}$$

The test is performed on a square where its four corners are loaded (Fig. 9a), an example taken from Stutz et al. (2020). This example has two trisectors, as shown in Fig. 9b. From Fig. 9c, it can be seen that the central region is largely grey after 1000 optimization iterations. The grey region disappears in the optimized result from the proposed initialization (Fig. 9d). The significant improvement in convergence can be seen from the evolution of density distributions shown in Fig. 9 and the plot of the sharpness over iterations, shown in Fig. 10(right). As the large grey region is replaced by a binary design, the material consumption reduces from 0.400 to 0.378 and the compliance value decreases marginally from 26.02 to 25.96.

In density-based topology optimization, distributed loads are known to be a source of potential low convergence. Fig. 11a sketches a disk with radially compression forces applied on its boundary. Eight vertices equally-spaced on the boundary are fixed in both x- and y-axis, indicated by small triangles. The topological skeleton of the stress field is visualized in Fig. 11b, while the stress field is visualized using tensor glyphs in Fig. 11c. From the visualizations it can be seen that the stress field has a complex topology, and that the stress tensors in the middle are isotropic and exhibit a tiny spatial gradient. This is a challenging case for infill optimization with a uniform density initialization (Fig. 11d). Figure 11e shows the optimized infill using the proposed topology-guided density initialization. The density distributions during the optimization are shown at the bottom. This example demonstrates the effectiveness of the proposed initialization in the case of distributed loads.

Interestingly, under certain design specifications, the original approach is able to create binary designs at the presence of degenerate points. This happens if the specified local volume bound is small. Figure 12a shows the cantilever example optimized with a uniform density initialization under $\alpha_e = 0.4$ (reduced from $\alpha_e = 0.6$ in previous examples). It is not precisely known how the different local volume bounds triggered the different convergence behavior. The proposed topology-guided density initialization is effective for small local volume bounds (Fig. 12b). In this case, the sharpness values of results from both initialization strategies are very close. The one with the proposed initialization leads to a slightly larger compliance (104.6%), while consuming 5.6% less material. From the intermediate density distributions shown in the following two rows, a noticeable difference between the two initializations can be found around the degenerate point after 300 iterations. Our experiments also revealed that the local convergence may, to some extend, be alleviated by a more aggressive move limit in the MMA solver. Figure 12c shows the optimized result with a move limit of 0.1 (in contrast to a limit of 0.01 in previous examples), under a homogeneous initialization. While a binary design is obtained, the design has irregular large void regions that do not agree with the intention of creating distributed porous infill structures. The introduction of the topology-guided initialization is able to fill the void (see Fig. 12d). The difference can be observed in the intermediate density distributions shown at the bottom, e.g., after 300 iterations, around the degenerate point. The latter design consumes 4.5% more material, and decreases the compliance by 4.2%.

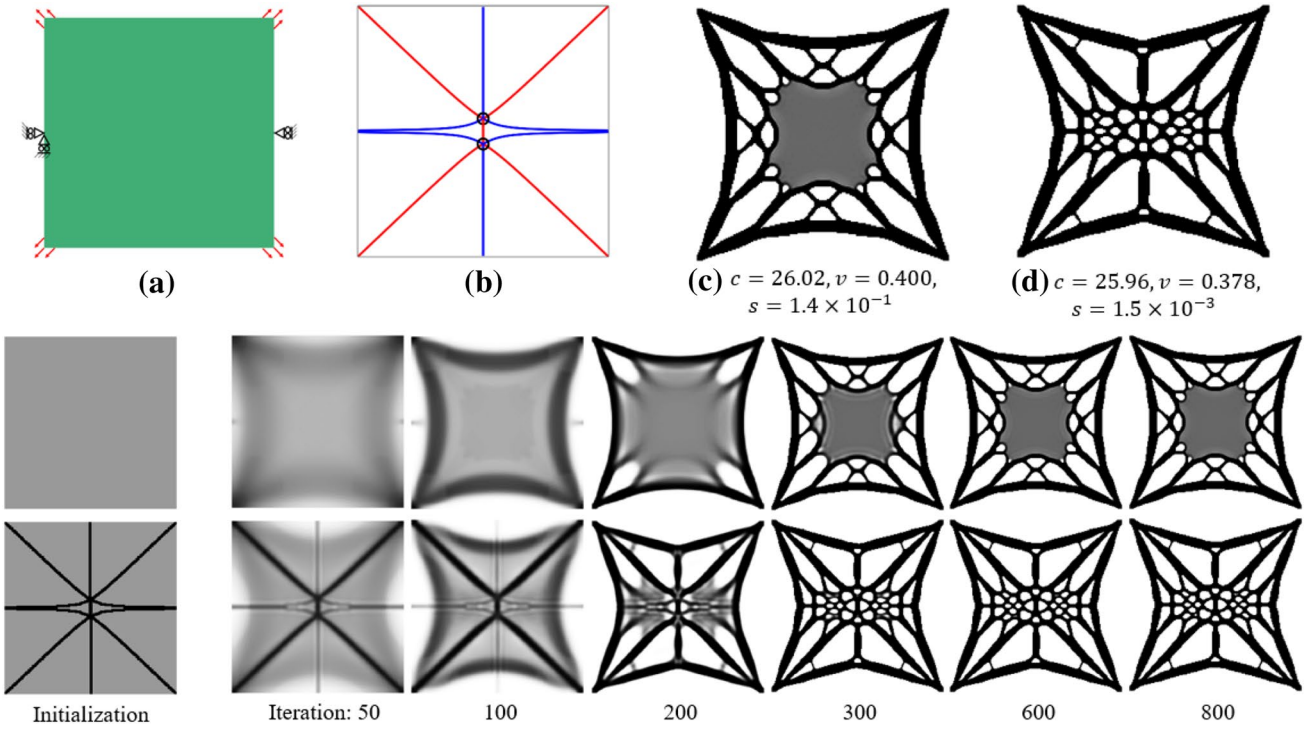

Fig. 9 Porous infill optimization with both local and global volume fraction constraints. The optimization settings are $\alpha_e = 0.6$, $\alpha_{global} = 0.4$, $R_e = 18$, $r_e = 4.5$ and 1000 iterations. **a** The design domain (200×200) and boundary conditions. **b** Trisector degenerate points and the corresponding topological skeletons. **c** The density distribution generated by porous infill optimization, and **d** using the proposed topology-guided density initialization. The two rows at the bottom show the intermediate density distributions during optimization, under the two different initializations

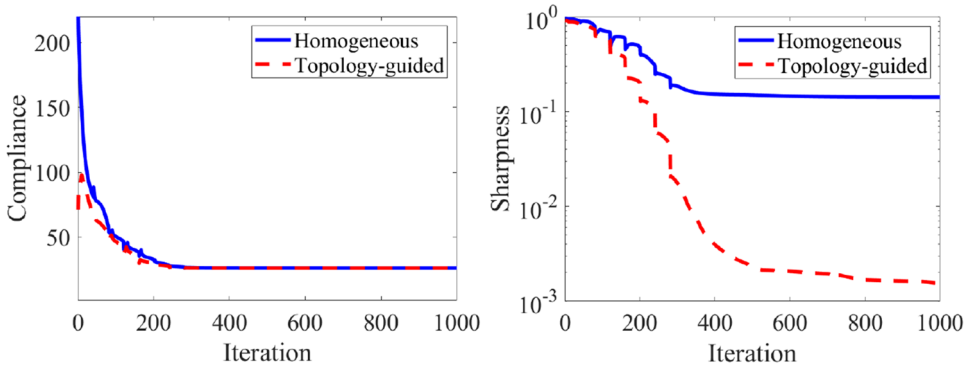

Fig. 10 Convergence plots for the example shown in Fig. 9, comparing the effects of homogeneous initialization and topology-guided initialization regarding the objective (left) and sharpness (right)

In this paper we focus on addressing the issue of low convergence associated with degenerate points. We note that there are other causes of low convergence in density-based topology optimization. As discussed in Sect. 3.2, the left hand side in Fig. 1b includes a region of $\sigma_1 \approx -\sigma_2$. It takes a few hundred iterations for this region to converge (c.f. Fig. 7 bottom). Extending the initialization from the topological skeleton to the entire domain is expected to reduce the number of iterations.

6 Conclusions

In this work, we have analyzed the convergence of porous infill optimization towards a stable binary design. In a number of experiments we have shown that low convergence regions may appear in this variant of topology optimization, prohibiting an automatic generation of a distinct and mechanically sound binary design. By analyzing the topology of the stress field that arises in the solid object, the existence of trisector degenerate points in this field

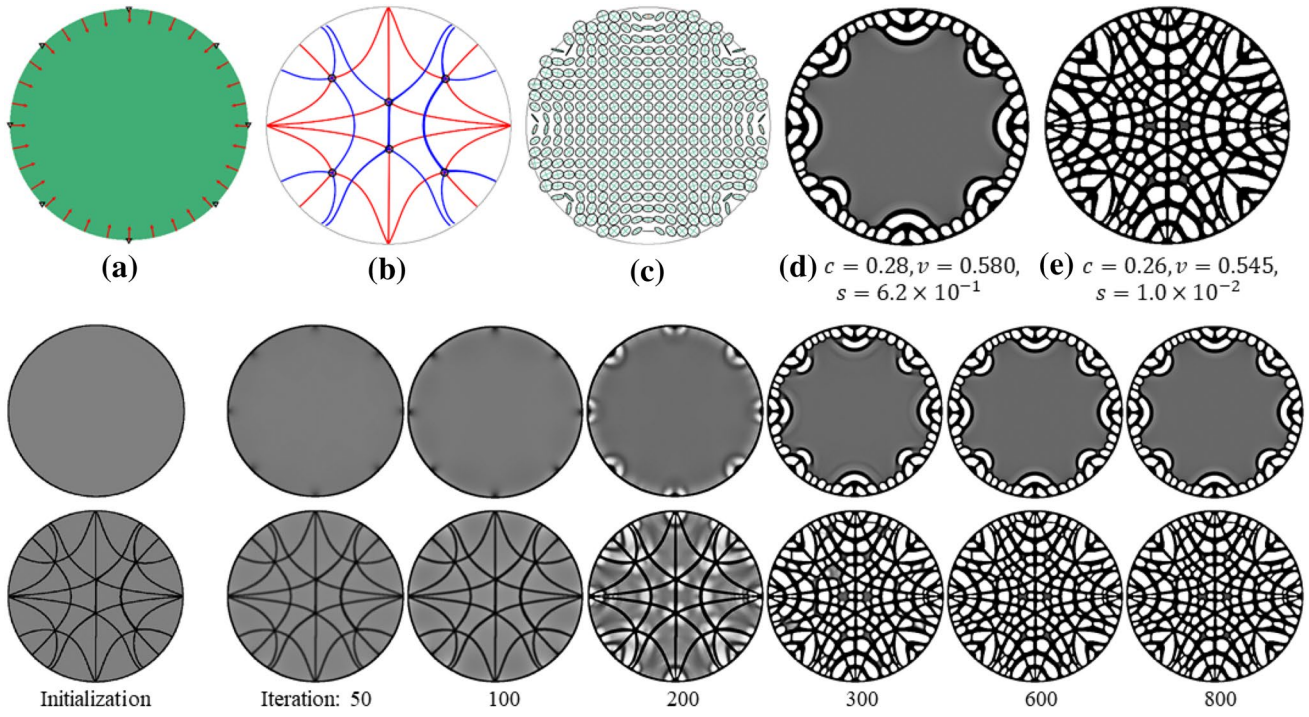

Fig. 11 Porous infill optimization under distributed loads. The optimization settings are $\alpha_e = 0.6$, $R_e = 36$, $r_e = 4.5$ and 1000 iterations. **a** The design domain (444×444) and boundary conditions. **b** Trisector degenerate points and the corresponding topological skeletons. **c** Stress visualization using tensor glyphs. **d** The optimized infills using a uniform density initialization **e** and the proposed topology-guided density initialization. The intermediate density distributions using different initializations are shown at the bottom

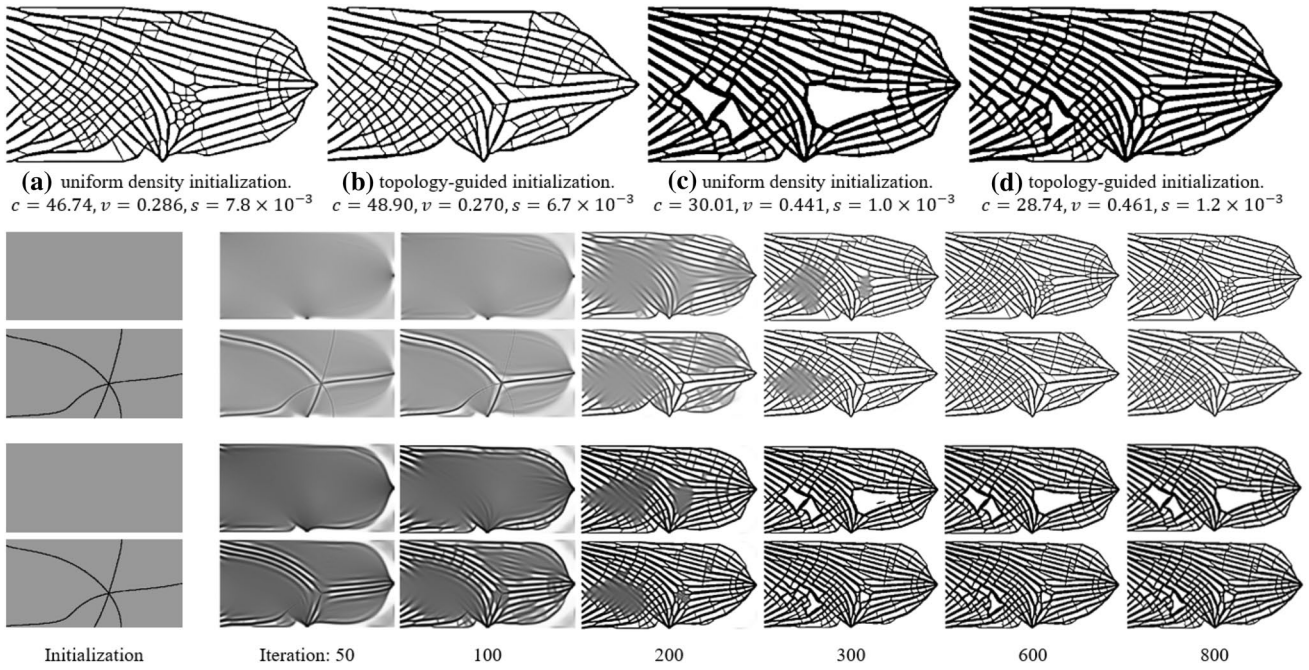

Fig. 12 Top row: Density distributions of special cases of 'Cantilever' after 1000 iterations. Control parameters are kept the same as in Fig. 1c if not stated otherwise. **a** Using a uniform initial density field and $\alpha_e = 0.4$. **b** Using a stress topology-guided initial density field and $\alpha_e = 0.4$. **c** Using a homogeneous initial density field and setting the moving limit of MMA to 0.1. **d** Using a stress topology-guided initial density field and setting the moving limit of MMA to 0.1. The intermediate density distributions using different initializations are shown at the bottom

could be determined as the major cause of low convergence. Based on this observation, we have proposed an initialization process for porous infill optimization that quickly guides the optimization towards a stable binary design. This process generates an initial solid material layout along the topological skeleton of the stress field, which is comprised of principal stress lines starting at the trisector degenerate points.

In the future, we intend to shed light on the following extensions of the proposed approach: Firstly, we aim to consider the application of stress topology-guided density initialization to three-dimensional (3D) domains. Therefore, the convergence of 3D porous infill optimization first needs to be analyzed, using dedicated visualization techniques for 3D scalar fields. Then, since degenerate points become lines and surfaces in 3D (Hesselink et al. 1997; Zheng et al. 2005), the relationships between the 3D stress field topology and the local convergence ratio needs to be investigated. Based on these investigations, specific initialization strategies and material growth processes need to be developed. Secondly, we will consider stress topology analysis for homogenization-based infill optimization. In particular, we will address the automatic generation of a 2D quad-dominant mesh where the mesh edges align with the principal stress directions. Porous infill optimization, under a single load case, tends to lay out the material along the mutually orthogonal principal stress lines, and—with our proposed initialization—automatically handles the material layout around degenerate points where quad meshing approach have difficulties to construct a consistent mesh structure (Wu et al. 2021b). We will build upon this observation and combine stress topology-guided porous infill optimization with the enforcement of material deposition along the principal stress lines.

Acknowledgements This work was supported in part by a grant from German Research Foundation (DFG) under Grant No. WE 2754/10-1.

Declarations

Conflict of interest The authors declare that they have no conflict of interest.

Replication of results All important details have been presented in the paper. To facilitate re-implementation and reuse of this method, we provide a demonstration program https://github.com/Junpeng-Wang-TUM/Infill_plus in Matlab. This demo works with rectangular design domains (i.e., Figs. 1 and 9). This demo additionally includes the functionality for topology analysis and visualization of the stress tensor field.

References

Bendsøe MP, Kikuchi N (1988) Generating optimal topologies in structural design using a homogenization method. Comput Methods Appl Mech Eng 71(2):197–224. https://doi.org/10.1016/0045-7825(88)90086-2

Cang R, Yao H, Ren Y (2019) One-shot generation of near-optimal topology through theory-driven machine learning. Comput Aid Des 109:12–21. https://doi.org/10.1016/j.cad.2018.12.008

Clausen A, Aage N, Sigmund O (2015) Topology optimization of coated structures and material interface problems. Comput Methods Appl Mech Eng 290:524–541. https://doi.org/10.1016/j.cma.2015.02.011

Das S, Sutradhar A (2020) Multi-physics topology optimization of functionally graded controllable porous structures: application to heat dissipating problems. Mater Des 193:108775. https://doi.org/10.1016/j.matdes.2020.108775

Delmarcelle T, Hesselink L (1994) The topology of symmetric, second-order tensor fields. In: Proceedings visualization'94, IEEE, pp 140–147. https://doi.org/10.1109/VISUAL.1994.346326

Guest JK (2009) Imposing maximum length scale in topology optimization. Struct Multidisc Optim 37(5):463–473. https://doi.org/10.1007/s00158-008-0250-7

Hesselink L, Levy Y, Lavin Y (1997) The topology of symmetric, second-order 3d tensor fields. IEEE Trans Vis Comput Graph 3(1):1–11. https://doi.org/10.1109/2945.582332

Li H, Gao L, Li H, Tong H (2020) Spatial-varying multi-phase infill design using density-based topology optimization. Comput Methods Appl Mech Eng 372:113354. https://doi.org/10.1016/j.cma.2020.113354

Li H, Gao L, Li H, Li X, Tong H (2021) Full-scale topology optimization for fiber-reinforced structures with continuous fiber paths. Comput Methods Appl Mech Eng 377:113668. https://doi.org/10.1016/j.cma.2021.113668

Qiu W, Jin P, Jin S, Wang C, Xia L, Zhu J, Shi T (2020) An evolutionary design approach to shell-infill structures. Add Manuf. https://doi.org/10.1016/j.addma.2020.101382

Schmidt MP, Pedersen CB, Gout C (2019) On structural topology optimization using graded porosity control. Struct Multidisc Optim 60(4):1437–1453. https://doi.org/10.1007/s00158-019-02275-x

Sigmund O (2001) A 99 line topology optimization code written in Matlab. Struct Multidisc Optim 21(2):120–127. https://doi.org/10.1007/s001580050176

Stutz F, Groen J, Sigmund O, Bærentzen J (2020) Singularity aware de-homogenization for high-resolution topology optimized structures. Struct Multidisc Optim 62(5):2279–2295. https://doi.org/10.1007/s00158-020-02681-6

Svanberg K (1987) The method of moving asymptotes-a new method for structural optimization. Int J Numer Methods Eng 24(2):359–373. https://doi.org/10.1002/nme.1620240207

Träff EA, Sigmund O, Aage N (2021) Topology optimization of ultra high resolution shell structures. Thin-Walled Struct 160:107349. https://doi.org/10.1016/j.tws.2020.107349

Wang F, Lazarov BS, Sigmund O (2011) On projection methods, convergence and robust formulations in topology optimization.

Struct Multidisc Optim 43(6):767–784. https://doi.org/10.1007/s00158-010-0602-y

Wang J, Wu J, Westermann R (2020) A globally conforming lattice structure for 2d stress tensor visualization. Comput Graph Forum 39:417–427. https://doi.org/10.1111/cgf.13991

Wu J, Clausen A, Sigmund O (2017) Minimum compliance topology optimization of shell-infill composites for additive manufacturing. Comput Methods Appl Mech Eng 326:358–375. https://doi.org/10.1016/j.cma.2017.08.018

Wu J, Aage N, Westermann R, Sigmund O (2018) Infill optimization for additive manufacturing-approaching bone-like porous structures. IEEE Trans Vis Comput Graph 24(2):1127–1140. https://doi.org/10.1109/TVCG.2017.2655523

Wu J, Sigmund O, Groen JP (2021) Topology optimization of multi-scale structures: a review. Struct Multidisc Optim. https://doi.org/10.1007/s00158-021-02881-8

Wu J, Wang W, Gao X (2021) Design and optimization of conforming lattice structures. IEEE Trans Vis Comput Graph 27(1):43–56. https://doi.org/10.1109/TVCG.2019.2938946

Zhao Z, Zhang XS (2021) Design of graded porous bone-like structures via a multi-material topology optimization approach. Struct Multidisc Optim 64(8):677–698. https://doi.org/10.1007/s00158-021-02870-x

Zheng X, Parlett B, Pang A (2005) Topological structures of 3d tensor fields. In: VIS 05. IEEE visualization, 2005, IEEE, pp 551–558. https://doi.org/10.1109/VISUAL.2005.1532841

Proceedings of the ASME 2022 International Design Engineering Technical Conferences & Computers and Information in Engineering Conference
IDETC/CIE 2022
August 14-August 17, 2022, St. Louis Missouri, USA

DETC2022-89030

STRESS TRAJECTORY GUIDED STRUCTURAL DESIGN AND TOPOLOGY OPTIMIZATION

Junpeng Wang*
Computer Graphics and Visualization
Department of Informatics
Technical University of Munich
Garching 85748, Germany
Email: junpeng.wang@tum.de

Jun Wu
Department of Sustainable Design Engineering
Delft University of Technology
Delft 2628 CE, The Netherlands
Email: j.wu-1@tudelft.nl

Rüdiger Westermann
Computer Graphics and Visualization
Department of Informatics
Technical University of Munich
Garching 85748, Germany
Email: westermann@tum.de

ABSTRACT

Density-based topology optimization using global and local volume constraints is a key technique to automatically design lightweight structures. It is known that stiffness optimal structures comprise spatially varying geometric patterns that span multiple length scales. However, both variants of topology optimization have challenges to efficiently converge to such a structural layout. In this paper, we investigate material layouts that are generated from stress trajectories, i.e., to compile a globally consistent structure by tracing the stress trajectories from finite element simulation of the solid design domain under external loads. This is particularly appealing from a computational perspective, since it avoids iterative optimization that involves finite element analysis on fine meshes. By regularizing the thickness of each trajectory using derived strain energy measures along them, stiff structural layouts can be generated in a highly efficient way. We then shed light on the use of the resulting structures as initial density fields in density-based topology optimization, i.e., to generate an initial density field that is then further optimized via topology optimization. We demonstrate that by using a stress trajectory guided density initialization in lieu of a uniform density field, convergence issues in density-based topology optimization can be significantly relaxed at comparable stiffness of the resulting structural layouts.

*Address all correspondence to this author.

1 Introduction

The design of optimal lightweight structures is a fundamental research topic in design engineering. It is known that stiffness optimal structures, i.e., with minimum compliance measured by strain energy, comprise spatially varying geometric patterns that span multiple length scales [1]. To approach theoretically optimal structures, early works in topology optimization (e.g. [2]) explored a material model corresponding to infinitely small square cells with rectangular holes. The resulting multi-scale structures were deemed challenging for manufacturing. This had promoted the field of topology optimization to shift its focus from homogenization-based approaches to "mono-scale" approaches that optimize the distribution of a homogeneous isotropic material [3,4,5], e.g., using a material model known as Solid Isotropic Material with Penalization.

Due to the increasing flexibility of additive manufacturing (AM), recent years saw a resurgent interest in optimal design of multi-scale structures. AM is effective for fabricating complex mono-scale structures as well as delicate multi-scale structures such as infill lattices. We refer to a recent review article for the history and latest developments in topology optimization of multi-scale structures [1]. Among these approaches, it is of particular interest to adapt the lattice orientation according to stress directions. Topology optimization approaches for designing conforming lattice structures can be categorised into two groups: full-scale density-based topology optimization using local volume constraints [6], and de-homogenization of optimized,

locally defined orientations [7, 8].

Density-based approaches. Density-based topology optimization commonly starts from a homogeneous initial density field and then iteratively performs finite element simulation of the current material distribution to optimize for structural performance, under a constraint on the total material volume. Since the theoretically optimal structures are multi-scale, the density-based approach in principle shall be able to achieve these multi-scale structures. This, however, is only possible by using sufficiently fine meshes for discretizing the material distribution, and requires careful continuation techniques. Therefore, commonly seen topology optimization results are predominantly mono-scale.

To promote the appearance of fine scale substructures, local volume constraints have been proposed to replace the total volume constraint [6]. This results in distributed substructures spreading across the design domain, which largely follow the principal stress directions. This approach has been extended in various directions, for instance, to design concurrently structures and porous substructures therein [9], porous structures with gradation in the porosity and pore size [10, 11], fiber-reinforced structures [12], and to incorporate multiple materials [13] and self-supporting constraints [14]. Lately, as demonstrated by Wang et al. [15], convergence issues may arise in the regions enclosing degenerate points in the stress field, i.e., points where the eigenvalues indicating major and minor stress direction become indistinguishable. To reduce the number of optimization iterations in these cases, Wang et al. proposed using the topological skeleton, i.e., principal stress trajectories connecting pairs of degenerate points, of the stress field in the solid object under load to initialize the density field.

De-homogenization. In the seminal work of Bendsøe and Kikuchi, they proposed a material model for infinitely small square cells with rectangular hole [2]. Using numerical homogenization to evaluate equivalent mechanical properties of these cells, one can optimize the spatially varying size as well as orientation of such cells. The challenge that is addressed by de-homogenization is to compile a globally consistent structure from these locally defined unit cell configurations. Pantz et al proposed one of the first solutions towards this end [7], which has been further developed [8, 16, 17]. A key component in these approaches is to seek a scalar field, whose gradient is aligned with the optimized orientation. An effective alternative is to use hexahedral meshing to create meshes with edges aligned to the optimized orientation [18].

In this work, we investigate material layouts that are generated from stress trajectories, i.e., to compile a globally consistent structure by tracing the stress trajectories from finite element simulation of the solid design domain under external loads. This is particularly appealing from a computational perspective, since it avoids iterative optimization involving finite element analysis on fine meshes. On this aspect, it is in line with the de-homogenization approaches. Similar ideas to tracing stress lines have been explored in [19, 20, 21, 22], yet a challenge is to get a (quasi-)uniform distribution of the stress lines. To generate such layouts, we exploit recent results in trajectory-based stress visualization [23], which automatically generate a regular, smoothly varying, and space-filling structure consisting of trajectories along the major and minor principal stress directions. The thickness of each trajectory can be further regularized by using derived strain energy measures along them. By converting the resulting trajectory ensemble to a corresponding density field, stiff structural layouts can be generated in a highly efficient way.

We then shed light on the use of the resulting structures as initial density fields in density-based topology optimization, i.e., to generate an initial density field that is then optimized via topology optimization. In density-based approaches, as with other topology optimization approaches, the results are heavily influenced by the initialization, both in terms of convergence and optimality of the optimized structural layout. This is because topology optimization is a non-convex problem, and depending on the initialization a different local optimum is reached. We demonstrate that by using a material initialization guided by stress trajectories instead of a uniform density field, convergence issues in density-based topology optimization can be significantly relaxed at comparable stiffness of the resulting layouts. In an exhaustive study we compare the layouts generated by all variants regarding their mechanical properties and computational cost.

The rest of our paper is organized as follows. In Section 2 we present the method to generate space-filling stress trajectories. The use of these stress trajectories for structural design and for topology optimization is presented in Sections 3 and 4, respectively. We then discuss the computational and structural performance of different variants in Section 5, before concluding the paper in Section 6.

2 Principal stress trajectories

A consistent visual representation of a 2D stress tensor field can be obtained via principal stress trajectories, which convey the directions of the principal stresses and are used in particular to show where and how loads are internally redirected and deflected. We will subsequently call such trajectories Principal Stress Lines (PSLs).

At each point in a 2D solid under load, the stress state is fully described by the stress vectors for two mutually orthogonal orientations. The second-order stress tensor

$$S(x,y) = \begin{bmatrix} \sigma_{xx} & \tau_{xy} \\ \tau_{xy} & \sigma_{yy} \end{bmatrix}_{(x,y)} \tag{1}$$

contains these vectors for the axes of a Cartesian coordinate system. σ_{xx} and σ_{yy} are the normal stress components along the x and y direction, respectively, τ_{xy} is the shear stress component.

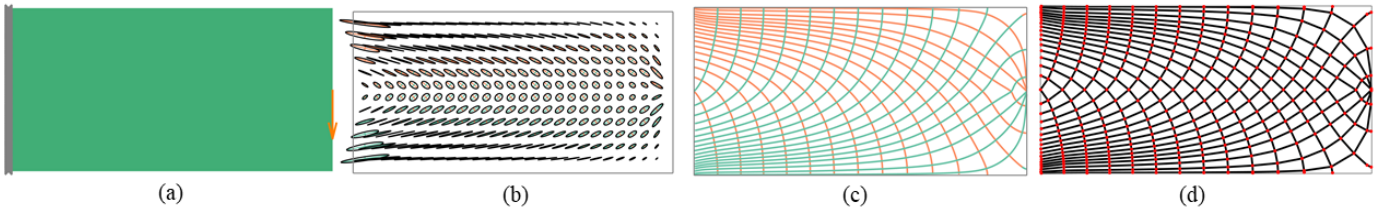

FIGURE 1. (a) Solid model discretized by 500×250 simulation elements. Gray and orange arrowheads, respectively, indicate fixation and loading conditions. (b) Tensor glyphs show the principal stress directions. Red and green, respectively, indicate positive and negative principal stresses. (c) Uniformly distributed PSLs. Orange and turquoise trajectories represent the major and minor principal stress directions, respectively. (d) Red dots indicate PSL intersections, and curved PSLs are converted into piecewise linear segments.

S is symmetric since the shear stresses are equal on mutually orthogonal lines. The principal stress directions of the stress tensor are given by the eigenvectors of S, indicating the two mutually orthogonal directions along which the shear stresses vanish. The corresponding eigenvalues σ_1 and σ_2 of S represent the magnitudes of the principal stresses. For $\sigma_1 \geq \sigma_2$, σ_1 is called the major principal stress, and σ_2 the minor principal stress, and the corresponding eigenvectors v_1 and v_2 are called major and minor principal stress directions. The signs of the principal stress magnitudes classify the stresses into tension (positive sign) or compression (negative sign). Since there are two principal stresses acting at each point, the classification is with respect to a specific direction. Figs. 1a,b, respectively, show a 2D solid under external loads and the principal stresses via elliptical tensor glyphs. The semi-major and -minor axes of the ellipses correspond to the major and minor principal stress directions.

PSLs are the trajectories that are everywhere tangent to either the major or the minor principal stress direction. They are computed by numerically integrating massless particles in each single (normalized) eigenvector field (see Fig. 1c). PSLs are started from an arbitrary seed points, and integrated until the domain boundary is reached, the PSL performs a loop, i.e. comes closer to a previous point than a predefined distance threshold, or the number of integration steps exceeds a user-defined bound. A Runge-Kutta (RK2) scheme with fixed integration step size δ is used for numerical integration. In each integration step, the stress tensor T is interpolated and the eigenvalues and eigenvectors are computed from the interpolated tensor. The next integration step is performed in the direction with the least deviation from the previous direction.

In addition to the regular PSLs, there are special PSLs comprising the so-called topological skeleton. These PSLs start from a degenerate point of the stress tensor field and separate areas of different stress behavior. Degenerate points are characterized by two equal eigenvalues, so that the principal directions cannot be decided. In the vicinity of such points a set of hyperbolic and parabolic sectors exist, in which similar patterns of neighboring trajectories are observed [24]. The topological skeleton consists of the boundaries between adjacent sectors—so-called separatrices—and indicate pathways along which the forces are steered towards the degenerate points. To extract the topological skeleton, first the locations of degenerate points are computed by using the invariant formulation by Delmarcelle and Hesselink [24], and then PSLs are started from these points (see Figs. 5h,i for an example including the topological skeleton).

2.1 Uniformly distributed stress trajectories

To generate a uniformly distributed set of PSLs, we use the publicly available visualization tool for 3D stress fields provided by Wang et al. [23] [1]. Designed for extracting and visualizing the PSLs along the three mutually orthogonal principal stress directions in 3D solids under load, with only minor modifications the tool can be adapted to work with 2D objects.

Starting with a set of seed points that are uniformly distributed across the domain, PSL extraction starts by selecting one of the candidate seed points and tracing the major and minor PSLs (the seed PSLs) passing through it. The point is then classified as visited by major and minor PSLs. All remaining seed points that have not yet been classified as major and minor, and are closer to a new PSL than a threshold ϑ, are processed in the following way: Firstly, the coordinate of such a point is set (i.e., snapped) to the coordinate of the closest integration point on the PSL (in the first step, the closest PSL of the seed PSLs). Secondly, if the new PSL is a major PSL, the classification major is added to the point, and minor if the new PSL is a minor PSL. Then, the seed point that is closest to the initial seed point and not yet classified as major and minor is selected, and a major (minor) PSL is traced if the point is classified as minor (major). *Snapping*, *classification*, and *selection* are then repeated until all points are classified as major and minor. By this procedure it is ensured that around each PSL a band is generated from which no more PSL is seeded, and new PSLs are always seeded from points on existing PSLs. This generates a fairly uniform and space-filling distribution of PSLs (see Fig. 1c and Fig. 5).

[1] https://github.com/Junpeng-Wang-TUM/3D-TSV

To include the topological skeleton, it is first extracted and all separatrices are considered as seed PSLs as described before.

2.2 Piecewise linear PSLs

Each PSL is a curved trajectory in the 2D domain, composed of a set of integration points that are connected via line segments. Especially if the density of PSLs is low, PSLs tend to curve strongly between two intersection points with other PSLs. When using PSLs to generate an initial density field in which the material is smeared out along them, curved segments require more material than straight lines and are less stable than lines. Therefore, after all PSLs are computed, we compute all intersection points between PSLs and convert each PSL into a polyline comprised of intersection points and linear connections between them. The result of this process is shown in Fig. 1d.

To efficiently compute piecewise linear PSLs, the following extensions are introduced: Firstly, once a PSL is computed, the integration points along this PSL are assigned an index relative to one of the end points of that PSL, i.e., an index I_i^{id} says that the point is the i-th point when counting from the selected end point of the PSL with unique identifier id. Secondly, additional information is stored at the cells of the simulation grid on which stresses are simulated. At every cell a PSL is passing through, the identifier of the PSL is stored. Thus, eventually each cell contains the identifiers of all PSLs that might intersect in this cell. Since only intersections between major and a minor PSLs can occur, all cells with at least one identifier of a major PSL and a minor PSL are considered, and the intersection points between the major and minor PSLs are computed. This results in line-line intersection test to obtain the locations of intersection points. In addition, for each intersection point the indices of that point along the PSLs it resides on are computed by linear interpolation of the indices at the line end points. Each PSL stores a separate list containing all intersection points that are found along it, so that by sorting these lists with respect to increasing index a sorted sequence of intersection points is obtained.

3 PSL-guided structural design

In the following, we describe how a density field is obtained from the set of piecewise linear PSLs. This density field is then used in a finite element stress simulation to compute the compliance of the layout. In the following chapters, this layout is then used as initial density field in topology optimization, and the results are compared regarding their mechanical properties.

Given the current and next point along a piecewise linear PSL, we use Bresenham line rasterization to compute all simulation cells that are hit by the line connecting both points. These cells are then set to solid, and the process moves on to the next pair of points along the PSL. The result of the rasterization is shown in Fig. 2a.

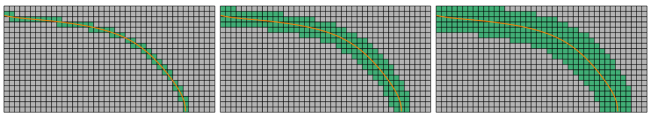

(a) $t = 1$. (b) $t = 2$. (c) $t = 3$.

FIGURE 2. Material layout via PSL rasterization. From (b) to (c), the thickness of the initial material structure in (a) is increased by morphological dilation.

The material layout can be flexibly and efficiently adjusted by using a lower or higher density of the computed PSLs. Concrete timings for PSL extraction depending on the resolution of the simulation grid and the PSL density are given in Sec. 5. When smearing out the material along the PSLs as described, rather thin structures are generated and the overall compliance of the layout is only acceptable if many PSLs are used. To address this limitation, the material structures can be thickened via a morphological dilation using a 3×3 structuring element, i.e., around each solid cell also the 8 adjacent cells are made solid. This process can be applied iteratively to increase the PSL thickness further (see Figs. 2b,c). Next, we describe an approach to automatically adapt the thickness of each PSL by considering a PSL's importance regarding the overall compliance.

3.1 Strain energy guided thickness control

Automatic thickness control aims at using the prescribed material budget in the most effective way so that a low compliance is achieved. Therefore, the importance of each PSL for reducing the compliance is used as an indicator of the PSL's thickness. The overall compliance of a material layout is computed via the strain energies of the elements in the simulation grid, i.e., by adding the strain energies of all solid elements in the domain. The overall compliance per PSL can be computed by adding the strain energies of all elements covered by a PSL. In this way, the contribution of each PSL to the overall compliance, i.e. to resist the external loads, can be quantified. Specifically, the stored strain energy of the i-th PSL is computed as

$$c_{T_i} = \sum_{k=1}^{M_k} c_e. \tag{2}$$

Where M_k is the number of elements covered by the PSL. To avoid that the importance of a PSL is dominated by its length, c_{T_i} is finally divided by the number of elements directly intersected by the PSL. The resulting values are then used to guide the adjustment of each PSL's thickness.

Material initialization starts by setting the initial PSL thickness (t_0) either to 2, i.e., at least there are three layers of cells surrounding the PSL (see Fig. 2b), or to a larger value specified

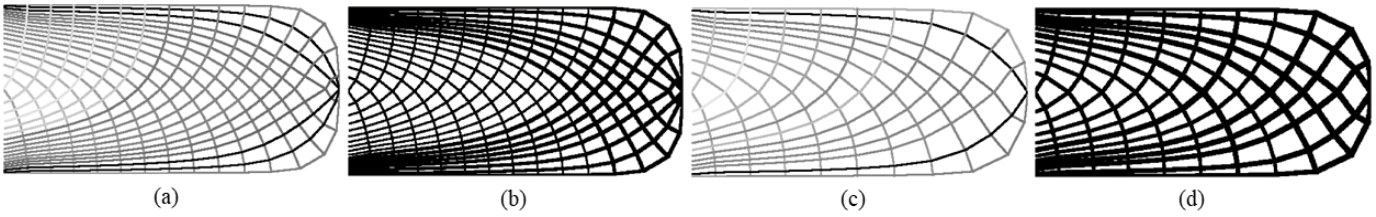

FIGURE 3. PSL-guided material layouts for two different PSL densities, with the used volume fractions (v) and resulting compliances (c). (a) ($v = 0.370$, $c = 2.657c_0$) and (c) ($v = 0.250$, $c = 4.436c_0$): Layouts using PSLs with $t_0 = 2$, decreasing brightness indicates increasing PSL strain energy. (b) ($v = 0.493$, $c = 1.839c_0$) and (d) ($v = 0.499$, $c = 1.780c_0$): layouts corresponding to (a) and (c) where thickness is adapted according to strain energy. $c_0 = 40.93$ is the compliance of the fully solid domain.

by the user. This enables to consider manufacturing constraints, for instance, to enforce a certain minimum thickness that is required by the printing process. Furthermore, a maximum thickness t_{max} is set to reduce the chance that adjacent PSLs merge and form thick strands. Now, in the case that the usable material budget α_{global} has not been reached by the initial material layout, in descending order with respect to c_{T_i} the PSL's thickness is set to t_{max} until all material has been deposited. Thus, a final layout comprising PSL-guided material structures with either the minimum or maximum allowed thickness are generated. We also performed tests using an assignment strategy that generates structures with thickness values within the whole range from t_0 to t_{max}, yet while this improved the overall compliance only marginally it increased the computational overhead considerably.

For two initial material layouts using different PSL densities, Figs. 3a,c show the importance values that are computed per PSL by greyscales ranging from bright (low importance) to dark (high importance). Figures 3b,d show the corresponding final layouts after automatic thickness control. The finite element simulation is then re-performed using the empty-solid material design to evaluate the mechanical performance of the layout. It can be seen that adaptive thickness control distributes the material along regions that are important for achieving mechanically sound layouts and improves the overall compliance.

4 PSL-guided structural topology optimization

In density-based topology optimization, the design variable is the pseudo density of each element in the discretized design space. A structural layout can be represented by a binary field, i.e., density ρ_e equals 0 or 1, indicating an empty or solid element. The objective is to find the stiffest structure, i.e., minimum compliance, for a prescribed set of boundary conditions, and under an upper bound on the global material fraction,

$$\frac{1}{n}\sum_e \rho_e \leq \alpha_{\text{global}}. \tag{3}$$

Here n is the number of elements, and α_{global} is the global material fraction.

To solve the optimization problem by mathematical programming, the binary variables are relaxed to take intermediate values between 0 and 1. The Young's modulus associated with intermediate density values ($E_e(\rho_e)$) is interpolated from that of a solid basis element E_0 (i.e., $\rho_0 = 1$).

$$E_e(\rho_e) = \rho_{\min} + \rho_e^p E_0. \tag{4}$$

$\rho_{\min}$ is a non-zero small value, to avoid the stiffness matrix becoming singular, typically $\rho_{\min} = 10^{-6}$. The power p is a key parameter for the validity of the optimized layout. $p = 1$ results in a convex optimization problem, but it overestimates the attainable Young's modulus for intermediate densities (cf. Hashin–Shtrikman bounds [25]). The resulting optimized layout consists of many intermediate density values, i.e. large grey regions when visualizing the layout as an image. $p = 3$ is a reasonable approximation of the Hashin–Shtrikman bounds [26], according to which, for instance, half density ($\rho_e = 0.5$) gets much less than half Young's modulus. This physically valid interpolation thus promotes the optimization to converge to a physically valid structural layout (i.e., a binary density field). $p > 1$, however, raises a challenge for mathematical programming as the optimization problem becomes non-convex. Given the fact that the number of design variables in topology optimization is large, there exist an extremely large number of local minima.

Strictly speaking, to approach theoretically optimal structures, one shall start with $p = 1$, and gradually increase its value after some iterations, until p eventually reaches 3. Practically, to cut down the number of iterations, one commonly starts directly with $p = 3$ (e.g., in the 99-line or 88-line Matlab versions [27, 28]). Meanwhile since the discretization resolution of the design space is limited, the optimized structural layout, under a global material volume constraint, often consists of distinctively bulk substructures (cf Fig. 4a) rather than a multi-scale structure.

To design bone-inspired porous structures, Wu et al. pro-

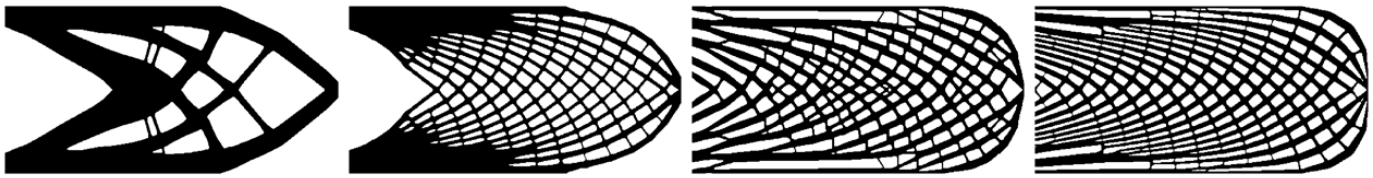

(a) $c = 1.541c_0, v = 0.500$, $s = 6.0 \times 10^{-3}, N = 281$. (b) $c = 1.543c_0, v = 0.500$, $s = 3.1 \times 10^{-3}, N = 281$. (c) $c = 1.901c_0, v = 0.530$, $s = 9.9 \times 10^{-3}, N = 433$. (d) $c = 1.801c_0, v = 0.549$, $s = 7.3 \times 10^{-3}, N = 281$.

FIGURE 4. (a), (c): Structural layouts generated via topology optimization with global and local volume constraint, respectively, starting with a homogeneous density field. (b), (d): Corresponding results when the initial density field is guided by PSLs, i.e., higher initial density is distributed along the PSLs in Fig. 3a, and lower initial density is prescribed in all other regions. c is the compliance and c_0 is the compliance of a fully solid domain, v is the deposition ratio. s is the sharpness value introduced in Sec. 5, where a smaller value indicates a sharper binary layout. N represents the number of iterations until s is reached.

posed to replace the global volume constraint with local volume constraints [6]. A local volume constraint is applied to each element, i.e.,

$$\bar{\rho}_e \leq \alpha_e, \forall e \tag{5}$$

where α_e is a prescribed upper bound on the local volume. $\bar{\rho}_e$ is the average of densities in a small region centered at the centroid of element e, computed by

$$\bar{\rho}_e = \frac{\sum_{i \in N_e} \rho_i}{\sum_{i \in N_e} 1}, \quad N_e = \{i | \parallel x_i - x_e \parallel_2 \leq R_e\}, \forall e, \tag{6}$$

where R_e denotes the radius of a circular region. x_i and x_e represent the centroid of elements, N_e represents the number of elements within this circular region.

Figure 4c shows an example of using the local volume constraint. The optimization problem is solved using the method of moving asymptotes (MMA) [29]. We refer to Wu et al. [6] for a detailed discussion of the computational steps for avoiding checkerboard patterns and stimulating a 0-1 design. The local volume constraints are more restrictive than the global volume constraint. Consequently, the optimized structure with the same amount of total material is somewhat less stiff than obtained with the global constraint. The benefits of the porous structures include robustness regarding material damage, unmodelled variation in boundary conditions, and buckling.

Density-based topology optimization under either global or local volume constraints is dependent on the initialization of the density field. Commonly in density-based topology optimization, one prescribes $\rho_e = \alpha_{\text{global}}$ or $\alpha_e, \forall e$, for global or local volume constraints, respectively.

We propose to use a PSL-guided density field to initialize $\boldsymbol{\rho}^{[0]}$. In particular, we use the PSL-guided layouts as shown in Figs. 3a,c for initialization. Here the elements corresponding to the thickened PSLs ($\mathscr{P}$) are prescribed a higher initial

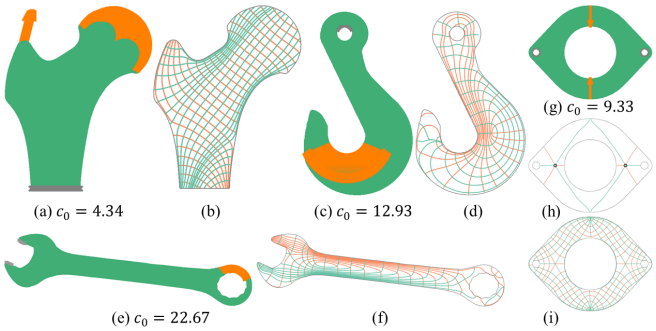

FIGURE 5. Models used in our experiments. Grey regions and orange arrowheads indicate fixations and loads, respectively. c_0 is the compliance of the fully solid layout under the boundary conditions. Orange and turquoise trajectories represent the major and minor PSLs, respectively. In (h), the topological skeleton that is traced from the two degenerate points (black circles) is shown. The number of simulation elements is 153,133 ('femur'), 70,042 ('hook'), 449,918 ('wrench') and 95,028 ('bracket').

value ($\rho^{[0]}_{e \in \mathscr{P}} = 1$ in this paper). The rest elements have a lower value, $\rho^{[0]}_{e \notin \mathscr{P}} = \alpha_{\text{global}}$ or α_e. Thus, the PSL trajectories are pre-embedded into the $\boldsymbol{\rho}^{[0]}$. Figures 4a,b compare optimized layouts using a homogeneous initialization and the proposed initialization, under the global volume constraint. Figures 4c,d compare the effects of initialization for local volume constraints.

5 Results

We use several examples to compare the mechanical properties of PSL-guided material layouts to the layouts generated by density-based topology optimization with and w/o PSL-guided material initialization. All experiments have been carried out on a desktop PC with an Intel Xeon CPU at 3.60GHz. The used operations have been implemented in MatLab, to ease the combination of finite element stress analysis with PSL integration and

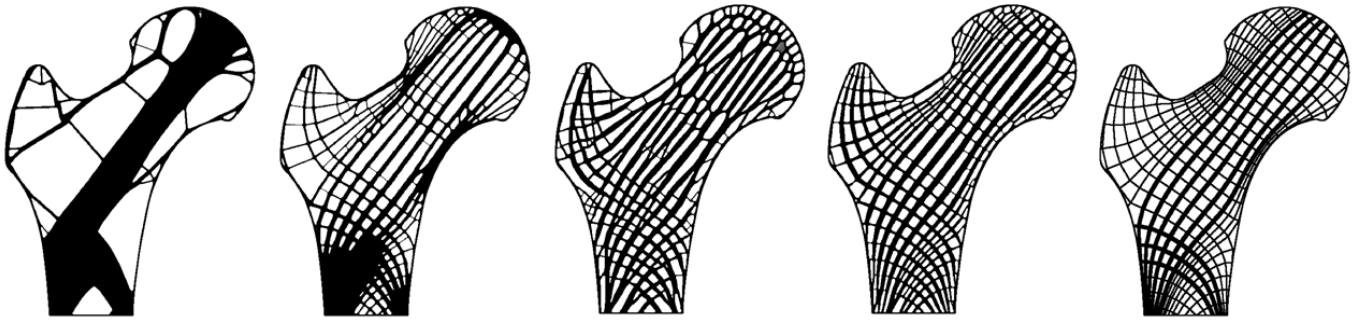

(a) $c = 1.711c_0, v = 0.500$, $s = 6.6 \times 10^{-3}, N = 281$. (b) $c = 1.764c_0, v = 0.500$, $s = 7.8 \times 10^{-3}, N = 281$. (c) $c = 2.048c_0, v = 0.539$, $s = 1.6 \times 10^{-2}, N = 1000$. (d) $c = 1.997c_0, v = 0.540$, $s = 9.9 \times 10^{-3}, N = 313$. (e) $c = 2.035c_0, v = 0.506$.

FIGURE 6. Layouts for 'femur'. (a) Topology optimization with global volume constraint, homogeneous material initialization. (b) Same as (a) but with PSL-guided material initialization. (c) Topology optimization with local volume constraint, homogeneous material initialization. (d) Same as (c) but with PSL-guided material initialization. (e) PSL-guided material layout.

material layout. All design domains are discretized by Cartesian finite element grids with unit-size simulation elements. The Young's Modulus and Poisson's ratio are set to 1.0 and 0.3, respectively.

To analyze the convergence improvements when using PSL-guided material initialization in topology optimization, we use the sharpness measure

$$s = \frac{4}{n} \sum_e \rho_e (1 - \rho_e). \tag{7}$$

A small value of s indicates a sharper binary design of the optimized layout. To facilitate the comparison of the convergence behavior, according to [6, 15] we define that the optimization process has converged once s is less than 0.01. Thus, the convergence of different approaches can be compared easily by counting the number of iterations (N) until the sharpness value is below 0.01.

Generating the PSL-guided material layout involves a finite element analysis to compute the stresses in the solid object under load, followed by PSL extraction and material deposition along PSLs. Strain-guided thickness control requires another finite element analysis to compute the strain energy of the initial material layout. A final simulation is used to evaluate the mechanical properties of the layout. Even for the largest model 'wrench' with 449,918 simulation elements (see Fig. 5e), the entire process takes less than 30 seconds. When using the PSL-guided layout as initialization for topology optimization, only the initial finite element analysis to simulate the stress field is required. In all our examples this is performed in less than 15 seconds.

In the following, the 'femur' model shown in Fig. 5 is used to compare the results of all proposed approaches and analyse their specific properties. Figure 6 shows the generated material layouts using the same external load conditions.

In Figs. 6b,a, the results of topology optimization with global volume constraint with and w/o the proposed material initialization are compared. While the compliance and the number of optimization iterations remain almost unchanged, very different material layouts are generated. It is in particular apparent that the final layout when the specific material initialization is used contains far more fine-grained sub-structures which are distributed over the domain. In Figs. 6d,c, the comparison is with respect to topology optimization under local volume constraint with and w/o the proposed initialization strategy. In this case, even at a significantly reduced number of optimization iterations the compliance is still comparable. Furthermore, the resulting layout appears more regular and is close to a 2D quad-mesh.

From Fig. 6e it can be observed that PSL-guided material layout achieves similar compliance than topology optimization with local volume constraint, yet the layout is generated at significantly lower computational cost. While it requires only three finite element simulations to generate the final layout, even with the proposed material initialization topology optimization requires over 300 iterations of finite element simulation and material update. In addition, a very regular and uniformly distributed layout is obtained.

Besides the compliance, we also evaluate the robustness of the material layouts generated by the different approaches with respect to local damage. Therefore, we remove a small piece of material from the optimized structures, but the boundary conditions are kept the same, see the region marked by a red box in Fig. 7 left. By comparing the compliances before and after local damage is applied (see Fig. 7 right), we see that the layout generated by topology optimization under global volume constraint has the weakest robustness in the tested scenario. However, by using the proposed material initialization, the robustness is improved significantly. The result by the topology optimization under local volume constraint is robust with respect to the local

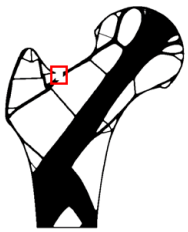

Cases in Fig. 6	Original compliance (c_0)	Compliance after local damage (c_0)
(a)	1.711	8.229
(b)	1.764	2.123
(c)	2.048	2.113
(d)	1.997	2.050
(e)	2.035	2.167

FIGURE 7. Robustness with respect to local damage. Left: Red box indicates where material is removed. Right: Compliance comparison before and after local damage. (a)-(e) correspond to the cases in Fig. 6.

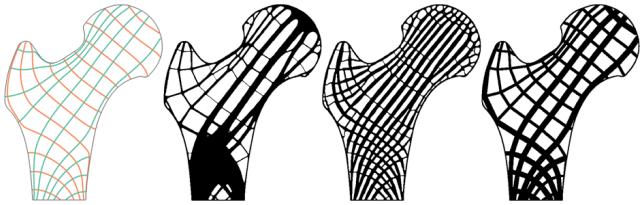

(a) PSLs (b) $c = 1.714c_0, v = 0.500$, $s = 5.8 \times 10^{-3}, N = 281$. (c) $c = 2.010c_0, v = 0.533$, $s = 1.0 \times 10^{-2}, N = 424$. (d) $c = 2.149c_0, v = 0.534$.

FIGURE 8. (a) PSLs used to guide material deposition. (b) and (c): PSL-guided material initialization of topology optimization with global and local volume constraints, respectively. (d) PSL-guided material layout with thickness control.

damage, which has also been demonstrated by the work [6], and our initialization strategy doesn't violate this feature. Furthermore, the result of using the PSL-guided structural design also shows this characteristic of the result by topology optimization under local volume constraint.

In addition to the experiments in Fig. 6 with a rather dense set of PSLs, a second row of experiments has been conducted with a more sparse set of PSLs for material initialization and PSL-guided layout (see Fig. 8a). Again, the result in Fig. 8b shows a more detailed and distributed material layout when these PSLs are used for initialization in topology optimization with global volume constraint. Figure 6c demonstrates improved convergence rate of topology optimization with local volume constraint, and Fig. 8d supports our finding that PSL-guided material layouts come at reasonably compliance yet significantly reduced computational load. On the other hand, it becomes less significant compared to Fig. 6d since less PSLs are used. In order to set an appropriate PSL distribution for the PSL-guided structural design or topology optimization, we recommend taking the affecting radius R_e in Eqn. 6 as a reference in selecting the snapping threshold ϑ of 3D-TSV, where the former determines the pore size of the porous infill, the latter controls the gaps among different PSLs.

To further demonstrate the potential of PSL-guided material initialization to improve the convergence of the optimization process, a comparison to the approach by Wang et al. [15] using only the topological skeleton of the stress field in the initialization is performed. We use the same 'bracket' model (see Fig. 5g) as in [15]. Figure 9 shows the generated material layouts and the performance statistics for both variants. While the generated layouts are similar in terms of compliance, our proposed initialization can reduce the number of optimization iterations until convergence by more than 30%.

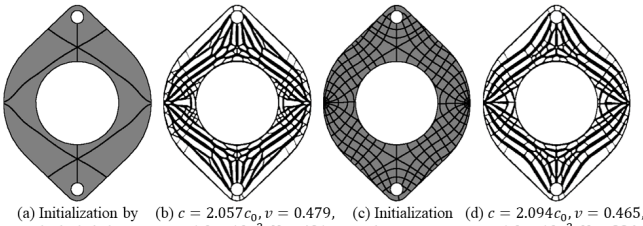

(a) Initialization by topological skeleton. (b) $c = 2.057c_0, v = 0.479$, $s = 1.0 \times 10^{-2}, N = 491$. (c) Initialization by PSLs. (d) $c = 2.094c_0, v = 0.465$, $s = 1.0 \times 10^{-2}, N = 326$.

FIGURE 9. (a), (b) Only using the topological skeleton of the stress tensor field as initial material field and the corresponding result [15]. (c), (d) The proposed approach.

By using the 'hook' and 'wrench' models, the basic features of material initialization are further emphasized (see Fig. 10). In particular, the results are in line with those obtained for 'femur', with respect to compliance and number of optimization iterations. Figure 11 shows rendering of 3D objects that were created by extruding the 2D material layouts.

6 Conclusion and future work

In this work, we have analyzed the use of PSL-guided material layouts for and as an alternative to density-based topology optimization. We have demonstrated that the convergence of topology optimization with local volume constraint can be significantly improved when such layouts are used to initialize the optimization process. When only a global volume constraint is enforced, the robustness of the final layout with respect to local damage is vastly improved. In both cases, the resulting layouts show improved regularity and are more evenly distributed across the domain.

When PSL-guided material layouts are used alone, with the thickness of PSLs adjusted according to their mechanical properties, the resulting compliances are en par with those generated by topology optimization with local volume constraint. In contrast, however, the computational complexity of the generation process is significantly reduced, and more regular and distributed layouts are generated. While compared to topology optimization with global volume constraint the overall resistance to the considered loading conditions is reduced, the layouts show significantly higher robustness to local damage. All of our experiments have shown that highly regular, smoothly varying, and distributed layouts are generated by PSL-guided material depo-

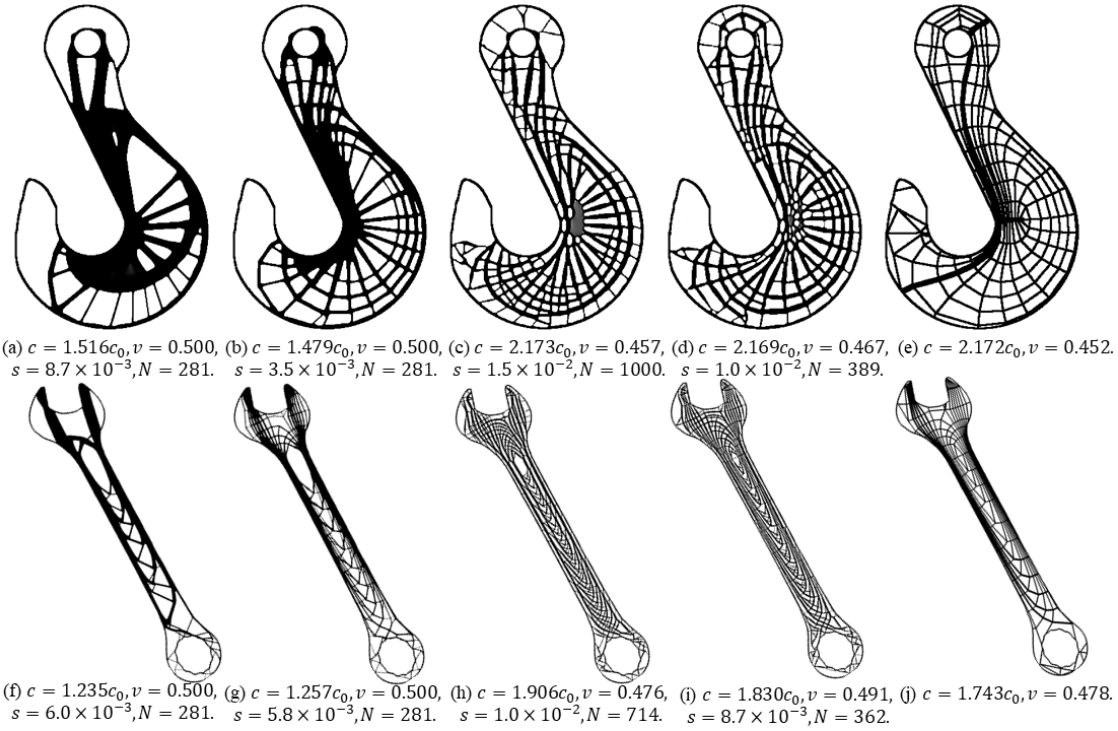

FIGURE 10. From (a) to (e), and (f) to (j), respectively: Material layouts generated via topology optimization with global volume constraint (with and w/o PSL-guided initialization), with local volume constraint (with and w/o PSL-guided initialization), and PSL-guided material layout.

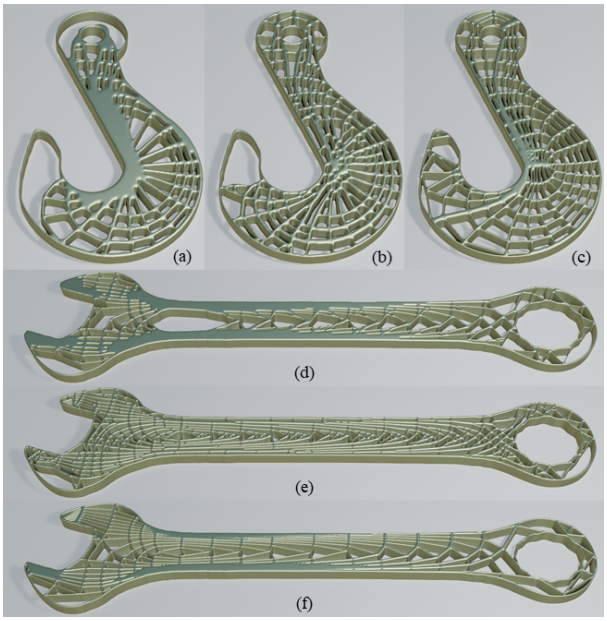

FIGURE 11. The 3D objects created by extruding the 2D designs. (a)-(f) correspond to Fig. 10b, d, e, g, i and j, respectively.

sition.

In the future, we intend to investigate the extension of PSL-guided material deposition to 3D domains. In particular, we aim at analyzing whether purely line-based structures can be obtained in 3D. Furthermore, it will be interesting to apply PSLs to compile global consistent structures from the local configuration of optimized orthotropic rectangular cells in homogenization-based topology optimization [18].

ACKNOWLEDGMENT

This work was supported in part by the German Research Foundation (DFG) under grant number WE 2754/10-1. Thanks to Christoph Neuhauser from TUM for supporting us with the 3D renderings.

REFERENCES

[1] Wu, J., Sigmund, O., and Groen, J. P., 2021. "Topology optimization of multi-scale structures: a review". *Structural and Multidisciplinary Optimization,* ***63***(3), p. 1455–1480.

[2] Bendsøe, M. P., and Kikuchi, N., 1988. "Generating optimal topologies in structural design using a homogenization

method". *Computer Methods in Applied Mechanics and Engineering,* ***71***(2), pp. 197–224.

[3] Bendsøe, M. P., 1989. "Optimal shape design as a material distribution problem". *Structural Optimization,* ***1***(4), pp. 193–202.

[4] Zhou, M., and Rozvany, G., 1991. "The COC algorithm, part ii: Topological, geometrical and generalized shape optimization". *Computer Methods in Applied Mechanics and Engineering,* ***89***(1), pp. 309–336.

[5] Mlejnek, H., 1992. "Some aspects of the genesis of structures". *Structural optimization,* ***5***(1-2), pp. 64–69.

[6] Wu, J., Aage, N., Westermann, R., and Sigmund, O., 2018. "Infill optimization for additive manufacturing – approaching bone-like porous structures". *IEEE Transactions on Visualization and Computer Graphics,* ***24***(2), February, pp. 1127–1140.

[7] Pantz, O., and Trabelsi, K., 2008. "A post-treatment of the homogenization method for shape optimization". *SIAM Journal on Control and Optimization,* ***47***(3), pp. 1380–1398.

[8] Groen, J. P., and Sigmund, O., 2018. "Homogenization-based topology optimization for high-resolution manufacturable microstructures". *International Journal for Numerical Methods in Engineering,* ***113***(8), pp. 1148–1163.

[9] Wu, J., Clausen, A., and Sigmund, O., 2017. "Minimum compliance topology optimization of shell-infill composites for additive manufacturing". *Computer Methods in Applied Mechanics and Engineering,* ***326***, pp. 358–375.

[10] Schmidt, M.-P., Pedersen, C. B., and Gout, C., 2019. "On structural topology optimization using graded porosity control". *Structural and Multidisciplinary Optimization,* ***60***(4), pp. 1437–1453.

[11] Das, S., and Sutradhar, A., 2020. "Multi-physics topology optimization of functionally graded controllable porous structures: Application to heat dissipating problems". *Materials & Design,* ***193***, p. 108775.

[12] Li, H., Gao, L., Li, H., Li, X., and Tong, H., 2021. "Full-scale topology optimization for fiber-reinforced structures with continuous fiber paths". *Computer Methods in Applied Mechanics and Engineering,* ***377***, p. 113668.

[13] Zhao, Z., and Zhang, X. S., 2021. "Design of graded porous bone-like structures via a multi-material topology optimization approach". *Structural and Multidisciplinary Optimization,* ***64***(8), pp. 677—698.

[14] Zhou, M., Lu, Y., Liu, Y., and Lin, Z., 2022. "Concurrent topology optimization of shells with self-supporting infills for additive manufacturing". *Computer Methods in Applied Mechanics and Engineering,* ***390***, p. 114430.

[15] Wang, J., Wu, J., and Westermann, R., 2022. "Stress topology analysis for porous infill optimization". *Structural and Multidisciplinary Optimization,* ***65***(3), pp. 1–13.

[16] Allaire, G., Geoffroy-Donders, P., and Pantz, O., 2019. "Topology optimization of modulated and oriented periodic microstructures by the homogenization method". *Computers & Mathematics with Applications,* ***78***(7), pp. 2197–2229.

[17] Groen, J. P., Wu, J., and Sigmund, O., 2019. "Homogenization-based stiffness optimization and projection of 2d coated structures with orthotropic infill". *Computer Methods in Applied Mechanics and Engineering,* ***349***, pp. 722 – 742.

[18] Wu, J., Wang, W., and Gao, X., 2021. "Design and optimization of conforming lattice structures". *IEEE Transactions on Visualization and Computer Graphics,* ***27***(1), pp. 43 – 56.

[19] Tam, K.-M. M., and Mueller, C. T., 2015. "Stress line generation for structurally performative architectural design". In 35th Annual Conference of the Association for Computer Aided Design in Architecture, ACADIA.

[20] Kwok, T.-H., Li, Y., and Chen, Y., 2016. "A structural topology design method based on principal stress line". *Computer-Aided Design,* ***80***, pp. 19–31.

[21] Daynes, S., Feih, S., Lu, W. F., and Wei, J., 2017. "Optimisation of functionally graded lattice structures using isostatic lines". *Materials & Design,* ***127***, pp. 215–223.

[22] Daynes, S., and Feih, S., 2022. "Bio-inspired lattice structure optimisation with strain trajectory aligned trusses". *Materials & Design,* ***213***, p. 110320.

[23] Wang, J., Neuhauser, C., Wu, J., Gao, X., and Westermann, R., 2021. "3D-TSV: The 3d trajectory-based stress visualizer". *arXiv preprint arXiv:2112.09202*.

[24] Delmarcelle, T., and Hesselink, L., 1994. "The topology of symmetric, second-order tensor fields". In Proceedings Visualization'94, IEEE, pp. 140–147.

[25] Hashin, Z., and Shtrikman, S., 1963. "A variational approach to the theory of the elastic behaviour of multiphase materials". *Journal of the Mechanics and Physics of Solids,* ***11***(2), pp. 127–140.

[26] Bendsøe, M. P., and Sigmund, O., 1999. "Material interpolation schemes in topology optimization". *Archive of Applied Mechanics,* ***69***(9-10), pp. 635–654.

[27] Sigmund, O., 2001. "A 99 line topology optimization code written in Matlab". *Structural and multidisciplinary optimization,* ***21***(2), pp. 120–127.

[28] Andreassen, E., Clausen, A., Schevenels, M., Lazarov, B. S., and Sigmund, O., 2011. "Efficient topology optimization in MATLAB using 88 lines of code". *Structural and Multidisciplinary Optimization,* ***43***(1), pp. 1–16.

[29] Svanberg, K., 1987. "The method of moving asymptotes—a new method for structural optimization". *International journal for numerical methods in engineering,* ***24***(2), pp. 359–373.

A Streamline-guided De-Homogenization Approach for Structural Design

Junpeng Wang
Computer Graphics and Visualization
Department of Informatics
Technical University of Munich
Garching 85748, Germany
Email: junpeng.wang@tum.de

Rüdiger Westermann
Computer Graphics and Visualization
Department of Informatics
Technical University of Munich
Garching 85748, Germany
Email: westermann@tum.de

Jun Wu*
Department of Sustainable
Design Engineering
Delft University of Technology
Delft 2628 CE, The Netherlands
Email: j.wu-1@tudelft.nl

We present a novel de-homogenization approach for efficient design of high-resolution load-bearing structures. The proposed approach builds upon a streamline-based parametrization of the design domain, using a set of space-filling and evenly-spaced streamlines in the two mutually orthogonal direction fields that are obtained from homogenization-based topology optimization. Streamlines in these fields are converted into a graph, which is then used to construct a quad-dominant mesh whose edges follow the direction fields. In addition, the edge width is adjusted according to the density and anisotropy of the optimized orthotropic cells. In a number of numerical examples, we demonstrate the mechanical performance and regular appearance of the resulting structural designs, and compare them with those from classic and contemporary approaches.

1 Introduction

Achieving the highest stiffness while using the least amount of material is a fundamental task in mechanical design. This is often formulated as an optimization problem, e.g., topology optimization, in which the material distribution is optimized [1,2]. Early works in topology optimization employ a material model corresponding to infinitely small square cells with rectangular holes [3]. The orientation of the cell and the size of the rectangular hole therein are optimized to minimize the compliance of the structure. The material properties of these orthotropic cells are constructed using homogenization. This homogenization-based approach generates a mathematical specification of theoretically optimal structures. Yet how to translate the specification of these spatially-varying orthotropic cells into a globally consistent geometry has remained a challenge. The lack of a consistent geometry means that the optimal structure is not manufacturable. To circumvent this problem, the focus of research in topology optimization has since the 1990s shifted to optimizing the distribution of solid isotropic materials. Popular approaches such as those based on density [4, 5], level-sets [6, 7], evolutionary procedures [8], and explicit geometric descriptions [9, 10], all belong to this category.

Recent years have seen a revival of homogenization-based approaches, with a focus on the post-process that translates the results of homogenization-based topology optimization into a manufacturable geometry. This post-process is now often referred to as *de-homogenization*. Special emphasis has been put on the efficient computation of a high-resolution structural design from the result of topology optimization on a coarse grid. Pantz et al. proposed one of the first solutions towards this end [11], which was revisited and improved by Groen and Sigmund [12] and Allaire et al. [13]. These approaches have since been extended to 3D [14, 15], and to deal with singularities in the optimized orientation fields [16]. It was also applied to simultaneously optimize the structural layout and the substructures therein [17]. A key component in these approaches is computing a fine-grid scalar field whose gradients are aligned with optimized orientations from homogenization-based topology optimization. Wu et al. reformulated this post-process as quad/hex-dominant meshing, i.e., constructing quad/hex-dominant meshes whose edges are aligned with the optimized orientations [18]. Stutz et al. [19] reported a method to generate high-resolution multi-laminar structures from frame fields by tracing the *stream surface*.

*Address all correspondence to this author.

They further formulated the finding of such a set of well-spaced stream surfaces as an optimization problem. Convolutional neural networks have also been found useful for de-homogenization [20]. Alternative de-homogenization approaches include [21, 22].

In the same line with previous works, we propose a de-homogenization approach which takes as input the width and orientation of spatially-varying square cells that are optimized via homogenization-based topology optimization. A significant difference of our approach is that it directly generates an explicit representation in the form of a quad-dominant mesh, instead of a binary material field that needs further post-processing to translate it into a geometric representation. The edges of the mesh represent beam-like substructures of varying width, which are aligned with the optimized cell orientations. This compact representation is beneficial for downstream operations such as user editing and fabrication process planning.

Our technical contribution is a novel method to convert the result of the homogenization-based optimization process, i.e., the optimized cell widths and orientations, into a domain-filling mesh whose elements are then de-homogenized consistently. This is achieved by first parameterizing the design domain using a set of domain-filling and evenly-spaced streamlines that are aligned with the edges of optimized cells. The streamlines are then converted into a graph, from which a quad-dominant mesh whose edges follow the optimized direction fields can be computed efficiently. For de-homogenization, the edge widths are varied per element and along different directions according to the average direction and volume fraction of the optimized cells covered by an element. Thus, it can avoid the projection step to optimize for a consistent fine-grid scalar field (e.g., in [12]).

We draw inspiration from prior work on structural design using principal stress lines (PSLs) [23, 24, 25]. The structures following principal stress directions are continuous, and this regularity is often appreciated in industrial design and architecture [26]. These prior explorations, however, make use of the principal stress directions in the stress field of a solid object with isotropic material. It deviates from the stress tensor field of the final optimized structure which is composed of orthotropic cells. Furthermore, the uniform sampling of the stress lines has been a challenge, and the beam width was typically assigned based on heuristics. For example, Kwok et al. [24] proposed an iterative optimization process in which lattice structures along PSLs appear incrementally. This method works for concentrated loads but it is challenging to cope with distributed loads on the design domain. Wang et al. [25] used the space-filling and evenly-spaced PSLs for structural design, where the beam width was adjusted using a strain energy-based importance metric. These approaches are attractive for their computational efficiency, yet the stiffness of the obtained structures are sub-optimal. In contrast to these works, we use the result of homogenization-based topology optimization for streamline tracing and to de-homogenize the single elements in the resulting mesh structure. We show that this creates structures with significantly improved stiffness.

The remainder of this paper is organized as follows. We first give an overview of the proposed method in Section 2. In Section 3, we review the problem formulation of homogenization-based topology optimization. In Section 4 we describe the construction process of a space-filling mesh from the direction fields that are optimized based on homogenization. Mesh-based de-homogenization is presented in Section 5, and we demonstrate the effectiveness of our approach in a variety of examples in Section 6. Section 7 concludes the paper with a discussion of the proposed approach as well as future research directions.

2 Method Overview

Our approach comprises three major stages, which are illustrated in Fig. 1. The input is a design domain including boundary conditions, i.e., the fixations of the domain and the external forces (Fig. 1a). Furthermore, the material properties and the volume fraction that can be consumed by the optimized layout are set by the user.

Optimization. In the first stage, homogenization-based topology optimization is used to optimize the orthotropic cell distribution (Fig. 1b). From this distribution, the direction fields (Fig. 1c) and the density distribution (Fig. 1d) are extracted. The direction fields locally coincide with the edges of orthotropic square cells whose deposition ratio and orientation are optimized. The size of the rectangular hole within each cell determines the local material consumption, and the ratio between the widths of the cell's edges determine the local material anisotropy.

Parametrization. In the second stage, first a domain-filling and evenly-spaced set of streamlines is computed in the direction fields (Fig. 1e). Then, a graph structure is constructed, in which adjacent streamline intersection points and intersection points with the initial domain boundary are connected via edges (Fig. 1f). The graph is finally converted into a mesh that is composed of mostly quadrilateral and few triangular cells bounded by the edges of the graph (Fig. 1g).

De-homogenization. In this last stage, the final structural design (Fig. 1h) is computed by jointly using the quad-dominant mesh, the optimized density distribution, and the anisotropy of optimized square cells. The mesh structure divides the design domain into a space-filling set of elements whose interior is filled with material according to the optimized density distribution and the anisotropy of each element.

3 Homogenization-based Topology Optimization

For structures under a single load, the theoretically optimal structural layout can be approximated by optimizing the distribution of square cells with a rectangular hole [3]. As illustrated in Fig. 2a, the design domain is discretized into finite elements. Each element represents a repetition of an adapted configuration of the unit cell. The square cell has a unit side length. Within it, there is a rectangular hole (Fig. 2c). The configuration of the unit cell is thus described

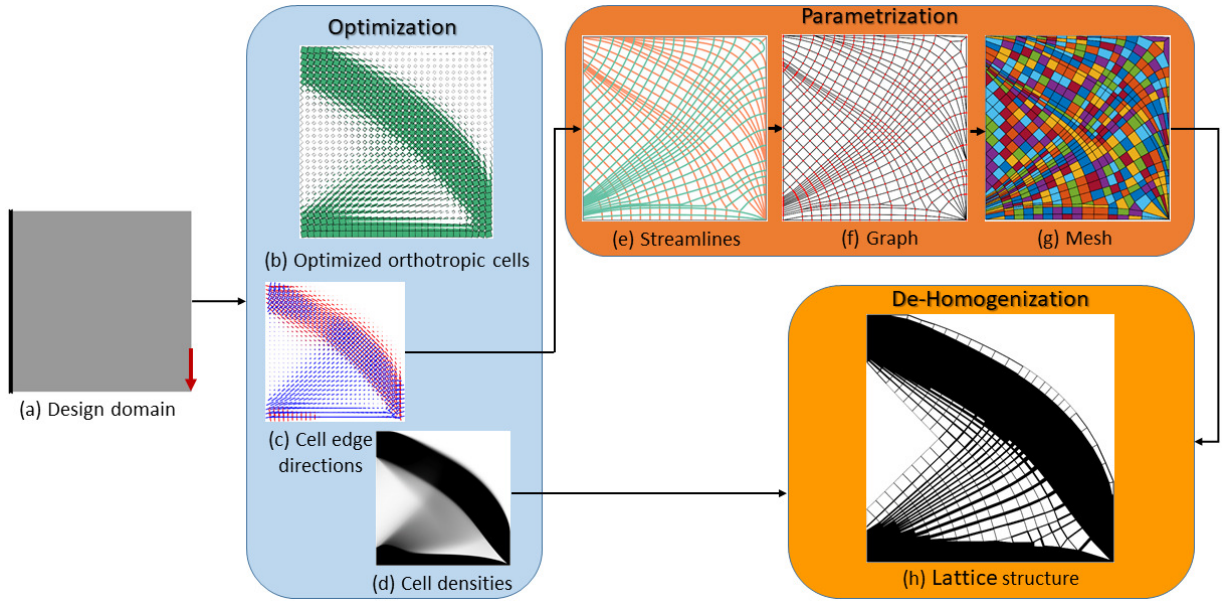

Fig. 1. Method overview. (a) The design domain and boundary conditions. (b) The optimized distribution of orthotropic cells from homogenization-based topology optimization. (c) The mutually orthogonal direction fields defined by the axes of the orthotropic cells. (d) The equivalent density distribution of the orthotropic cells. (e) Streamlines traced along the two orthogonal direction fields. (f) The graph structure extracted from the streamlines. (g) The quad-dominant mesh obtained from the graph structure. (h) The final structural design.

by the hole sizes α_x and α_y and rotation angle θ. The mechanical properties of the unit cell is orthotropic. In this paper we refer to these adapted cells as *orthotropic cells*. The density or deposition ratio (ρ_e) of each cell is measured by $1-\alpha_x\alpha_y$. The elasticity tensor of the orthotropic cell is computed by

$$C(\alpha_x,\alpha_y,\theta) = R^T(\theta)C^H(\alpha_x,\alpha_y)R(\theta), \tag{1}$$

where $R(\theta)$ is the rotation matrix, and $C^H(\alpha_x,\alpha_y)$ represents the effective elasticity tensor for an axis-aligned unit cell with α_x,α_y, evaluated by homogenization.

The structural design is formulated as compliance minimization,

$$\min_{\boldsymbol{\alpha}_x,\boldsymbol{\alpha}_y,\boldsymbol{\theta}} \quad \frac{1}{2}\boldsymbol{F}^T\boldsymbol{U}, \tag{2}$$

$$\text{subject to} \quad \boldsymbol{K}(\boldsymbol{\alpha}_x,\boldsymbol{\alpha}_y,\boldsymbol{\theta})\boldsymbol{U} = \boldsymbol{F}, \tag{3}$$

$$\frac{1}{n}\sum_e \rho_e - \alpha_{global} \leq 0, \tag{4}$$

$$0 \leqslant \alpha_x, \alpha_y \leqslant 1. \tag{5}$$

Here the objective is to minimize the elastic energy. $\boldsymbol{F}$ is the loading vector. $\boldsymbol{U}$ is the displacement vector, obtained by solving the static equilibrium equation (Eq. 3). $\boldsymbol{K}$ is the stiffness matrix in finite element analysis. n is the number of finite elements. α_{global} is the volume fraction prescribed by the user.

We use the procedure reported by Groen and Sigmund [12] for solving the optimization problem. The educational code for this was provided in the review article [27].

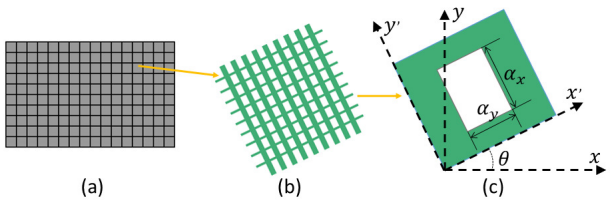

Fig. 2. (a) The design domain is discretized into bilinear square grids. (b) Each square element is assumed to be filled by the orthotropic material. (c) The size and orientation of the approximately equivalent orthotropic cell, i.e., the square element with rectangular hole, are taken as design variables in homogenization-based topology optimization.

In this procedure, α_x and α_y are optimized by gradient-based numerical optimization, while the rotation angle (θ) in each iteration is determined by the corresponding principal stress direction.

Figure 3 demonstrates the results of the homogenization-based optimization for the "Cantilever" model, showing the initial domain and external forces (a), the extracted density layout (b) and the direction fields of the optimized orthotropic cell distribution (c). Fig. 3d provides a closeup view of the layout of the orthotropic cells. This layout is not directly manufacturable, and needs to be transformed into a consistent geometry.

4 Parametrization

The goal of our approach is to convert the locally spatial-varying orthotropic cells into a globally consistent geometry. While thick sub-structures or one single solid block should

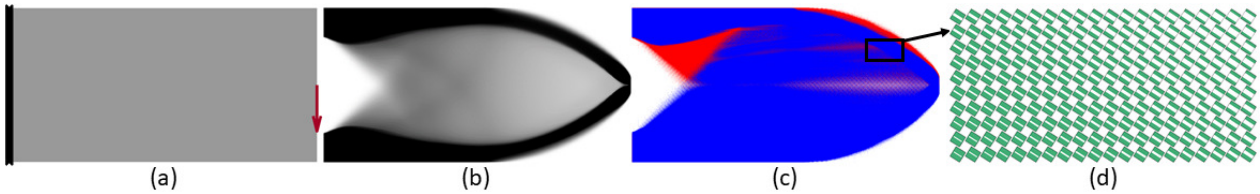

Fig. 3. (a) The design domain. (b), (c) The optimal density layout and the corresponding direction field produced by the homogenization-based optimization. (d) Closeup of the optimized orthotropic cells sampled from the highlighted region in (c).

be placed in dense regions, in less dense regions only few thin sub-structures are required. These sub-structures follow the optimized direction fields. In contrast to previous approaches that find a fine-grid scalar field with constraints on its gradient, we trace streamlines along the optimized direction fields. This ensures a global consistency of the sub-structures, and their alignment with the optimized direction fields.

We use the direction fields that are optimized via the homogenization-based approach and generate a trajectory-based parametrization of the design domain. Therefore, a uniformly distributed set of streamlines in the direction fields is computed by using the stress tensor visualization tool by Wang et al. [28]. It enables to compute and visualize a space-filling and evenly-spaced set of streamlines in three mutually orthogonal direction fields. By setting the third vector field to zero, it can be used right away to work with 2D fields (i.e., the u- and v-field in our current application). We will subsequently call the corresponding streamlines in the u- and v-field the u-streamlines and v-streamlines, respectively. The streamline seeding strategy ensures that around each streamline an empty band is generated from which no streamline is seeded, and new streamlines are always seeded from points on existing streamlines. In this way, a fairly uniform and space-filling set of streamlines is computed (see Fig. 4a).

Each streamline can be converted into a polyline consisting of a set of intersection points and linear connections between them [29]. From this representation, a graph structure with the nodes and edges, respectively, being the intersection points and piecewise linear connections between them can be easily constructed. By connecting adjacent integration points on the domain boundaries, the final graph —due to the mutual orthogonality of the u- and v- streamlines—comprises mostly regions that are bounded by exactly four edges. Only at degenerate points and at points lying on a boundary, regions that are bounded by three edges can occur. The result of this process is shown in Fig. 4b.

Finally, the graph structure is used to discretize the design domain into a set of independent elements, i.e., the interior regions of the graph structure, so that each element can be de-homogenized independently. The orientation of the elements is given by the streamline skeleton, and the de-homogenization process proceeds by filling the elements with material according to the optimized density field. This is performed by extruding material from the edges of each element inward, according to the volume fraction of the continuous density field in each element. To do so, the graph structure first needs to be converted into an explicit cell-based mesh structure.

Since the 2D graph structure represents the connectivity (i.e. the edges) between the coordinates of the streamline intersection points, a quad-dominant mesh can be constructed in a straight forward way from this structure. By iteratively processing the local vertex and edges topology along streamlines, a mesh comprising quadrilateral and triangular elements can be computed, along with the cell topology that represents the cell adjacency information. Note that the local ordering of nodes of each quadrilateral and triangular cell needs to be consistent, i.e., either clockwise or counter-clockwise. Figure 4c shows the constructed mesh from the graph structure in Fig. 4b.

Singularities. To obtain a consistent mesh structure from the streamline skeleton, singularities in the direction fields need to be determined and treated in a special way. In our case, where the direction fields coincide with principal stress directions, singularities occur at so-called degenerate points of the corresponding stress field, i.e., points where the two eigenvalues of the stress tensor in the underlying stress tensor field become indistinguishable. In the seminal work by Delmarcelle and Hesselink [30] both the classification of degenerate points and their numerical computation is discussed. In the vicinity of degenerate points a set of hyperbolic and parabolic sectors exist, in which similar patterns of neighboring trajectories are observed. The topological skeleton consists of the boundaries between adjacent sectors—so-called separatrices—and indicate pathways along which the forces are steered towards the degenerate points. By first extracting the degenerate points and computing the topological skeleton, the separatrices can then considered as seed streamlines as described before, so that an evenly-spaced set of streamlines is computed in each sector. Let us refer to the work by Wang et al. [29] for a more detailed description of the implemented procedure. Figure 11b and 13f show the embedding of singularities into the computed streamlines.

5 De-Homogenization

In order to de-homogenize the optimal density layout, i.e., to convert the continuous density layout into a binary one, we utilize the constructed quad-dominant mesh and de-homogenize the region covered by each mesh element separately. As shown in Fig. 5, each element covers a certain region in the domain. The material in each region, i.e., the deposition ratio, should be re-distributed so that a) a binary

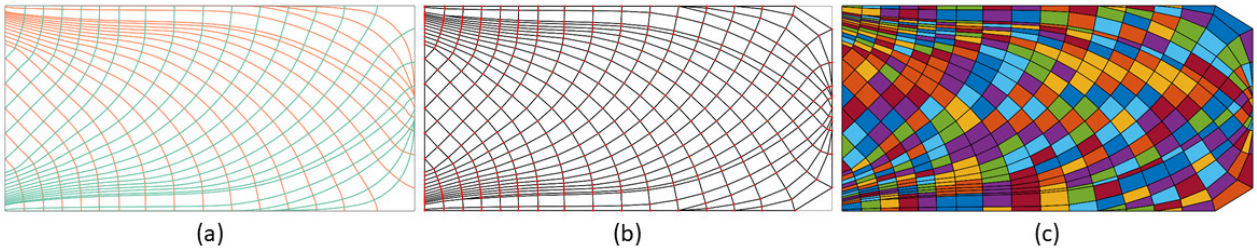

Fig. 4. Parametrization by streamlines. (a) Space-filling and evenly-spaced streamlines. (b) Graph structure. (c) Quad-dominant mesh.

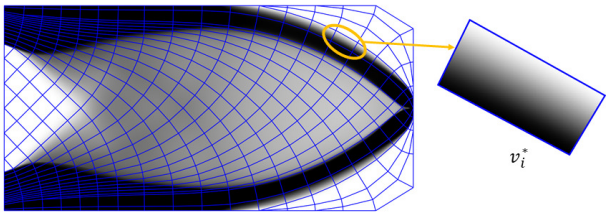

Fig. 5. Correspondence between continuous material field and mesh elements, facilitating the assignment of a material budget v_i^* to each mesh element and de-homogenization of each element separately.

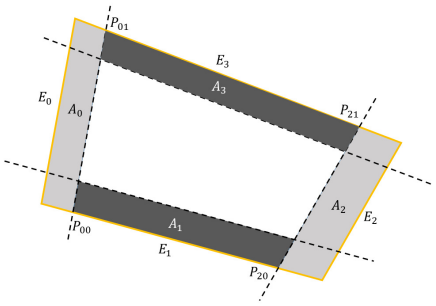

Fig. 6. Schematics of computing the area subtended by edges of a certain thickness. From intersection points between dashed lines (extruded edges) and edges of the mesh element the areas can be computed.

material layout is generated, b) a continuous transition at the element boundaries is obtained, and c) the orthotropic cells' orientations, which have been optimized with respect to the object's compliance, is reflected in the binary material layout. The target deposition ratio v_i^* of a mesh element (see Fig. 5) is measured by $\frac{D}{M}$, where M is the number of orthotropic cells located in the region covered by the element, and D is sum of the density values over all these cells. The de-homogenized mesh element should keep this deposition ratio after de-homogenization.

Our approach can generate the final design at different granularity levels in a straight forward way, by varying the width of the empty bands around each computed streamline. The width is controlled by the distance threshold in the streamline seeding process (refer to [28] for details). Since the resolution of the corresponding quad-dominant mesh varies spatially and is not necessarily at a resolution comparable to the finite element discretization used in topology optimization, the density and directions need to be resampled from the finite element grid to compute the target deposition ratio of a mesh element. This is performed via bilinear interpolation at a set of sampling points in each mesh element.

5.1 Anisotropic mesh element

To distribute the material in a mesh element according to the mentioned requirements, we propose to extrude the available material from the edges of each element inward. By starting with a minimal edge thickness, the edges are iteratively thickened until all available material is used. In this way, we enforce a layout that aligns with the element orientation, seamlessly connects adjacent elements, and can furthermore account for an anisotropic stress distribution by adapting the edge thickness according to the mechanical properties of each element.

The process starts by removing mesh elements which have a very low target deposition ratio (e.g., $v^* < 0.05$), in order to avoid the generation of very thin mesh edges that can cause difficulties in the manufacturing process. Similarly, mesh elements with a large deposition ratio (e.g., $\frac{D}{M} > 0.95$) are made fully solid. The edges of all remaining mesh elements are set to a minimum thickness t_0.

Taking a single mesh element as shown in Fig. 6, its deposition ratio v is computed as the sum of the areas A_i covered by each extruded edge, subtracting the sub-areas that are counted twice, and then dividing by the total area of the element. We start with two opposite edges and compute for each edge the intersection points between the extruded edge and the respective other mesh edges ($P_{00}, P_{01}, P_{20}, P_{21}$ in Fig. 6). Including the endpoints of the mesh edges, this gives two quadrilaterals A_0, A_2, whose areas can be computed via triangulation. For the other two mesh edges, we use the newly computed edge intersection points and the intersection points between the four extruded edges, and compute two quadrilaterals representing the missing areas A_1, A_3. Now, the thickness t of each edge can be increased iteratively from the initial value t_0, until the actual deposition ratio v approaches the target v^*, i.e., the available material budget is used.

In order to match the mechanical properties of the set of orthotropic cells covered by a single mesh element, we start with a minimal edge thickness, and then thicken the edges according to the ratio of the edge thicknesses of the orthotropic cells (Fig. 7). The edge thicknesses $1 - \alpha_x$ and

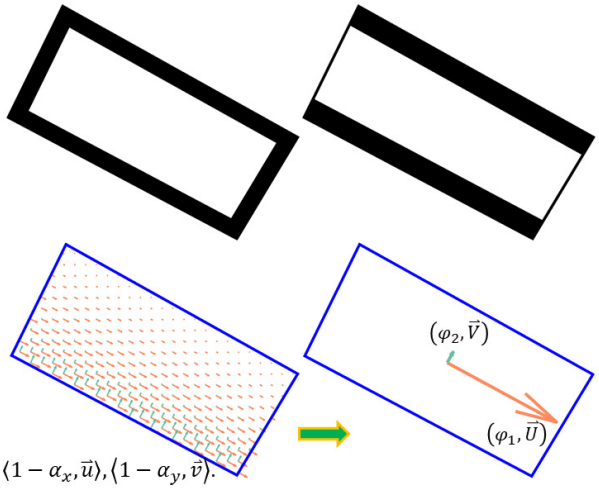

Fig. 7. Top: the edges are equally thickened (left) or thickened (using the same amount of material) according to the edge thicknesses of the orthotropic cells they cover (bottom left). Bottom: For the set of orthotropic cells covered by a mesh element, representative edge thicknesses and orientation are computed via averaging. The arrow length indicates the thickness of edges along the pointing direction.

$1-\alpha_y$ as well as the orientation of an orthotropic cell have been optimized to maximize stiffness of the resulting layout. As such, if all cells covered by a mesh element have the same thickness ratio, and are consistently orientated with the mesh element, the material should be deposited along the element edges so that the thickness ratio of the cells is maintained. However, since the ratio and orientation vary across the cells, in general, we first need to compute representative values for both (see Figure 7 bottom for an illustration).

We do so by first computing the normalized thickness of the cell edges φ_1 and φ_2 following the u- and v-field, respectively, by adding up the values of the per-cell thicknesses and dividing through the maximum of the resulting values, i.e.,

$$\begin{aligned} &\varphi_1^* = \sum(1-\alpha_x^i),\ \varphi_2^* = \sum(1-\alpha_y^i), \\ &\varphi_1 = \varphi_1^*/\max(\varphi_1^*, \varphi_2^*),\ \varphi_2 = \varphi_2^*/\max(\varphi_1^*, \varphi_2^*). \end{aligned} \tag{6}$$

Then, to determine which edge of the mesh element corresponds to φ_1 and which to φ_2, we compute the average direction vectors $\overrightarrow{U}$ and $\overrightarrow{V}$ of all the per-cell direction vectors $\overrightarrow{u_i}$ and $\overrightarrow{v_i}$, i.e., $\overrightarrow{U} = \text{norm}(\sum \overrightarrow{u_i})$ and $\overrightarrow{V} = \text{norm}(\sum \overrightarrow{v_i})$. We let the mesh edges correspond to $\overrightarrow{U}$ or $\overrightarrow{V}$ to which they have the least directional deviation.

Now, we can introduce for each mesh edge e_j a scaling factor w_j, which is calculated by $e_j = t_0 + w_j\delta$. Here δ is an increment used for adjusting the edge thickness iteratively. With the thicknesses and directions $(\varphi_1, \overrightarrow{U})$ and $(\varphi_2, \overrightarrow{V})$, the corresponding weighting factor w_j of the j-*th* element edge is given by

$$w_j = \begin{cases} \varphi_1 & \theta_{j1} \leqslant \theta_{j2} \\ \varphi_2 & \theta_{j1} > \theta_{j2} \end{cases}. \tag{7}$$

Here, θ_{j1} and θ_{j2} are the included angles between the j-*th* element edge and the directions $\overrightarrow{U}$ and $\overrightarrow{V}$, respectively, and we consistently use the same thickness for opposite edges in each quadrilateral element, and the triangular elements are treated as degenerate quadrilaterals where one of the edges is collapsed, specifically, for each edge, the weighting factor w_j is determined by Eqn. 7.

It is worth mentioning that in rare cases the per-cell directions may change considerably in a single mesh element, and thus the per-element direction becomes less representative. To cope with this, the mesh element can be subdivided into a set of smaller elements, for each of which the de-homogenization is performed as described.

6 Results

We demonstrate our de-homogenization approach with several examples, and compare the results to those of density-based and de-homogenization approaches. In all cases, the design domains are discretized by Cartesian grids with unit-size. The Young's modulus and Poisson's ratio are set to 1.0 and 0.3, respectively. Homogenization-based topology optimization is performed with the Matlab code provided in [27]. We terminate the optimization process after 200 iterations. We have implemented the proposed parametrization and de-homogenization operations in Matlab as well. All experiments have been carried out on a desktop PC with an Intel Xeon CPU at 3.60GHz.

Comparison to density-based approaches. In our first experiment, we use the cantilever model described in Fig. 3a to demonstrate the properties of the proposed de-homogenization approach and compare the results to those of density-based topology optimization.

Figure 8 (top) shows the de-homogenization results for different streamline densities, resulting in an increased or decreased number of ever smaller or larger mesh elements, respectively. The compliances of the designs with different granularity vary only slightly. With c_0 being the compliance of the fully solid domain, one can see that with the same amount of material all resulting designs achieve almost the same compliance of roughly $1.5c_0$. The compliance of the de-homogenized binary layouts is slightly higher than that from homogenization-based optimization ($1.447c_0$).

In Fig. 8 (bottom), we compare our results to those generated by the stress trajectory-guided structural design by Wang et al. [25], the porous infill approach using local volume constraints by Wu et al. [31], and density-based topology optimization with a global volume constraint. In all examples, the same number of simulation element as for de-homogenization in our approach is used.

Fig. 8d,e show the results of stress trajectory-guided structural design. In (d), the material is distributed along

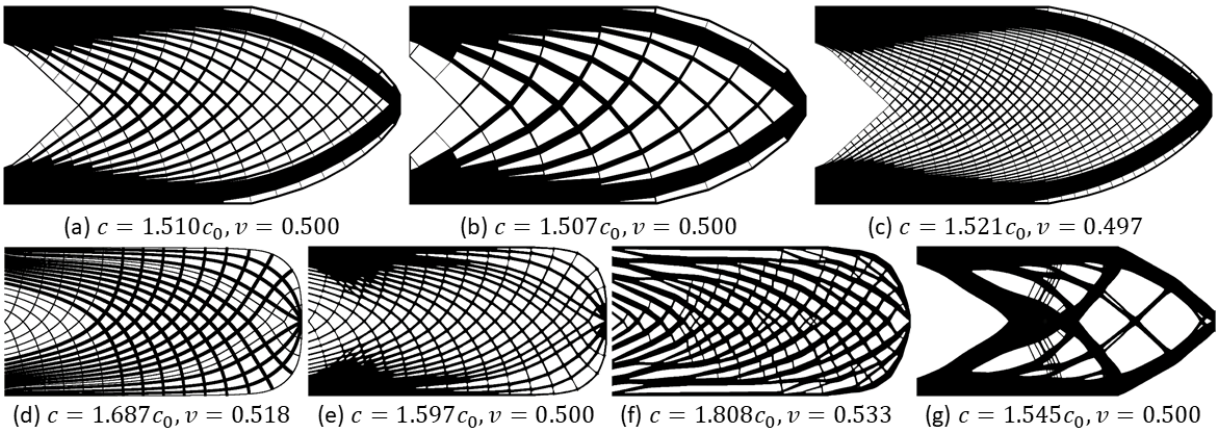

Fig. 8. Top: Results with the proposed de-homogenization strategy. (a) to (c) demonstrate the changes due to different amounts of streamlines used in the parametrization stage. Bottom: Comparison to alternative approaches for generating a binary design via topology optimization. (d) PSL-guided material layout [25]. (e) PSLs-initialized density-based topology optimization using a global volume constraint [25]. (f) Porous-infill optimization with local volume constraints [31]. (g) Density-based topology optimization with a global volume constraint. c_0 and c, respectively, are the compliances of the fully solid domain and the shown results, v is the volume fraction.

principal stress trajectories of the solid object under load, and the thickness of the material is adapted according to the accumulated strain energy along each trajectory. Fig. 8e shows the optimized material layout when the material field in (d) is used as initialization for topology optimization with a global volume constraint. The generated layouts also show a very regular structural design, but a considerably higher compliance than the de-homogenization approach. The latter can also be observed when comparing to porous infill optimization (Fig. 8f) which applies a strict constraint on local volume. Here, besides having a smaller compliance, the de-homogenized layout (Fig. 8a-c) also shows a more regular structural layout. Notably, while porous infill optimization generates many bifurcations, i.e., solid strands that merge and split, the de-homogenization approach, per construction, results in a grid-like structure mostly comprising quadrilateral elements. Finally, compared to density-based topology optimization with a global volume constraint (Fig. 8g), our result still shows a slightly smaller compliance, yet the results are far more regular and, are expected to exhibit higher stability when the load conditions are changed or certain parts undergo damage, as demonstrated for evenly-spaced, space-filling structures in [31, 29].

Comparison to de-homogenization approaches. A major difference between our approach and previous de-homogenization approaches (e.g., [12, 13]) is the representation of the optimized structure. Our design is encoded by a graph, rather than a density distribution. The graph-encoded representation is more convenient for downstream operations such as user editing and fabrication tool-path generation, though these advantages are not explored further here.

In Fig. 9, we compare the result that is obtained with our approach to the result of projection-based de-homogenization by Groen and Sigmund [12]. To match their model configuration, the force applied to the cantilever model has been changed accordingly, and homogenization-based topology optimization is performed at a coarse grid resolution of 100×50. Density based topology optimization using a global volume constraint is also included here as a reference. It is computed at a grid resolution of 1600×800. It can be seen that the compliance of the layout generated by our approach (d) is only slightly higher than that of the layout produced by the method of Groen and Sigmund in (e), yet using a little less material. The layout in (e) has some concentrated clusters in the middle of the domain, while our approach generates a more uniform grid-like material layout. This difference is likely due to the parameter setting (e.g., the filter size) in the homogenization-based topology optimization. While Groen et al. perform an optimization to generate a consistent binary pattern at finer resolution (1600×800 in the example) from the coarse grid results, in our method the resolution of the final layout is controlled by the density of seeded streamlines. Since streamlines are always traced in the initial domain, they always stay entirely within the domain. The optimized quantities required to trace streamlines and de-homogenize the final mesh elements are reconstructed via bilinear interpolation from the coarse grid.

Figure 10 shows the structural design that is generated by our method when applied to the Michell's structure according to the specification in [12]. The coarse and fine grid resolutions used for optimization and de-homogenization are 80×60 and 1280×960, respectively. As can be seen, perfect symmetry is not achieved, because the streamline seeding process does not consider symmetry in the design domain or the underlying direction field. If symmetry is known beforehand, however, the seeding process can be adapted accordingly. The compliance of the streamline-guided design (Fig. 10d) is even lower than the design that is generated via projection-based de-homogenization (Fig. 10e). Overall, our experiments indicate that streamline-based de-homogenization generates designs with a compliance that is

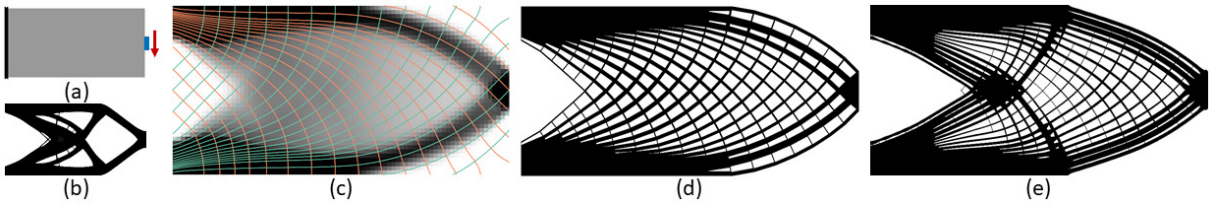

Fig. 9. Comparison of de-homogenization approaches on a cantilever beam. (a) The design domain and boundary conditions. (b) The result of density-based topology optimization with a global volume constraint simulated ($c = 62.56$, $v = 0.500$). (c) Optimal density layout ($c = 57.21$, $v = 0.500$), superimposed with streamlines. (d) The de-homogenized structural design by our method ($c = 60.04$, $v = 0.500$). (e) The result of the projection-based de-homogenization ($c = 58.57$, $v = 0.510$). The image (e) is reprinted from [12] with permission from *John Wiley & Sons*.

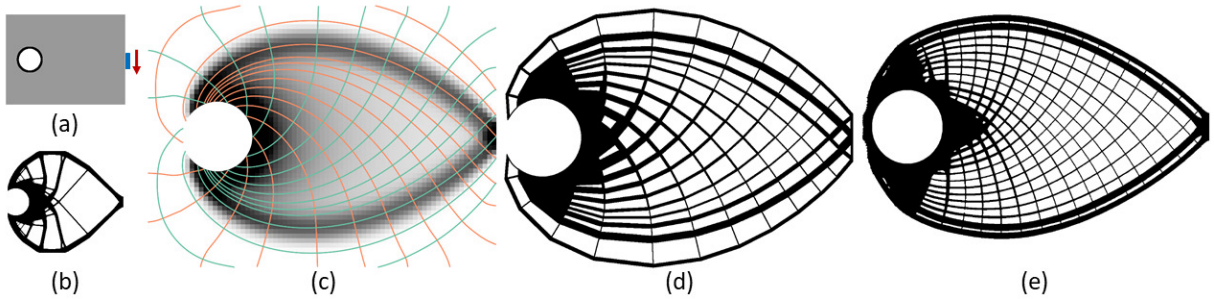

Fig. 10. Comparison of de-homogenization approaches on a Michell's structure. (a) The design domain and boundary conditions. (b) The result of density-based topology optimization with a global volume constraint ($c = 64.452$, $v = 0.250$). (c) Optimal density layout ($c = 55.64$, $v = 0.250$), superimposed with streamlines. (d) The de-homogenization using our approach ($c = 62.301$, $v = 0.250$). (e) The result of the projection-based de-homogenization ($c = 67.830$, $v = 0.252$). The image (e) is reprinted from [12] with permission from *John Wiley & Sons*.

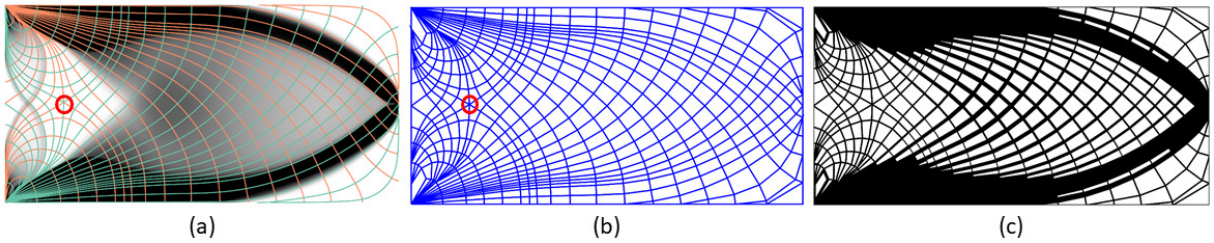

Fig. 11. Tests on a cantilever beam fixed by the endpoints of its left boundary. (a) Optimal density layout ($c^* = 1.138c_0$, $v = 0.500$) and streamlines. (b) The generated streamline graph. The degenerate point (singularity) is marked by the red circle. (c) The de-homogenized structural design ($c = 1.170c_0$, $v = 0.500$).

comparable to what can be achieved with a projection-based approach.

Performance analysis. Our proposed strategy can be split into *Parametrization* and *De-homogenization*. In the parametrization stage, it is first required to compute a set of domain-filling and evenly-spaced streamlines. Under the assumption that the streamline density is selected so that the initial seed points are about a distance of one cell size from each other, the computational complexity is $O(N)$, where N is the number of cells. In addition, whenever a new streamline is computed, all remaining seed points within a band of a selected width around that streamline are discarded. Since this band can be represented in the grid structure by flagging cells entirely outside the band, this operation requires to investigate only few of all possible seed points. Finally, to generate a mesh structure, the intersections between the streamlines along one optimized direction field with all other streamlines of the respective other direction field need to be computed. A straight forward realization is to first compute all intersection points, including the indices of the intersecting streamlines, to store them in a shared point representation, and then sort these points along each streamline individually. Notably, intersection computations and sorting can be parallelized effectively, so that we even expect interactive update rates for the grid resolutions used in our work when using an optimized GPU solution.

In the de-homogenization stage, it is first required to determine the target deposition ratio v_i^* of each mesh element, and then to compute the widths of the element edges

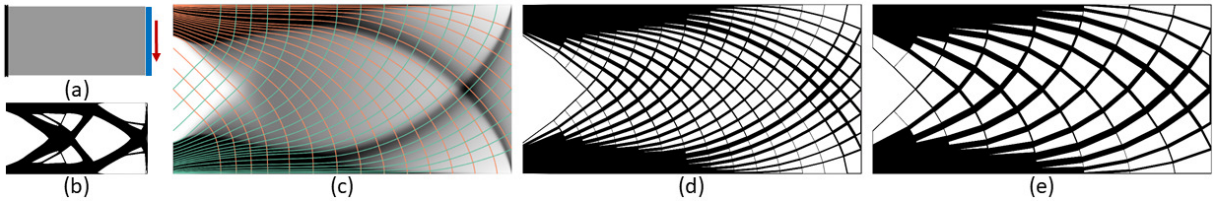

Fig. 12. (a) A cantilever under a distributed load along the right edge. (b) Result of density-based topology optimization with a global volume constraint ($c = 1.675c_0$, $v = 0.500$). (c) Optimal density layout ($c^* = 1.533c_0$, $v = 0.500$) and streamlines. (d) De-homogenized structural design ($c = 1.661c_0$, $v = 0.500$). (e) De-homogenized structural design with less streamlines ($c = 1.680c_0$, $v = 0.500$).

to enforce the same deposition ratio before and after de-homogenization. Notably, since the mesh elements can be processed independently, also this process can be effectively parallelized.

In contrast to our approach, previous de-homogenization approaches (e.g., [12, 13]) require solving a linear system of equations with as many degrees of freedom as cells on the finest level. Even with optimized solvers, the number of iterations is of the order N and, thus, computationally more demanding than our approach. As an indication of improved computational complexity, our approach took 10 seconds or less for most of the examples, while in [12] under the same problem settings the computations took 100 seconds. The computers used for testing were not precisely the same but comparable.

Table 1 provides a performance and quality assessment of all examples used in this work, including the compliances of the de-homogenized designs (c), the deviations (ξ) to the homogenization-based analysis (c^*), the number of used streamlines, the number of elements of the generated mesh, and the corresponding computation times. We further split the computation times required by parametrization into streamline generation (t_1) and mesh construction (t_2), and the times required by de-homogenization into the target deposition ratio calculation (t_3) and edge width identification (t_4). In all of our experiments, the time for parametrization and de-homogenization combined is about 10 seconds or even less. We also list the compliance (c^+) of the results that are generated by topology optimization with a global volume constraint under the same design specifications.

Singularity treatment. As we described in Section 4, our proposed approach can handle situations where singularities exist in the direction fields that are obtained via homogenization-based optimization. Such singularities usually incur discontinuities during streamline tracing, and they furthermore result in low convergence for density-based topology optimization under local volume constraints [29]. The singularity can be detected by topology analysis of the orthogonal direction fields. As an example, we again use the cantilever model (Fig. 3a), but now replace the distributed fixation condition with point fixations applied on the endpoints of the left boundary. Fig. 11a highlights a singularity in the left part of the domain, where 3 u-streamlines and 3 v-streamlines converge to a single point. This type of singularity is termed a trisector degenerate point in stress topology analysis, and the 6 streamlines are the corresponding topological skeleton. Figure 11b shows the generated mesh, which demonstrates that a consistent structure can be obtained around the singularity. The de-homogenized result is shown in Fig. 11c.

Distributed loads. Our de-homogenization approach naturally works well also for distributed loads. Fig. 12a shows the structural design problem under distributed loads. Fig. 12 compares the results of density-based topology optimization with a global volume constraint to those of our proposed de-homogenization method using different streamline densities. The compliance from density-based topology optimization is between the tight range of compliances of de-homogenized structures with two different streamline densities. The deviation of the compliances of the de-homogenized structures (d and e) from the compliance in homogenization (c) is less than 10%.

L-shaped beam and MBB beam. We have also tested our approach on an L-shaped beam and a double-clamped beam. Figure 13 shows the optimized results. In both cases, the compliance of the de-homogenized layout is about 5% higher than the compliance after homogenization. It is worth noting that also in the stress field of the double-clamped beam a degenerate point occurs, which, according to the topological skeleton, generates a grid composed of triangular and quadrilateral mesh elements around it. In these two examples, as in previous examples, the compliance of the de-homogenized structure is lower than that from the density-based approach with a global volume constraint.

7 Conclusion and Future Work

In this paper, we have introduced a novel streamline-based parametrization of a design domain to de-homogenize the optimal continuous density layout produced by homogenization-based topology optimization. The compliance of the de-homogenized high-resolution structures is very close to that of the optimal design from homogenization-based optimization, and it is consistently superior to the compliance achieved via density-based topology optimization. The resulting structures exhibit a globally regular appearance, uniformly covering the domain with quad-dominant mesh elements.

In the current work we did not strive for an efficient implementation of the method. However, streamline integration and intersection computation can be effectively parallelized, for instance, on a GPU. The intersection points are already ordered along the streamlines, and graph as well as mesh

Examples	c ($\cdot c_0$)	c^* ($\cdot c_0$)	c^+ ($\cdot c_0$)	ξ ($\frac{c-c^*}{c^*} \times 100\%$)	#Streamlines	#Elements	t_1 (s)	t_2 (s)	t_3 (s)	t_4 (s)	T (s)
Square (Fig. 1h)	1.261	1.242	1.276	1.53%	57	647	0.85	2.46	3.74	2.17	9.22
Cantilever 1 (Fig. 8a)	1.510	1.447	1.545	4.35%	46	464	0.76	2.24	3.66	1.50	8.16
Cantilever 2 (Fig. 11c)	1.170	1.138	1.156	2.81%	66	574	1.34	3.31	4.83	1.83	11.31
Cantilever 3 (Fig. 12d)	1.661	1.533	1.675	8.35%	40	416	0.70	1.68	3.25	1.61	7.24
Cantilever 4 (Fig. 9d)	1.564	1.493	1.629	4.76%	40	376	0.63	1.40	3.13	1.55	6.71
Michell's structure (Fig. 10d)	3.176	2.837	3.286	11.95%	32	198	0.41	0.79	1.24	1.23	3.67
L-shaped beam (Fig. 13c)	1.397	1.332	1.399	4.88%	58	504	0.75	2.04	1.65	1.58	6.02
MBB beam (Fig. 13g)	1.763	1.663	1.808	6.01%	55	396	1.61	1.37	2.14	1.65	6.77

Table 1. Quality and timing statistics for streamline-guided de-homogenization. c^* and c, respectively, are the compliance of the optimal layout resulting from homogenization-based topology optimization and after streamline-guided de-homogenization. ξ measures the deviation. c^+ is the compliance by conventional topology optimization with a global volume fraction constraint. #Streamlines and #Elements refer to the number of the used streamlines, and the number of resulting mesh elements, respectively. t_1 and t_2 are the times for streamline generation and mesh construction (incl. graph extraction) during parametrization, respectively. t_3 and t_4 are the times for computing the available material budget for each mesh element and the edge thicknesses during de-homogenization, respectively. T is the overall time.

construction requires only local access operations to adjacent streamlines or intersection points. Thus, we believe that the entire approach can be implemented on the GPU so that even instant de-homogenization is possible once the continuous density layout is available. We will consider such an implementation in future work, and investigate the possibility for designers to probe different streamline densities and seeding strategies. We will also investigate post-processing techniques, either automatic or with user interaction, e.g., to remove sparse thin layers that correspond to low stiffness regions (see Fig. 11 left middle, top right and bottom right). Finally, we are particularly interested in extending this approach to design 3D beam-like lattice structures. A challenge here is that the intersection of independently traced streamlines in 3D happens only coincidentally. A possible solution is to locally relax the streamline alignment, e.g., using field-guided hex-dominant meshing [32, 18]. An alternative solution is to explore the optimization approach for constructing stream surfaces [19].

Acknowledgements

This work was supported by the German Research Foundation (DFG) under grant number WE 2754/10-1.

References

[1] Bendsøe, M., and Sigmund, O., 2004. *Topology Optimization: Theory, Methods, and Applications*. Springer Berlin Heidelberg.

[2] Sigmund, O., and Maute, K., 2013. "Topology optimization approaches". *Struct. Multidiscip. Optim.,* **48**(6), pp. 1031–1055.

[3] Bendsøe, M. P., and Kikuchi, N., 1988. "Generating optimal topologies in structural design using a homogenization method". *Computer Methods in Applied Mechanics and Engineering,* **71**(2), pp. 197–224.

[4] Bendsøe, M. P., 1989. "Optimal shape design as a material distribution problem". *Structural Optimization,* **1**(4), pp. 193–202.

[5] Sigmund, O., 2001. "A 99 line topology optimization code written in Matlab". *Structural and multidisciplinary optimization,* **21**(2), pp. 120–127.

[6] Wang, M. Y., Wang, X., and Guo, D., 2003. "A level set method for structural topology optimization". *Computer Methods in Applied Mechanics and Engineering,* **192**(1), pp. 227–246.

[7] Allaire, G., Jouve, F., and Toader, A.-M., 2004. "Structural optimization using sensitivity analysis and a level-set method". *Journal of Computational Physics,* **194**(1), pp. 363–393.

[8] Xie, Y., and Steven, G., 1993. "A simple evolutionary procedure for structural optimization". *Computers & Structures,* **49**(5), pp. 885 – 896.

[9] Norato, J., Haber, R., Tortorelli, D., and Bendsøe, M. P., 2004. "A geometry projection method for shape optimization". *International Journal for Numerical Methods in Engineering,* **60**(14), pp. 2289–2312.

[10] Guo, X., Zhang, W., and Zhong, W., 2014. "Doing topology optimization explicitly and geometrically—a new moving morphable components based framework". *Journal of Applied Mechanics,* **81**(8).

[11] Pantz, O., and Trabelsi, K., 2008. "A post-treatment of the homogenization method for shape optimization". *SIAM Journal on Control and Optimization,* **47**(3), pp. 1380–1398.

[12] Groen, J. P., and Sigmund, O., 2018. "Homogenization-based topology optimization for high-resolution manufacturable microstructures". *International Journal for Numerical Methods in Engineering,* **113**(8), pp. 1148–1163.

[13] Allaire, G., Geoffroy-Donders, P., and Pantz, O., 2019. "Topology optimization of modulated and oriented periodic microstructures by the homogenization method". *Computers & Mathematics with Applications,* **78**(7), pp. 2197–2229.

[14] Groen, J. P., Stutz, F. C., Aage, N., Bærentzen, J. A., and Sigmund, O., 2020. "De-homogenization of optimal multi-scale 3d topologies". *Computer Meth-*

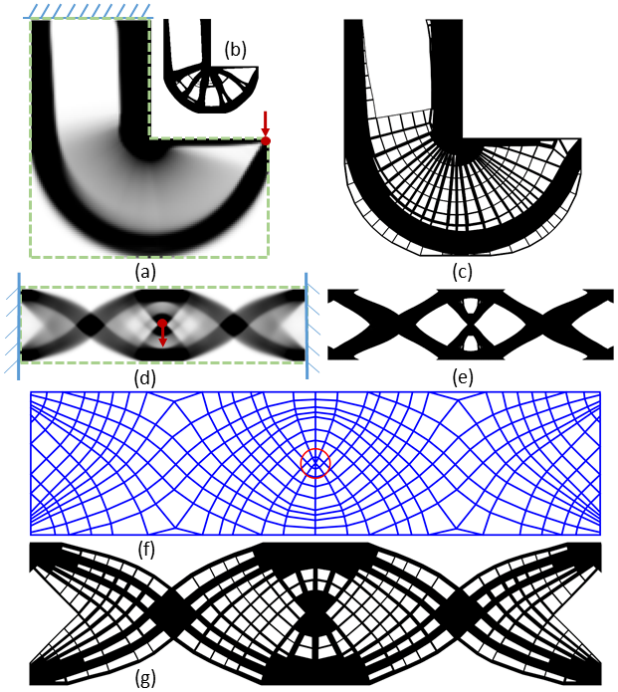

Fig. 13. (a) Optimal density layout ($c^* = 1.332c_0$, $v = 0.500$) for an L-shaped beam under a point load. (b) Inlet shows the binary result of density-based topology optimization with a global volume constraint ($c = 1.399c_0$, $v = 0.500$). (c) De-homogenization result ($c = 1.397c_0$, $v = 0.500$). (d) Optimal density layout ($c^* = 1.663c_0$, $v = 0.500$) for a double-clamped beam. (e) Binary result of density-based topology optimization with a global volume constraint ($c = 1.808c_0$, $v = 0.500$). (f) Streamline graph used for de-homogenization. A degenerate point is marked by a red circle. (g) De-homogenization result ($c = 1.763c_0$, $v = 0.500$).

ods in Applied Mechanics and Engineering, **364**, jun, p. 112979.

[15] Geoffroy-Donders, P., Allaire, G., and Pantz, O., 2020. "3-d topology optimization of modulated and oriented periodic microstructures by the homogenization method". *Journal of Computational Physics,* **401**, jan, p. 108994.

[16] Stutz, F. C., Groen, J. P., Sigmund, O., and Bærentzen, J. A., 2020. "Singularity aware de-homogenization for high-resolution topology optimized structures". *Structural and Multidisciplinary Optimization*, aug.

[17] Groen, J. P., Wu, J., and Sigmund, O., 2019. "Homogenization-based stiffness optimization and projection of 2d coated structures with orthotropic infill". *Computer Methods in Applied Mechanics and Engineering,* **349**, pp. 722 – 742.

[18] Wu, J., Wang, W., and Gao, X., 2021. "Design and optimization of conforming lattice structures". *IEEE Transactions on Visualization and Computer Graphics,* **27**(1), pp. 43 – 56.

[19] Stutz, F. C., Olsen, T. F., Groen, J. P., Aage, N., Sigmund, O., Solomon, J., and Bærentzen, J. A., 2022. "Synthesis of frame field-aligned multi-laminar structures". *ACM Transactions on Graphics*.

[20] Elingaard, M. O., Aage, N., Bærentzen, J. A., and Sigmund, O., 2022. "De-homogenization using convolutional neural networks". *Computer Methods in Applied Mechanics and Engineering,* **388**, p. 114197.

[21] Lee, J., Kwon, C., Yoo, J., Min, S., Nomura, T., and Dede, E. M., 2021. "Design of spatially-varying orthotropic infill structures using multiscale topology optimization and explicit de-homogenization". *Additive Manufacturing,* **40**, p. 101920.

[22] Zhu, Y., Li, S., Du, Z., Liu, C., Guo, X., and Zhang, W., 2019. "A novel asymptotic-analysis-based homogenisation approach towards fast design of infill graded microstructures". *Journal of the Mechanics and Physics of Solids,* **124**, pp. 612 – 633.

[23] Kratz, A., Schoeneich, M., Zobel, V., Burgeth, B., Scheuermann, G., Hotz, I., and Stommel, M., 2014. "Tensor visualization driven mechanical component design". In 2014 IEEE Pacific Visualization Symposium, IEEE, pp. 145–152.

[24] Kwok, T.-H., Li, Y., and Chen, Y., 2016. "A structural topology design method based on principal stress line". *Computer-Aided Design,* **80**, pp. 19–31.

[25] Wang, J., Wu, J., and Westermann, R., 2022. "Stress trajectory guided structural design and topology optimization". In International Design Engineering Technical Conferences and Computers and Information in Engineering Conference, American Society of Mechanical Engineers.

[26] Loos, S., Wolk, S. v. d., Graaf, N. d., Hekkert, P., and Wu, J., 2022. "Towards intentional aesthetics within topology optimization by applying the principle of unity-in-variety". *Structural and Multidisciplinary Optimization,* **65**(7), pp. 185, 11.

[27] Wu, J., Sigmund, O., and Groen, J. P., 2021. "Topology optimization of multi-scale structures: a review". *Structural and Multidisciplinary Optimization,* **63**(3), p. 1455–1480.

[28] Wang, J., Neuhauser, C., Wu, J., Gao, X., and Westermann, R., 2022. "3D-TSV: The 3d trajectory-based stress visualizer". *Advances in Engineering Software,* **170**, p. 103144.

[29] Wang, J., Wu, J., and Westermann, R., 2022. "Stress topology analysis for porous infill optimization". *Structural and Multidisciplinary Optimization,* **65**(3), pp. 1–13.

[30] Delmarcelle, T., and Hesselink, L., 1994. "The topology of symmetric, second-order tensor fields". In Proceedings Visualization'94, IEEE, pp. 140–147.

[31] Wu, J., Aage, N., Westermann, R., and Sigmund, O., 2018. "Infill optimization for additive manufacturing – approaching bone-like porous structures". *IEEE Transactions on Visualization and Computer Graphics,* **24**(2), February, pp. 1127–1140.

[32] Gao, X., Jakob, W., Tarini, M., and Panozzo, D., 2017. "Robust hex-dominant mesh generation using field-guided polyhedral agglomeration". *ACM Trans. Graph.,* **36**(4), July, pp. 114:1–114:13.